TARGETING AND CHARACTERIZING POTENTIALLY HIGH YIELD AQUIFERS IN THE NEOTECTONIC ZONES IN THE EASTERN CAPE PROVINCE IN SOUTH AFRICA

KAKABA MADI

A thesis submitted in fulfillment of the requirements for the degree of

DOCTOR OF PHILOSOPHY IN GEOLOGY

SUPERVISOR: PROFESSOR BAOJIN ZHAO

CO-SUPERVISOR: PROFESSOR OSWALD GWAVAVA

In the

Department of Geology

Faculty of Science and Agriculture

University of Fort Hare

2014

DECLARATION

This thesis is my own work and has not previously been submitted in fulfillment of the requirement of another degree or to another university.

Signature

…  ……..

11th December, 2014

DECLARATION ON PLAGIARISM

“I, Kakaba Madi, student number 200704357, hereby declare that I am fully aware of the University of Fort Hare’s policy on plagiarism, and I have taken every precaution to comply with the regulations”.

Signature

……  ……

DECLARATION ON RESEARCH ETHICS CLEARANCE

"I, Kakaba Madi, student number 200704357, hereby declare that I am fully aware of the University of Fort Hare's policy on research ethics, and I have taken every precaution to comply with the regulations. I confirm that my research constitutes an exemption to Rule G17.6.10.5 and an ethical certificate with a reference number is not required".

Signature

……  …….

ABSTRACT

The Eastern Cape Province has, besides the three known neotectonic belts (southern, eastern and northern) a fourth zone, which is inactive. This inactive zone is located almost in its central part north of the southern neotectonic zone, and south of the northern neotectonic belt. The three above mentioned neotectonic belts (southern, eastern and northern) were chosen for this study, each one with its own characteristics.

This study aims at characterizing and targeting potentially high yield aquifers in the neotectonic zones in the Eastern Cape Province.

The methods used in this study include:

1) A comprehensive literature review on neotectonics in South Africa in general and in the Eastern Cape Province in particular;

2) Extraction of lineaments through remote sensing and examination of digital elevation models;

3) Examination of seismic data for the subsurface visualization onshore and offshore;

4) Study on the genesis of the Grahamstown kaolin deposits through the structural component; and

5) Acquisition and interpretation of magnetic, electromagnetic and radiometric data from three of the hot springs in the northern neotectonic belt.

The results indicate the following:

1) Old map of seismic epicentres in South Africa need to be reviewed continually. The Eastern Cape was regarded as quiescent in terms of seismicity. However, the investigation from recent

seismic epicenters downloadable from the IRIS website has shown that recent seismic events occurred in the Eastern Cape Province especially in the northern and southern neotectonic belts. The central part located north of the southern neotectonic belt and south of the northern neotectonic belt is inactive. This inactive zone can be considered for the storage of nuclear wastes.

2) The eastern neotectonic belt has, like the northern neotectonic belt, a higher density of lineaments oriented northwest-southeast, which makes it the second important neotectonic belt. These lineaments correlate with the normalized difference vegetation index indicative of a good circulation of groundwater.

In the south, the Eastern Cape great lineament oriented east-west is now considered a neotectonic domain because many seismic epicentres occur therein. Its geomorphologic shape in graben type form is a favourable structure for groundwater catchment.

The surface topography is not uniform and high elevations in the east are related to the uplift that took place in the Quaternary. Most vector gradients are oriented east-west, a fact to be reckon with in the study of surface water flow and aquifers characterization.

3) Offshore along the east coast, the subsurface is affected by neotectonic faults, which are probably splays of the Agulhas Falkland Fractured Zone (AFFZ). The folds that occur are related to the regional compressional stress known as the Wegener Stress Anomaly (WSM). On land, straight lines from seismic profiles indicate that weathering occurs in consolidated materials probably along faults or fractures, unconsolidated sediments always have wavy profiles. On the other hand, field observations in King Williams Town have clearly shown that a tectonic uplift took place on a dolerite sill overlain by mudstones and sandstones. The uplift is possibly related

to the Amatole-Swaziland event that occurred in the last five millions years. The escarpment along this dolerite sill overlain by sedimentary rocks is a meso-scale fault with a dip-slip component. Healthy vegetation and a river flowing parallel to the cliff indicate groundwater flow in the zone of weakness.

4) In the southern neotectonic belt there is a clear northwest-southeast horizontal compression and a southwest-northeast vertical to sub-vertical extension. Enrichment of granitic breccias and feldspar in the Grahamstown Dwyka tillite is the source for the formation of kaolin deposits. The weathering starts in the granitic breccias through their extensional fractures and then extends in the matrix, which has micro-fractures that are only visible with the transmitted microscope. Combined extensional strike-slip and dip-slip faulting is responsible for the earthquakes in the region of Grahamstown where the kaolin is formed. There is also an unreported thermal (quartz veins) and neotectonic event identified in this region.

5) The hot springs in the northern neotectonic belt are connected by a regional neotectonic fault. The use of magnetic and electromagnetic methods helped to decipher the occurrence of faults, fractures, dolerite dykes, and variable degree of weathering.

Uranium/potassium ratios derived from radiometric surveys show that areas around some hot springs are characterized by enrichment in uranium. High concentrations of thorium are related to its low capacity of being easily dissolved in water.

It can be concluded that seismicity, hot springs and accordingly deep groundwater circulation, high density of lineaments, quaternary tectonic uplift, are the predominate characteristics of the three neotectonic zones.

Furthermore, on the environmental point of view, thorium concentration is higher than that of either uranium or potassium. Although it is nonetheless below the world average threshold of 7.4 ppm according to United Nations Scientific Committee on the Effects of Atomic Radiation (UNSCEAR), it may be a source of radiation hazard to humans and animals if they are subjected to prolonged exposure.

All the neotectonic zones in the Eastern Cape Province present potentials to host good and important aquifers.

It is suggested that the Eastern Cape great lineament in the southern neotectonic belt and the Kokstad-Koffiefontein seismic belt in the northern neotectonic belt, be monitored for future research regarding, neotectonics, seismic risk assessment and hydrogeology.

Keywords: Neotectonics, Lineament, Seismic Profile, Stress, Kaolinisation, Hot Spring

ACKNOWLEDGMENT

First and foremost I would like to thank the Lord Jesus Christ for all the help I got from Him, this thesis was completed because of the blessings He bestowed upon me. I greatly give praises to Him for his divine intervention from the beginning to the end of this project.

I would like to thank the National Research Foundation (NRF) South Africa for financial support during the two first years of this project through the IRDP at the University of Fort Hare. The Govan Mbeki Research and Development Center of the University of Fort Hare is thanked for all the support in terms of finance. Mrs Rina Flanegan and Mrs Michelle Flanegan are kindly remembered.

I sincerely thank my supervisor Professor Baojin Zhao who has encouraged me to continue with the neotectonic project at doctoral level; I also thank him for his supervision, mentorship, and moral support.

Acknowledgement goes also to my Co-Supervisor Professor Oswald Gwavava for his assistance regarding logistical and technical support, and constructive remarks.

I wish to thank the Council for Geoscience (CGS) through Peter Nyabeze for the geophysical data collection, without forgetting Sekiba Matome (also from CGS) who was very instrumental during our data collection campaign.

I would like to express my gratitude to PetroSA to have supplied its offshore and onshore seismic data free of charge, and to have given authorization to use them.

I also remember all the staff members from the Department of Geology at the University of Fort Hare for their support.

I would like to thank Mrs Aletta Vos and Dr Monyai for English edition and Ms Lindani Ncube for proof reading.

I extend my gratefulness to my brothers and sisters in Christ Jesus for their continuous prayers.

I do not forget my mother and my family members for their advices and their moral support during my time of research.

My heartfelt gratitude to my wife Sikhanyiso Madi who was very supportive and constantly praying for me.

LIST OF ABBREVIATIONS AND GLOSSARY OF TERMS

AFFZ: Agulhas Falkland Fractured Zone

CBF: Cape Fold Belt

CGS: Council for Geoscience

DEM: Digital Elevation Model

DWAF: Department of Water and Forestry

ECGL: Eastern Cape Great Lineament

EM: Electromagnetic

ETM: Enhanced Thematic Mapper

GLOVIS: Global Visualisation Viewer

GLS: Global Land Survey

IRDP: Institutional Research Development Programme

IRIS: Incorporated Research Institutions for Seismology

LOI: Loss of Ignition

MOSSGAS: Mossel Bay Gas

NASA: National Aeronautic and Space Administration

NDVI: Normalized Difference Vegetation Index

NMO: Normal Move out Correction

PCA: Principal Component Analysis

SACS: South African Committee for Stratigraphy

SOEKOR: Southern Oil Exploration Corporation

SPN: Shot Point Number

SPOT: Système Pour L'Observation de la Terre (System for the Observation of the Earth)

SRTM: Shuttle Radar Topography Mission

UNSCEAR: United Nations Scientific Committee on Effects of Atomic Radiation

USGS: United States Geological Survey

WSM: Wegener Stress Anomaly

XRD: X-ray Diffraction

XRF: X-ray Fluorescence

TABLE OF CONTENTS

LIST OF TABLES

LIST OF FIGURES

1. INTRODUCTION

1.1General background

The Eastern Cape Province is mostly dominated by the rocks of the Karoo Supergoup in terms of geology. Botha et al. (1998) indicated that there is a potential that aquifers in the Karoo Supergroup can significantly contribute to the water budget of the country; unfortunately, Karoo aquifers are very complex and unpredictable in their behavior. Another important factor to mention is the very low permeability of the sandstone, mudstone, shale and siltstone, and the very low yield (< 3.6 m^3 h^{-1}) of previously drilled boreholes in the Karoo sediments.

In order to target and to characterize the neotectonic zones in terms of aquifers yield in the Eastern Cape Province, different approaches have been taken into account, namely: remote sensing, seismicity and stress inversion methodology and the geophysical investigations of hot springs.

Remote sensing has been used in groundwater exploration as a reliable method to carry out quantitative determination of lineament densities on the Earth's surface, and is quite essential to outline linear structures that are undoubtedly good conductors for groundwater.

Geological interpretation derived from remote sensing has been extensively used for the purpose of identification of lineaments and fractured zones along which the flow of groundwater may take place. Mohamed (2010) indicated that the surface lineaments are in parallelism with the subsurface basement fault. Ölgen (2004) stated that Earth scientists have been interested in linear features on the earth's crust since the early period of each observation. Elmahdy and Mohamed (2012) highlighted that lineaments are features that represent pathways for groundwater

accumulation, groundwater discharge and seawater intrusion into coastal and inland aquifers. Burnett (2011) pointed out that lineaments and surface dips are useful for locating trapped groundwater. Contes and Carla (2011) used remote sensing in Puerto Rico, and found that geomorphic data agrees with lineaments as faulting and fracturing in addition to linear bedding control features. Moreover, Ali et al. (2012) mentioned that remote sensing has been used in geology for lithological discrimination of different rock types and delineation of geological and structural features.

The use of remote sensing in this study was aimed at extracting lineaments in order to find zones of high density lineaments that can be used for groundwater exploration. High density lineament zones can also be used while considering environmental issues. Nuclear wastes dump sites can be placed in zones not affected by high seismicity and high density lineaments in order to avoid groundwater contamination.

Neotectonics is a branch of structural geology that studies the more recent tectonic movements of the earth, which activity is related to the earth movement, stress building and results in seismicity. The Eastern Cape Province, which is not very seismically active, except its northern region near the country of Lesotho, has been affected by seismic magnitude, up to 6 on the Richter scale. Barth et al. (2008) highlighted that earthquakes are one of the most evident effects of stress release in the crust. Focal Mechanism Solution can be determined by P-wave first motion, polarization and amplitudes of S-waves (e.g. Khattri, 1973), the analysis of P/S amplitude ratio (e.g. Kisslinger et al., 1981) and the moment tensor inversion (Stein and Wysession, 2003). The methods of Delvaux et al. (2007) adopted in this study used the stress inversion model developed by Angelier and Mechler (1977) as a graphical method. This graphical method is used for the determination of the possible orientation of the compressional

stress σ_1 and the extensional stress σ_3 incorporating the application of the Right Dihedron method. The Right Dihedron method is based on a reference grid of orientations predetermined in such a way they appear as rectangular grids on the stereonet in the lower hemisphere Schmidt projection. The Focal Mechanism Solution (stress regime) helps to determine what type of faults such as normal, thrust, strike-slip, transtension (combination of normal and strike-slip), transpression (combination of thrust and strike-slip) was at the origin of the earthquake. The stress regime related to neotectonics can cause seismic activities triggering fracturing and faulting in the Quaternary deposits such as the kaolin from the Grahamstown area, and other recent formations such as calcretes, silcretes, and ferricretes.

High yield wells in the Karoo aquifers of the Eastern Cape can be targeted as zones of high density lineaments and seismically active zones. These seismic zones are of prime importance if they host hot springs, which can discharge a lot of water because of the movement in the crust. For instance, the hot springs of Aliwal North, Badfontein and Polile Tshisa near the border of the country of Lesotho are found in what is a known as the Kokstad-Koffiefontein seismic belt. This belt hosts seven hot springs along an east-west trending active fault.

Anderesn and Ainslie (1994) indicated that the origin of the thermal springs is attributed to the presence of deep structures, principally fault-zones, which provide continuously circulating convection or artesian systems in the Pietersburg area (South Africa). In the same context, it can also be considered that the basaltic eruption of 1983 in Lesotho as reported by Maud et al. (1998) might have been related to the ascension of magma in the area, heating the water from beneath. Dirik and Goncuoglu (1996) found that in the central Anatolia (Turkey), alignment of hot springs, cinder cones, drainage offset, and linear valleys are the characteristic features of strike-slip fault patterns observed in the region.

Three neotectonic zones were identified in the Eastern Cape that is the second largest of the South Africa nine provinces in terms of surface area. The potentially high yield aquifers are related to neotectonic zones, namely the southern, the eastern and the northern neotectonic zones. Neotectonics causes the creation of new fractures and the reactivation of old ones.

Apart from remote sensing, potentially high yield aquifers can be targeted and characterized by using geophysical techniques. Seismic reflection is an important tool used in the exploration of groundwater. It is however mainly used in oil exploration to characterize the subsurface reservoir. This will include the genesis, evolution and internal architecture of sedimentary-basin fills in order to come up with a model that can display the sequence stratigraphy, structure geology, subsidence and the uplift (e.g. Catuneanu et al., 2009). Through the use of other known geophysical methods in groundwater exploration (e.g. Van dongen and Woodhouse, 1994), regional aquifers can be mapped using gravity and magnetic methods. It is however important to note that though various geophysical methods have been used for groundwater characterization, the electrical and electromagnetic methods have proven to be successful in mapping both contaminated and clean groundwater. Radiometric methods are used to interpret and map the concentration of uranium, thorium and potassium and their effects on groundwater in subsurface rock formations (e.g. Maxwell et al., 2012). In this project the Eastern Cape northern neotectonic belt was targeted for geophysical characterization, primarily because it is located in the Kokstad-Koffiefontein seismic belt, and secondly because it has many hot springs. Three of these springs were selected for this purpose.

Radiometric or gamma ray spectrometry methods can also be used to characterize the regolith up to 40 centimeters below the earth's surface (e.g. Cooke et al., 1996); K, Th and U have different radiometric signatures during weathering and pedogenesis (Wilford, 2002). Targeting and

characterizing the neotectonic zones in an effort to maximize the production of groundwater in the Eastern Cape Province is of great importance in solving the problems related to water scarcity. Radiometric surveys cannot be neglected and not only must potentially high yield aquifers be found, but the environmental impact must also be considered.

1.2 Research area

The Eastern Cape Province is surrounded by three neotectonic belts; the southern, eastern, and northern neotectonic belts. Although the southern neotectonic belt is characterized by the reactivation of the Kango-Baviaanskloof fault, areas of research were targeted mainly in the eastern region along the coast and the northern region near the country of Lesotho. The east coast was affected by the Pliocene uplift stretching from Swaziland to the Amatole District in the Eastern Cape Province. The northern region is of interest because of its seven hot springs and its seismic belt that is characterized by a tight clustering of epicenters (Figure 1.2). Figure 1.1 and Table 1.1 indicate different localities for field investigation and data collection.

Table 1- 1: Areas of field investigation and data collection

Site	Latitude	Longitude	Place name
1	-33.17215	26.32628	Eastern Cape Great Lineament (ECGL)
2	-33.31466	26.51736	Grahamstown
3	-32.98334	27.86330	East London
4	-32.77449	26.63326	Fort Beaufort
5	-32.78207	26.85066	Alice
6	-32.45673	28.00040	Butterworth
7	-31.04806	30.21571	Port Saint Johns
8	-30.68668	26.70084	Aliwal North
9	-30.77698	25.79513	Venterstad
10	-30.68634	25.76924	Orange Fish Tunnel
11	-30.48730	28.64274	Polile Tshisa
12	-28.59083	20.33431	Augrabies Falls
13	-30.82105	26.54353	Badfontein

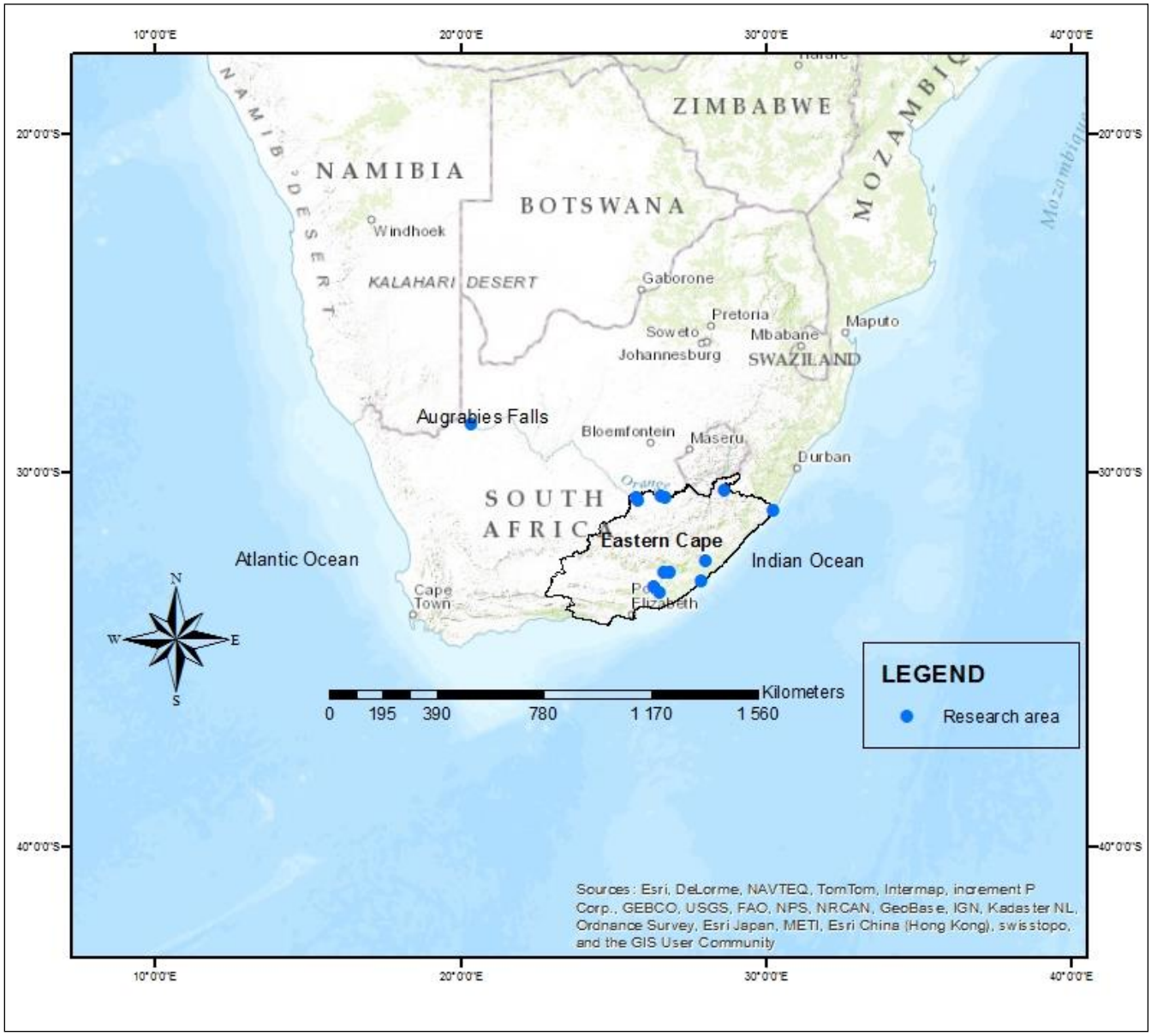

Figure 1- 1: Map showing localities chosen for field investigation. (Source: ESRI).

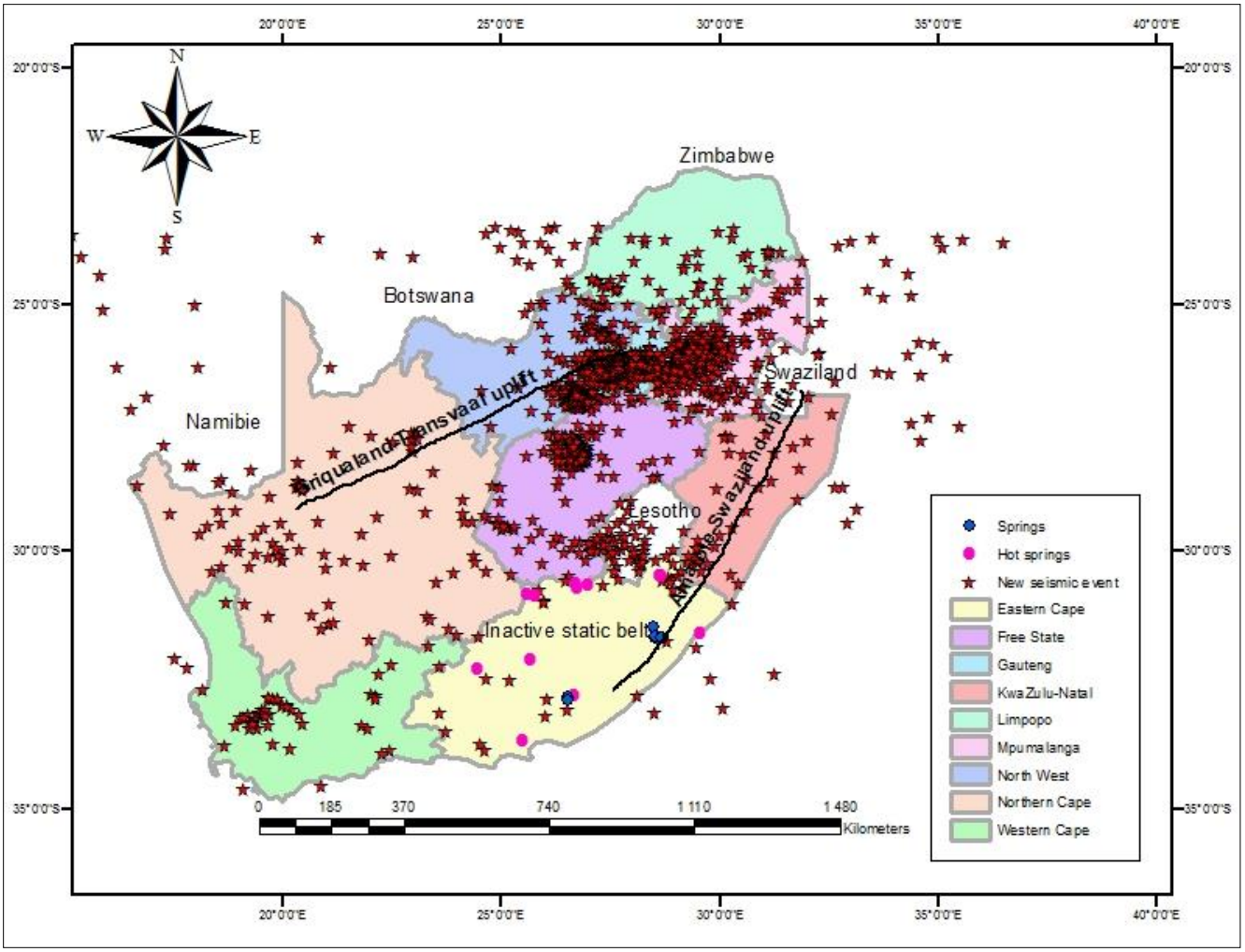

Figure 1- 2: Seismic epicenters in southern Africa and hot springs in the Eastern Cape Province.

1.3 Problem statement

The province faces the challenge of groundwater scarcity. The Department of Water and Forestry (DWAF) in its Groundwater Master Plan Report has for instance indicted that there are few productive aquifers in the Eastern Cape Province. Should still there be any water, a wind pump or hand pump could be installed. At best this could be enough for individual household consumption. One can generally expect enough water for either hand- and/or wind pumps, i.e. small supplies for small communities and/or stock watering or single households. Little

additional groundwater could be available for community gardening or other poverty alleviation actions. Many boreholes will have to be drilled to obtain a yield at the high-end of the range. Targeting and characterizing of the neotectonic zones is necessary in order to determine the best site to drill so many boreholes. As neotectonics implies the creation of new fractures and the reactivation of old ones it is a good indication for future drilling programs.

Neotectonics is strongly related to seismic activity in any given region; if there are no earthquakes, there is no neotectonics either. The Eastern Cape Province is known for being dormant in terms of earthquake activities. If this is to be taken into account, the location of neotectonic zones would be problematic. With this in mind other factors can be considered, such as zones of the late Quaternary uplift along the east coast. The fault regime can be indirectly derived by stress inversion only in the recent formations, which are scarce in the province.

1.4 Aims and objectives

This study is aimed at characterizing the neotectonic belts in the Eastern Cape Province in terms of surface lineament density, subsurface visualization, neotectonic stress fields, and geophysics. The objectives of this project are as follows:

- To apply remote sensing in order to extract all possible linear features in the Eastern Cape Province, this will help to analyze the lineament distribution.
- To compare the lineaments density from the neotectonic belts and the non-neotectonic areas such as the Queenstown area in the central, inactive zone.
- To analyze zones of high density lineaments in terms of predominant orientation, this is of prime importance regarding groundwater potential in the Karoo aquifers.

- To have an insight in some neotectonic zones below the Earths' surface by examining the 2D seismic data offshore and onshore along the east coast.
- To determine the type of fault regime (normal, thrust, strike-slip) that triggers the seismicity in the neotectonic zones (e. g. Grahamstown area).
- To apply geophysical methods especially in the hot springs of the Eastern Cape northern neotectonic belt in order to confirm and predict target areas of future productive wells, incorporating the environmental points of view for health concerns.

1.5 Project rationale

Though the Eastern Cape Province is characterized by a quasi seismic scarcity, some seismic events were recorded as mentioned above. The fault regime has never been determined before. Targeting of high yield aquifers in the Eastern Cape remains a challenge. Most of the Karoo aquifers have very low discharge rates, and the Province is confronted by water shortages.

With the increased population growth and productivity, the consumption of groundwater is also increasing dramatically. In a media release, the Department of Water and Forestry (DWAF, 2005) outlined that the particular dry areas are along the west coast of South Africa and in the Karoo area. Other activities like mining and drilling may have a negative impact on the recharging of the aquifers. The Karoo is mainly characterized by a semi-arid climate. A report from Karoo Space (www.karoospace.co.za) for instance, highlights the fact that mining programs that requires convoys of massive trucks travelling over the Karoo veld will undoubtedly damage the veld; this is valid in areas which get very little rain. Many boreholes that were dug before are not operational at present, especially in rural areas and some villages due to poor management and carelessness. There is a need to dig new boreholes in order to

provide water to the growing population. Finding groundwater in the Karoo requires a good understanding of the nature of the aquifers, methodologies and techniques as one can often end up targeting dry aquifers. To avoid all foreseeable difficulties in the Karoo, a detailed study and good planning must be taken into account to come up with productive wells.

The combination of the stress field study (with emphasis on the orientation), neotectonics, remote sensing, and geophysics can alleviate the difficulties encountered when trying to position or target potentially highly productive boreholes, mainly in dry areas.

1.6 Research outline

This thesis is subdivided in nine chapters. Chapter 1 gives a highlight of the complexity of the Karoo aquifers and includes the approach used to target and to characterize the aquifers in the neotectonic belts. The approaches include seismic interpretation, remote sensing analysis, study of current neotectonic stress derived from the kaolin deposit, and geophysical investigation. It also gives an overview on the research area (eastern, southern, and northern neotectonic belt), the aims and objectives, and the project rationale.

The Eastern Cape is covered by rocks of the Cape Supergroup and predominantly those of the Karoo Supergroup. Their structural evolution and lithostratigraphy are presented in the literature review in Chapter 2. Chapter 2 also gives a background on neotectonics and geomorphology in the Eastern Cape in particular and in South Africa in general. Detailed methodologies of this project can be traced in Chapter 3. Chapter 4 deals with the surface lineaments extraction, lineaments predominant trend, Normalized Difference Vegetation Index characterizing green vegetation synonymous with considerable amount of groundwater flow, Digital Elevation Model, and overview of the Eastern Cape Great Lineament (ECGL), which is a neotectonic domain. The

seismic data collected by SOEKOR and provided by PetroSA were used in Chapter 5 to visualize the subsurface offshore and on land. Investigation of the formation of the Grahamstown kaolin deposit used for the study of the neotectonic stress, and geophysical investigation in the vicinity of hot springs in the northern neotectonic belt is documented in Chapter 6 and 7 respectively. All data were discussed in Chapter 8 followed by conclusions in Chapter 9.

2. LITERATURE REVIEW

2.1. Introduction

The Eastern Cape (Figure 2.1) comprises of rocks of the Cape Fold Belt (CFB) in the south and rocks of the Karoo Supergroup in the north.

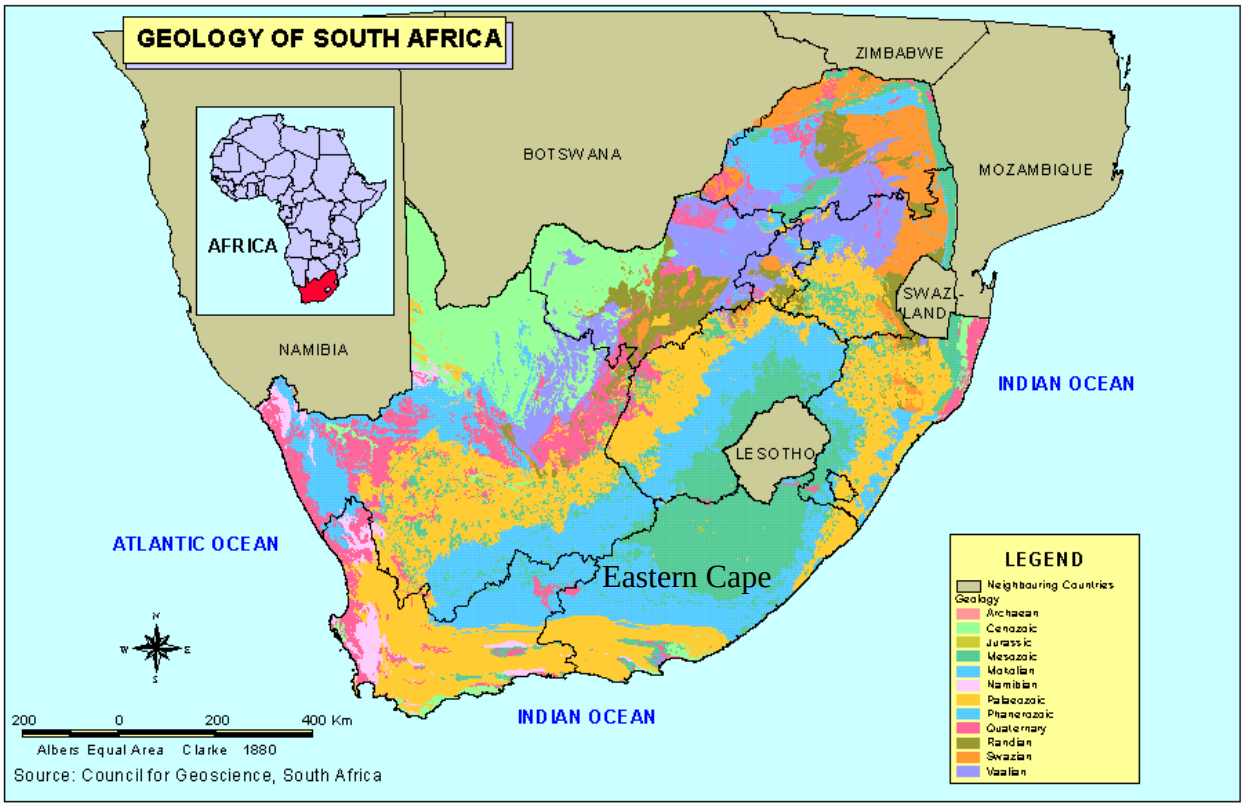

Figure 2- 1: Geology of South Africa, source of the map: Council for Geoscience.

Newton (1973) advocated a gravity tectonic model in an intracratonic setting for the CFB, while Lock (1980) suggested a flat-plate subduction model to explain the long distance between the fold belt and a proto-Andean subduction zone around the southern periphery of Gondwana.

Current ideas (Johnson, 1990; Visser, 1992a) regard the CFB as a fold thrust situated along an inner arc, and the Karoo Basin as a foreland basin north of it.

2.2 Cape Orogeny (western and southern branch)

The Hercinian Cape Fold Belt (CFB) consists of two branches that form a mountain chain along the south coast and part of the west coast of the Republic of South Africa. The Permo-Triassic Cape Orogeny deformed the precursor stratigraphic succession. The pre-deformation setting consisted of a Late Proterozoic volcano-sedimentary basement that was intruded by the later 520 – 585 Ma Cape Granite Suite. This was overlain by an Ordovician to Triassic cover sequence made up by the Cape Supergroup and a portion of the Karoo Supergroup (R. Scheepers, pers. comm.).

The western branch

During the Cape Orogeny, Malmesbury Group basement rocks were refolded by kinking of existing Pan-African foliation. The structure of the cover rocks in the northern domain is dominated by open synclines and parallel minor folds which may display steep dips in places. The generally northerly trend of the fold axes swing progressively northwest towards Lamberts Bay; north of Clanwillian the flexures fade out so that the Table Mountain Group horizontally overlies basement in the Klaurk-Niewoudtville axe (De Swardt and Russell, 1974).

The southern domain of the Malmesbury basement is characterized by granite that intrudes into Malmesbury Group. In the Cape Peninsula area the Table Mountain Group is essentially horizontal, while further east dips rarely exceed 15^{o}. De Villiers (1994) observed a minor monoclinal fold while occasional steep dips may be related to block faulting or incipient fold generation. De Beers (1990) believed that the apparent zonal development of high buckling

strains in the Table Mountain Group rocks is linked to transpression that may have played a part in the folding.

The southern branch

The southern branch displays northerly verging, often overturned first-order folds and recrystallization cleavage in pelites sliced by thrusts and normal faults striking roughly east. Hälbich and Swart (1983) found in the CFB the following features:

1. The basement was affected by three approximately coaxial phases of compressional deformations. Basement granites display cataclastic deformations as widespread mylonitization and brittle thrusting, with kinking of Pan-African foliation.
2. There are changes in styles and intensity of deformation in the cover rocks across the CFB.
3. In zone 1, north of the Swartberge, the cleavage is only locally developed at the leading edges of small listric thrusts, while horizontal shortening is minimal. The northern boundary coincides with the northern edge of the Southern Cape Conductive Belt in the crust (De Beer, 1983). The southern boundary of zone 1 coincides with the Beattie Magnetic Anomaly.
4. Zone 2 displays open symmetric and upright flexural slip folding. A spatial spaced axial-planar cleavage S_4 (Hälbich et al., 1983) is developed in fine grained pelites. Quartz microfabrics indicate N-S-oriented maximum principal stress.
5. Zone 3 is characterized by asymmetric and inclined concentric folds. A well-developed, fanning axial-planar cleavage S_1 becomes slaty in fine-grained rocks and displays evidence of dewatering, followed by final mica recrystallization.

6. Zone 4 presents second-order cascade folds on overturned limbs. Two recrystallized cleavages developed in fine grained pelites.
7. The sudden rapid increase in fold intensity in the cover rocks in the third and fourth zones is ascribed to rapid stratigraphic thickening of the Table Mountain Group.
8. The southern edge of the Southern Cape Conductive Belt (approximately coincides with the Kango fault) joins the northern boundary of zone 5 between the inland Swartberge and coastal Outeniqua Range.
9. The coastal Outeniqua Range of zone 6 contains acute to isoclinals folds with flat south-dipping axial plans S_2 slaty cleavage, S_3 crenulation cleavage, kinks and a prominent down-dip mineral elongation lineation. In the Eastern Cape Province, the general Stratigraphy is represented by the Cape Supergroup (Table Mountain Group, Bokkeveld Group and Witterberg Group) as can be seen in Table 2.1; 2.2 and 2.3.

Table 2- 1: Stratigraphy, lithology and palaeoenvironments of the Table Mountain Group. Figures in brackets are the approximate thickness in metres. "Shallow marine" denotes high-energy coastal environments (beach, shoreface, barrier, etc.). (After Thamm and Johnson, 2006).

AGE		WEST OF~ 21°E		EAST OF~ 21°E	LITHOLOGY	PALAEOENVIRONMENT
		FORMATION		FORMATION		
DEV	NARDOUW SUBGROUP	Ritvlei (200)	NARDOUW SUBGROUP	Baviaanskloof (200)	Sandstone (+shale in East)	Shallow marine (+offshore shelf in east)
SILURIAN		Skurweberg (300)		Skurweberg (400)	Sandstone (thick bedded)	Fluvial braid-plain, shallow marine
		Goudini (200)		Goudini (300)	Sandstone (red-brown)	Shallow marine, fluvial braid-plain
ORDOVICIAN		Cedarberg (120)		Cedarberg (50)	Shale, siltstone	Offshore shelf
		Pakhuis (80)		-	Diamictite, sandstone	Glacial
		Peninsula (2000)		Peninsula (2700)	Sandstone	Fluvial braid-plain, shallow marine
		Graafwater (430)		Sardinia Bay (900?)	Sandstone, siltstone, shale	Distal fluvial, tidal flat, shallow marine
		Piekenierskloof (900)			Sandstone, conglomerate	Fluvial braid-plain

Table 2- 2: Stratigraphy, lithology and palaeoenvironments of the Bokkeveld Group. Figures in brackets are the approximate maximum thickness in metres. “Shallow marine” denotes high-energy envirnments (beach, shoreface, barrier, etc.). (After Thamm and Johnson, 2006).

AGE	WEST OF~ 21°E		EAST OF~ 21°E		LITHOLOGY		PALAEOENVIRONMENT	
		FORMATION		FORMATION				
DEVONIAN	BIDOUW SUBGROUP	Karoopoort (150)	TRAKA SUBGROUP	Sandpoort (400)	Mudrock, Siltstone, sandstone		Tidal flat, delta front, prodelta slope, shelf	
		Osberg (55)		Adolphspoort (600)	Sandstone (siltstone in east)		Distributary channel, shallow marine, (prodelta slope in east)	
		Klipbokkop (300)		Karies (1300)	Mudrock,siltstone, sandstone	Karies Formation: Mudrock, rhythmite	Tidal flat, delta front, prodelta slope, shelf	Karies Formation: Deep marine
		Wuppertal (70)			Sandstone, siltstone		Tidal flat, delta front, shallow marine	
		Waboomberg (200)			Mudrock, siltstone, sandstone		Offshore shelf, prodelta slope	
	CERES SUBGROUP	Booplaas (100)	CERES SUBGROUP	Booplaas (100)	Sandstone		Delta front, shallow marine	
		Tra-Tra (85)		Tra-Tra (350)	Mudrock, siltstone		Offshore shelf, prodelta slope	
		Hex River (60)		Hex River (60)	Sandstone		Delta front, shallow marine	
		Vooerstehoek (200)		Voorstehoek (300)	Mudrock, siltstone		Offshore shelf, prodelta slope	
		Gamka (70)		Gamka (200)	Sandstone		Delta front, shallow marine	
		Gydo (150)		Gydo (600)	Mudrock, siltstone		Offshore shelf, prodelta slope	

Thamm and Johnson (2006) mentioned that the Table Mountain Group is a typical early Palaeozoic cratonic sheet sandstone. It has subdivided in several formations whose basement onlapping character has been demonstrated by Rust and Theron (1964). The Bokkeveld Group comprises a cyclic alternation of fine-grained sandstone and mudrock units. The Witterberg Group comprises quartzitic sandstone and micaceous mudrock in approximately equal proportions.

Table 2- 3: Stratigraphy of the Witteberg Group (Tankard et al., 1982).

	Western part of Basin			Eastern part of Basin			
SUBGROUP	**FORMATION**	**(m)**	**LITHOLOGY**	**FORMATION**	**(m)**	**LITHOLOGY**	**INTERPRETATION**
KOMMADAGA				Dirkskraal	110	Feldspathic sandstone, orthoquartzite	Fluvial
				Soutkloof	165	Mudstone, shale, varved shale	Proglacial/lacustrine
				Swartwaterspoort/ Miller	6 95	Sandstone, diamictite, intertonguing	Glaciofluvial/glaciogenic
LAKE MENTZ	Waaipoort	250	Mudstone, greywacke	Waaipoort	460	Greywacke, mudstone, feldspathic sandstone	Glaciofluvial/lacustrine
	Floriskraal	120	Feldpspathic sandstone	Floriskraal	120	Shale, mudstone, orthoquartzite	Fluvial and shore zone
	Kweekvlei	130	Black fossile Shale	Kweekvlei	200	Shale, siltstone	Lacustrine shelf?
	Witpoort	310	Orthoquartzite, rare shale lentils	Witpoort	850	Orthoquartzite with rare shale lenses	Barrie sands; tidal flats
WELTEVREDE	Swartruggens	400	Siltstone, shale, interbedded sandstone				Tidal flats
	Blinkberg	100	Orthoquartzites	Weltevrede	850	Shale, siltstone, thick orthoquartzite	Barrier sands of reworked delta
	Wagen Drift	165	Shale, siltstone, interbedded sandstone				Subaqueous delta

2. 3 Karoo geology

During the Early Carboniferous, sedimentation of the Cape trough ceased because of a lowering of global sea levels (Visser, 1990). The axis of maximum downwarp of the crust was displaced farther towards the north and the remarkable Karoo foreland basin, which covers fully two third of South Africa, came into existence. Figure 2.4 gives a detailed lithostratigraphy of the Karoo.

Table 2- 4: Detailed lithostratgraphy of the Karoo Supergroup (Johnson et al., 2006)

SUPER GROUP	GROUP	SUBGROUP	FORMATION	MEMBER	LITHOLOGY	MAXIMUM THICKNESS (M)
KAROO			Drakensberg		Basalt Pyroclastic Deposits	1400
			Clarens		Sandstone	300
			Elliot		Red Mudstone Sandstone	500
			Molteno		Coarse Sandstone Grey & Khaki Shale Coal Seam	450
	BEAUFORT	TARKASTAD	Burgersdorp		Red Mudstone Sandstone Light Grey Sandstone Grey Shale	1000
			Katberg		Light Grey Sandtone Red Mustone Grey Shale	900
		ADELAIDE	Balfour	Palingkloof	Red Mudstone Light Grey Sanstone	50
				Elandsberg	Sandstone Siltstone	700
				Barberskrans	Light Grey Sandtone Khaki Shale	100
				Daggaboersnek	Grey Shale Sandstone Siltstone	1200
				Oudeberg	Light Grey Sanstone Khaki Shale	100
			Middleton		Grey & Black shale Light Grey Sandstone Red Mudstone	1500
			Koonap		Grey Sandstone Shale	1300
	ECCA		Waterford (Not present in ECCA Pass)		Sandstone Shale	800
			Fort Brown		Shale Sandstone	1500
			Ripon		Sandstone Shale	1000
			Collingham		Grey Shale Yellow Claystone	30
			Whitehill		Black Shale Chert	70
			Prince Albert		Khaki Shale	120
	DWYKA				Diamicite, Tillite, Shale	

A generalised vertical column (from Flint et al., 2011) for the Cape and Karoo Supergroups can be seen in Figure 2.2 below.

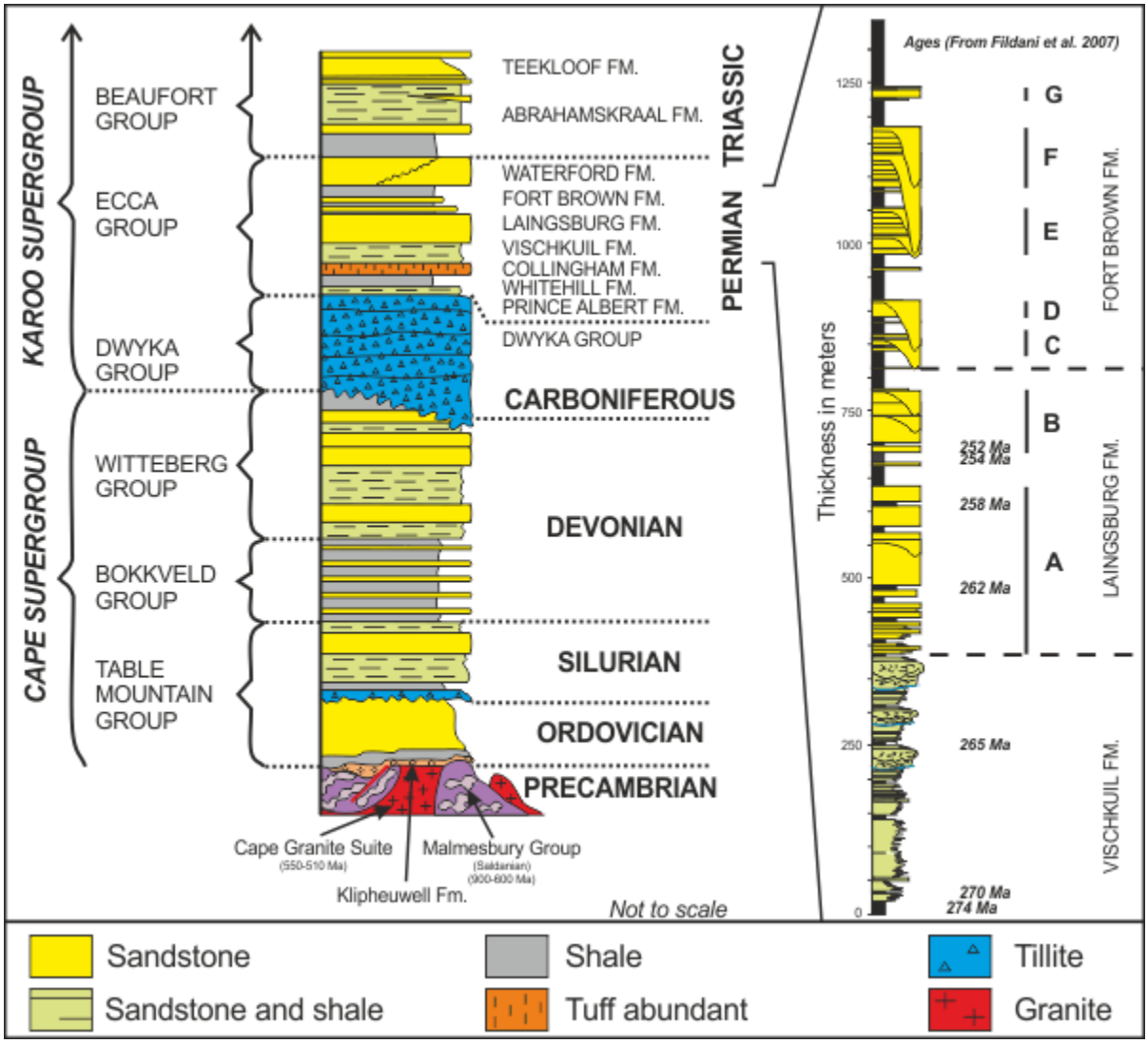

Figure 2- 2: A generalised vertical column for the Cape and Karoo Supergroups (Flint et al., 2011)

Tankard et al. (2009) found that the Cape Fold Belt is a strike-slip orogen with a sinistral sense of displacement on the Worcester and Kango shear zones. This srike-slip displacement was related to the reactivation of the southern Namaqua suture.

Catuneanu et al. (1998) interpreted the Karoo as a retro-arc foreland basin that developed behind an inferred magmatic arc and fold thrust belt. However Tankard et al. (2009) argued that no geophysical evidence related to a nearby magmatic arc is present. On the other hand the Cape Fold Belt dates to late Karoo time and confirmed that the basement architecture timing of the Cape orogeny and stratigraphic relationships are typical of a flexural foreland basin.

Pysklyvec and Mitrovica (1999) alternatively explained that the long-wavelength component of subsidence resulted from lithospheric deflection due to mantle flow coupled to distinct subduction.

Tankard et al. (2009) demonstrated that the sedimentary fill in the Cape and Karoo basins is made up of several unconformity-bounded megasequences. These megasequences indicate that each basin episode consists of a three-stage evolution, involving crustal uplift, fault controlled subsidence and long periods of regional subsidence during which faulting was subordinate. Subsidence of the Cape and Karoo basins was facilitated by rigid blocks of Precambrian basement and crustal scale faults that separated them. The Hartbees-Mbyoti fault (Figure 2.3) played an important role regarding the late Karoo subsidence. Boundary forces associated with the fold belt and the echelon Hartbees –Mbyoti and Doringberg-Tugela fault zones created a late Karoo transitional foreland basin.

The Final phase of Karoo sedimentation was brought to a close by the eruption of at least 1400 m of Drakensberg Group basalts lava and the intrusion of the Karoo dolerite dykes and sills into the underlying sediments. The sedimentation of the Karoo Basin began by the deposition of the Dwyka Formation, followed by the Ecca Group, the Beaufort Group, and the Molteno, Elliot and

Clarens Formations, each having its hydrological properties. As can be seen in Table 2.4, the thickness of different formations is not uniform.

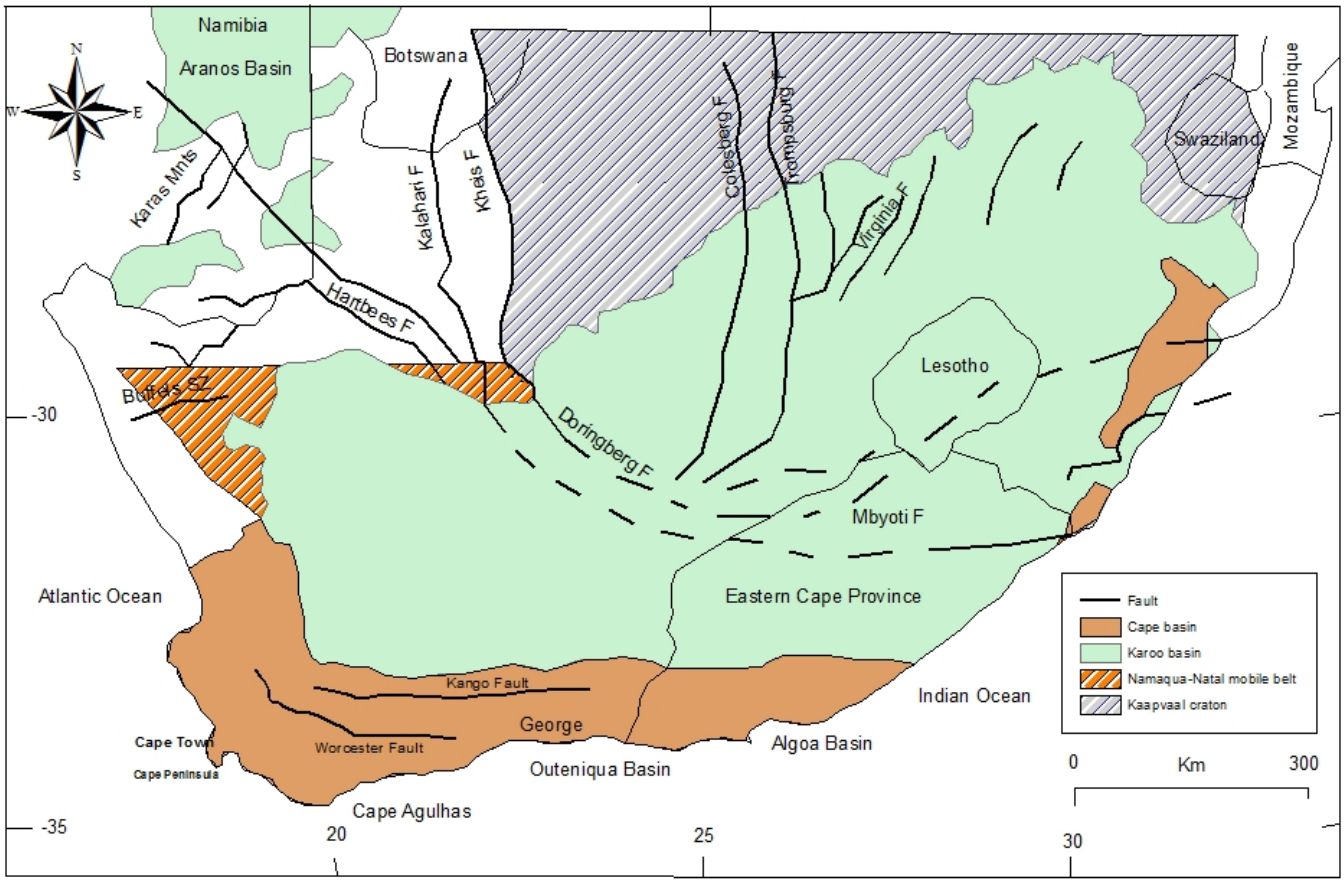

Figure 2- 3: Map showing crustal scale faults that were associated with subsidence of Precambrian basement. (Tankard et al., 2009).

2.4 Neotectonic zones in the Eastern Cape

2.4.1 Overview of neotectonics in Southern Africa

The commencement of neotectonics in Southern Africa has never been established (Friese et al., 2006). According to Burke (1996) the beginning of neotectonic activity in southern Africa is envisaged to have started with the Oligocene at ~35Ma, which coincides with the African

continent becoming stationery over the so called African Superplume. Andreoli et al. (1996) proposed neotectonic activity in South Africa to have been initiated in the Miocene (~25Ma).

The works of Andreoli et al. (1996) as well as Viola et al. (2005) highlighted that seismicity in southern Africa is driven by regional stresses originating from large-scale features that include intracontinental rifts, large-scale topographic elevations (such as the border of Lesotho and South Africa north of the Eastern Cape Province), and the network of mid-oceanic ridges.

The South Africa-Lesotho border is characterised by the Kokstad-Koffiefontein seismic belt. Baichund et al. (2009) quoting Joubert et al. (1991) and Brandt (2000) pointed out that this area has two seismic clusters:

-the Koffiefontein cluster characterised by a large earthquake (Mw 8) that occurred some 50,000 years ago, and;

-the Lesotho cluster characterised toward the west and south of Lesotho by a seismicity of natural origin, undoubtedly the high topographic feature.

On the other hand, Kent (1981) confirmed that earthquakes occurrences in Lesotho occur near the Cedarville fault and Cedarville Flats alluvial deposits that are located on the inland flank of the Amatole-Swaziland axis of uplift.

At present neotectonics in southern Africa is increasingly associated with two zones of compressive stress fields: one zone with a predominant NNE trend corresponding to the East Africa Rift System, and a second one characterized by a NW-WNW trend (Zoback et al., 1989). According to Viola et al. (2005), the WSA is also anomalous because the continental margin of the SE Atlantic should be of the passive type in terms of plate tectonics. Nonetheless, the WSA

is characterised by the Andersonian strike-slip fault regime (σ_2 vertical, σ_1 and σ_3 horizontal). Bird et al. (2006) found that the orientation of the WSA varies from NNW-SSE in Namaqualand, west Namibia, and the adjacent SE Atlantic offshore, to NW/WNW-SE/SSE in the southern Cape, the Bredasdorp basin, and in the Witwatersrand basin.

Singh et al. (2011) from their work on a seismotectonic model of South Africa compiled a list of faults that are considered to be evidence of neotectonics. Each one of these is characterised by its own features:

1. The Kango-Baviaanskloof fault in the south of the Eastern Cape Province, which is still active, has fault scarps in some places of between of 2 and 4 m high;
2. The Kuiseb-Hebron fault has displaced Cenozoic/Quaternary sediments up to 65 m;
3. The Riefontein fault system in the Gauteng province runs from Edenvale in the east beyond Krugersdorp in the west. This fault is also marked by the presence of landslides;
4. The Port-Dunford Late Pleistocene to Holocene coastal faults extend northwards into southern Mozambique;
5. The Tshipise fault has young fault scarps, and has displaced aeolian sands;
6. The Bosbokpoort fault with young scarps has also displaced aeolian sands;
7. The younger Coega fault has some seismicity;
8. The Thabazimbi-Murchison lineament located in a greenstone belt has natural seismicity, and has two remarkable faults: the Zebediela and the Thabazimbi faults related to subsidence of the Bushveld basin has numerous hot springs.

Of importance to this study is the fact that the Eastern Cape northern neotectonic belt is marked by the presence of the Kokstad-Koffiefontein seismic belt. Singh et al. (2009) indicated that

earthquakes in the Koffiefontein cluster occur near the Lithani/Matigulu thrust in the amphibolitic Mzumbe terrain. They also mentioned that Andreoli et al. (1996) discovered a recent fault zone reaching the surface 10 km southwest of Bultfontein. The linear feature appears as a flat-bottomed furrow 30 cm deep and 0.5 m wide, which could represent a belt of ground depressed as a result of extensional faulting.

Titus et al. (2009) quoting Andreoli et al. (1989, 1990, etc) indicated that there is a striking match between the tectonic fabric of the south east Atlantic and south-west Indian Ocean on the one hand and the tectonic fabric of the African subcontinent on the other. A number of major oceanic transform faults or fractured zones such as the Cape/False Bay, the Falkland-Agulhas, the Trans Indian/Ceres Prince Edward and the Mozambique/Madagascar fractured zones (Figure 2.4) continue into the on-shelf and on-shore joints/faults of the South African continent. Titus et al. (2009) in their study of aquifers in Namaqualand found that a set of NNE-SSW striking fault/fracture zones represents continental continuations of oceanic transform faults. Andersen and Ainslie (1994) argued that stress orientation can be related to visible structures and to kinematic pattern; moreover, once the orientation of the present day stress field is determined, it is possible to predict which pre-existing structures are favourably oriented for reactivation for strike-slip or normal motion. Thus these structures would be the most favourable aquifers.

2.4.2 Overview of neotectonics in the Eastern Cape Province

2.4.2.1 The southern neotectonic zone

This zone stretches from the Cape Fold Belt to the lower Beaufort Group. In the Cape Fold the Kango-Baviaanskloof and Sauer faults were reactivated during the Quaternary (Hill, 1988).

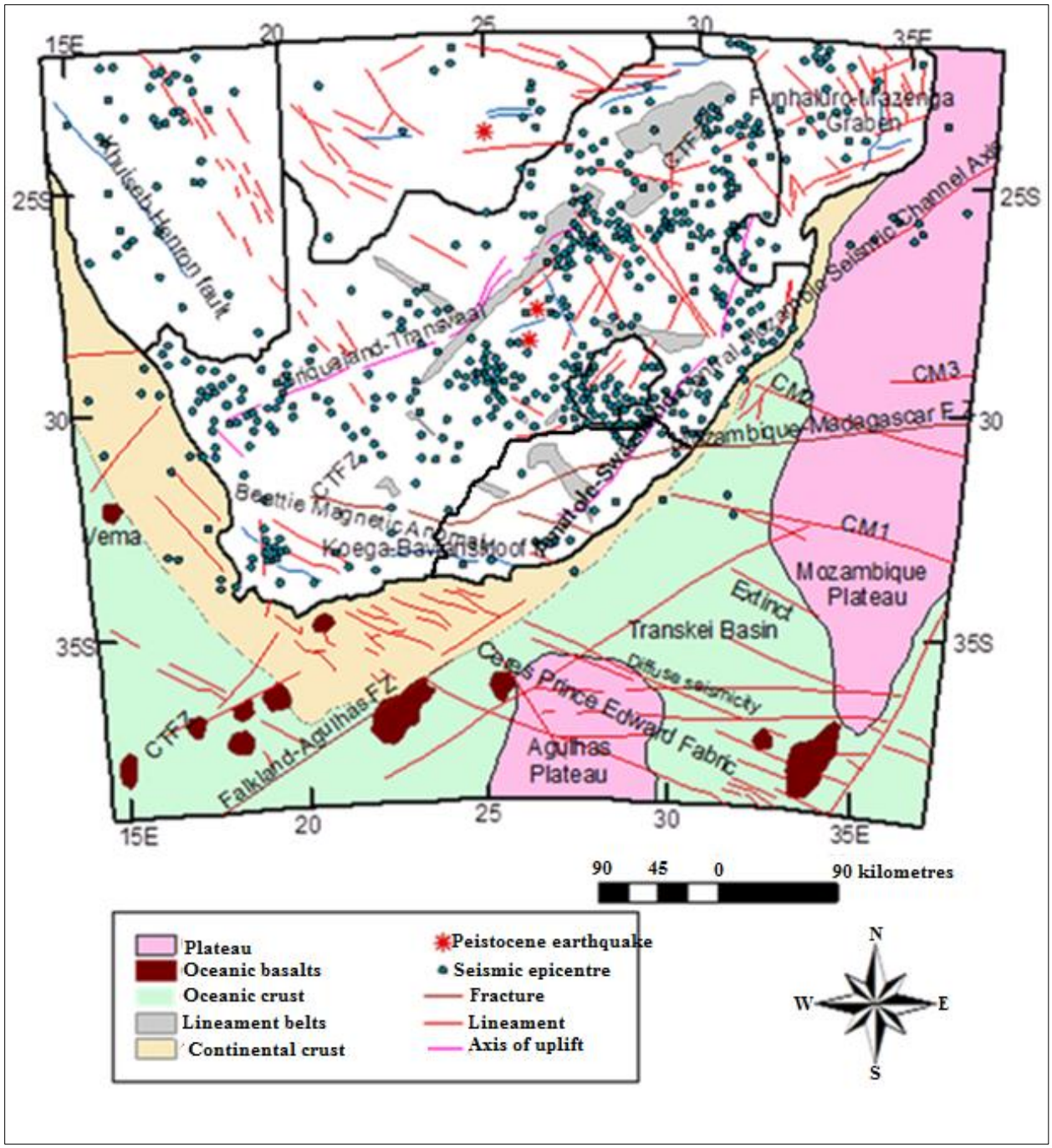

Figure 2- 4: Seismic epicentres in relation to the post-Karoo tectonic framework of South Africa and nearby regions (Andreoli et al., 1996)

Goedhart and Booth, (2009) made mention of the Kango-Baviaanskloof neotectonic fault, and confirmed the occurrence of a 84 km long extensional surface rupture along it within the

southern Cape Fold Belt in the Eastern Cape Province. The map of seismic epicentres (Figure 1.2) from IRIS displays clusters south of Port Elizabeth offshore.

This southern neotectonic zone is also characterized by recurrent seismic activity in the Grahamstown area. Near Fort Beaufort there is a hot spring, with a reactivated fault, neotectonics in this area might be related to fractures that are being reactivated (Madi and Zhao, 2010).

Andreoli et al. (1996) showed that offshore in the south there are many lineaments that have the same trend as those they called the "Ceres Prince Edward Fabric", (which is an anomalous neotectonic feature (Figure 2.4). Madi and Zhao (2010) made mention of discrete slicken lines on the Alice-King Williams Town road in a road cut showing alternating sandstones and mudstones of the Daggaboersnek member, Balfour Formation. Neotectonics can also be induced by engineering works as has been highlighted on the King Williams Town-East London road, a neotectonic fault in a road cut was possibly the result of the overburden pressure generated by the overhead bridge (Madi and Zhao, 2010). The works of Lock (1978); Hill (1988); Ben-Avraham (1995), Goedhart (1997) and many others have contributed to the documentation of neotectonic activity in the Eastern Cape southern neotectonic belt.

2.4.2.2 The northern neotectonic zone

No neotectonic activity was noted in that area (Woodford and Chevallier, 2002). On the contrary, this zone is to be considered as a true neotectonic zone because seven of the twelve hot springs of the Province (Figure 2.5) are found in it. A big seismic belt (Kokstad-Koffiefontein) is present near the border of Lesotho (Figure 1.2). On the other hand, very high discharge rates (42 *l*/s) were reported in the area of Tabankulu. This zone is characterized by the axis of uplift that took

place in the Quaternary (5Ma). This uplift might have generated some fractures in the Karoo aquifers (Andreoli pers. com).

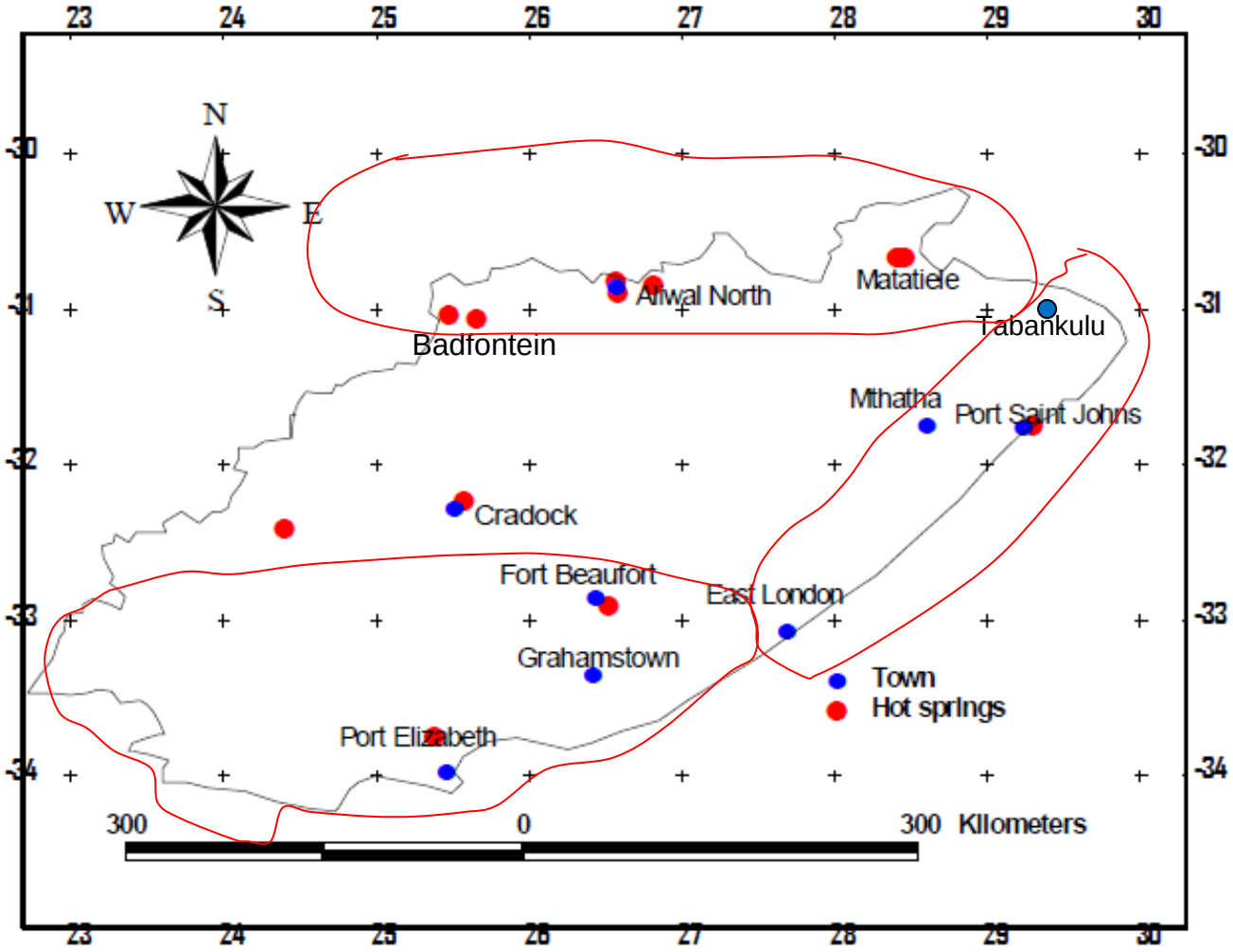

Figure 2- 5: Hot springs of the Eastern Cape Province. Regions encircled with red lines indicate the three neotectonic zones (southern, eastern, and northern neotectonic belts).

This uplift has caused most of the rivers in the east to flow towards the Indian Ocean, and the coastal areas to tilt seawards (Esterhuizen, 2008; Burke and Gunnel, 2007). Viola et al. (2005) reported that the morphostructural studies of regional uplift and modification of the regional drainage systems and escarpment demonstrate that recent uplift reinitiated only about 20 Ma.

The works of Olivier (1975) highlighted the flooding that occurred during the Orange-Fish tunnel Project at the shaft 2 tunnel within the Kokstad-Koffiefontein seismic belt. In this area neotectonics is indicated by:

1) The presence of a thermal spring approximately 1800 m to the east of tunnel route with water temperatures of up to 31^{o}C, indicating deep circulation of groundwater;
2) Water level fluctuations seen in the records as a result of recharge by rainwater, earth-tides and earthquakes. Furthermore, selected samples submitted for age determination indicated the age of the groundwater to vary from zero to approximately 4000 years (Olivier, 1975), which is a very recent age in terms of neotectonics.

It was found that flooding occurred after an abnormally well-developed fissure-zone was intersected approximately 550 m south of the shaft 2. The inrush of water was associated with the collapse of the tunnel roof, as part of the roof major fissure was exposed by the fateful blast. However the influence of earthquakes and accordingly of neotectonics on the pattern of semi-diurnal tidal fluctuations is of special interest as regards the flooding problem. Wittingham (1970) indicated that the flow of the central thermal spring, on the Badfontein hot spring for instance increased markedly for a period of at least 3 months after a local earthquake was felt during August 1956

2.4.2.3 The eastern neotectonic zone

The seaward tilting of the Eastern Cape on the coastal side of the axis of uplift led to the invasion of the land by the sea. Andreoli et al. (1995) demonstrated that this uplift known as the Ciskei-Swaziland axis of uplift has been accompanied by many spas and springs. Many of these springs

occur in the north and north-eastern part of the Eastern Cape Province like the one in Port Saint Johns (Isinuka) (Figure 2.6 left) and south of Matatiele (Polile Tshisa) (Figure 2.6 right). This uplift is controlled by the N-S Amatole-Swaziland and NNE-SSW trending Miocene-Pliocene Griqualand-Transvaal related to the subsidence of the Kalahari basin

The whitish substance visible in the Port Saint Johns spring (Isinuka, Figure 2.6 left) is nothing other than salt (NaCl). As the area is very close to the Indian Ocean, there is a very strong interaction between fresh water and sea water. Some travertines are found in the vicinity of the Isinuka spring, which the local people believe has therapeutic value; the Isinuka spring emits a sulphurous odour called by them as vicks that they inhale. The Ciskei-Swaziland (Amatole-Swaziland) axis of uplift in the east coast has been accompanied by river readjustment in relation to equilibrium; this uplift has caused the Mbashe River near Mthatha to have more asymmetric and more sinuous meanders (Madi and Zhao, 2010).

Figure 2- 6: left) spring near Port Saint Johns; right) hot spring near Matatiele.

Dobson et al. (2010) proposed three competing evolutionary models for the uplift: (1) the major phase of uplift occurred in the late Cretaceous, (2) the major phase of uplift occurred at ~30 Ma,

and (3) ~ 900 m of the modern topography being generated rapidly 100 m/Ma in the Plio-Pleistocene (c. 3 Ma).

Besides the Amatole-Swaziland uplift, the country of South Africa experienced another uplift known as the Miocene-Pilocene Griqualand-Transvaal uplift (see Figure 2.4). In the Northwest Province of South Africa, this uplift caused major faulting and formed the Augrabies Falls. It is noteworthy to indicate that water in the Augrabies Falls flow through metamorphic rocks (gneiss) known to be not good aquifers because of very low porosity and permeability. The water flow in the Augrabies Falls can only be explained by the presence of the fault (Figure 2.7 left) as a result of the uplift. On the other hand, some potholes at a very elevated area (617 m above sea level) are still visible. At this altitude, the possible explanation for the presence of dry potholes (Figure 2.7 right) is undoubtedly the consequence of the Griqualand-Transvaal uplift (Figure 1.2, Figure 2.4).

Figure 2- 7: (left) water in the Augrabies Falls, note the jointed gneiss on the left side of the fault; (right) pothole in the gneiss at 600 m above sea level near the Augrabies Falls.

2.5 Overview on the geomorphology

2.5.1 African Erosion Surface

According to Maud (1996) the African Erosion Surface was initiated by the disintegration of Gondwana. After the disintegration of Gondwana, erosion took place on the newly formed high and steep margins of the subcontinent.

On the other hand, in the Late Cretaceous Period, most of the marginal regions had been reduced to a gentle plain across which the rivers meandered to the sea in the geomorphic stage of old age. Maud (1996) outlined that in the interior, the area known as the Great Escarpment and the Lesotho Highlands, erosional resistant flat-lying sandstone and Karoo dolerites continued to stand above the inland erosion surface. The erosional products derived when the landscape was being reduced to a plain were deposited offshore at 3000 m.

Jacob et al. (2004) highlighted that the Grahamstown formation silcrete forms a remnant of an extensive peneplane that developed on the African Erosion Surface during the Cretaceous-Tertiary Period. Most of this silcrete are up to 2 m thick and overlie deeply weathered and kaolinised rocks (Frankel and Kent, 1937). The African Surface is a composite surface of continental extent that developed as a result of erosion following two episodes of the initiation of ocean floor accretion around Afro-Arabia ca 180 Ma and 125 Ma, respectively.

2.5.2 Coastline configuration

One of the more confusing aspects of coastal geomorphology is the extremely wide scale cover by the landforms. These include small-scale features such as beach cusps (no more than a few meters across), medium-scale features such as salt-marshes or sand dunes (several kilometres across) and large-scale features – the configuration of the coastline itself for instance (covering

tens, even hundreds of kilometres). This scale can be called “Capes and Bays geomorphology (Pethick, 1984).

According to Illgner (1995) the configuration of the coastline of the Eastern Cape, between the Storms River mouth and Cape Padrone, is dominated by two east-facing ‘half-heart’ shaped bays, namely Saint Francis Bay and Algoa Bay. The northern section of the Eastern Cape north of the Keiskamma River mouth is much straighter than the southern section, possibly due to the relatively uniform nature of the lithology and its close proximity to the Agulhas Falkland Fracture Zone (AFFZ: Figure 2.4). The Eastern Cape coastline, particularly in northern Transkei, (Mthatha) can be classified as emergent since it essentially resulted from tectonic uplift.

3. METHODOLOGIES

3.1 Introduction

The methodology adopted in this study includes a comprehensive literature review, desktop study through remote sensing, location of sites, examination of seismic data, stress inversion techniques, use of scanning electron microscopy, transmitted electron microscopy, X-ray fluorescence, X-ray diffraction, collection of geophysical data and interpretations.

3.2 Remote sensing

Remote sensing was used in order to depict zones of high-density surface lineaments for groundwater targets. Remote sensing was extensively used in groundwater exploration and mapping of lineaments. The seismic epicentres were overlain by some major lineaments in the Eastern Cape (e.g. Figure 6.39). In a continental intraplate context, earthquake seismic epicentres are aligned along lineaments. Joining epicentres with lineaments enables one to delineate zones of seismic risk assessment in the Eastern Cape. This provides a highlight on how facilities like nuclear waste sites should be chosen in order to avoid possible contamination of groundwater. Satellite images (Landsat 4-5 TM) were chosen because they offer good scenes that can be exploited from remote sensing in order to extract linear features. These were downloaded for free from Glovis (Global Visualization View), USGS website. The scenes have already been processed with systematic correction (Level 1G) due to processing constraints. The systematic correction (Level 1G) provides radiometric and geometric accuracy. Different scenes covering the three neotectonic belts (south, east and north) plus the central inactive zone were used for lineament extraction using ENVI 4.8. Enhancement of images was done in different stages as follows:

1) Linear interactive stretching;
2) Smoothing using Median filter 3x3; and
3) Edge detection using Sobel filter.

Images were processed using the Sobel operator with non-editable kernels. Geo-referenced processed images were then exported to Arc Map for lineament editing. After editing the lineaments, rose diagrams were produced using Rose Plot 2.2 developed by Mattner (2009).

Satellite images of the three neotectonic belts were downloaded for lineament study and in an attempt to find possible neotectonic faults. Two possible neotectonic strike-slip faults were found in the northern neotectonic belt near Matatiele. TM images were used; these were complemented by SPOT data due to the fact that a great part of the Eastern Cape is covered by rocks of the Karoo Basin. The Karoo basin is characterised by a thick soil cover. SPOT data imageries are found to better depict structures that cannot be seen on other types of satellite images. This has led to the discovery of another fault, which is characterised as a neotectonic fault around the Mangaloaneng village 40 km south of Matatiele.

3.2.1 Ancillary data and Normalized Difference Vegetation Index

Some satellite scenes were then chosen due their lineament density for further Digital Elevation Models and Normalized Difference Vegetation Index (NDVI) in regions where the major focus is directed towards groundwater exploration. DEMs from GLOVIS were downloaded with satellite images that have already been processed as SRTM version 4.1 to provide seamless continuous topography surfaces. At the GLOVIS, areas with no data in the original SRTM, data were filled using the interpolation method described by Reuter et al. (2007). These DEMs were then reprocessed using ArcMap 9.3 at the standard deviation method level 2 in order to enhance

visualization. The aim of using the DEMs was to compare them with the NDVI output map in the regions of interest for the possibility of positioning potential high yield wells in the future.

3.2.2 Ancillary data and flow

In order to have an idea concerning the water flow direction, samples of Digital Elevation Models from each neotectonic belt were selected with associated grids; the southern neotectonic belt with grid 3327, the eastern neotectonic belt with grid 3228, and the northern neotectonic belt with grid 3028. The Digital Elevation Model acquired from the National Geo-Spatial Information in the Western Cape (www.cdsm.gov.za) were in Excel™ format (X,Y and Z) with coordinates in WGS84 datum, Hartebeestoek 94 reference system. Samples of each of these grids were visualized using the Surfer 10 software in order to depict the possible predominant water flow direction and to see the elevation in meters; first, the surface topography was plotted, followed by the contour lines and finally the vector gradients. They were then overlaid in order to produce a graphic representation in 3D. Only the grid 3327 was chosen for illustration because of the important structure (Eastern Cape Great Lineament) hosted within it.

3.3 Mapping

The mapping was conducted in the field mainly in the neotectonic domains of the Eastern Cape Province. In the south both the Grahamstown kaolin deposit and the Eastern Cape great lineament were considered. The Grahamstown kaolin deposit is controlled by neotectonic structures; the great lineament hosts some seismic epicentres and is considered to be neotectonic domain. In the east, emphasis was on remote sensing because the (Ciskei-Swaziland) Amatole-Swaziland uplift took place in the Quaternary together with the Griqualand-Transvaal uplift. Part of the Griqualand-Transvaal uplift was also mapped in the Augrabies Falls near Upington in the

Western Province to highlight the neotectonic activity marked by exposure of potholes because of the Quaternary uplift. The neotectonic belt near the Lesotho-South African border (Kokstad-Koffiefontein seismic belt) was mapped during the collection of geophysical data.

3.4 Examination of vertical 2D seismic data

Some areas in the east coast (onshore and offshore) were selected for the study of structures below the Earth's surface. Seismic data used for this purpose were acquired by SOEKOR (PetroSA). During data processing, the amplitude recovery was done at the value of α= 3.5DB/sec. The velocity was analysed using the NMO (Normal Moveout Correction). The NMO is defined as the time difference between travel time at a given offset and at zero offset. The shot point interval was 200 m and the polarity convention was done with a compression wave at the seismometer that was given a negative number on tape, this polarity was retained throughout the processing to yield a downswing on display. A time variant deconvolution was applied using 7 filters/trace of 76 Ms.

3.5 Current neotectonic stress

It was decided that the current stress regime should be deduced from kaolin deposit outcrops, because these outcrops are Quaternary in age. Good exposures of outcrop are found along the N2 road around the area of Grahamstown. To determine the neotectonic stress factor, fractures and faults were measured, and all measurements were then computed using Win-Tensor software to depict the orientation of compressional and extensional stress and the focal mechanism solution. Fault kinematic and earthquake focal mechanism analysis for reconstruction of tectonic stress (past and present), are increasingly used in neotectonic and seismotectonic investigations (Delvaux and Spener, 2003). For stress inversion derived from the kaolin deposit, brittle

fractures (faults and fractures) were considered using the classical right dihedron method and the iterative rotational optimisation.

3.6 Scanning electron microscopy, x-ray diffraction, x-ray fluorescence, and transmitted electron microscopy

According to the degree of alteration and structural features from the Grahamstown kaolin, the outcrop was divided into two parts: the east zone, which is more fractured and weathered with more developed kaolinised material, and the western part with less fractures and less weathered material. Microscopic studies within the Dwyka tillite, which is the parent rock that was weathered to produce the kaolin, have revealed the presence of extensional micro fractures that cannot be seen at a macroscopic scale. However, breccias of granite and quartzite clearly show extensional fractures at a macroscopic scale, suggesting that breccias fracture more easily than the matrix in the Dwyka tillite. Thin sections were used to study the alteration and kaolinization. The study of the degree of alteration for comparison was done by sampling three different areas; these are zone 1 (fresh rock), zone 2 (a rock that is being weathered) and zone 3 (a more weathered zone) from the kaolin deposit. The samples from these three zones were analysed for XRD peak patterns. The samples were first crushed to fine powder at the Fort Hare University Geology Department, and then analysed at Ithemba Labs in the Western Cape using the Bruker D8. Eleven samples were also collected in a zone showing a slight change from a fresh rock to a comparatively weathered rock at one-meter intervals, the geochemical analysis was then conducted at the Council for Geoscience in Pretoria. In the case of major element analysis, the milled sample (<75 μ fraction) was placed in a 100 ^{o}C oven for at least one hour to calculate the H_2O content. It was then roasted at 1000 °C for no less than three 3 hours to oxidise Fe^{2+} and S, and to determine the loss of ignition (L.O.I.). Glass disks were prepared by fusing a 1.5 g

roasted sample and 9 g flux consisting of 35% $LiBO_2$ and 64.71% $Li_2B_4O_7$ at 1000 °C. The glass disks and wax pellets were analysed by a PANalytical Axios X-ray fluorescence spectrometer equipped with a 4 kW Rh tube.

3.7 Magnetic, electromagnetic, and radiometric studies

The northern neotectonic belt of the Eastern Cape Province, due to the remarkable seismic belt that runs from the east coast to Koffienfontein and the presence of many hot springs, is considered as an area of remarkable neotectonics. On the ground of this fact it was suggested that this neotectonic belt be characterized using geophysics (Electromagnetic, Magnetic and Radiometric measurements). Magnetic field data were acquired in the walking mode using a Geometrics Proton Processor Magnetometer (G-859) set to operate in the Julian calendar at a cycle time of 1.5 sec, with a resolution of 0.1nT and an accuracy of 0.5 nT, at temperatures between -20 and 50^{o}C, and a gradient tolerance of 1000 nT/meter. The magnetic maps around the hot spring (Polile Tshisa, Aliwal North hot spring, and Badfontein hot spring) were produced using the Geosoft 7.3 first at a grid cell size of 1m in order to see the data acquisition lines, then the grid cell size was changed to 14 m so that a generalized complete image can be visualized making it easier to depict a preliminary interpretation.

The electromagnetic profiling was used around three hot springs (Polile Tshisa near Matatiele, Aliwal hot spring and the Badsfontein hot spring). Electromagnetic measurements are mainly used to depict fissured zones, and were conducted using the Geonics EM- ground conductivity meter. The data acquisition was not easy due to accessibility problems. In the area of the hot spring of Polile Tshisa, for instance, houses have been built and big gullies, difficult to cross, were great obstacles. The Aliwal hot spring is being used as a spa and is enclosed, measurements

could be taken from outside, but only at short distances because the facility is fenced. The Badfontein hot spring is located on a farm and authorization to work for long periods was not granted, hence only a few measurements were taken.

For electromagnetic measurements, a 10-m, 20-m and 40-m coil separation cable was used . At Polile Tshisa the conductivity was measured both in horizontal and vertical dipole modes, whereas at Aliwal North and Badfontein the conductivity was measured using only the horizontal dipole mode. These measurements were then plotted against the station intervals for each coil separation cable on a binary diagram in order to obtain a profile. At Polile Tshisa the electromagnetic survey was done in the southeast-northwest, northeast-southwest and south-north directions, while at Aliwal North and Badfontein it was done in the southeast-northwest direction. These survey lines were set in order to possibly cross cut the fault that host the hot springs.

A gamma ray spectrometry survey was carried out in order to characterize three of the seven hot springs in the seismic belt, namely Polile Tshisa, Aliwal North, and Badfontein. Uranium, potassium, thorium were collected using a RS-125 spectrometer along two parallel lines close to each of the hot springs at about a 2 m station spacing. The portable RS-125 gamma ray spectrometer has a Bluetooth connectivity providing wireless connection to a Bluetooth equipped external GPS receiver conceived to operate with 1024 channel spectra with an energy response of 30 to 3000 keV, at an internal sampling of 20/second. Radiometric data (uranium, potassium and thorium in ppm) for the three hot springs were plotted using Surfer 10. Three types of ratios were also used and plotted, namely U/K, U/Th, and K/Th in order to see variation related to the three elements.

4. THE EASTERN CAPE NEOTECTONIC BELTS, REMOTE SENSING AND GROUNDWATER TARGETS.

4.1 Introduction

Remote sensing, through the study of satellite images, is used in many disciplines as a cost effective tool, particularly in groundwater, gas, and oil exploration. Herman et al. (1986); Guo and Caroll, (1995) used surface linear features to search for reserves in natural oil and gas fields. Mohamed, (2010) indicated that the surface lineaments are in parallelism with the subsurface basement fault. Ölgen (2004) stated that Earth scientists have been interested in linear features on the earth's crust since the early period of each observation. According to Isiorho (1985) lineaments are traces on the earth's surface of planar breaks in the crust of the earth. Cracknell and Hayes (1993) pointed out that lineaments are the terrain surface expression of fractures, jointing and other linear geological phenomena that occur anywhere from the terrain surface down to possibly great depths. Among other elements that can be used to recognize faults are offsets of layers so that units (and age) that are different become juxtaposed, abrupt topographic discontinuities of landforms, depressions along the fault trace, scarps or cliffs and sudden shifts of drainage courses. According to Salama et al. (1993) geological interpretation derived from remote sensing has been extensively used for the purpose of the identification of lineaments of fractured zones along which the flow of groundwater may take place. It has also been used for landforms investigations suitable for groundwater prospecting particularly in hard rocks.

Satellite images provide quick and useful baseline information of the parameters controlling the occurrence and movement of groundwater like geology, lithology/ structural, geomorphology, soils, land use and lineaments (e.g. Mogaji et al., 2011). Al-Bakri and Al-Jahmany (2013)

highlighted that exploration of groundwater in countries with scarce water resources requires the implementation of effective tools that save time and money. They also indicated that remote sensing and GIS provided efficient tools for mapping promising sites for groundwater exploration.

From the maps of the seismic epicentres (Figure 1.2 and Figure 6.39) and the hot springs (Figure 2.5), it is clear that the northern part of the province is, strictly speaking, a neotectonic zone. It is however also clear from the works of Hill (1988) that reactivation took place in the Cape Fold Belt in the southern neotectonic belt. These hot springs are probably controlled by faults. Andersen and Ainslie (1994) for instance confirmed the presence of an active fault with related to thermal springs NNW of Pietersburg, thus confirming that hot springs are controlled by neotectonic faults.

4.2 Overview on some methods used in remote sensing for enhancement

4.2.1 Stretching

This technique is used to enhance certain features of interest to be studied. These features may sometimes not be visible or can appear vaguely on the images. Neawsuparp and Charusiri (2004) on the other hand highlighted the fact that contrast stretching is known to be effective in enhancing Landsat data, and that unstretched parts of an image appear to be very flat.

4.2.2 Filtering

This descriptive approach on filtering was taken from NASA online archives. Filtering can be used for smoothing, sharpening, removing noise, and edge detection. A filter is defined by a kernel, which is a small array applied to each pixel and its neighbours within an image. Often the

centre of the kernel is aligned with the current pixel, and is square with an odd number of elements in each dimension.

4.2.2.1 Low pass filter

A low pass filter is frequently used to smooth an image by decreasing the disparity between pixel values by averaging nearby pixels.

4.2.2.2 High pass filter

A high pass filter generally used to sharpen an image when the contrast is enhanced between adjoining areas with little variation in bright- or darkness.

4.2.2.3 Directional filtering

Directional filtering is mainly used for edge detection; an edge within an image is visible when a large change (a steep gradient) occurs between adjacent pixel values. This change in values is measured by the first derivatives (often referred to as slopes) of an image.

4.2.2.4 Laplacian filtering

Laplacian filtering is another method for edge detection; unlike the directional filtering, the Laplacian filtering can be used to compute the second derivatives of an image, which measure the rate at which the first derivatives change. Kernels of Laplacian filters usually contain negative values in cross patterns.

4.2.2.5 Gaussian filter

The Gaussian filter operator is a 2-D convolution operator that is applied to blur images and remove detail and noise. It uses a kernel that represents the shape of a Gaussian hump. Convolution is a simple mathematical operation that is fundamental to many common image-processing operators.

4.2.2.6 Adaptive filter

Adaptive filter is designed to eliminate the problems faced with the Standard median filter. The difference between the two types of filters is that, with the adaptive median filter, the size of the window surrounding each pixel is variable (Al-amri et al., 2010).

4.2.2.7 Sobel filter

The Sobel operator performs a 2-D spatial gradient measurement on images (Vincent and Foloruno, 2009). The Sobel edge detector uses a pair of 3x3 convolution masks, one estimating gradient in the x direction, and the other estimating gradient in the y direction. The Sobel detector is sensitive to noise pictures, and is therefore recommended in massive data communication.

4.2.2.8 Robert filter

A Robert filter is a non-linear edge detector filter similar to the Sobel. It is a special case filter and uses a 2x2 approximation of the true Robert function a simple two-dimensional differencing method for edge sharpening and isolation.

4.2.3 Rationing

According to Shaoqing and Lu (2008), rationing is the operation in which a pixel value of a time image divides the corresponding pixel of another time image; the ratio of corresponding pixels in each band from two images of different periods needs to be calculated. Ratio can help accentuate subtle differences as well as minimize unwanted information. Interpreting ratio images requires knowledge of target reflectance illumination and ground conditions.

4.2.4 Principal component analysis (PCA)

Tsai et al. (2006) agreed that principal component analysis is the most commonly adopted feature reduction technique in remote sensing image analysis. The principal component analysis might not necessarily be an optimal method for feature extraction of hyper-spectral data, for target detection (Cheriyadot and Bruce, 2003). The principal component analysis is however straightforward and easy to use. It has been implemented in almost all available remote sensing image processing and analysis packages. It can also be used to develop an appropriate feature extraction system.

4.2.5 Hough transform

The Hough transform is another method used in remote sensing for line extraction. It has however, the distinct disadvantage of not detecting break lines, nor does it distinguish the width and length of lines. Karnieli et al. (1996) found that the Hough transform is an established tool used to discover linear features in images. The Hough transform is designated to detect collinear sets of edge pixels in an image by mapping these pixels into a parameter space defined in such a way that collinear sets of pixels in the image give rise to peaks in the Hough space (Ballard and Brown, 1982).

4.3 Lineament extraction procedure adopted for this study

4.3.1 Smoothing filter

This process entails the enhancement of satellite imagery before any lineament extraction can be done. Apart from smoothing filter, other processes that can be adopted to enhance satellite imagery are linear equalization enhancement, Gaussian enhancement, Square root enhancement. However, of all these processes, ETM images used in this study seem to be better enhanced when a smooth filter (3x3) kernel is applied.

Smoothing filters are also called low-pass filters because they let low frequency components pass, and reduce the high frequency component. The impulse response of a normal low-pass filter implies that all the coefficients of the mask should be positive. One has to bear in mind that low-pass filtering blurs the image and removes speckles of high frequency noise. On the other hand, larger masks will definitely result in a noise blurring effect. The parametric low-pass filter is given by a 3x3 kernel where the coefficients are determined by a factor b; when b is equal to 1 the parametric low filter is equal to a mean filter (see equation below).

$$c(b) = \left(\frac{1}{a+b}\right)^2 \begin{bmatrix} 1 & b & 1 \\ b & b^2 & b \\ 1 & b & 1 \end{bmatrix}$$

4.3.2 Stretching

Gonzalez and Woods, (1992) indicated that an image pixel distribution can be monitored. A high contrast image contains a wide distribution pixel count covering the entire amplitude range,

whilst an image that have a low contrast has pixel amplitudes confined to a relatively narrow range.

4.3.3 Convolution morphology (Sobel operator)

Before deciding on which filter to be used for automatic extraction of lineaments, satellite images underwent different filters for testing, such as Laplacian, Robert, and Sobel. It was found the Sobel operator was convenient; on the processed image ridges appear white, while valleys appear darker.

4.2 Approach

In the case of remote sensing, SPOT data for the Eastern Cape were considered first because of the thick soil cover in the Karoo. In these instances geological structures from SPOT imagery can be easily depicted. Additional study material such as Landstat TM downloadable from Global Visualisation View Cover and Digital Elevation data from the National Geo-Spatial Information (South Africa) were also used. Aerial photos were also examined for this purpose. All images however do not have the same resolutions. For instance, features like the Grahamstown Quaternary kaolin deposits that can be used in the study of neotectonics are not easily depicted on aerial photographs. They can be identified and appear clearly visible (Figure 4.1) on Google Earth.

The images first pre-processed by the USGS are displayed as RGB composites, bands 5, 4, and 3 with 1% linear stretch applied. Images were selected from the Global Land Survey (GLS 2010), all the standard Landsat bands designated for each sensor. Information from the USGS indicates that the Landsat Thematic Mapper (TM) images consist of seven spectral bands with a spatial

resolution of 30 meters for bands 1 to 5 and 7. Spatial resolution for 6 (thermal infrared) is 120 meters, and is then resampled to 30-meter pixels. These are resampled to a pixel size of 240 meters from the original 28.5-meter data. The TM scene covers an area of approximately 183 (north south) x170 km (east west). The GLS 2010 has an advantage in that it includes a corrected terrain, is georeferenced, and downloadable in Geotiff format free of charge.

Figure 4- 1: Areas around Grahamstown showing kaolin deposits in white

4.3.4 Algorithm adopted for this study

An algorithm is a systematic procedure used for calculation, data processing and automated reasoning. Instructions in an algorithm describe a number of well-defined successive stages that will produce an output at the final ending state. The algorithm adopted in this study can be easily understood in the below flow chart (Figure 4.2). The satellite imagery downloaded free of charge from GLOVIS (Global Visualisation) were processed using the software ENVI 4.8. The images were exported to ArcGis 9.3 in order to edit lineaments. These lineaments can be seen on different output maps.

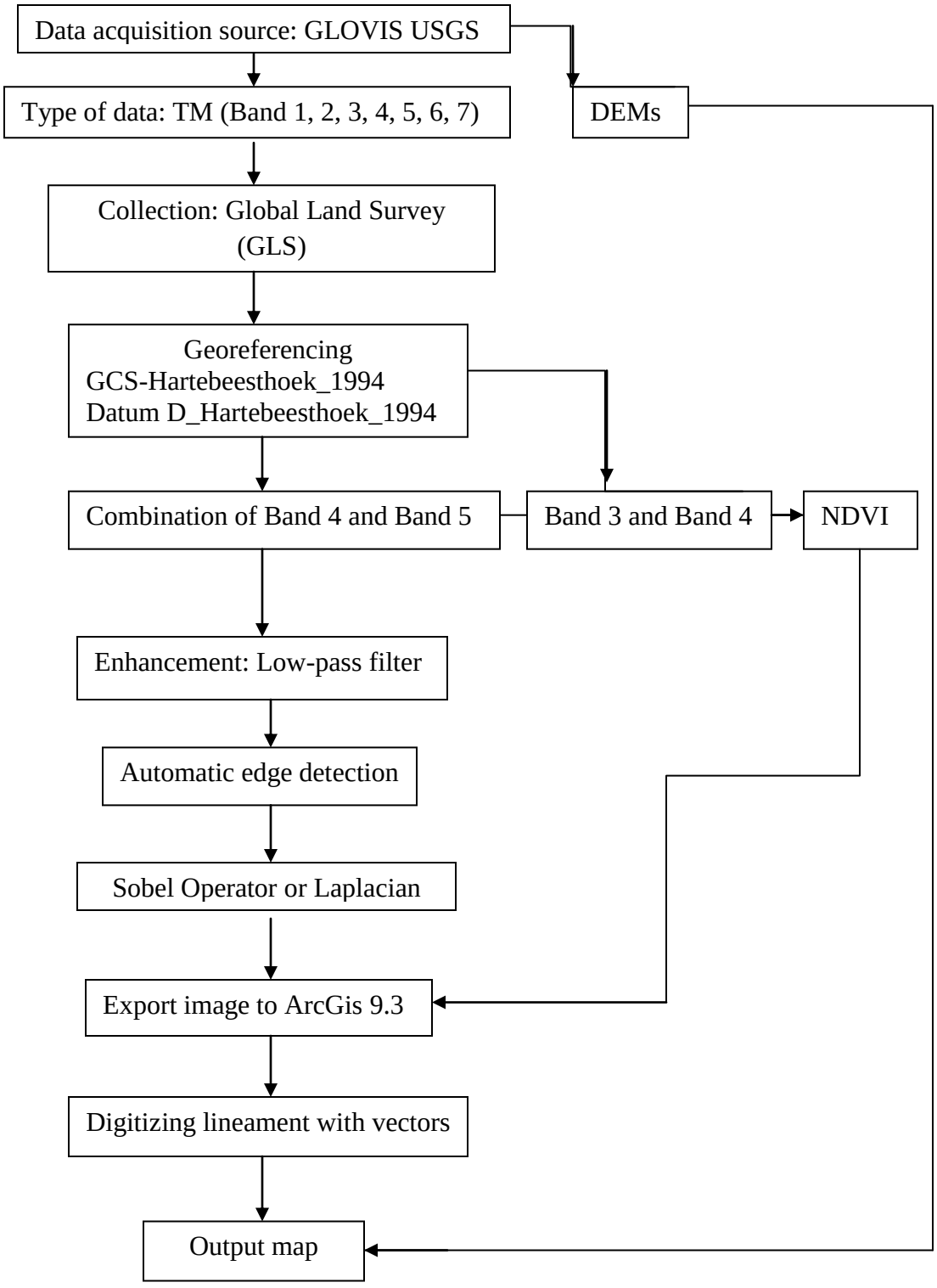

Figure 4- 2: Flow chart showing the algorithm used to produce an output map

4.3 Study areas

4.3.1 Basement in the Eastern Cape

The Eastern Cape Province is predominantly covered by rocks of the Karoo Supergroup, from the Dwyka tillite to the Clarens formation, with dolerite sills and dykes that intruded during the opening of Gondwana. Harris et al. (1990) described the Karoo igneous province of southern Africa and its continuation into east Antarctica as the largest of the Gondwana magmatic provinces consisting of thick sequences of volcanic and sub-volcanic rock. A large part of the Karoo in the Eastern Cape Province lies over a basement consisting of rocks of the Proterozoic Natal-Namaqua mobile belt in the central part, and just a small part in the north near the country of Lesotho overlays the Archean Kaapvaal Craton. To the south, the Cape Supergroup is the predominant unit. The Kaapvaal Craton has greenstone belts (e.g. Barberton, Giyani, Murchinson, Pietersburg, Rhenostterkoppies, Bendelierkop complex, Kraaipan, Amalia, Marydale, Nondweni, Dwalile, Assegaai, De Kraalen , Commondale, Muldersdrif), (e.g.Anhaeusser and Wilson, 1981), granites and gneiss terrains (e.g. Makhutswi Gneiss, Ancient Gneiss Complex, Granodiorite Suite, Tonalitic gneiss domes, Nelspruit porphyritic granite). The Natal-Namaqua mobile belt has tectonic-metamorphic sub provinces (e.g. Kheis, Richtersveld, and Bushmanland), (e.g. Joubert, 1986).

4.3.1 Regions of interest

As the Eastern Cape is divided in three major neotectonic belts (south, east and north), a lineament density study of these belts was carried out separately in order to depict the most affected zone by geological lineaments. Zones of high-density lineaments may be characterised as zones prone to neotectonics.

It was decided to methodically extract lineaments and all possible faults of areas covering the neotectonic zones and the central inactive zone. The aim is to compare the active and inactive zones in terms of density of lineaments.

4.3.2 Selection of paths and rows

A detailed study of lineaments in the neotectonic zones, mainly the northern, eastern and southern neotectonic zones was carried out. It was also found necessary to study the central zone around Queenstown where neotectonics is not very prominent. Selection of satellite images were done according to paths and rows. For the zones of interest, the following areas were choosen: 170/081, 169/081, 168/081, 168/082, 169/082, 169/083, 170/083, 171/083, 172/083 for the neotectonic zones, and 170/082 for the central inactive zone. All these areas are represented in Figure 4.3.

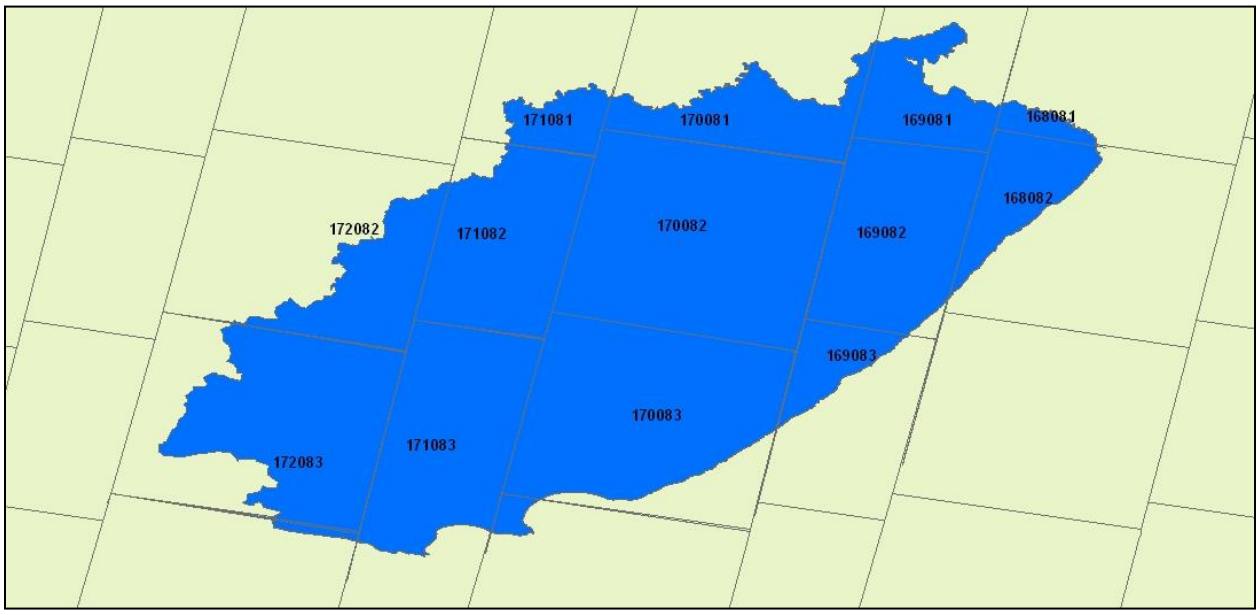

Figure 4- 3: Scenes in the Path/Row format for the Eastern Cape Province

4.3.3 Lineament extraction

The lineament extraction was done in two stages. After smoothing the image was exported to ArcMap, and lineaments that could be easily depicted were edited. The images were first convoluted in ENVI with the Sobel Operator using a 30 percent darkening with non-editable kernel, and re-exported to ArcMap to complete the editing of lineaments. This method was adopted for all the areas. Figure 4.4 is an example of the Sobel filter.

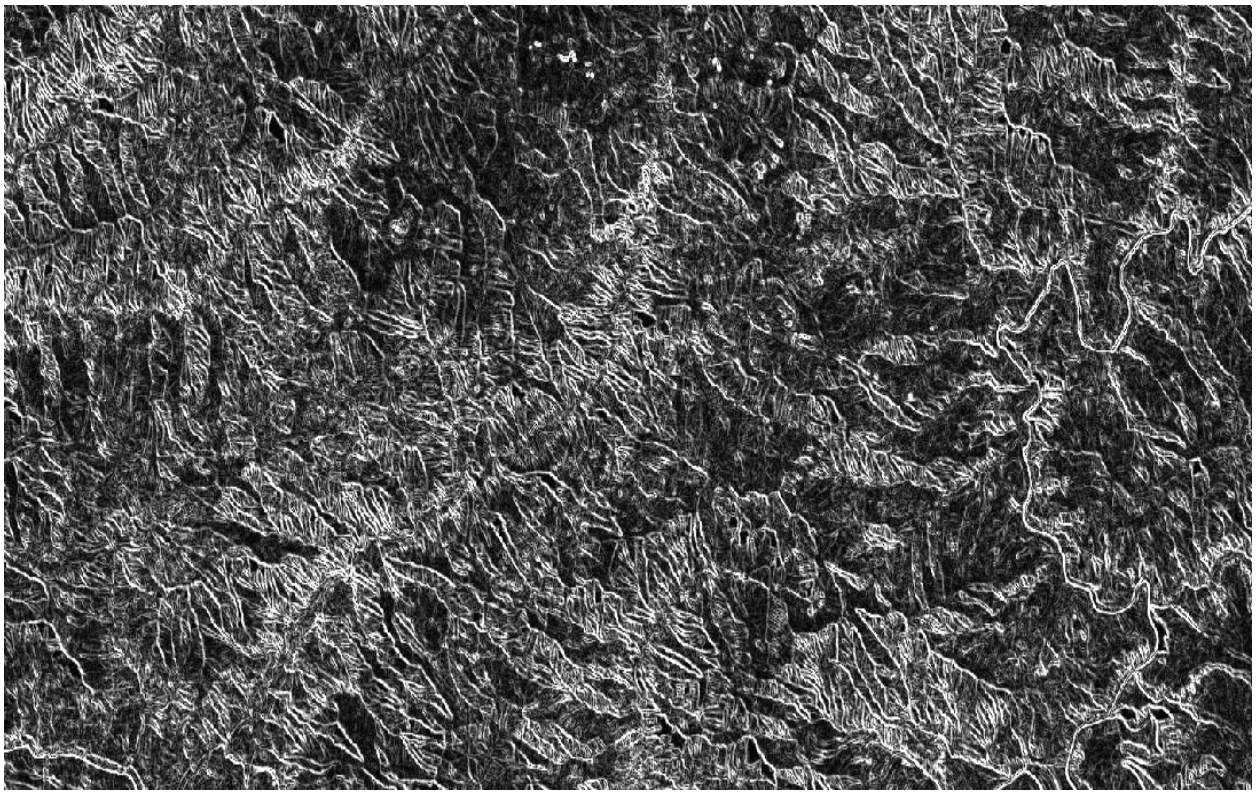

Figure 4- 4: Illustration of image processed using the Sobel convolution from path/row 169/082

4.3.3.1 Path 170/ Row 081

Maged et al. (2009) indicated that histogram equalization is applied to Landsat TM images to obtain high quality image visualization. Marghany and Hashian (2010) mentioned that an image

histogram is an analytical tool used to measure the amplitude distribution of pixels within an image. They also stated that a high contrast image contains a wide distribution of pixel counts covering the entire amplitude range, whereas a low contrast image has most of the pixel amplitudes congregated in a relatively narrow range. Every time, before convolution, a histogram for each area is created in order to decide whether the quality of the image is up to standard.

To enhance the visualization, images were linearly stretched. According to Marghany and Hashim (2010), this quality of the image used to extract lineaments is highly improved because of the amplitude distribution covering the entire range (Figure 4.5 right).

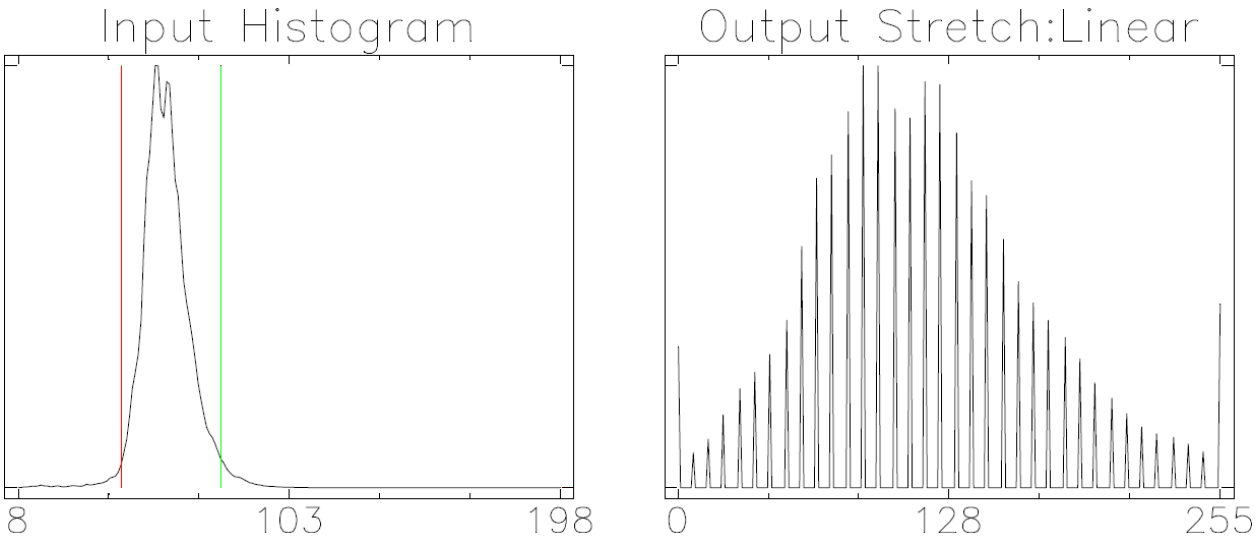

Figure 4- 5: On the left hand side, image before stretching; on the right hand side, an output histogram showing amplitude distribution over the entire range.

The 170/081 area (Figure 4.6) is characterised by scattered lineaments, though located in the northern neotectonic zone with the presence of the Aliwal North, Badfontein, and Polile Tshisa

hot springs, no neotectonic fault could be perceived. It requires deep airborne geophysical investigations to highlight the presence of deep structures below.

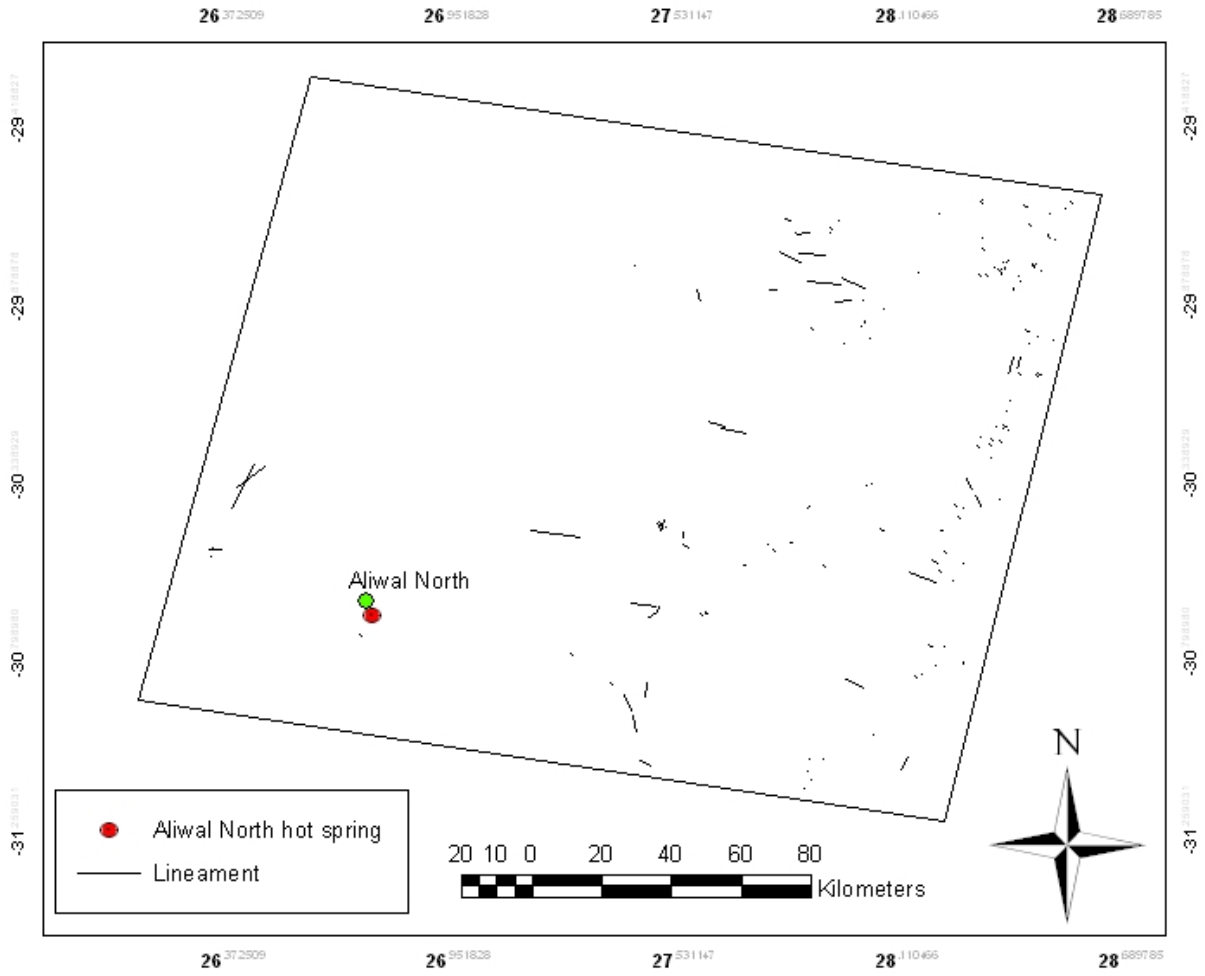

Figure 4- 6: Extracted lineaments from scene 170/081

The lineament extraction methodology used for this area, was also used for all the scenes that were chosen in the neotectonic zones. Figure 4.5 (right) shows the amplitude distribution over the entire range for all the scenes; the stretching was applied to all of them in order to enhance the visualization.

4.3.3.2 Path 169, Row 081

This area in the northern neotectonic belt is located near the Kokstad-Koffiefontein seismic belt (previously known as the Senqu seismo-tectonic belt) near the border of Lesotho. The area is also characterised by high altitudes that can reach 1600 m at some points.

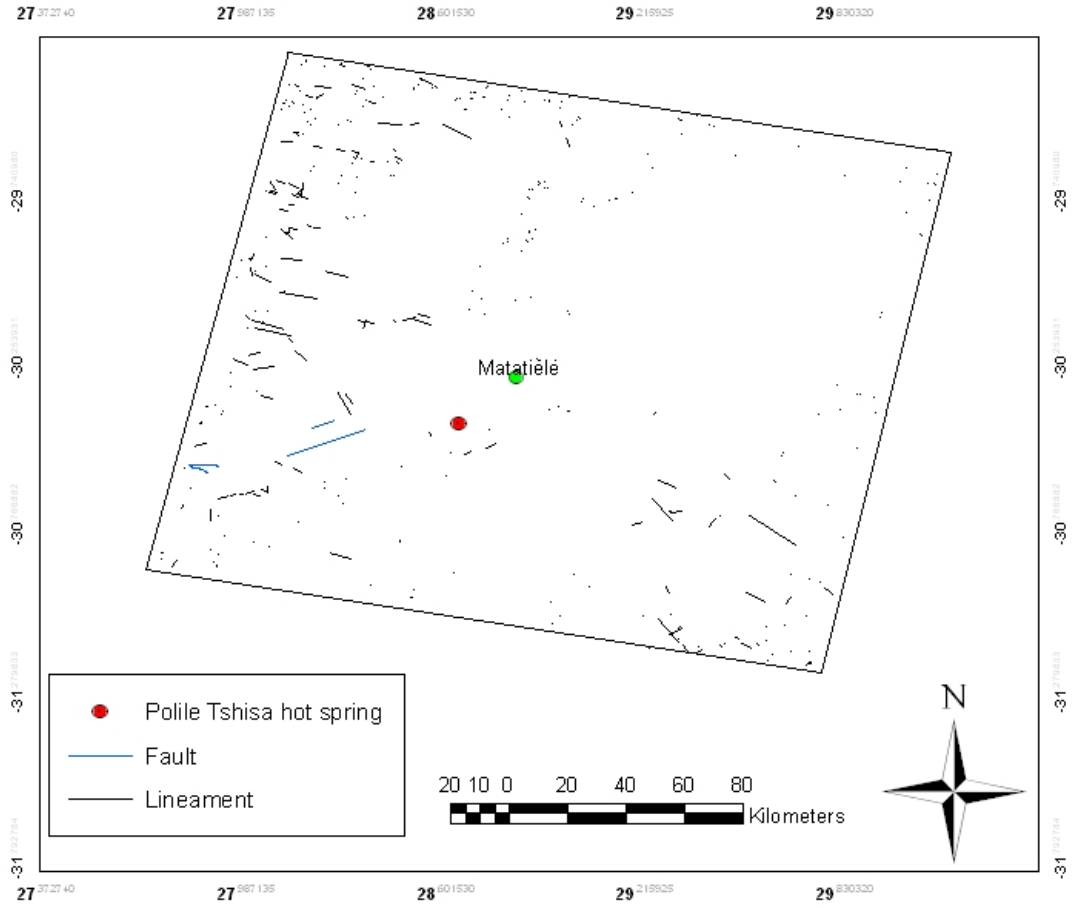

Figure 4- 7: Map showing structures extracted from scene 169/081

This area has also the hot spring (Polile Tshisa). The faults (in blue) are probably neotectonic with a left-lateral strike-slip component south-west of Matatiele (Figure 4.7). On the satellite image it clearly appears that new rivers are deflected by the long fault; the short fault has

beheaded the new rivers. The hot spring might be aligned in a fault system parallel to the strike-slip fault, or it is possibly related to an E-W neotectonic fault that extends to Aliwal North. Many lineaments occur in the western part of the scene, correlating very well with the east part of the previous scene (170/081). These faults are oriented SW-NE and are good indication for groundwater exploration. The satellite image showing the strike-slip faults can be seen in the Figure 4.8.

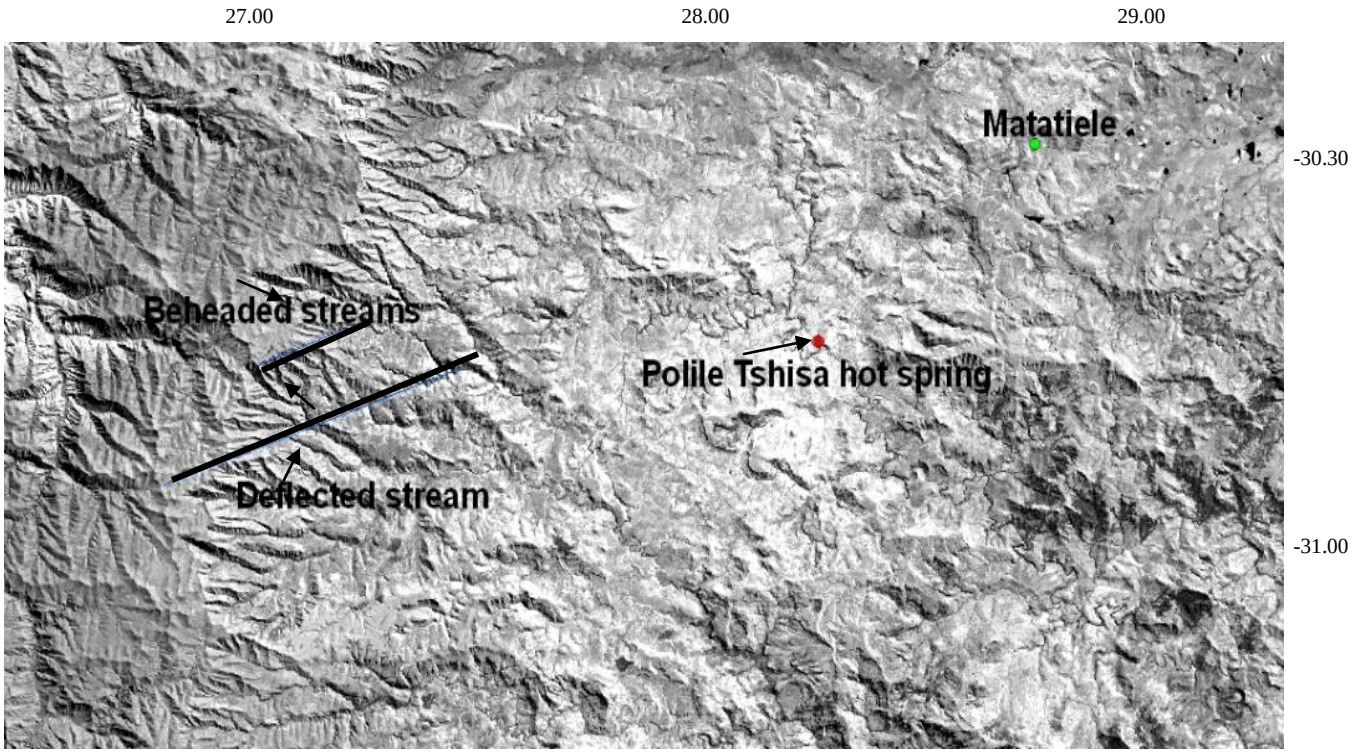

Figure 4- 8: Map showing the neotectonic zone around Matatiele, the strike-slip fault (dark lines) and the hot spring in red.

The water from this hot spring with a pH of 9.2 (alkaline) wells up from a very small diameter mouth of approximately 1cm (Figure 4.9 left). Calcium carbonate precipitates around the mouth forms the whitish travertine. The flowing water forms a small stream that tends to follow a valley (Figure 4.9 right). This water is used for domestic purposes by villagers around.

Figure 4- 9: The Polile Tshisa hot spring (left), the water from the hot spring helps for domestic use (right).

A fault oriented N120^{o} was depicted from SPOT data around the Mangaloaneng East village near Matatiele (Figure 4.10 left), its scarp is visible in Figure 4.10 on the right.

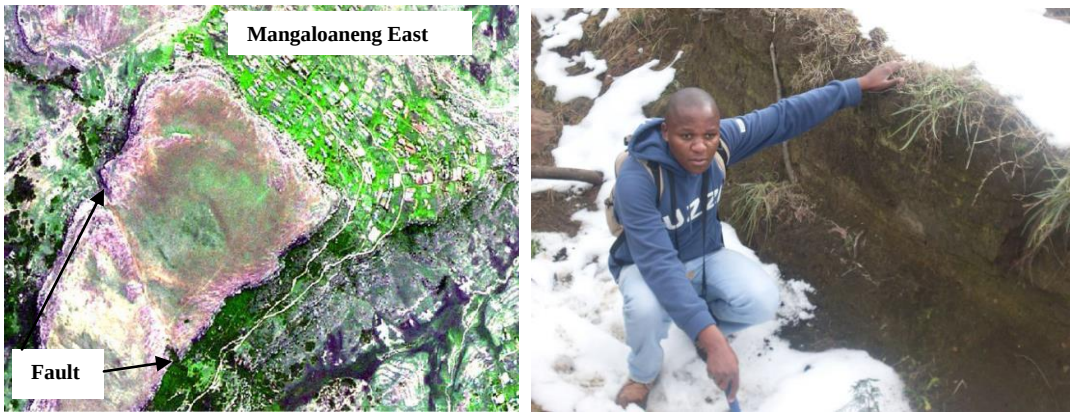

Figure 4- 10: Neotectonic fault (left) located in the grid 3028 across the sandstone of the Molteno Formation, the fault scarp can also be seen at the right (right).

Apart from few mudstones, the area is predominated by coarse grain sandstones; the faulting is associated with the occurrence of quartz veins crosscutting the jointed outcrops. The joints oriented N240^{o} are parallel and are opened up on surface with an aperture that can vary from few mm to 5 cm. The quartz veins are almost perpendicular to the joints, strike N 320^{o} and dip 35^{o}

with N 50^{o} as dip direction; sedimentary features like trough-cross bedding are also remarkable. All these structures can be seen in the Figure 4.11 (left and right). These sandstone outcrops have a strike that varies from place to place, examples of these different strikes are illustrated in Figure 4.12 (right: strike N205^{o}; dip 40^{o}) and Figure 4.12 (left: strike N 250^{o}; dip 30^{o}) respectively. These sandstones can be named as conglomeratic sandstones because of the size of their grains that can vary from 2 to 5 mm. They are whitish grey and can show at some places the beginning of oxidation as can be seen in Figure 4.11.

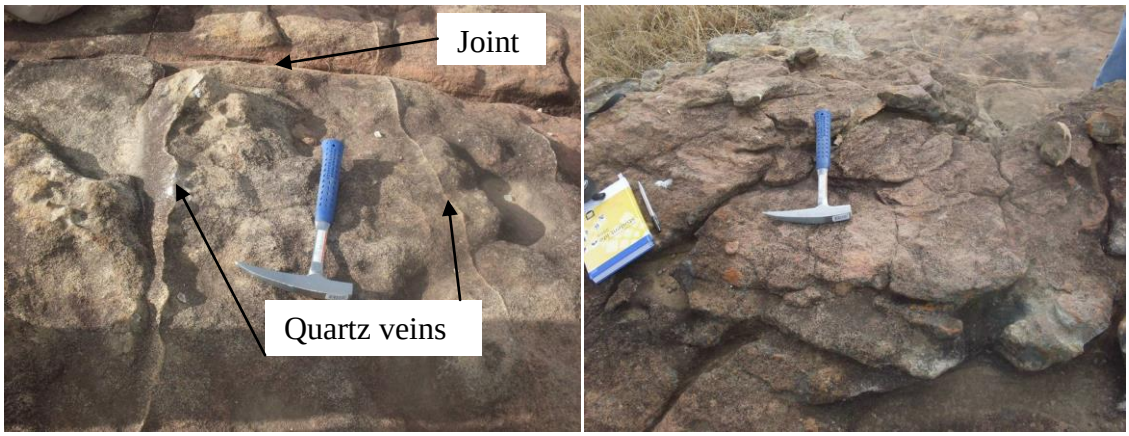

Figure 4- 11: (left) sandstone with some quartz veins perpendicular to the joints; (right) trough in the same coarse grain sandstones.

Figure 4- 12: (left) the sandstone (S30^{o}.51408/E028^{o}.51267), and right) S30^{o}.39829/E028^{o}.67405 with different strike.

Mineralogical aspect

Samples collected from these sandstones were analysed using Electron Backscattered Diffraction. These sandstones contain typical minerals such as quartz, feldspar and biotite. Heavy minerals such as rutile, zircon are also present. This area has phosphorous and rare earth minerals because of the presence of monazite, which is a phosphate mineral containing rare earth metals, and apatite. Other minerals include magnetite, sphene and barite. The barite may come from solutions because it is found in interstitial spaces, sometimes it is granular or elongated. All these minerals can be seen in Figure 4.13, 4.14 and 4.15.

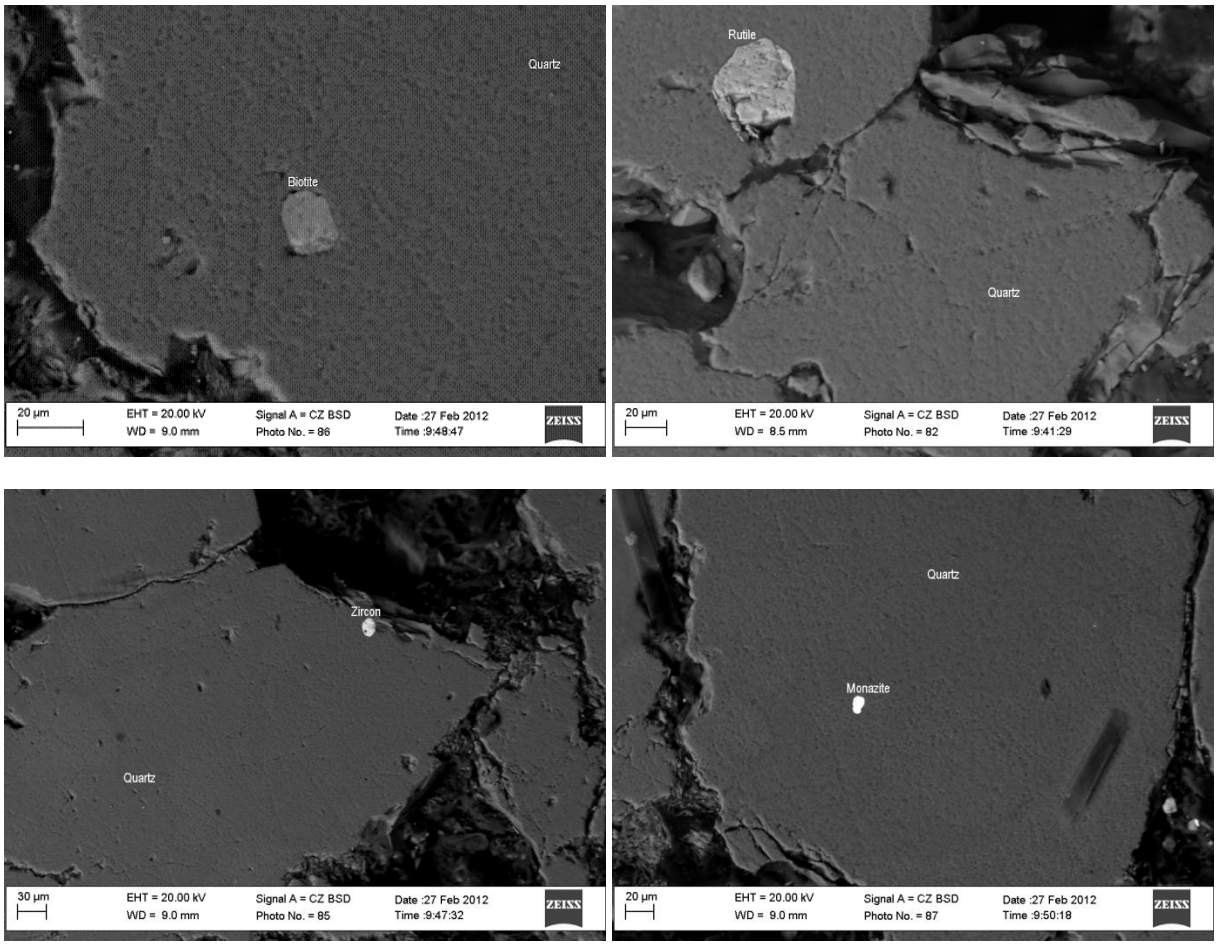

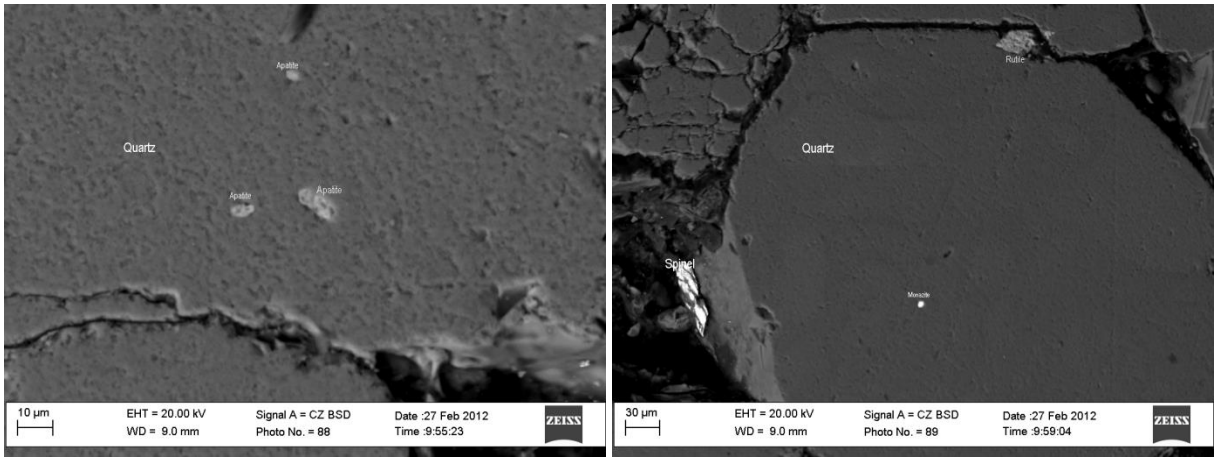

Figure 4- 13: a) Quartz and Biotite, b) Quartz and Rutile, c) Quartz and Zircon, d) Quartz and Monazite, e) Quartz and Apatite, f) Quartz and Monazite and Rutile

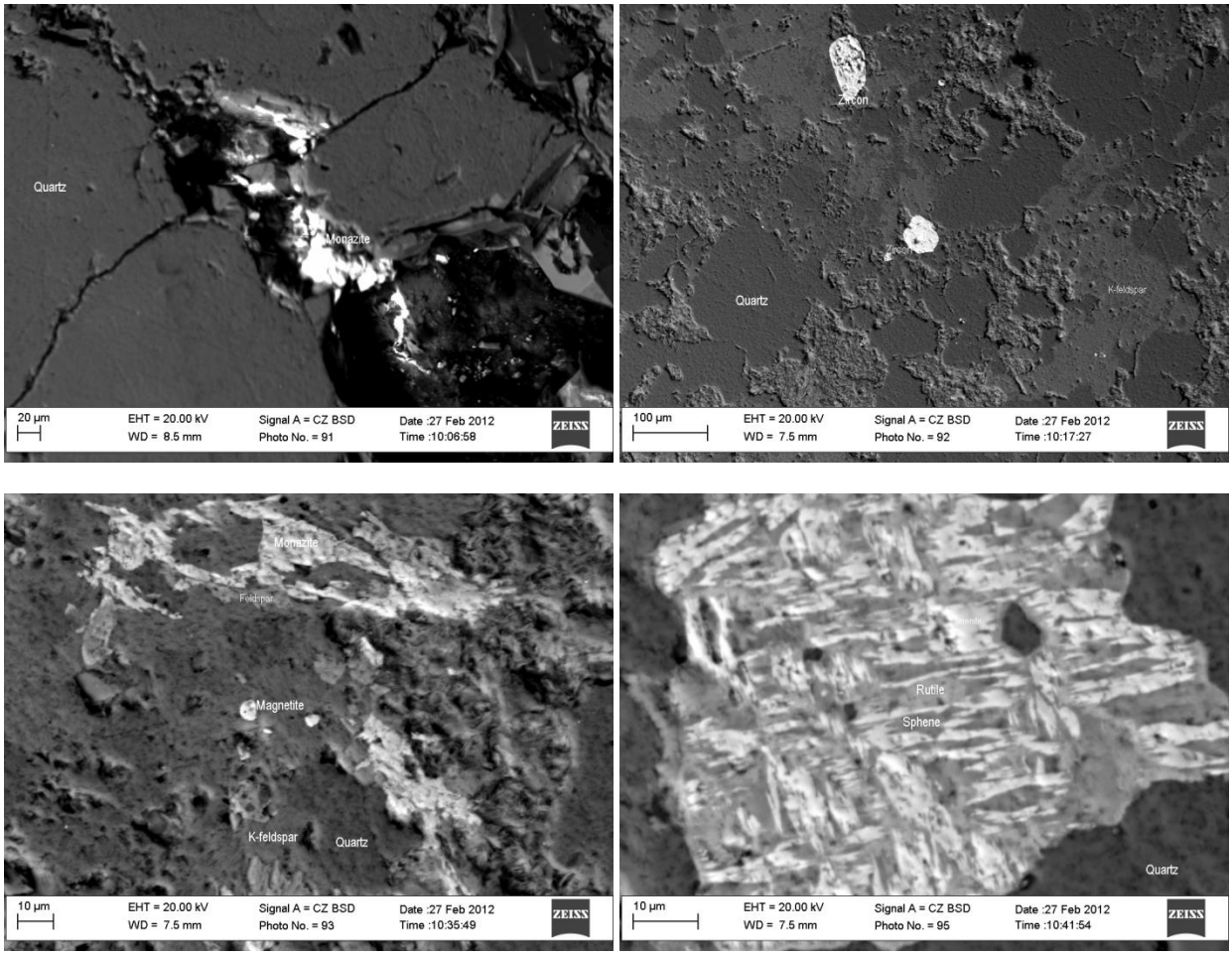

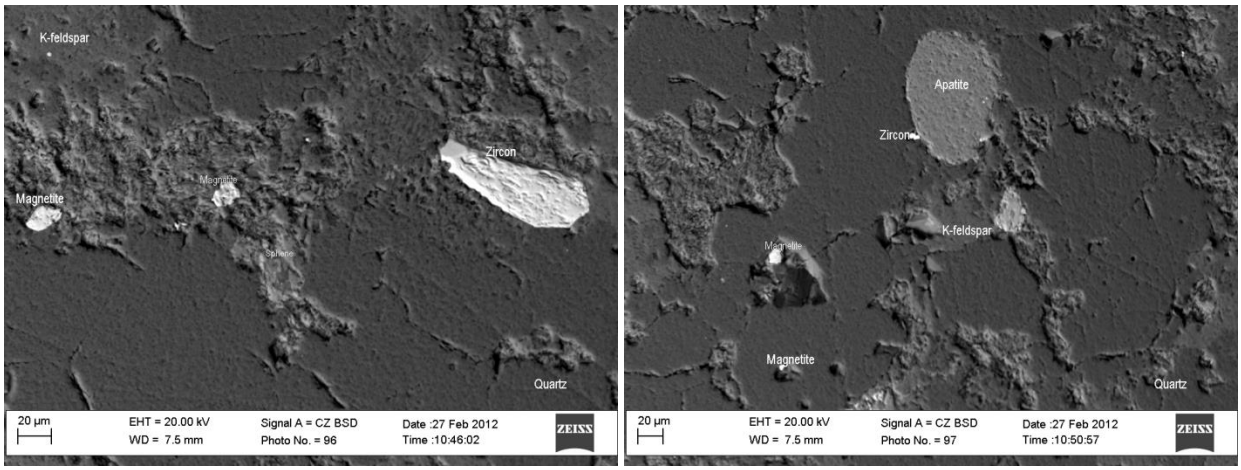

Figure 4- 14: a) Quartz and Monazite, b) Quartz, K-Feldspar and Zircon, c) Quartz, K-Feldspar, Magnetite and Monazite, d) Quartz, Rutile, Sphene, e) Quartz, K-Feldspar, Magnetite, Sphene, Zircon, f) Quartz, K-Feldspar, Apatite, Magnetite, Zircon

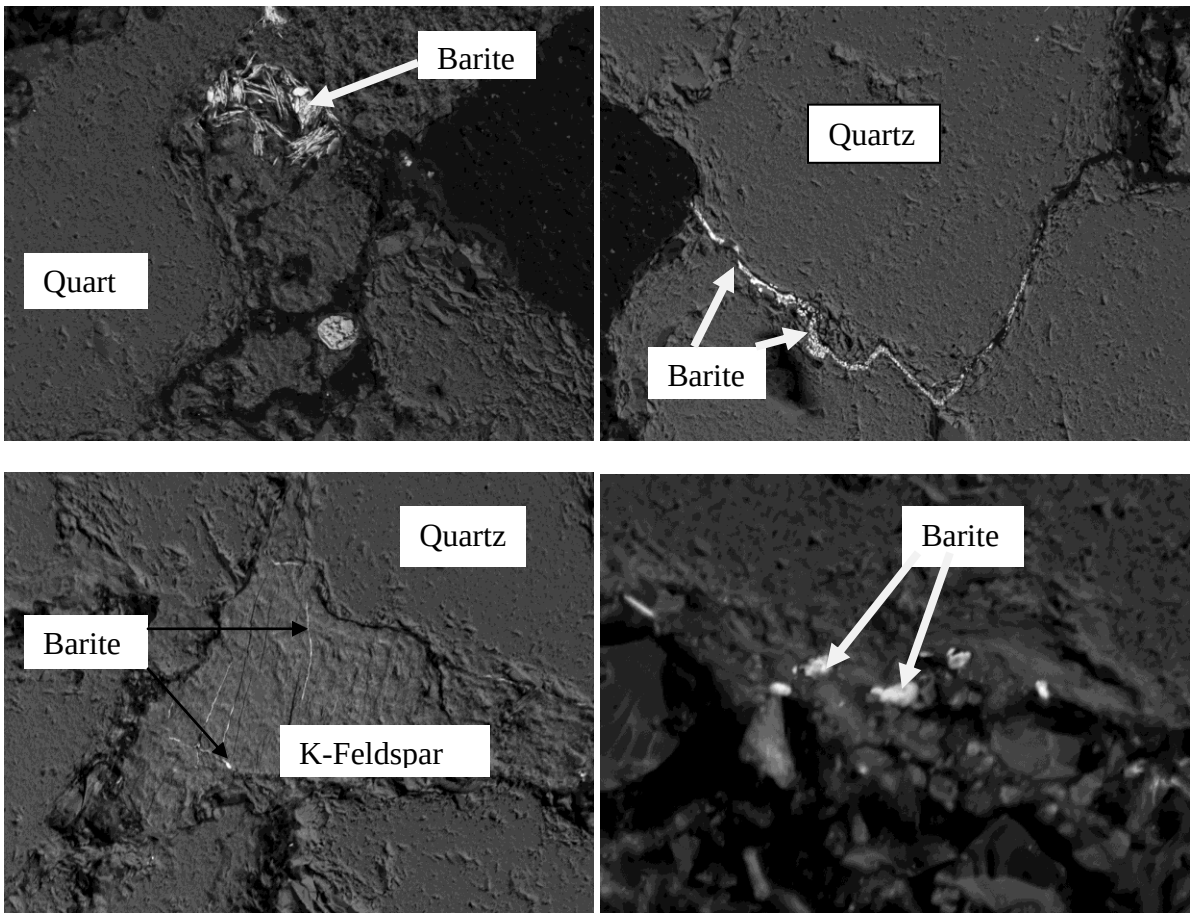

Figure 4- 15: a) Quartz ,Barite and Magnetite, b) Quartz and Barite filling the interstice, c) Quartz, Interstitial Barite in K-Feldspar, d) Barite.

4.3.3.3 Path 168, Row 081

This area near Mount Ayliff is characterised by NW-SE trending lineament, which tend to be grouped into two major classes. One class in the west block and the other in the east block in a NE-SW trend (Figure 4.16). Mount Ayliff is also located almost at the border of the KwaZulu-Natal Province, and is also characterised by high altitudes that can reach 1020 m. Like the area of Matatiele, Mount Ayliff is also characterised by seismicity, which can only be induced by stress accumulation because of higher topography.

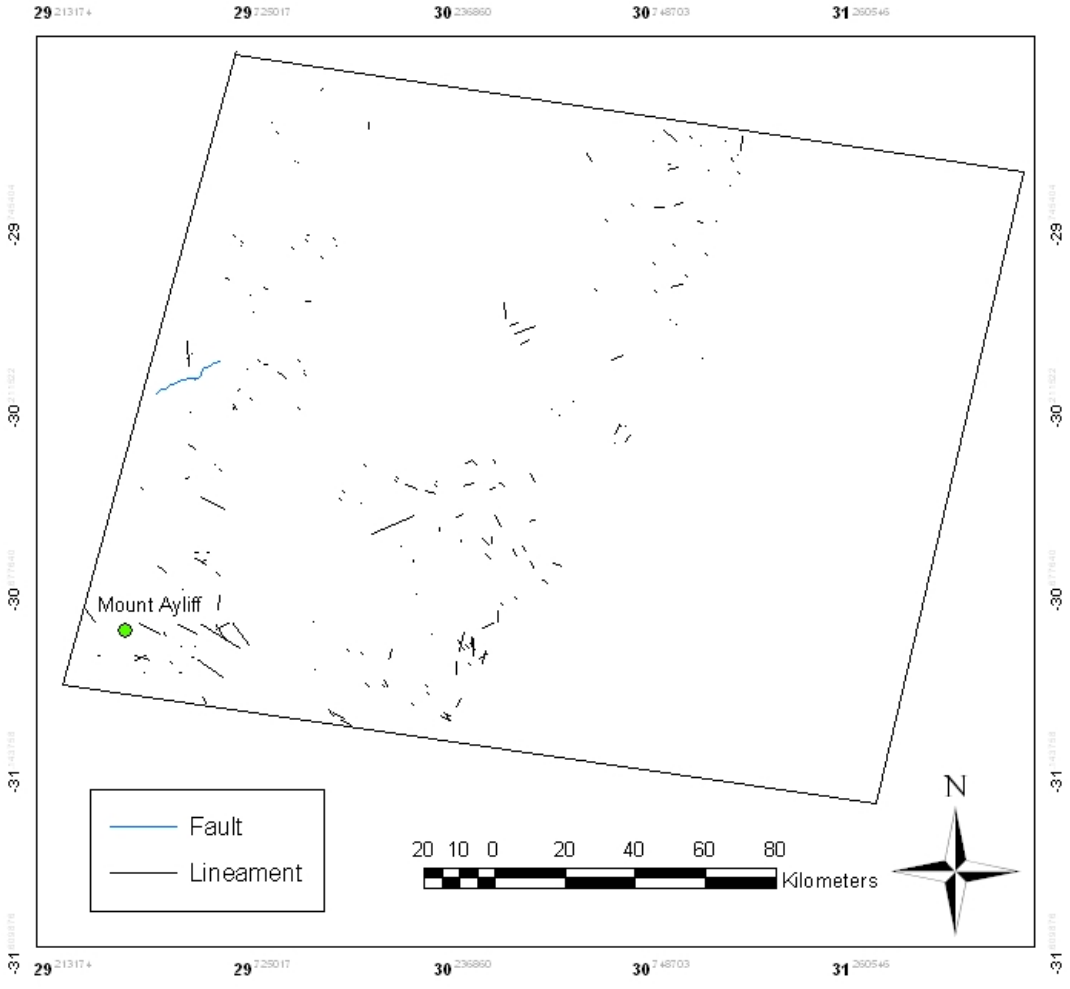

Figure 4- 16: Map showing lineament extracted from scene 168/081

4.3.3.4 Path 168, Row 082

This area around Port Saint Johns near the East coast is characterized by the presence of three major features: lineaments, faults and dolerite dykes. This area is located near the zone where the Amatole-Swaziland uplift axis took place in the Quaternary. Most lineaments and the few remarkable dolerites are quasi oriented NW-SE, except for the faults that trend in an almost NE-SW at the extreme coast (Figure 4.17).

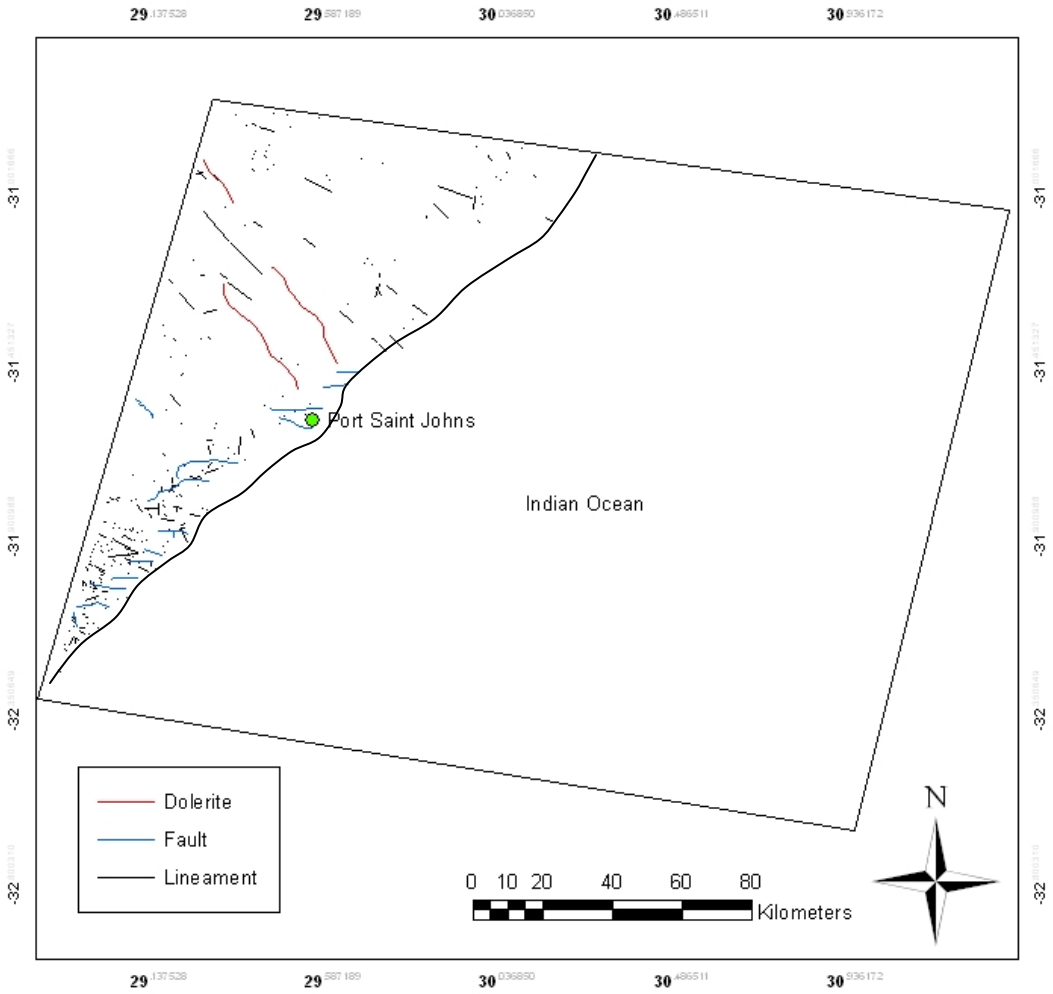

Figure 4- 17: Faults, lineaments and dolerites from scene 168/082

4.3.3.5 Path 169, Row 082

This area is characterized by increase in density of lineaments along the east coast. It is almost similar to the area of Port Saint Johns, since this area is also located in the vicinity of the Quaternary Amatole-Swaziland axis of uplift. Dolerites and lineaments in this neotectonic zone indicate places of potential high yield aquifers, the increase in lineament intensity along the coast (Figure 4.18) might be the consequence of the reactivation along the Agulhas Falkland Fracture Zone in the Indian Ocean combined with the uplift inland.

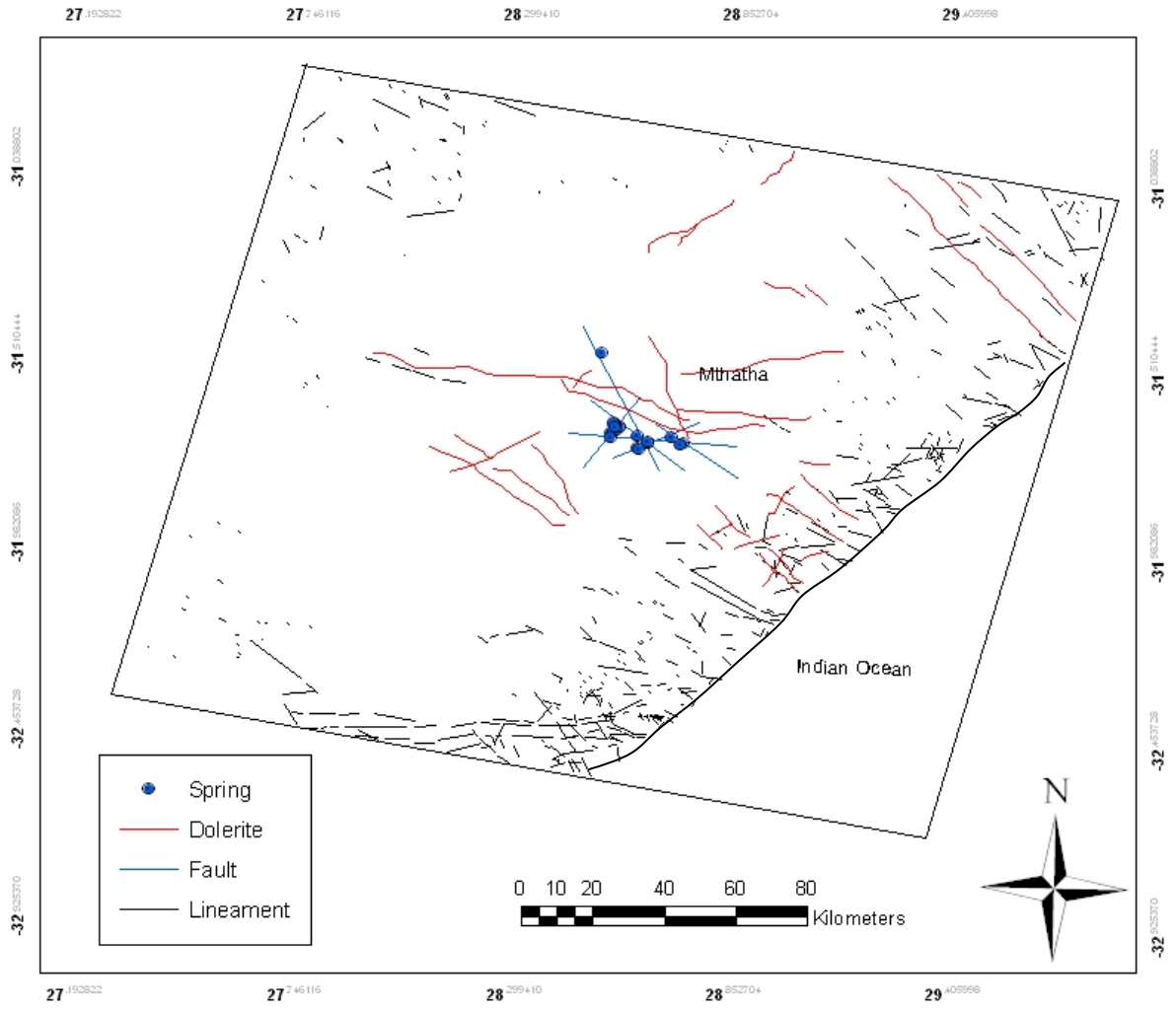

Figure 4- 18: Lineaments extracted from satellite image 169/082

4.3.3.6 Path 169, Row 083

This area around the city of East London is characterised by the presence of faults, lineaments, dolerites. Faults and dolerites are trending NE-SW, though few lineaments are oriented SE-NW (Figure 4.19). What seems to appear at first as lineaments as proper surface discontinuity at the geological term sensu stricto, are only negative weathering of dolerites. This can be seen both on the satellite image (Figure 4.20), and in a picture that was taken on the N2 highway to Butterworth from East London (Figure 4.21).

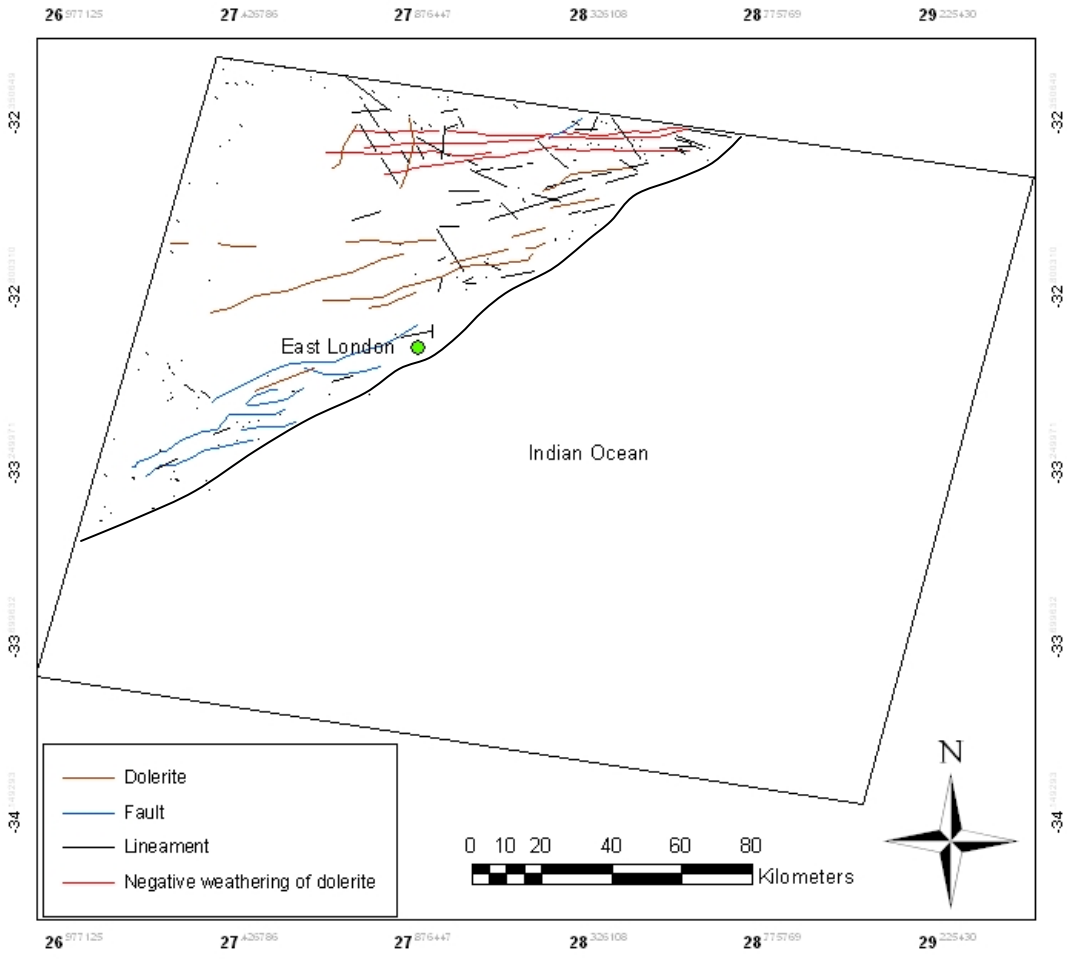

Figure 4- 19: Lineaments extracted from scene 169/083

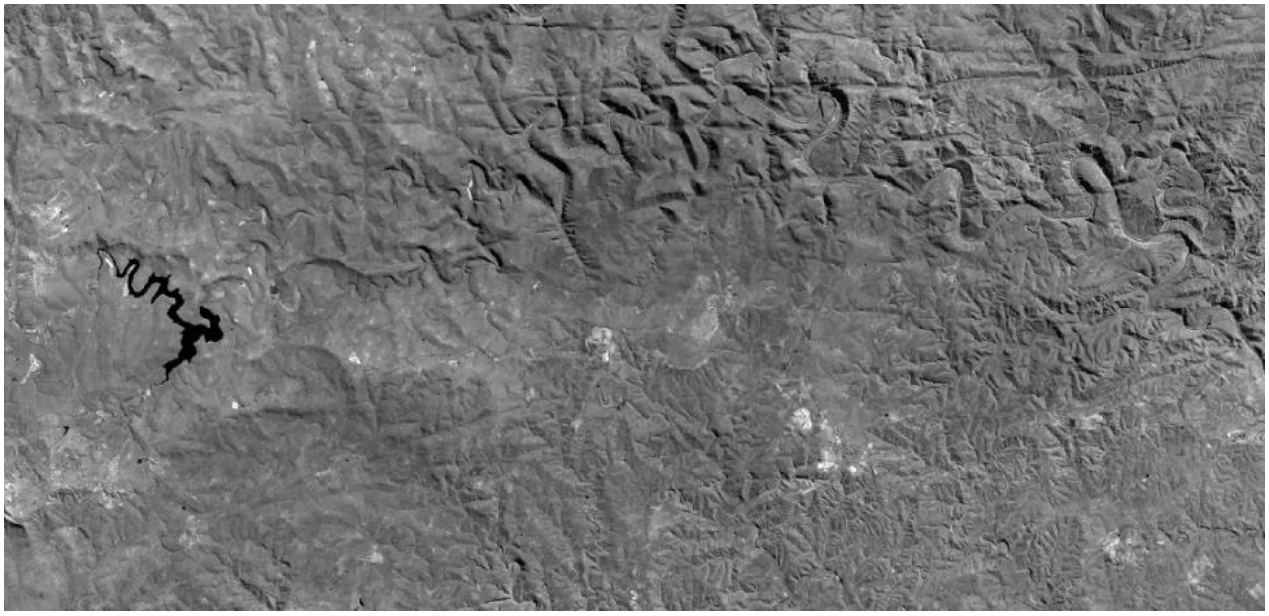

Figure 4- 20: Example of negative weathering of dolerites depicted as lineaments

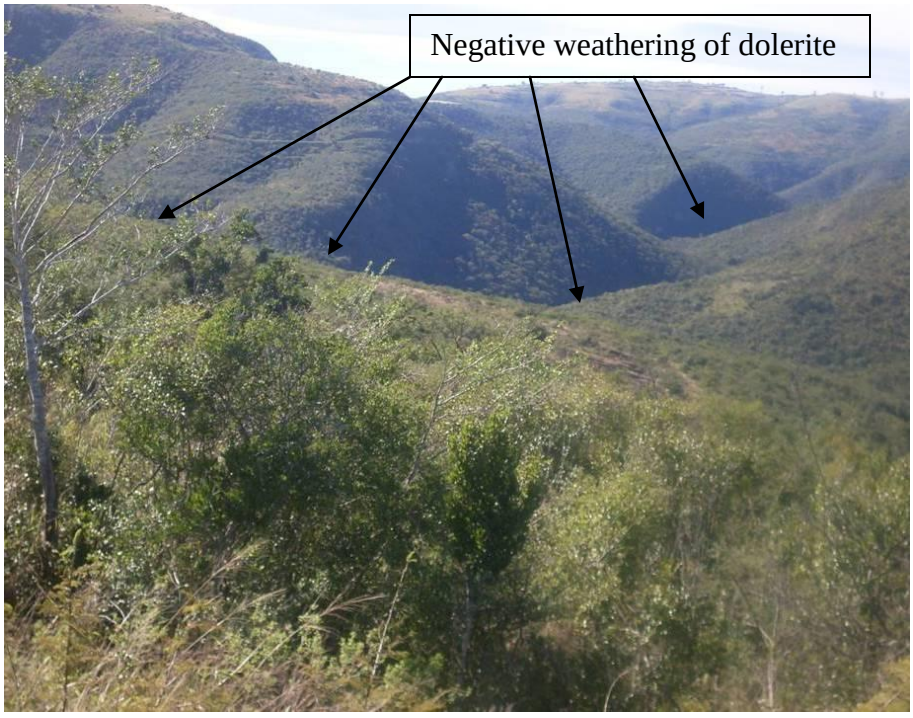

Figure 4- 21: Example of negative weathering of dolerite seen as a lineament on satellite image in Figure 4.20. Arrows point to the negative weathering of dolerites.

There is a conspicuous negative weathering of dolerite illustrated by a very long linear structure. This type of feature can only be initiated if there is a zone of weakness below the earth surface. Dolerite dyke emplacements in the Karoo Basin are unequivocally a consequence of the opening of the Gondwana. Extensional fractures were generated and the doleritic magma emplaced itself within the fractures to form what are known today as the Karoo dolerite dykes. This is to say that if there was a negative weathering of dolerites, this negative weathering is a subsequent event. A negative weathering can only occur where there is already a preexisting zone of weakness (fault or fracture beneath the Earth surface). Water can permeate and weather little by little the dolerite on the surface. This negative weathering could also certainly result from the Quaternary uplift near the east coast, or from reactivation offshore along segments of the Agulhas Falkland Fracture Zone. Dingle and Robinson (1985) for instance, highlighted that the reactivation probably caused the large slumps on the continental margin of South Africa, the slump lobes being positive features on the continental rise.

4.3.3.7 Path 170, Row 083

This area, located in the southern neotectonic belt, is characterised by a big lineament extending from east to west. If more lineaments were observed in the two previous scenes, it clearly appears that the further the examined area is far from the coast, the less the intensity of lineaments (Figure 4.22). The big lineament intersects both the Fort Beaufort and the Grahamstown fractures, these two intersections are good possibilities for groundwater exploration. Moreover, the Grahamstown area receives more rains that can continually recharge the aquifers. The evidence of more rain and groundwater flow is unequivocally the occurrence of the kaolin deposits. Kaolin deposits derived from the weathering of the Dwyka Group tillite of the Karoo Supergroup as will be discussed in Chapter 6.

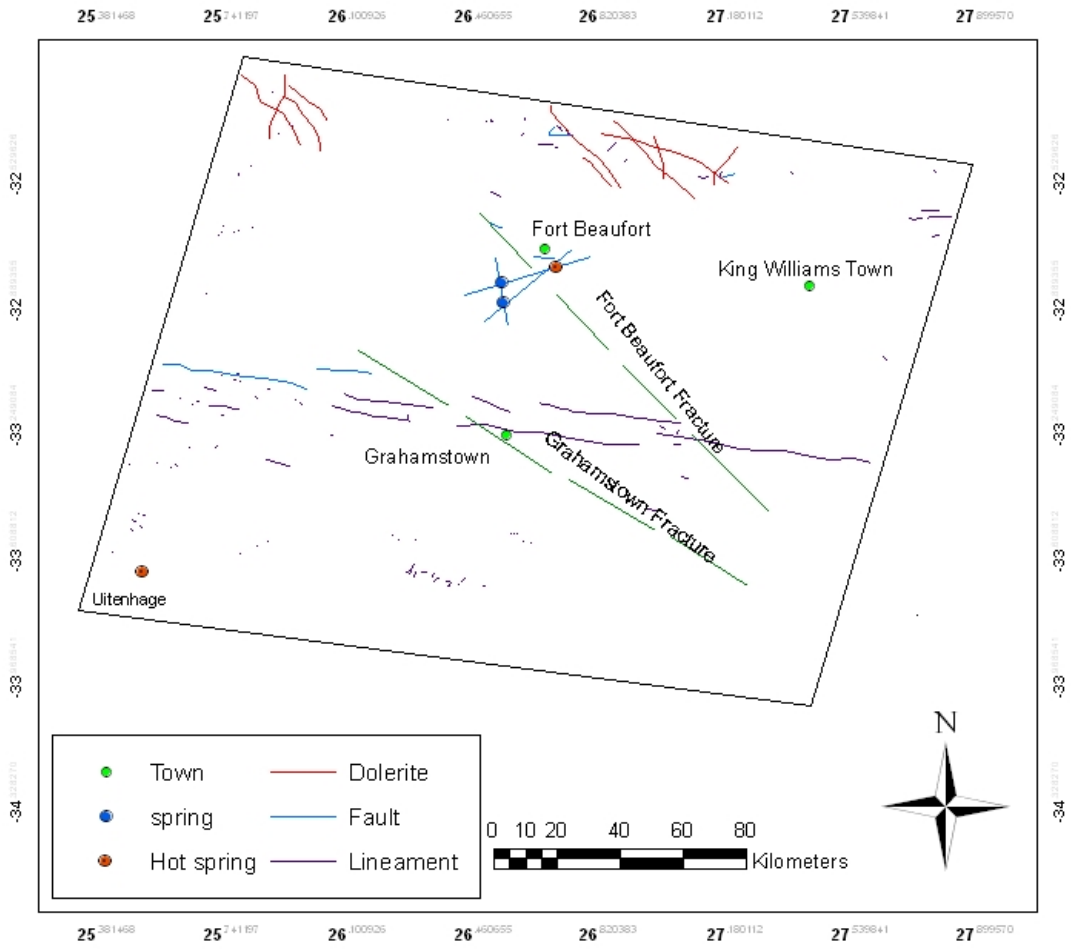

Figure 4- 22: Structures extracted from scene 170/083

4.3.3.8 Path 171, Row 083

In Figure 4.23 most lineaments seem to occur more in the south, which is near the south coast. The lineament density appears low in this region. Of importance in this scene is that it is located in the southern neotectonic belt known for the Kango-Baviaanskloof fault, which was reactivated during the Quaternary. (Goedhart and Booth, 2009) mentioned that his fault is a deep-seated (>10 km) crustal-scale zone of weakness.

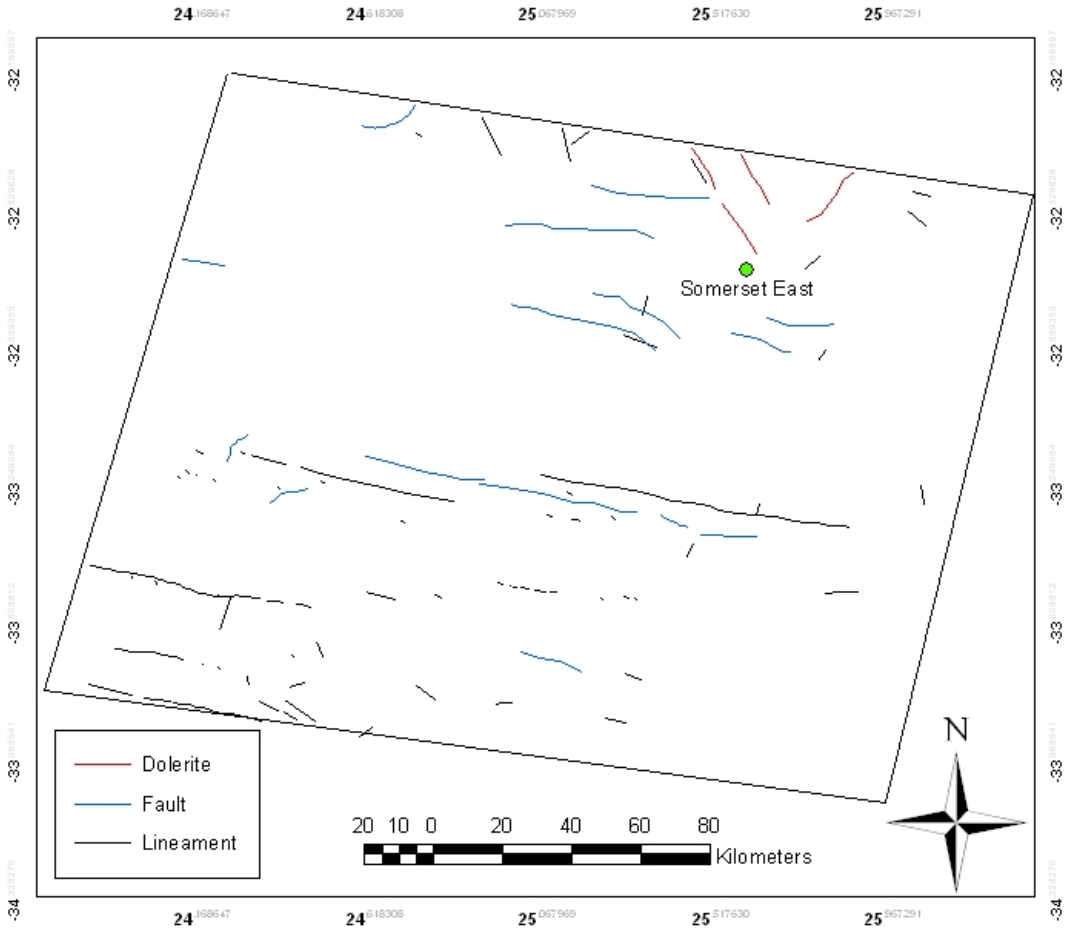

Figure 4- 23: Structures extracted from scene 171/083

4.3.3.9 Path 172, Row 083

Two types of lineaments in terms of direction can be singled out, the first type showing a ESE-WNW trending mostly to the right, which appears to be predominant, and the second one showing a WSW-ENE trend, which is minor (Figure 4.24).

4.3.3.10 Path 170, Row 082

This area located north of the southern neotectonic belt is very poor as far as lineament density is concerned (Figure 4.25). No real neotectonics is present. In terms of a nuclear waste storage, it

can be considered, because there is not much zones of weakness that can allow water to permeate and contaminate the groundwater below.

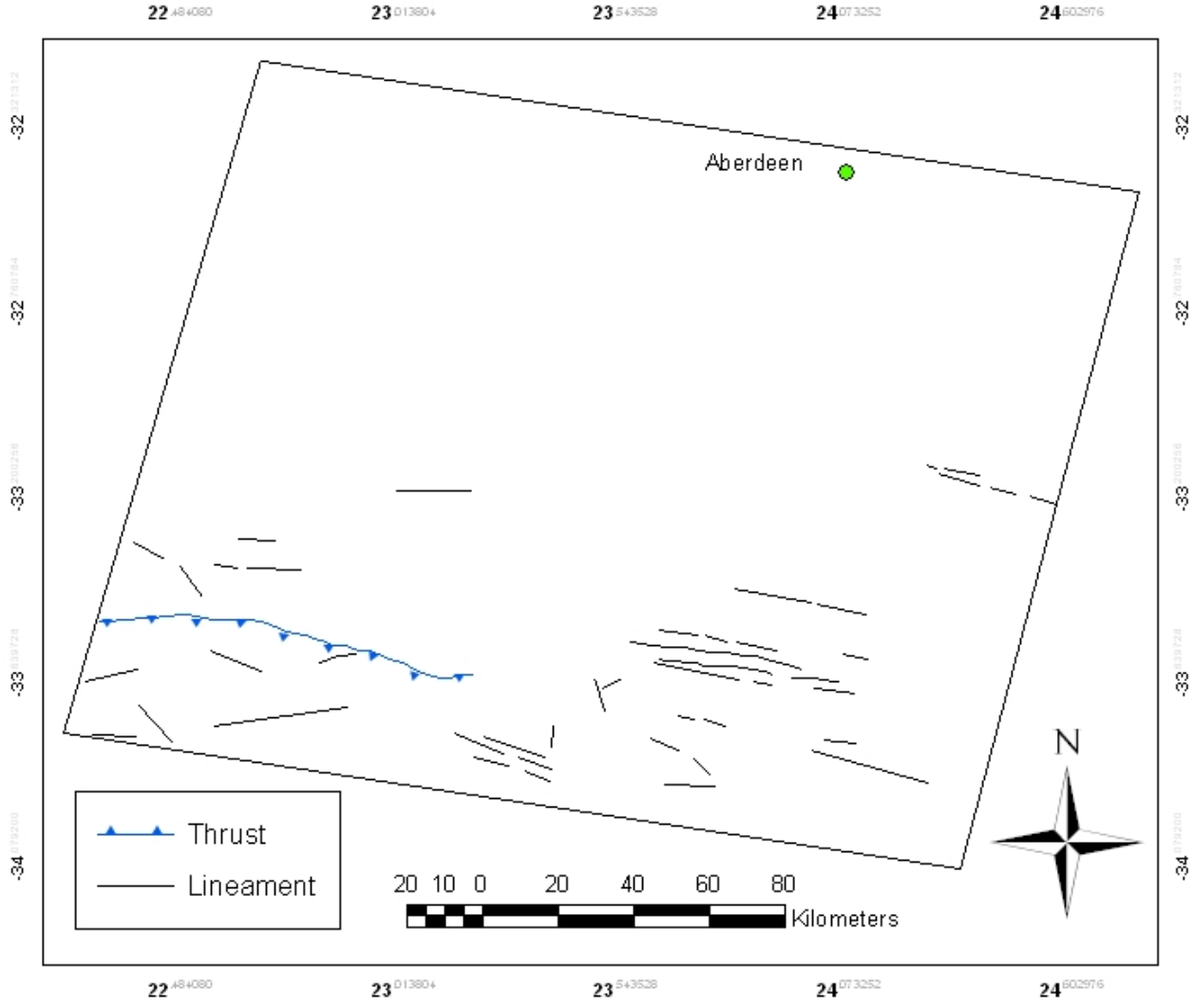

Figure 4- 24: Lineaments extracted from scene 172/083

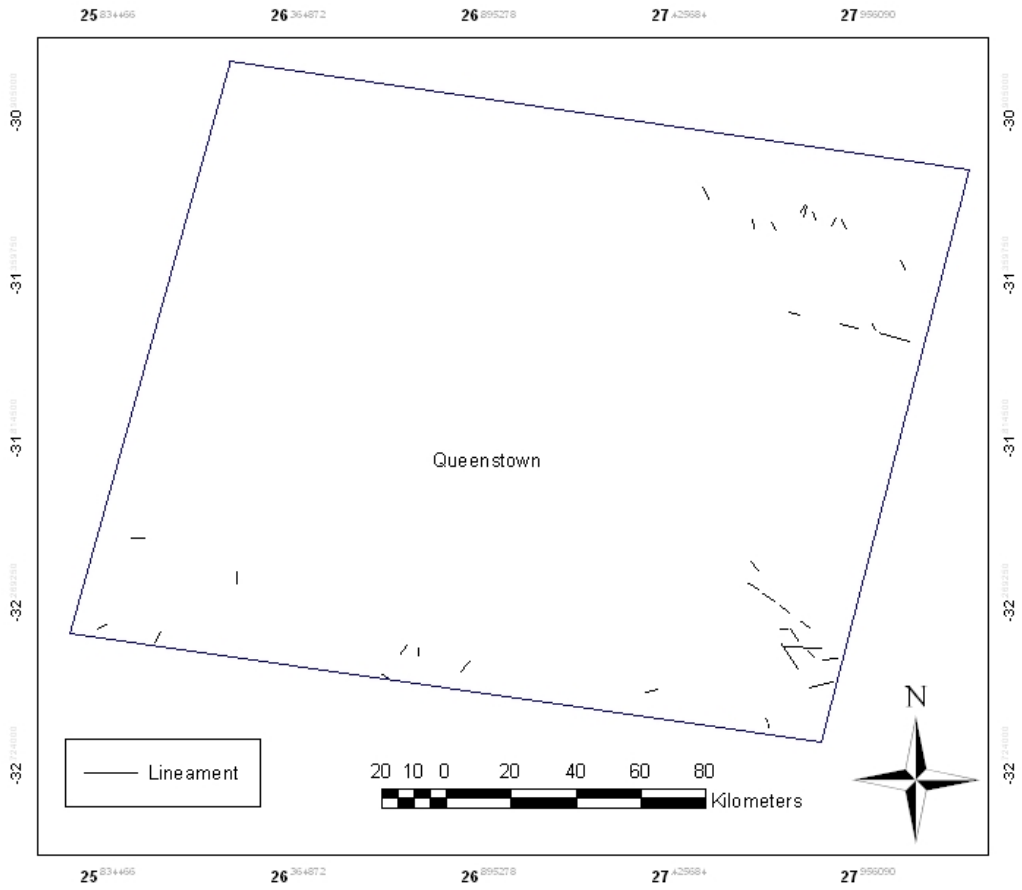

Figure 4- 25: Lineaments extracted from scene 170/082

4.4 General trend of lineaments

The lineament trends for the ten areas in the three neotectonics belts were deduced in ArcMap using Rose Plot 4.0. Different notable orientations were categorized using different colours in order to have the major predominant trend. The predominant trend can be considered for possible future groundwater exploration. It looks like that the general trend of lineaments in the Eastern Cape Province is oriented NW-SE. This trend may be related to the occurrence of the great compressional horizontal stress (Wegener Stress Anomaly), which is also oriented in the same direction. All rose diagrams for the three neotectonic belts can be seen in Figure 4. 26 a and b.

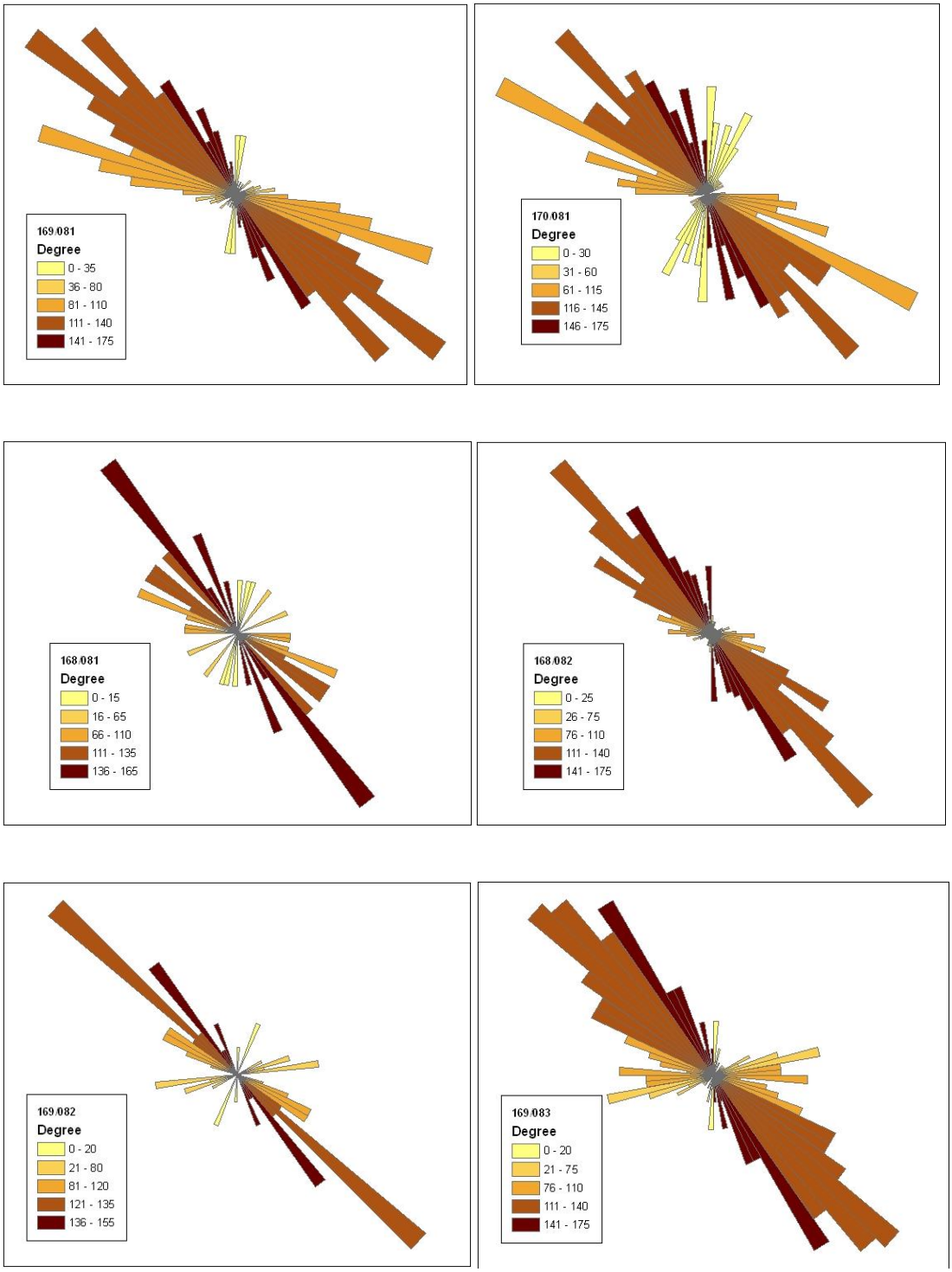

Figure 4- 26: a) Rose plots derived from the lineament maps in selected scenes

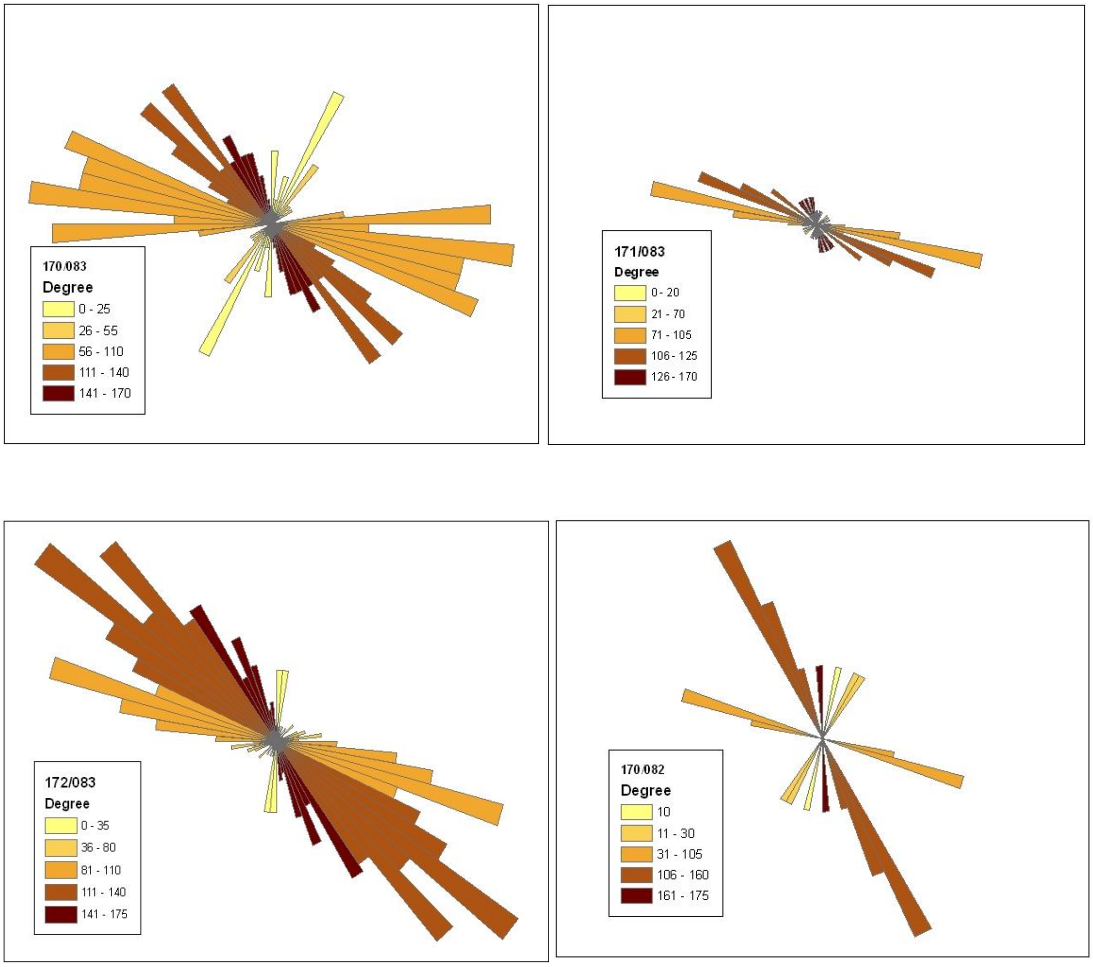

Figure 4.26:b) Rose plots derived from the lineament maps in the selected scenes

From the rose plots, it was found that the scenes (169/081, 170/081, 169/083, 170/083, 172/083, 169/082) are characterised by a uni-frequency of angle interval between 111 and 140 degrees in the ten examined scenes. Six of the ten scenes show this major trend, which is to be taken into account during groundwater exploration. Histograms in Figure 4.27 indicate that five scenes, three in the northern neotectonic belt (170/081, 169/081 and 168/081) and two in the eastern neotectonic zone (169/082 and 169/083) have high lineament density. One can surmise that a geomorphologic induced neotectonics would generate more lineaments than a seismically active zone. Kumanan (2001) found in India that lineament density maxima zones and lineament

intersections were buffered out as possible neotectonic zones. In the same line of thought, no considerable high density of lineament was depicted from the Queenstown area (scene 170/082). The histograms of all these lineaments can be seen in Figure 4.27 a and Figure 4.27 b.

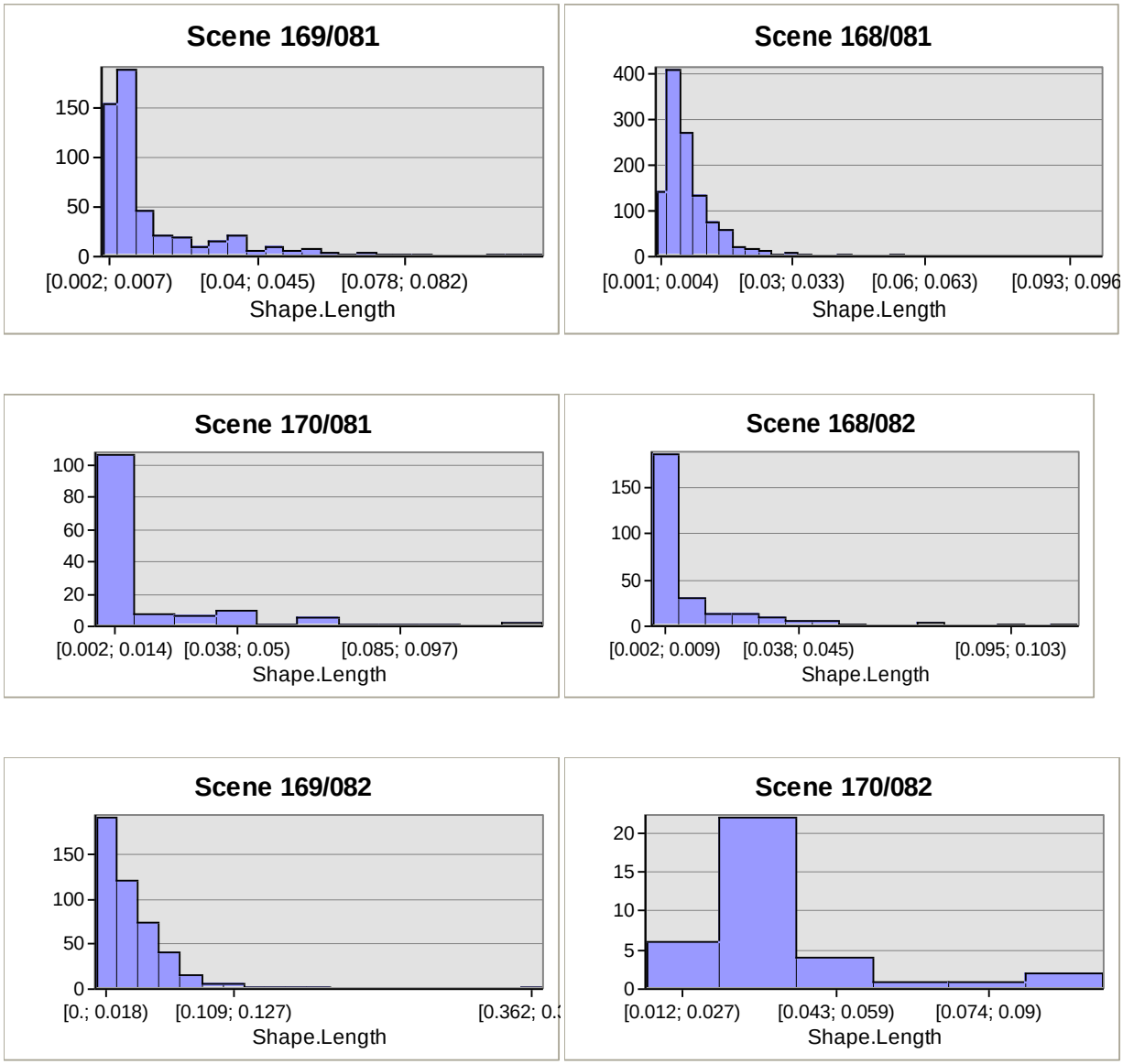

Figure 4- 27: a) Histograms deduced from lineament maps in the Eastern Cape neotectonic belts.

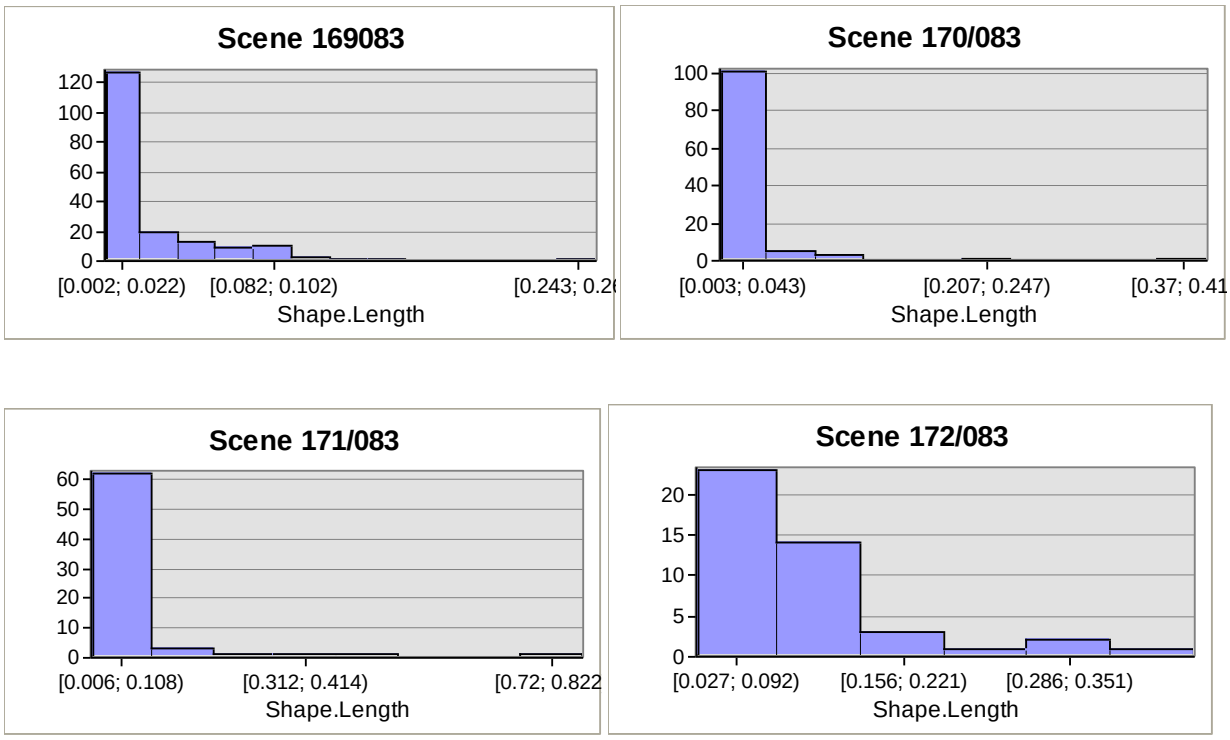

Figure 4.27: b) Histograms deduced from lineament maps in the Eastern Cape neotectonic belts.

4.5 Normalized difference vegetation index (NDVI)

The NDVI can in most of the cases be associated with the study and exploration of groundwater exploration. It normally indicates the degree of live green vegetation. Live green vegetation can be the surface expression of the presence of considerable amounts of water below the earth surface. The high amount of water is definitely related to fractures and faults, and to a certain extent to good catchments. The water is stored and accumulates in the catchments by flowing along the fractures and faults assimilated to lineaments. The NDVI is calculated from the individual measurements as follows:

$$NDVI = \frac{(NIR - \mathrm{Re}\,d)}{(NIR + \mathrm{Re}\,d)}$$

Red and NIR stand for the spectral reflectance measurements acquired in the red and near infrared regions, respectively. The NDVI varies itself between -1.0 and +1.0. Healthy vegetation absorbs most of the visible light that hits it, and reflects a large portion of the near infrared light. Unhealthy or sparse vegetation reflects more visible light and less near infrared light. Dark areas have low chlorophyll and light areas have more.

The eastern neotectonic belt can also be considered very important in terms of neotectonic activity because of high lineament densities. The high density of lineaments is consequence of what can be called morphotectonic induced neotectonics. This is only true when it is referred to the Quaternary uplift along the Amatole-Swaziland axis. The NDVI is applied only to this zone for the purpose of groundwater exploration. Four scenes (168/081, 168/082, 169/082, 169/083) were chosen, these scenes can be complemented with one scene in the northern neotectonic belt located in the Kokstad-Koffiefontein seismic belt. The NDVI was computed on band 3 and Near Infrared band using ENVI 4.8 software according to the following band math expression:

$$\mathrm{NDVI} = \frac{(float(B4) - (\mathrm{B3}))}{(float(B4) + (B3))}$$

In this equation, B4 represents the Near Infrared band and B3 the visible band (Red). Images were then interpreted in terms of colour differentiation, lighter areas being representatives of more chlorophyll, and accordingly potential good catchments. Dark areas being representatives of possible poor catchments or areas not affected by fractures and faults, mainly in the neotectonic zones. Scenes chosen for NDVI are those that were depicted as being more affected by high-density lineaments, mainly Path/Row: 169/081; 168/082; 169/082 and 168/083. All the output maps with the NDVI can be seen in Figure 4.28, 4.29, 4.30 and 4.31.

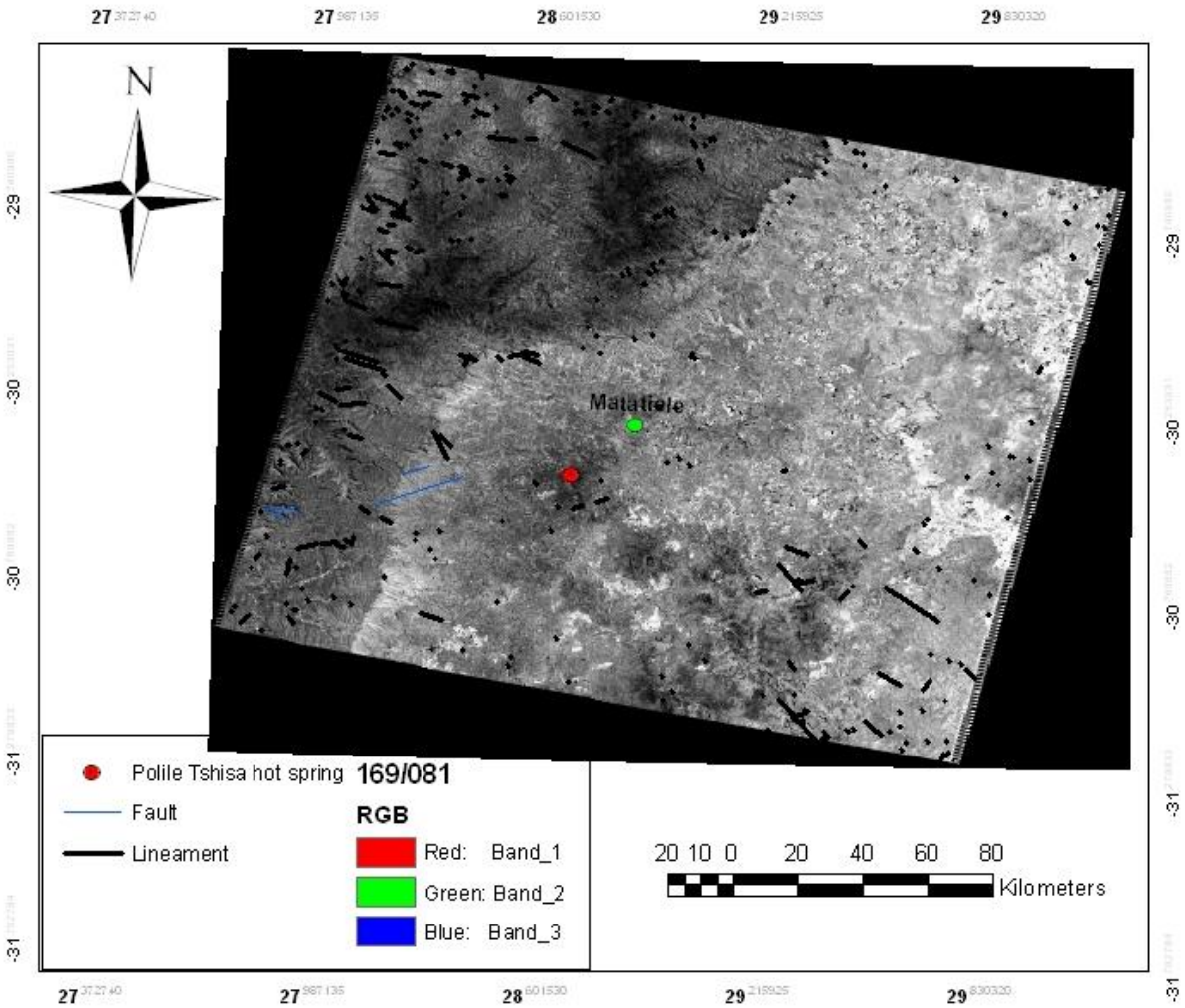

Figure 4- 28: NDVI from the scene 169/081, the darkish area in Lesotho and west and south-west of Matatiele is poor in vegetation.

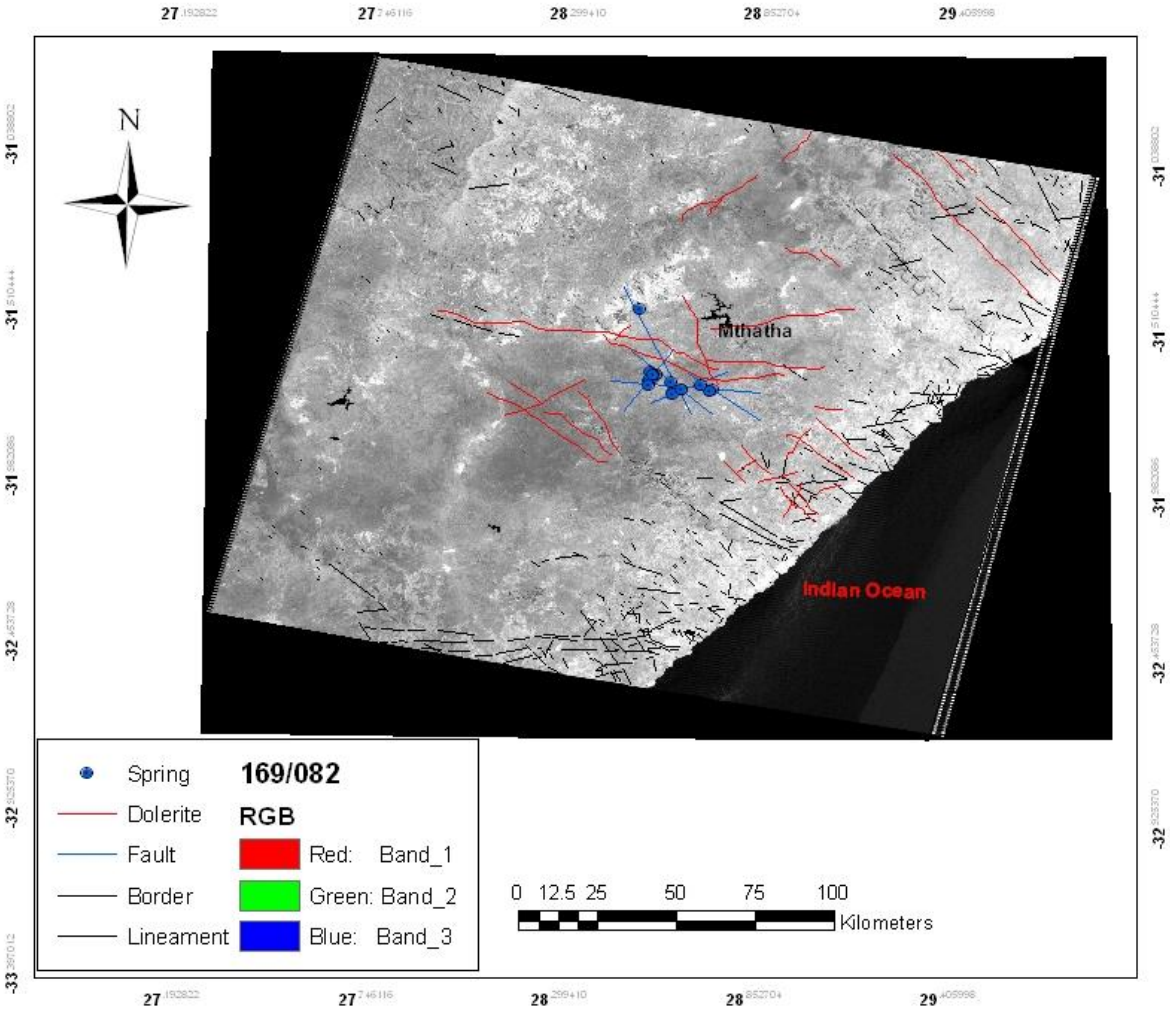

Figure 4- 29: NDVI from the scene 169/082, potential groundwater resources where light colour is predominant.

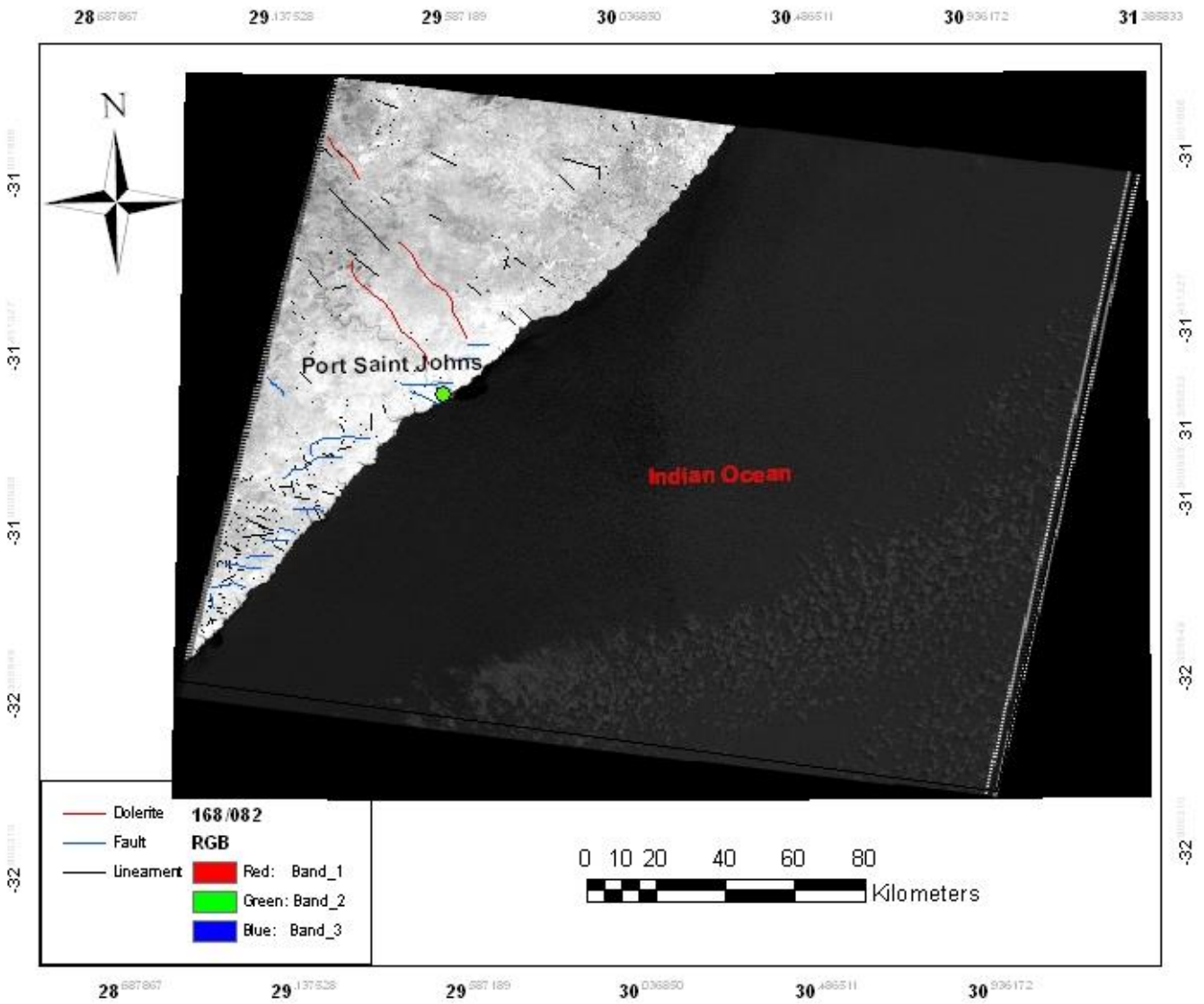

Figure 4- 30: NDVI from the scene 168/082, there is good indication for groundwater resources

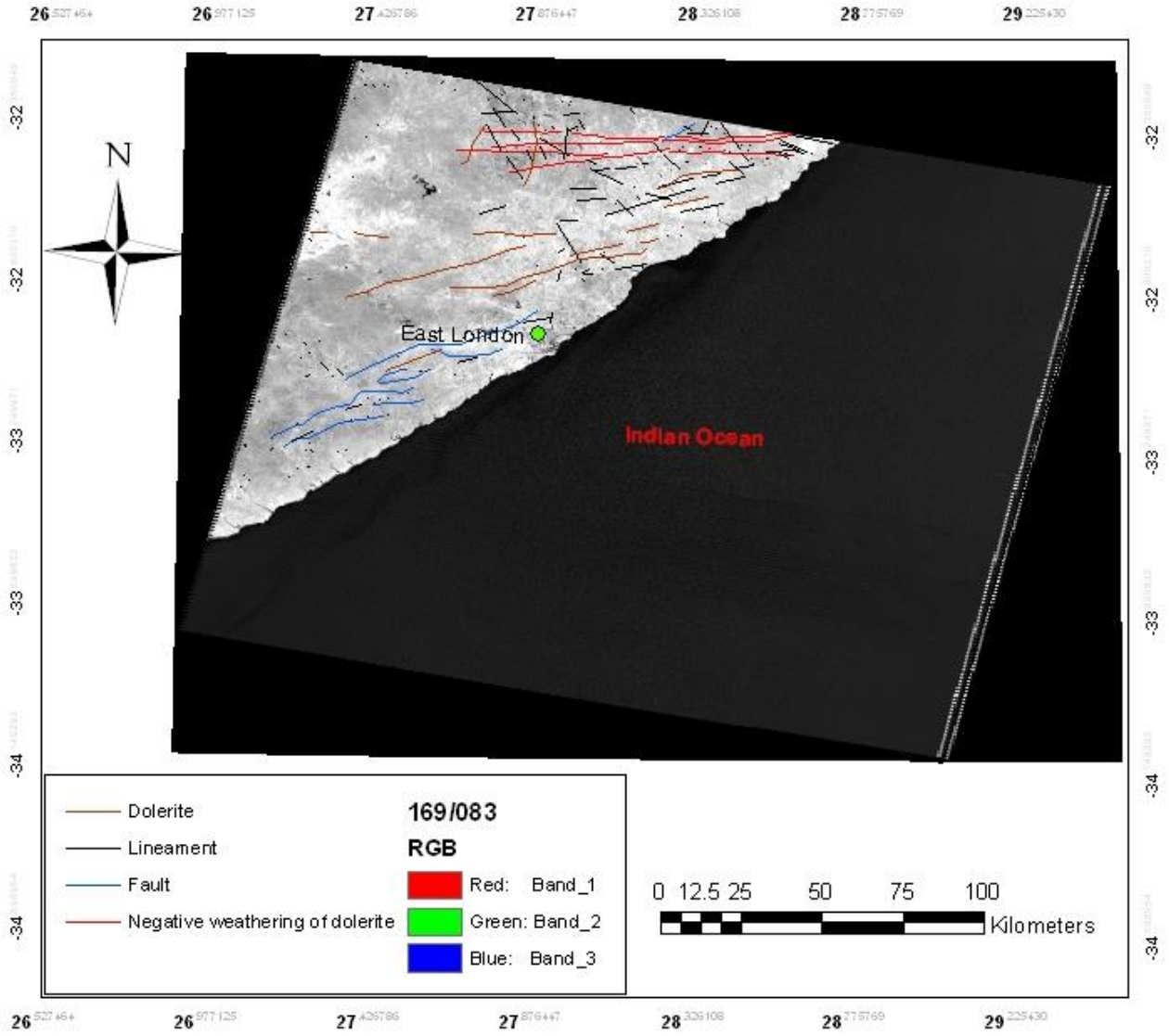

Figure 4- 31: NDVI from the scene 169/083, good potential for groundwater is highlighted.

The Port Saint Johns and East London NDVI results show high levels of chlorophyll, and accordingly dense vegetation. Though the Eastern Cape Province seems to be semi-arid, the high level of chlorophyll seen at the East London scenario is confirmed by the dense vegetation seen in Figure 4.32 a, b, c, and d. This is also indicative of high-density lineaments as was previously highlighted.

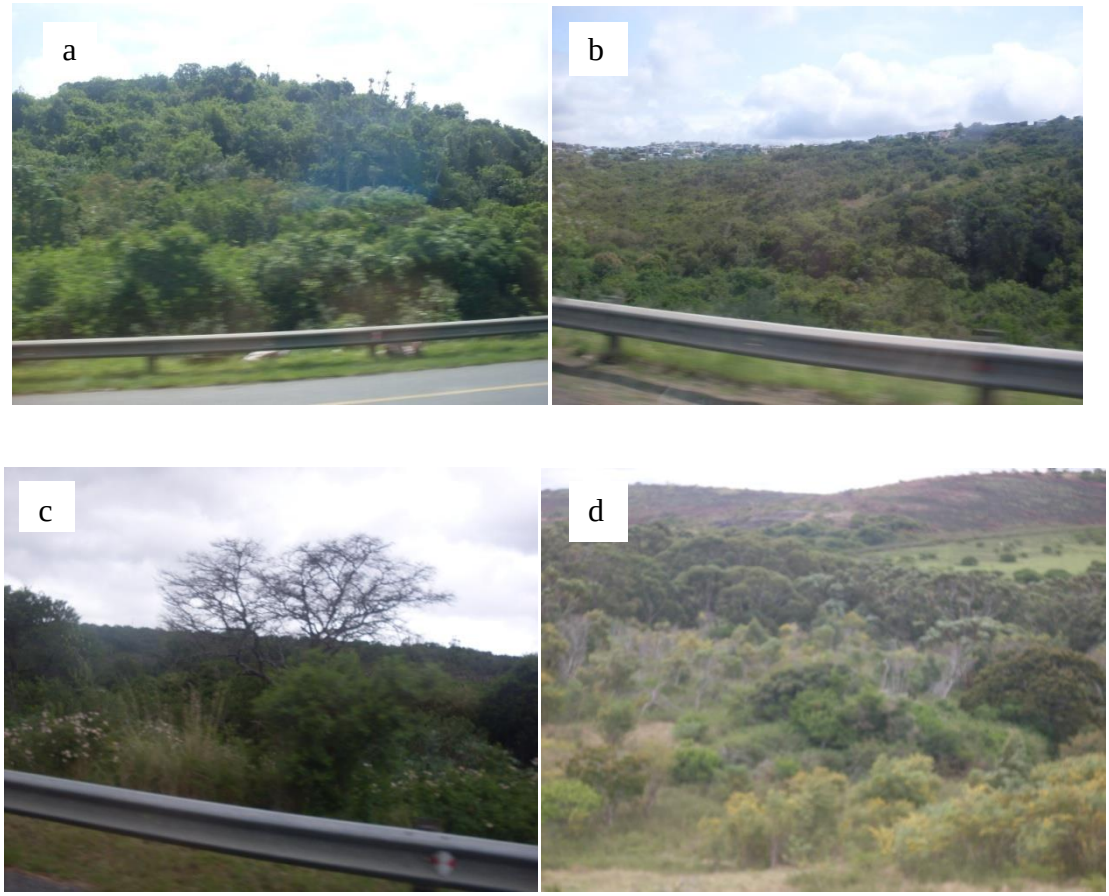

Figure 4- 32: a, b, c and d: Some sceneries at the east coast in the vicinity of the city of East London showing dense vegetation, possibly related to lineaments and faults.

4.6 Digital elevation models (DEMs)

The previous selected scenes are the same used above for the study of normalized difference vegetation index. SRTM 90 m Digital Elevation version 4.1 displaying these four scenes downloaded from Glovis/USGS present the following enhancements:

- Improved ocean mask used, which includes some small islands previously lost in the cut data;
- Single no data line of pixels along meridians fixed;
- All Geotiffs with 6000 x 6000 pixels; and
- For Geotiff format files the projection definition is the .tfw (ESRI TIFF World) and a .hdr file that reports PROJ. 4 equivalent projection definitions.

The DEMs data was processed in ArcMap 9.3 with a standard deviation stretching method level 2 in order to improve the resolution. These four scenes are all characterized by high density of lineaments, one in the northern neotectonic belt and three in the eastern neotectonic belt.

A digital elevation model in the neotectonic zones, especially in the chosen scenes can be used specifically for predicting possible catchments using high and low topography. In the area of Matatiele (Figure 4.33) the violet colour code is related to the high elevation while light brown to yellow areas are good indicators of water recharge. The strike-slip faults seen before (Figure 4.8) southeast of the hot spring near Matatiele can be considered as flowpath for groundwater. They are located immediately east of the high topography. Some of the lineaments that appear south of Matatiele (Figure 4.7), are located precisely in zones of low topography as indicated by an arrow in Figure 4.33 (Latitude: -30.776; Longitude: 28.977). When used for potentially high yield wells, boreholes can be drilled around these coordinates in a radius of approximately 20 km.

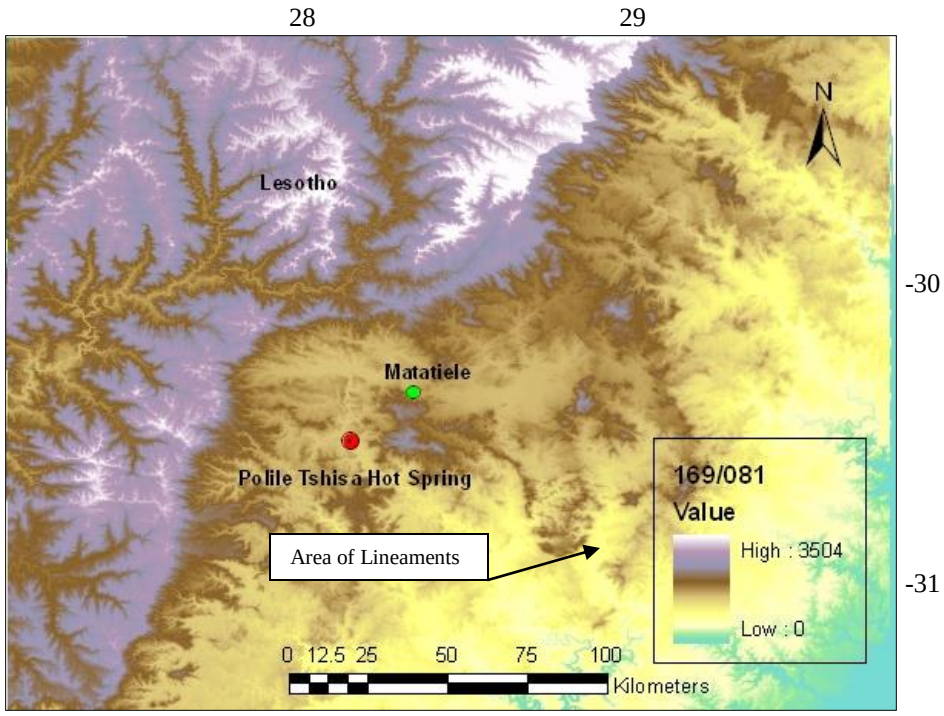

Figure 4- 33: DEM from scene 169/081

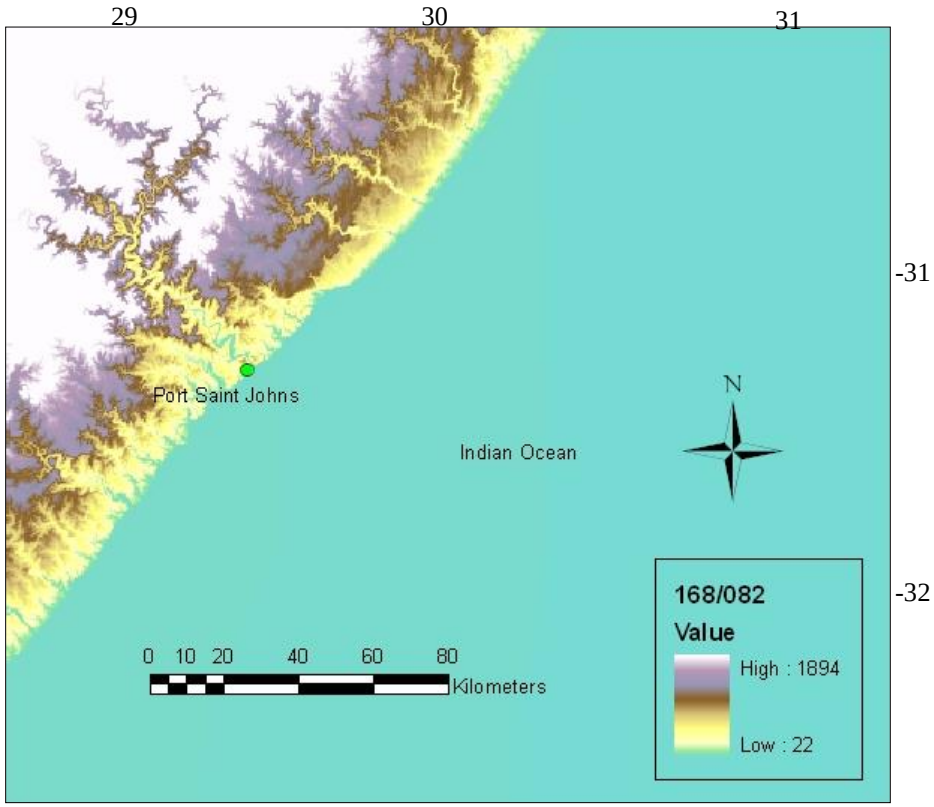

Figure 4- 34: DEM from the scene 168/082

The area south of Port Saint Johns (Figure 4.17) has a remarkable presence of lineaments. From Figure 4.34, it is obvious that potentially productive boreholes can be positioned within a radius of 15 km from the ocean to the continent. The only problem that might arise in the coastal area is the strong interaction between fresh and seawater. The Isinuka spring (Figure 2.6 a) near Port Saint Johns is an illustration of this interaction.

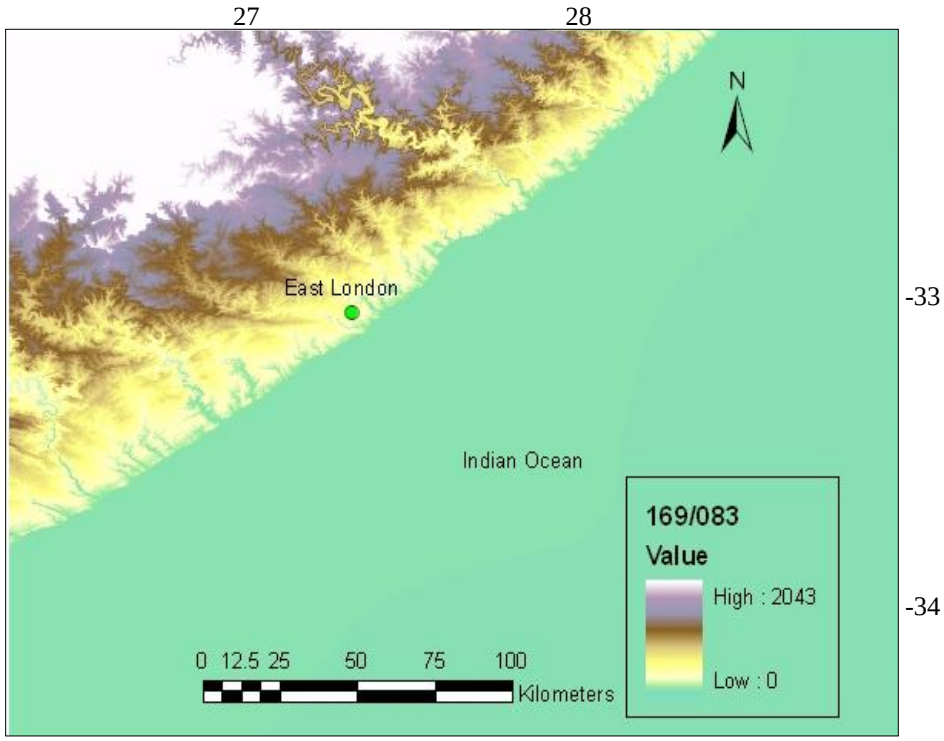

Figure 4- 35: DEM from the scene 169/083

The area around East London (Figure 4.35) is characterized by faults in the south with many lineaments to the north depicted from remote sensing analysis. As for the Port Saint Johns area, boreholes can be placed between 25 and 40 km from the coast depending on the characteristics of chosen location. The Mthatha area has lineaments throughout the east coast. It appears that this area was most affected by the Cenozoic uplift. Groundwater exploration can also take place here due to the presence of some remarkable dolerite dykes, which are considered as

groundwater localisers. With the same logic of considering new catchments, boreholes can be positioned within a radius of 40 km from the coast (Figure 4.36). Lineaments occurring in the major catchments in all these neotectonic areas play an important role for targeting groundwater. From all the chosen scenarios, the one that contains the area of Mthatha appears to be very promising for additional high potential boreholes. Many springs occur in the region of Mthatha. Springs can be indicative of movements along faults due to the flow of water.

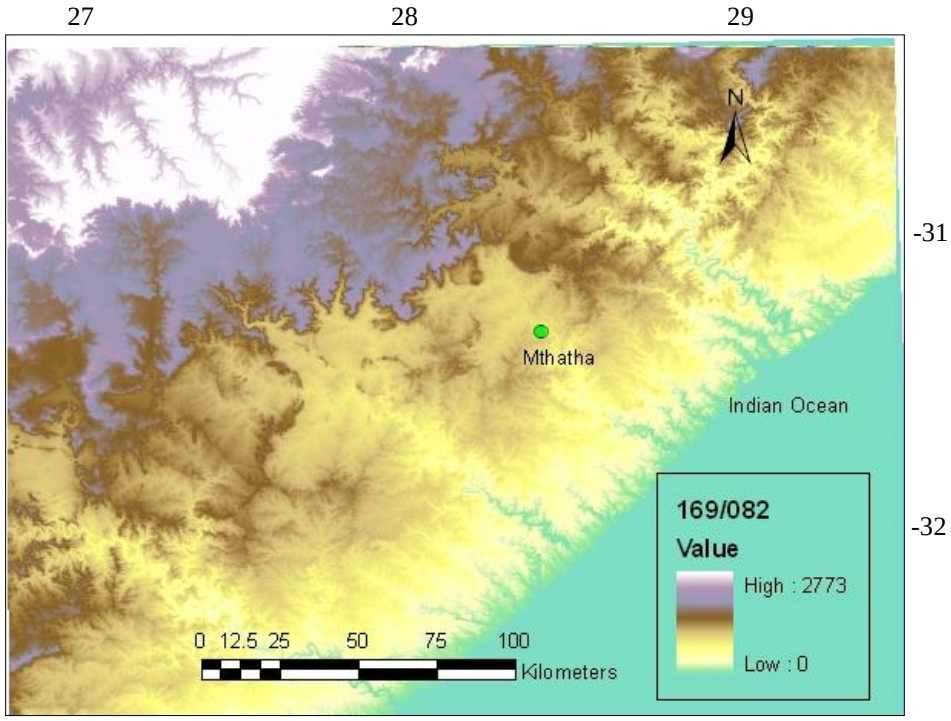

Figure 4- 36: DEM from the scene 169/082

Examples of geomorphological landform from DEMs

Digital Elevation Models can be used to support hydrological application. Data acquired from the South African National Geo-Spatial Information Centre for the three neotectonic belts were processed using Surfer 10. A small comparative study between these three neotectonic belts were done only on the basis of surface topography. Only one illustration was used from grid 3327.

This illustration of surface topography model can be seen in Figure 4.37. It appears in this figure a conspicuous lineament oriented east-west sampled from grid 3327 block D. This remarkable and striking feature can be called the Eastern Cape Great Lineament (ECGL).This is the second important structure in the southern neotectonic belt. The other structure is the Kango-Bavianskoof fault, which was reactivated in the Quaternary. This linear feature can be easily tracked few kilometers west of Grahamstown on the road to Bedford. This great lineament is also highlighted in Figure 4.39.

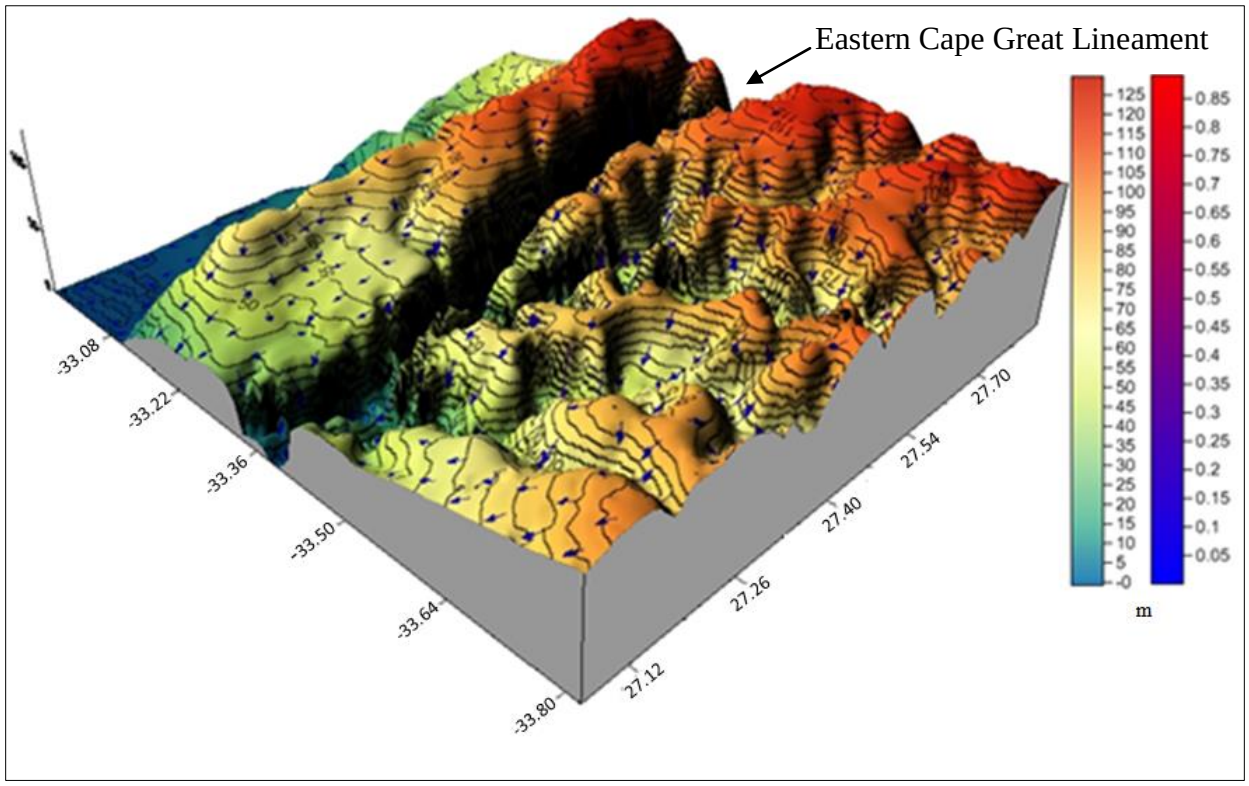

Figure 4- 37: DEM from grid 3327 block D. (the first legend on the left is for the altitude, and the second legend on the right is for the gradient vectors.

Other blocks in grid 3327 were examined; it was found that the altitude does not exceed 450 m. From a hydrological point of view, if the gradient vectors are considered, the flow direction from the surface topography is mostly oriented east-west (see blue arrows in Figure 4.37).

In the eastern neotectonic zone, DEMs from grid 3228 were also considered in order to see what the surface topography and the drainage pattern should look like. It was found from these models that the elevation increase reaches 1020 m above sea level with a varied geomorphic surface. This might be a consequence of the uplift that took place in the Cenozoic, or this can be a result of dolerite dykes that have resisted the erosional processes to form these outstanding and conspicuous morphologies at such an altitude. However the hypothesis of uplift is favoured more. It must be noted that in the eastern neotectonic belt, altitudes are not uniform and vary considerably (190 m, to 500 m, 700 m and 1020 m). The vector gradients indicate that the surface water would, in general, flow in an east-west trend.

Samples of Digital Elevation Model in the northern neotectonic belt near the country of Lesotho were taken from the grid 3028. The vector gradients have a mostly east-west and north-south orientation. This orientation of vector gradients in a sort of east-west trend would be an important factor to consider for future hydrogeological works for flow direction. It was observed also that in the northern neotectonic belt can reach 2000 meters

The Eastern Cape great lineament, a neotectonic domain (Figure 4.37 and Figure 4.39)

Digital elevation models of the Eastern Cape Province complemented the satellite imagery examination. In Figure 4.22 there appears a conspicuous linear feature north of the town of Grahamstown. This linear feature traverses the province and stretches from east to west. Field observations indicate that this linear feature is similar to a graben, and is located around the

contact of the Cape-Karoo Supergroup. It was observed NW of the town of Grahamstown at latitude S 33.17215 and longitude E 026. 32628.

Though it generally strikes in an east-west direction, the recorded strike was N 120^{o}. The space between the two surfaces of the normal faults, which are part of the graben-like feature, is almost 200 meters. One surface of the fault has an outcrop of quartzite of the Witteberg Group (Figure 4.38 left). The graben-like feature can also be seen in Figure 4.38 (right).

Figure 4- 38: (left), One surface fault of the graben with quartzite of the Witteberg Group, Cape Supergroup; right) the graben morphology

This graben forming the major lineament of the Eastern Cape Province has some seismic epicentres. These epicentres can be followed all the way from the east coast to the border of the Eastern and Western Cape Provinces (Figure 4.39). This indicates that this lineament is a neotectonic domain, and its shape is undoubtedly a good catchment area. These seismic epicenters indicate possible reactivations, which is good for groundwater targeting. Some extensional fractures were found on a quartzite outcrop. The strike of these extensional fractures is, astonishingly, the same direction of the graben itself (N120^{o}). Their development are possibly

concomitant with the extensional movement responsible for the graben formation, or they are related to extensional normal faulting that triggers earthquakes in and around Grahamstown.

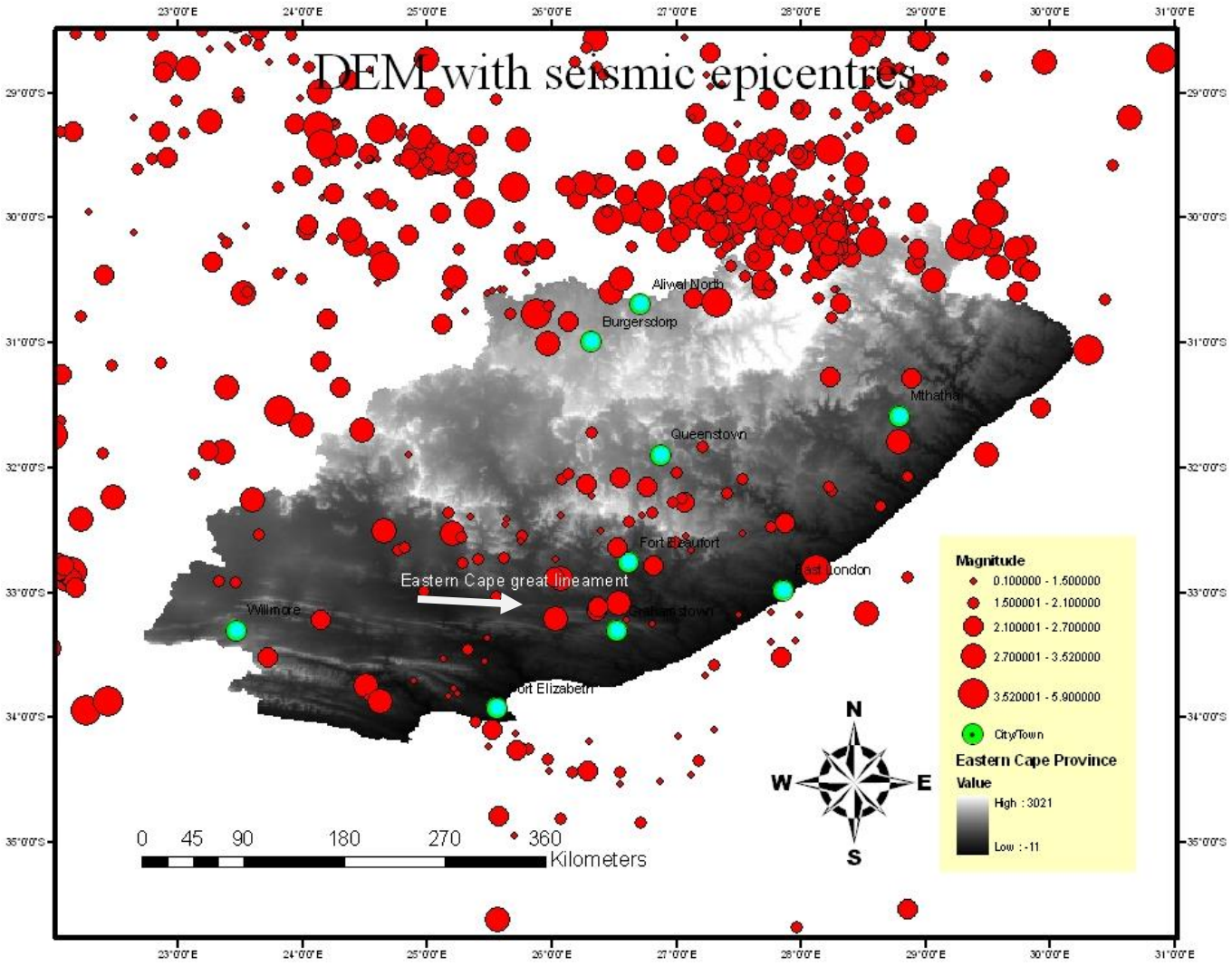

Figure 4- 39: Digital elevation model of the Eastern Cape Province, the great lineament has seismic epicenters within it.

These extensional fractures can be seen in Figure 4.40 (left). In places these fractures are filled with quartz veins, either in the quartzite or in some quartzo-phyllites (Figure 4.40 right).

This great lineament, which is a neotectonic domain, has at some places, indications of ongoing movement due to the occurrence of horizontal extensional fractures filled with fibrous calcite (Figure 4.41 left) or quartz. The fibrous calcite vein filling indicates that the extension direction is perpendicular to the vein wall. In Figure 4.41 (right), the open space above the vein possibly indicates a neotectonic horizontal compressional stress acting in the area. The proposed graben-like structure in this regional lineament is evidenced by a dip-slip movement indicated by the occurrence of slicken lines on a surface of siltstone. (Figure 4.42).

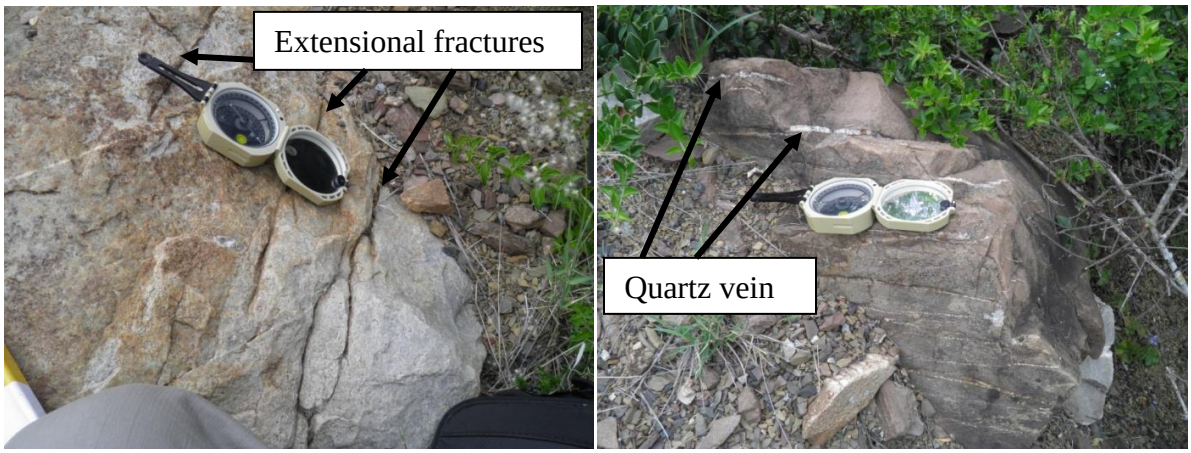

Figure 4- 40: (left) Quartzite affected with extensional fractures, quartz veins in quartzo-phyllite

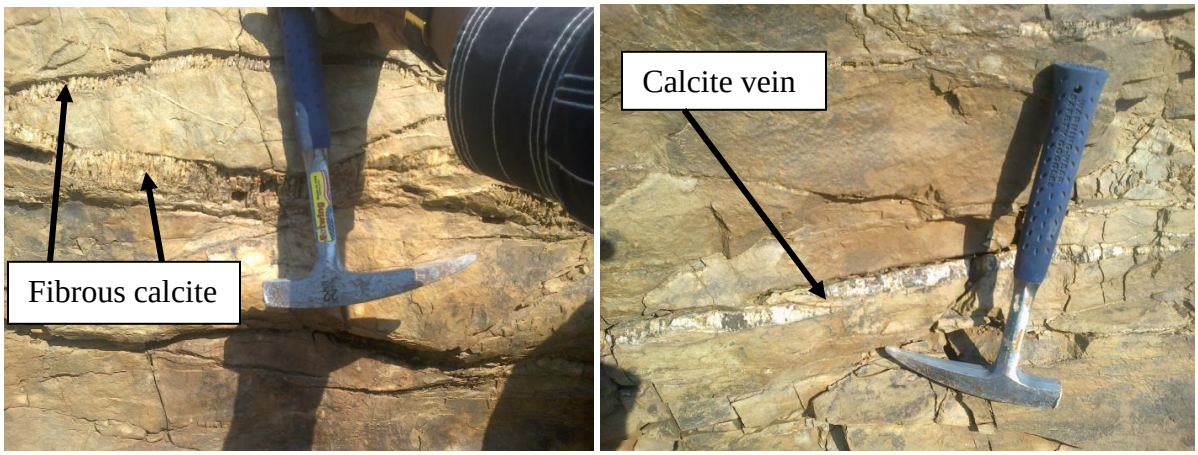

Figure 4- 41: (left) Fibrous calcite vein filling perpendicular to the direction of extension; (right), horizontal fracture with an opening space above the calcite vein

Figure 4- 42: Dip-slip movement indicated by the occurrence of slicken lines on a surface of siltstone

4.7 Drainage and rainfall

Woodford and Chevallier (2002) observed that in the Eastern Cape one can have peripheral drainage, with the highest gradient rivers flowing from the escarpment to the coast in the east. This flow pattern characterises the eastern neotectonic belt in the Eastern Cape. Figure 4.43 displays all the rivers of the Eastern Cape Province.

In the area of scenario 169/081, in the northern neotectonic belt south of the country of Lesotho, there seems to be two major trends of river flow; one in an east-west direction, mostly consisting of tributary rivers, and the other in a NW-SE direction mostly consisting of main rivers. These rivers are highlighted in red in Figure 4.43. Woodford and Chevallier (2002) noted that rainfall is the cause of the highest river flow in the east Karoo, this is in agreement with the NDVI results as shown above.

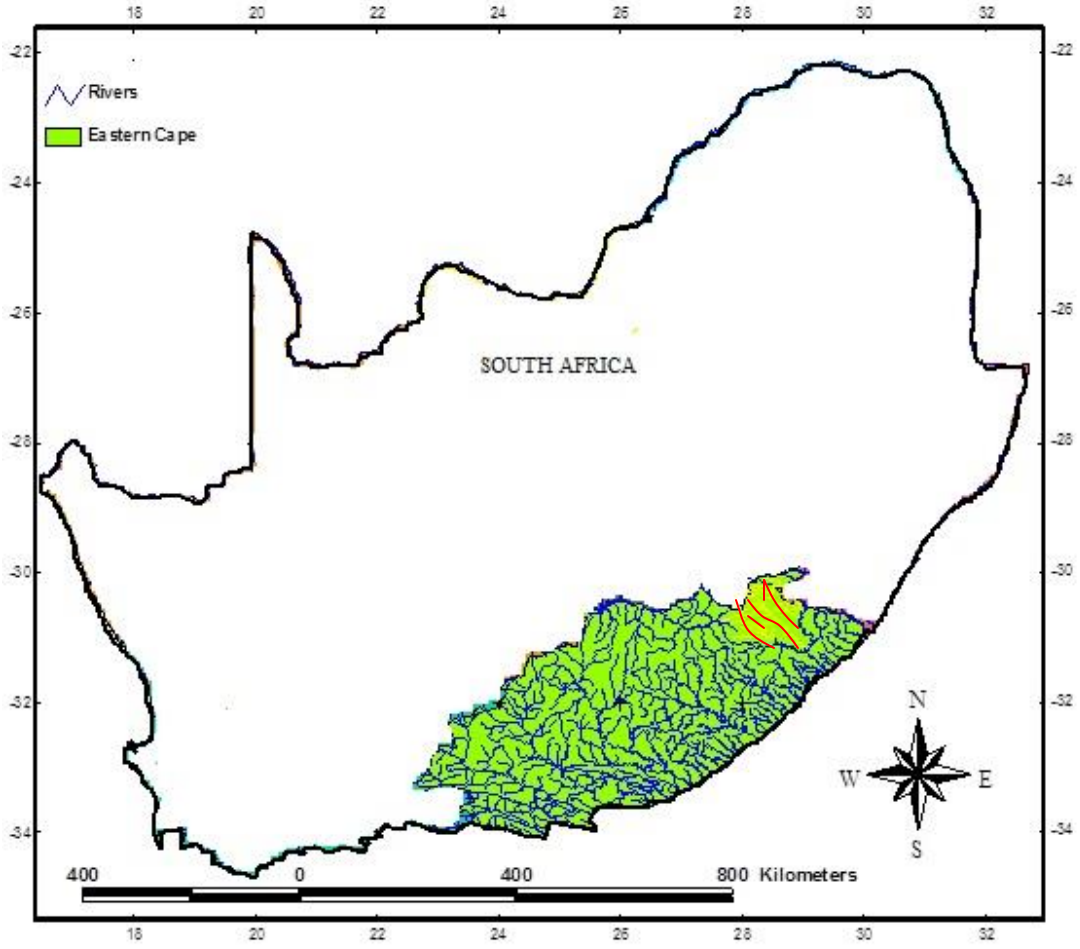

Figure 4- 43: Rivers of the country of South Africa (source: CGS, South Africa)

4.8 Summary

In the exploration and characterisation of potentially high yield aquifers, remote sensing has always played an important part, primarily because it can be used to find the maximum lineament density. This can, in turn, be correlated with the strike; which is useful in the exploration of groundwater. Most of the lineaments that were depicted using remote sensing have a predominant NW-SE orientation. The biggest lineament (ECGL) is an important feature to be reckoned with in the Eastern Cape as far as work related to groundwater is concerned. This,

because of the alignment of seismic epicenters related to earthquakes, which can reactivate the structures to allow the movement of groundwater. The eastern neotectonic belt has a high density of lineaments, which makes it another important neotectonic domain of the Province.

5. VERTICAL SEISMIC DATA INTERPRETATION IN THE EAST COAST

5.1 Introduction

Vertical seismic profiling has and is widely being used for the interpretation of stratigraphic and structural components below the Earth's surface. It has been proven as a useful tool for the delineation of seismic wave propagation properties (e.g. Hordage, 1985). Nton and Easn (2010) highlighted that sequence stratigraphy is a recent tool used to better understand stratigraphic distributions and prediction of source beds and reservoirs. On the other hand Van Wagoner et al. (1990) indicated that sequence stratigraphy is a multidisciplinary approach to the study of genetically related facies within chronostratigraphically significant surfaces. According to Daley et al. (1988), the use of vertical seismic profiling to study fracture-induced anisotropy is a growing field, and can give information where structure and fracture properties are not well understood. What is worth to mention in this section is that, besides the groundwater issue that is being dealt with, seismic stratigraphy is also widely used for oil exploration in order to locate structural traps for petroleum deposits. Seismic methods can be used to delineate rock bodies with distinctive geometries and internal structures, which can be thought of as constituting seismic facies (Boggs, 2001).

The purpose of using vertical seismic profiling in some parts of the east coast in the Eastern Cape is aimed at trying to have a clear picture of the stratigraphic sequences and possible associated structural elements below the surface. This will assist in targeting other areas for future groundwater exploration, since sequence stratigraphy or structural elements such as faults can be identified through analysis and interpretation of a 2D seismic line data. A complete map indicating all prospecting seismic lines used in this study can be seen in Figure 5.1. Most of the

processed data are from the King Williams Town area in the eastern neotectonic belt. The profiles are marked as KW (or Line KW); other data was acquired offshore and was marked as HC 74. Figure 5.2 is a magnification of some areas in Figure 5.1 essentially the area of King Williams Town and the offshore. Five prospecting lines onshore (Line KW-5, KW-26, KW-28, KW-29 and KW-30) and three prospection lines offshore (HC74-006, HC74-007 and HC74-009) were used in this study. Sequence stratigraphy is not only used for sedimentology such as analyzing changes in facies and geometric characters of strata, and the chronological order of basin filling (e.g. Catuneanu et al., 2009), but is also used for structural analysis. As the current research study is related to characterization of aquifers and groundwater exploration, efforts to depict the geometry below surface can speed up target detection of areas of secondary permeability. According to Catuneanu et al. (2009), other uses of sequence stratigraphy include stratigraphy, geophysics, geomorphology, isotopes geochemistry, structural geology, basin analysis, sea-level change, subsidence, climate, sediment supply, basin physiography, environmental energy, and biota.

Reservoir performance can be controlled by fractures and faults. Lachaal et al. (2013) indicated that lateral and vertical aquifer extension and its conceptual structure, which contribute to determine boundary conditions, are derived from integrating oil and water well data and seismic profile interpretation. They also found in their study on the aquifer of Zéramdine-Béni Hassen (east-central Tunisia) that seismic profiles interpretation highlighted the existence fault corridor, anticline, and grabens that represent lateral boundaries for the study aquifer. The use of seismic profile is very relevant for characterizing potentially high yield aquifers, especially in dry environments such as the Karoo in the Eastern Cape.

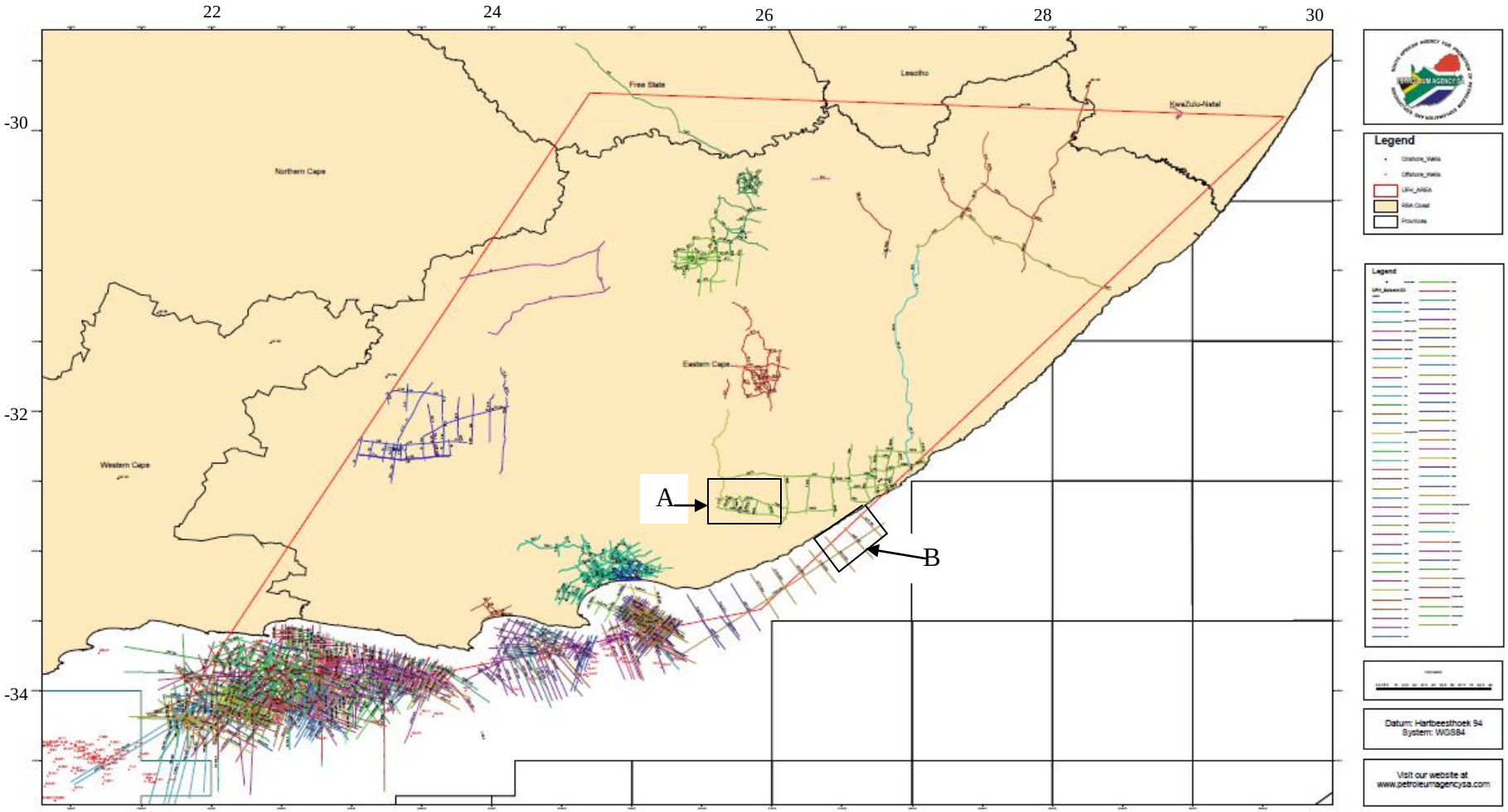

Figure 5- 1: Prospecting seismic lines by PetroSA onshore and offshore and the Eastern Cape. Blocks A and B are areas containing the investigated vertical seismic profiles in this study. Lines in different colours are seismic lines.

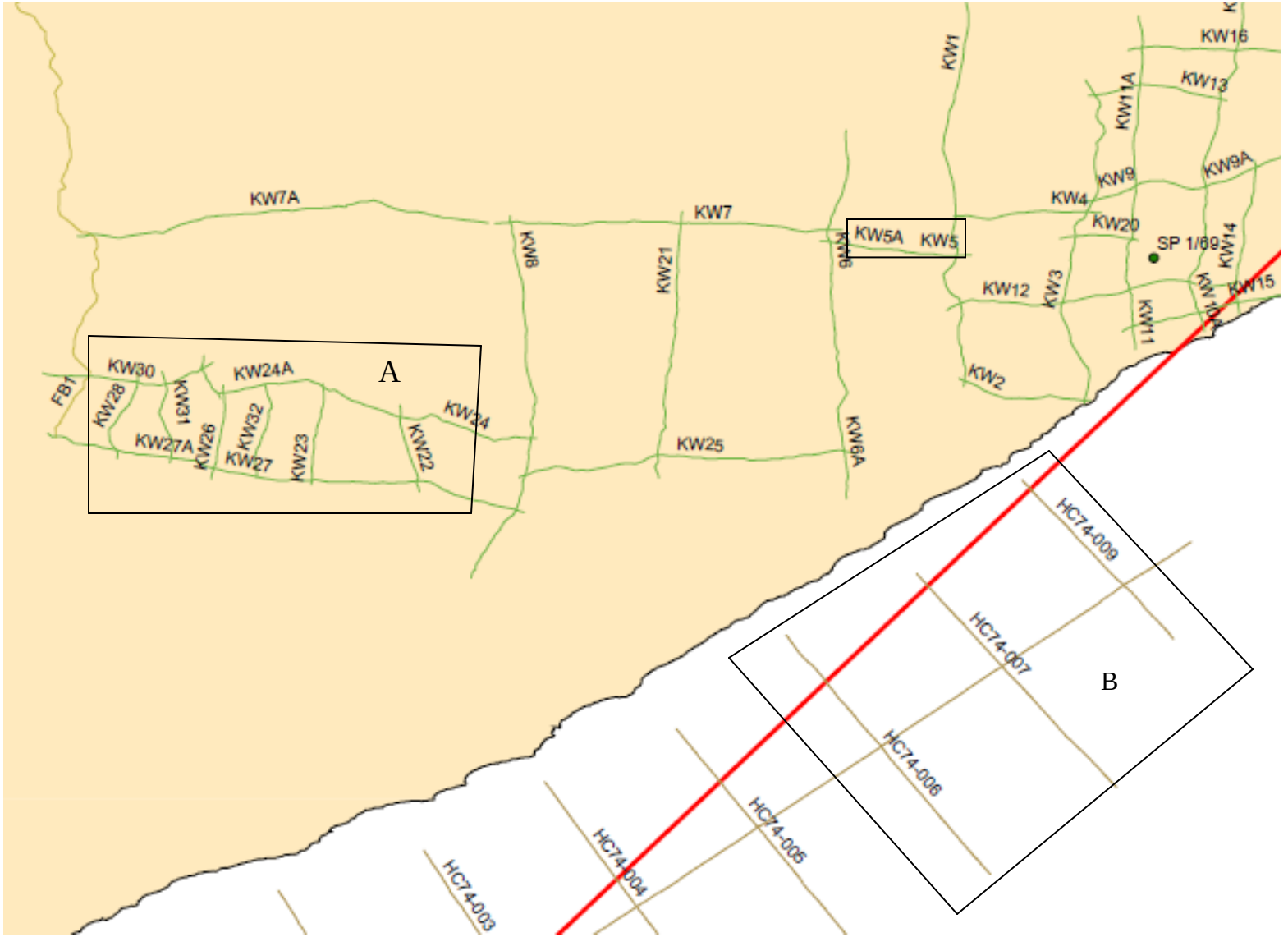

Figure 5- 2: Zoomed in map showing selected areas of investigations from Figure 5-1

5.2 Data acquisition and processing

The acquisition of field data and processing was done by the SOEKOR (Southern Oil Exploration Corporation), which was merged with MOSSGas to form what is known today as PetroSA.

The amplitude recovery was done at the value of $\alpha = 3.5$ DB/sec. The velocity of seismic waves was analysed using the NMO (Normal Moveout Correction). The NMO is defined as the time difference between travel time at a given offset and at zero offset. The shot point interval was 200 m and the polarity convention was done with a compression wave at the seismometer that was given a negative number on tape. This polarity was retained throughout processing to yield a downswing on display.

A time variant deconvolution was applied using 7 filters/trace of 76 ms. Deconvolution (a process that improves the temporal resolution of seismic data by compressing the basic seismic wavelet) was applied to billions of seismic traces and, most of the time, proved to yield satisfactory results.

The record length was 6 s (seconds) and the sample rate 4 ms (milliseconds). Two recording frequencies were used; one with a low frequency (12 Hz) and the other with a high frequency (62 Hz). The length of the cable was 2400 m set for 48 groups recorded in channels 1-24 and 33-56 and processed to yield 24 folds 48-trace coverage.

The recording instrument used was the DFS 3 (Digital Field System 3), with the advantage that it is easily portable and has 440 W power consumption. It proved to be a very robust and reliable system.

5.3 Subsurface interpretation

The 2-D images for subsurface visualization provided by the company PetroSA differ in terms of the way units were presented on the Y axis. For offshore images, the Y axis is related to the time in seconds, whereas on land images have on the Y axis the depth in miles. For both offshore and on land images, the X axis has the same variable (SPN: shot point number). These variables (on the X and Y axis) were highlighted for a better view.

5.3.1 Offshore

The seismic line length is 8.19 km, and set in a NW-SE direction. The processed image shows that the sediments might have been deposited in a transgressive manner. The strata dip at a shallow angle of almost 25^{o}. There appears to be four stratigraphic units A, B, C and D (Figure 5.3). This vertical seismic profile displays faulting beneath, and this is a good indication of fluid migration; either groundwater or oil.

The type of reflection configuration in Figure 5.3 looks typically like a divergent type configuration. These types of configurations are characterized by a wedged shape with typical lateral thickening of the different units. This configuration is normally interpreted to signify lateral variations in rates of deposition or progressive tilting of the sedimentary surface during deposition.

This aforementioned tilting can also be related to the tectonic uplift along the Ciskei-Swaziland (Amatole-Swaziland) axis in the eastern neotectonic belt of the Eastern Cape Province. Line HC74-007 with a distance of 3.41 km in the same direction as HC74-006 appears to display the same type of divergence, with layers dipping at a given angle (Figure 5.4).

Some faults appear; the first one occurs as a splay of long fault, which is perpendicular to a third one oriented SW-NE. At the lower part of the long fault, there appears to be a series of folds (anticlines). If these are not merely noise, it could be an indication of good traps for either groundwater or oil.

In Figure HC74-009 (Figure 5.5) what appear to be folds in Figure 5.4 were indeed confirmed as anticlines. Furthermore, it appears that the sediments were disturbed seemingly due to the presence of few faults, which were formed concomitantly with the folds.

Because these seismic lines are oriented NW-SE, this probably means that the compressional horizontal stress, that caused this folding, is in the same direction, and probably is related to the Wegener Stress Anomaly (Viola et al., 2005). Andreoli et al. (2009) indicated that it is uncertain when the current Wegener Stress field was re-established, and argued in favour of evidence pointing to a pre-Quaternary event. The seismic line HC74-009 has a distance of 3.22 km.

In these three figures, sediment layers might have undergone erosional truncation, seeing that there is clearly a lateral termination of strata at the right side.

5.3.2 On land

Most of the on land seismic lines were traced in the eastern neotectonic belt around King Williams Town. The seismic line KW 26 which is 11.03 km long in a quasi N-S direction portrays no distinct stratigraphic units (Figure 5.6) with two weathered sections, (Figure 5.7 and Figure 5.8).

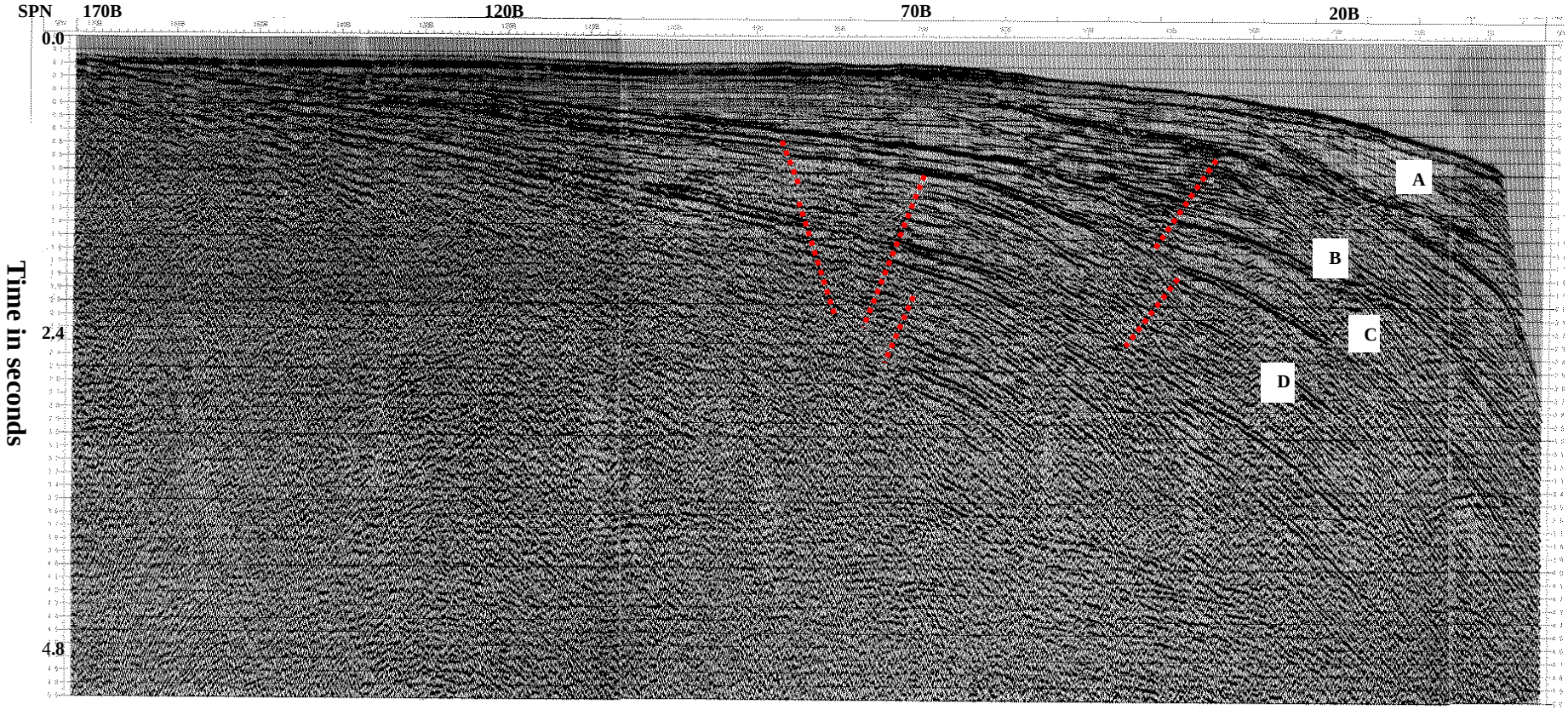

Figure 5- 3: Line HC 74-006 offshore (source: PetroSA. SPN stands for shot point number). Red lines represent faults.

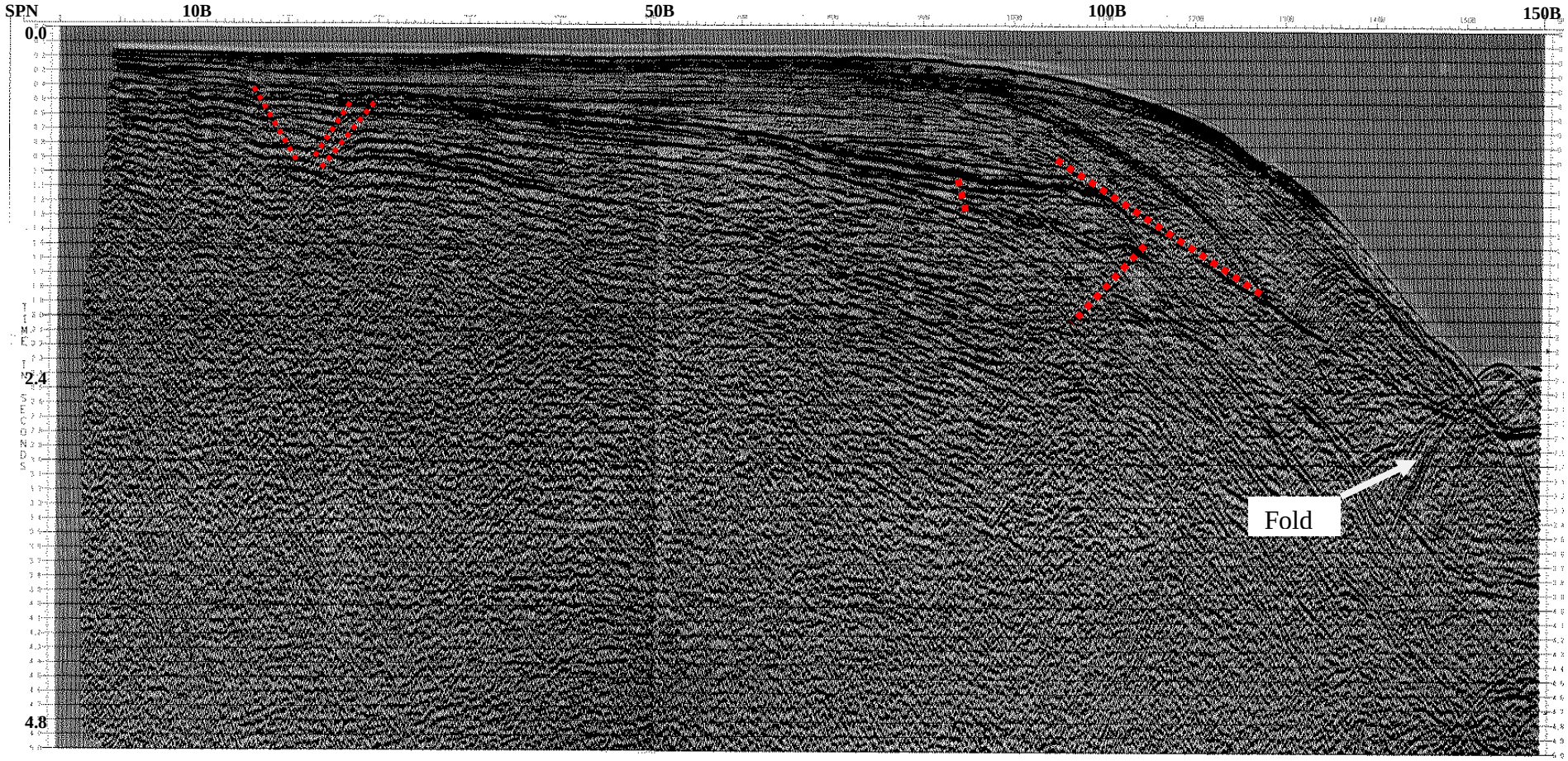

Figure 5- 4: Line HC74-007 offshore (lines in red are faults; source: PetroSA)

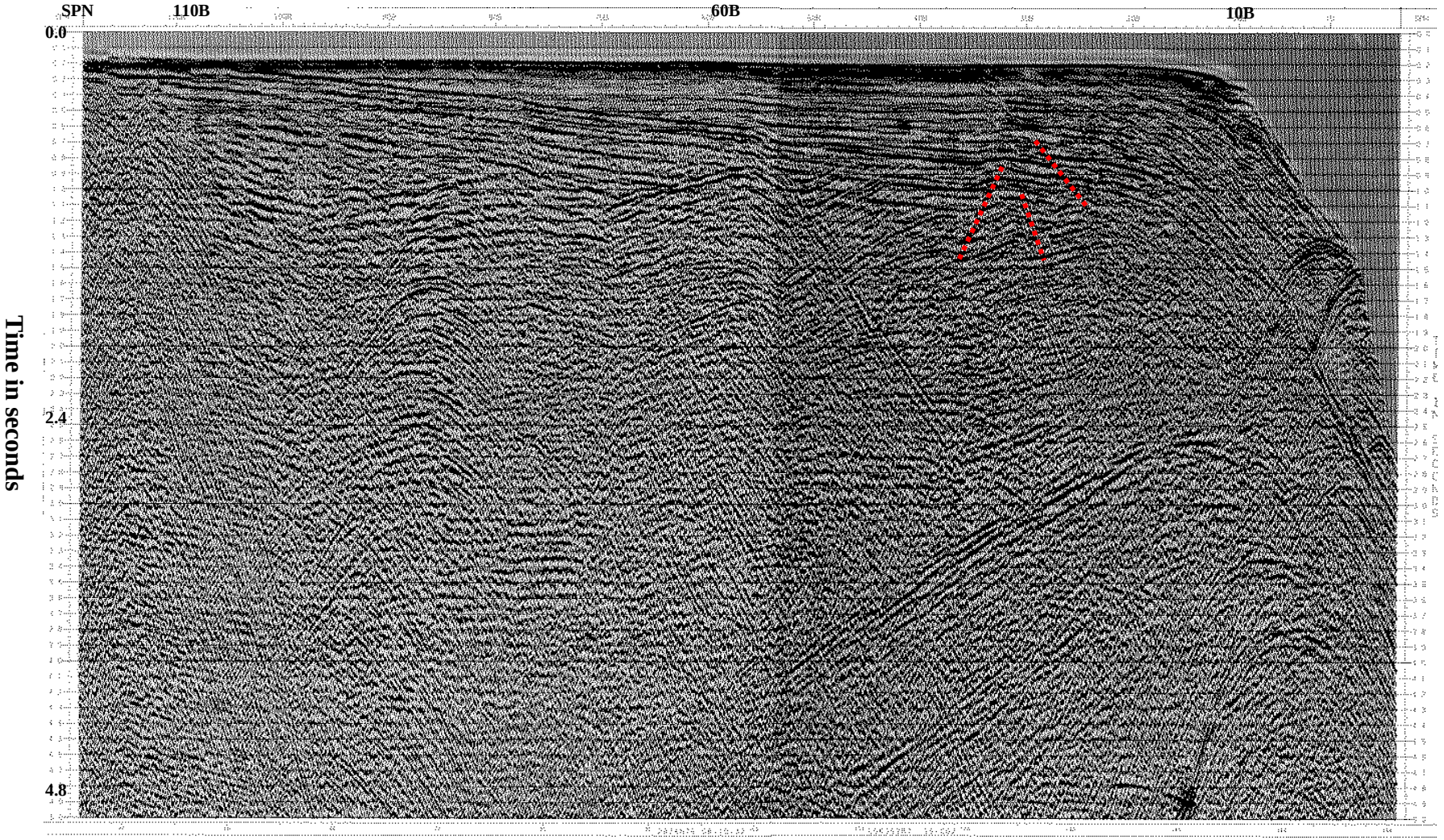

Figure 5- 5: Line HC74-009 showing some folds (source: PetroSA)

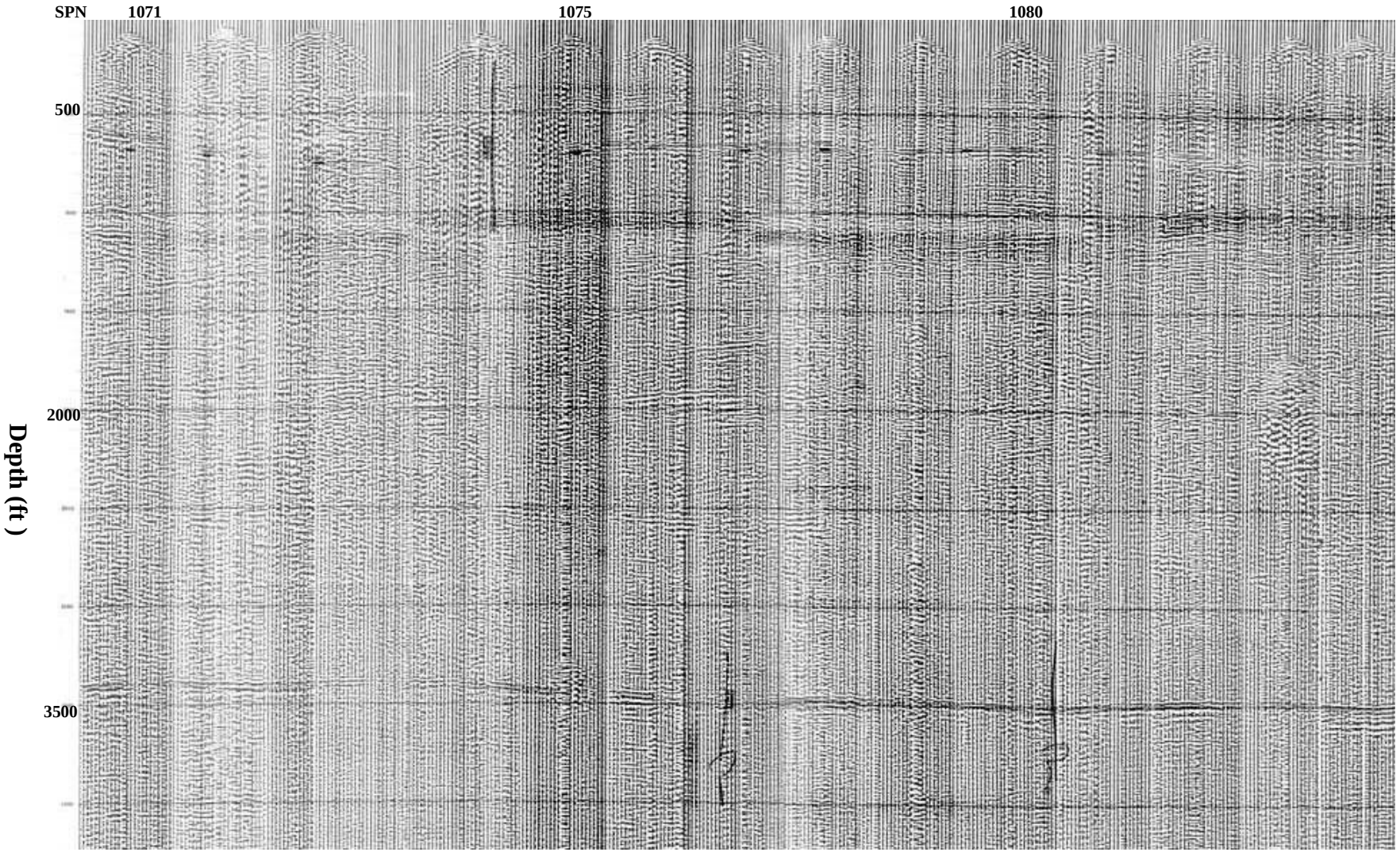

Figure 5- 6: Line KW-26 is almost reflection free (source: PetroSA)

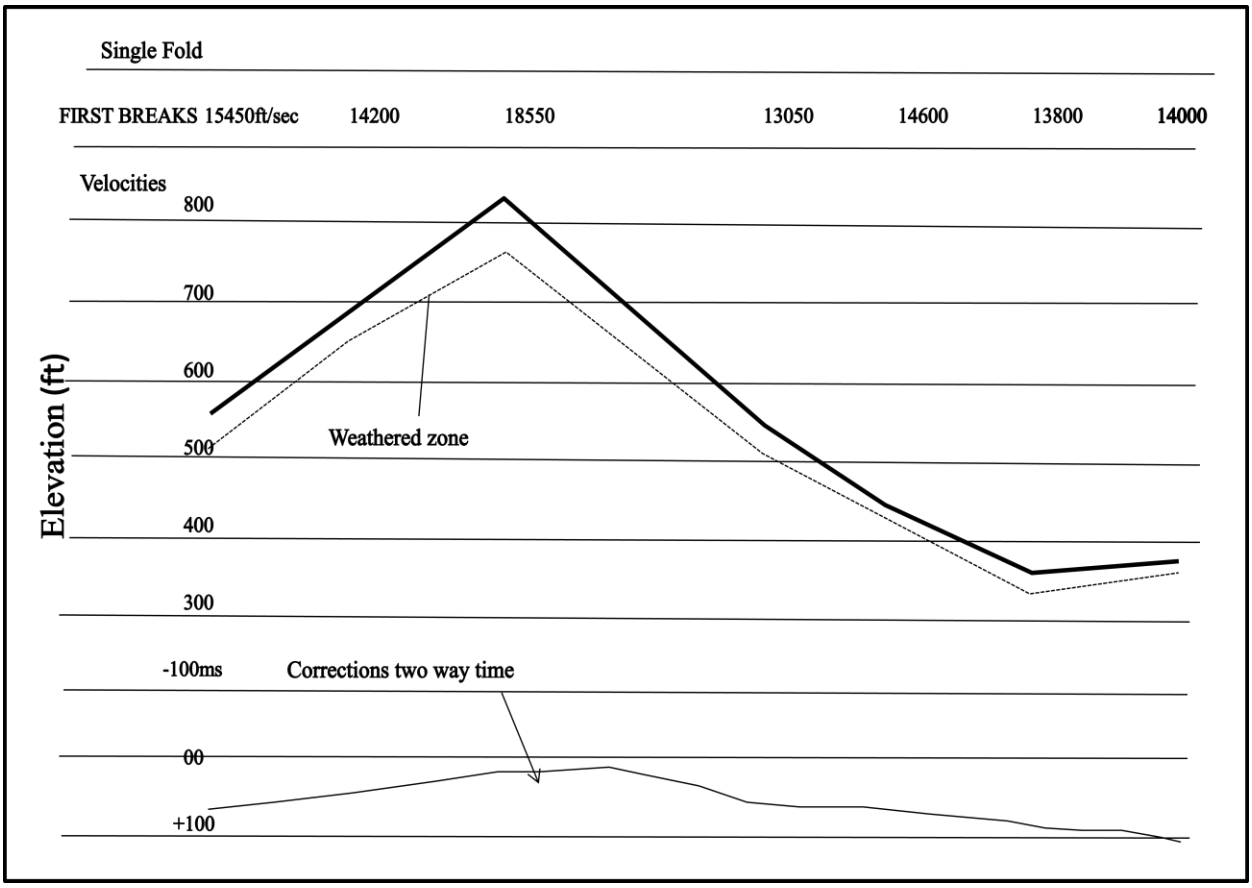

Figure 5- 7: Profile from seismic line KW-26 showing weathered zone

The weathered zone is observed at the elevation of 220.5 m; this weathered zone might be related to a fault or a fractured zone. The same can be inferred for the image in Figure 5.8. In this figure, the weathered zone is depicted at depth of about 132 m. In both these figures, the velocity corrections were applied and are represented at the bottom.

The increase in velocity may indicate a decrease in moisture. At a velocity of 18550 ft. /sec (5,654.04. m/s) (Figure 5.7), there is a peak that corresponds with the elevation of 800 ft. (243.84 m), whereas low velocities correspond to an increase in moisture, mainly below 400 ft. (121.92 m). On the contrary, in Figure 5.8 the highest velocity (14650 ft. /sec or 4,614.75 m/s)

corresponds to an elevation of almost 650 ft. (198.12 m). The increase in velocity is almost linearly correlated with the increase in elevation.

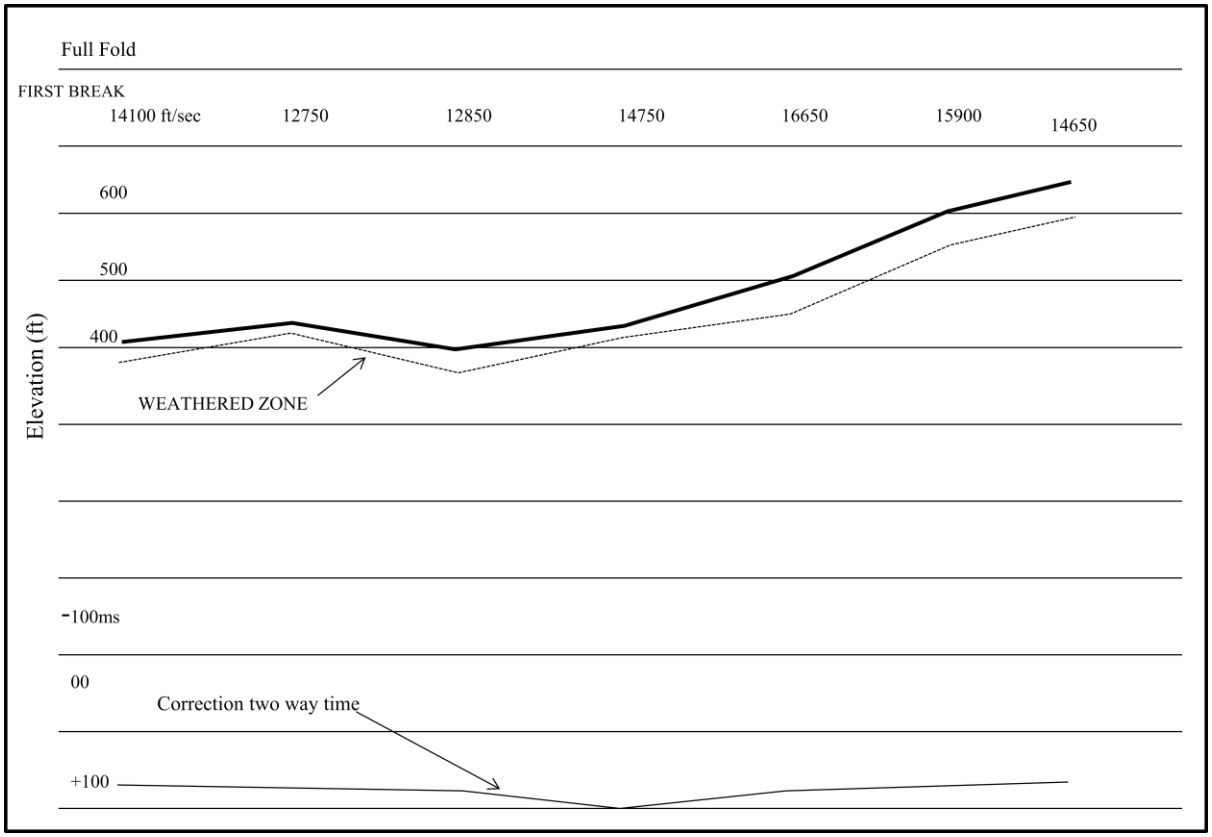

Figure 5- 8: Seismic line KW-26 showing the second weathered zone.

As was observed in Figure 5.8, the lowest velocities are in the elevation range of 400 ft (121.92 m). Thus for line KW-26, the highest velocities are found within the range of 600 to 800 ft. (182.88 to 243.84 m) elevation, this may correspond with a zone of low hydraulic conductivity.

The 11.54 km seismic line KW-28 at an orientation of almost N-S produced a reflection-free image (Figure 5.9). This might be a case of seismically homogeneous strata (e.g. Sangree, 1977). As for the previous line KW-26, weathered zones were also depicted (Figure 5.10 and Figure 5.11). In Figure 5.10 the weathered zone appears at an elevation of 189 m, and in Figure 5.11 the

weathered zone appears at the altitude of 252 m. Figure 5.12 (line KW-29, 5.3 km) on the contrary seems to display three stratigraphic units on top, but not very evident. It shows a weathered zone at a height of 284 m (Figure 5.13).

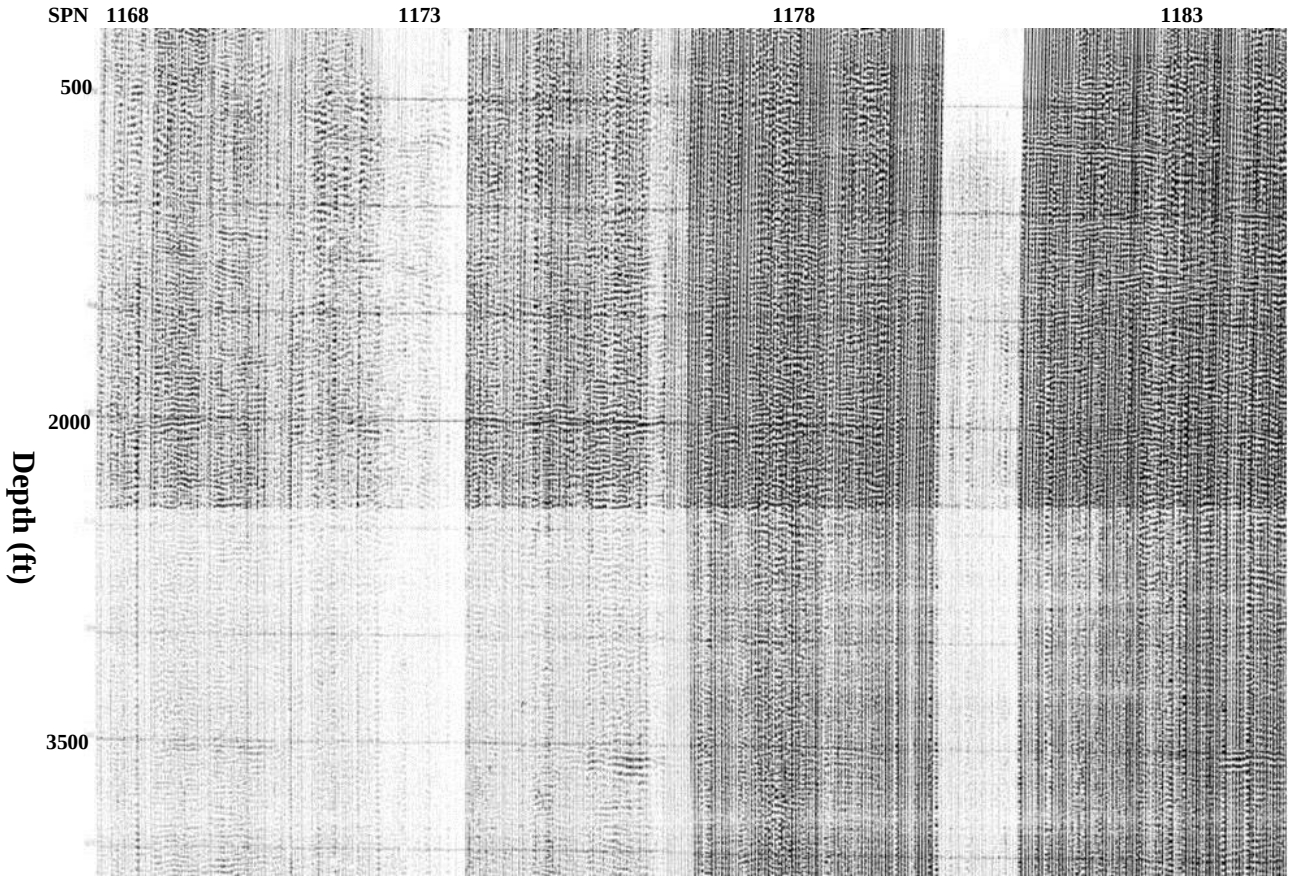

Figure 5- 9: Seimic line KW-28 showing no relfection (source: PetroSA)

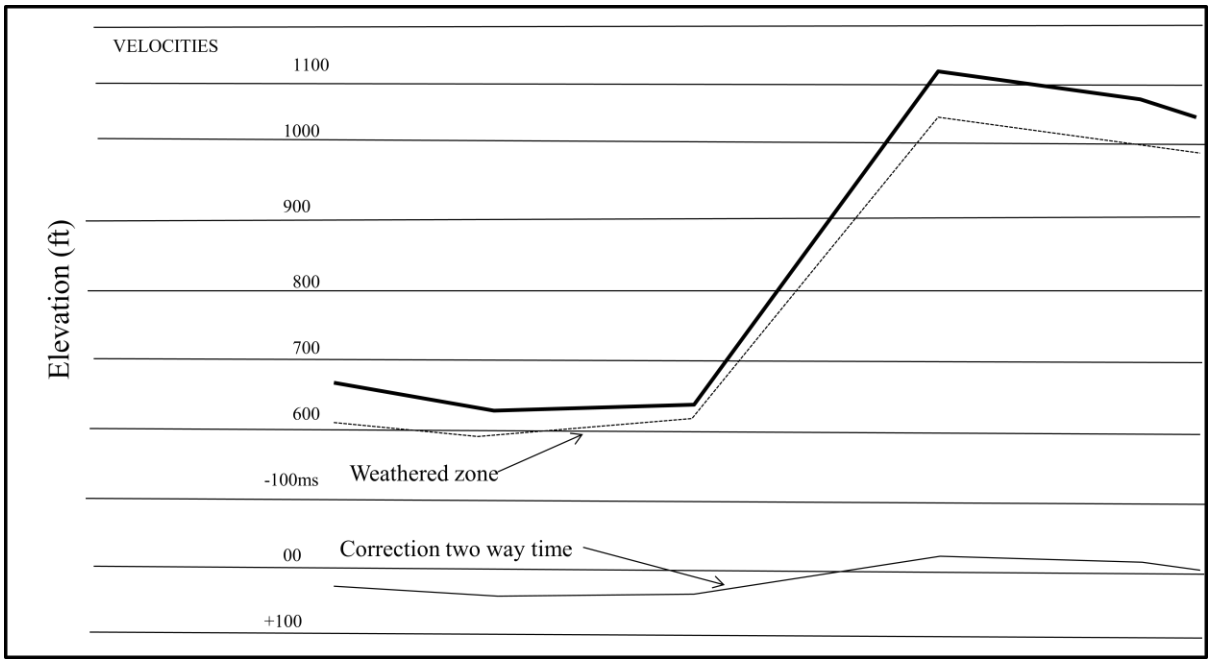

Figure 5- 10: Weathered zone from line KW-28

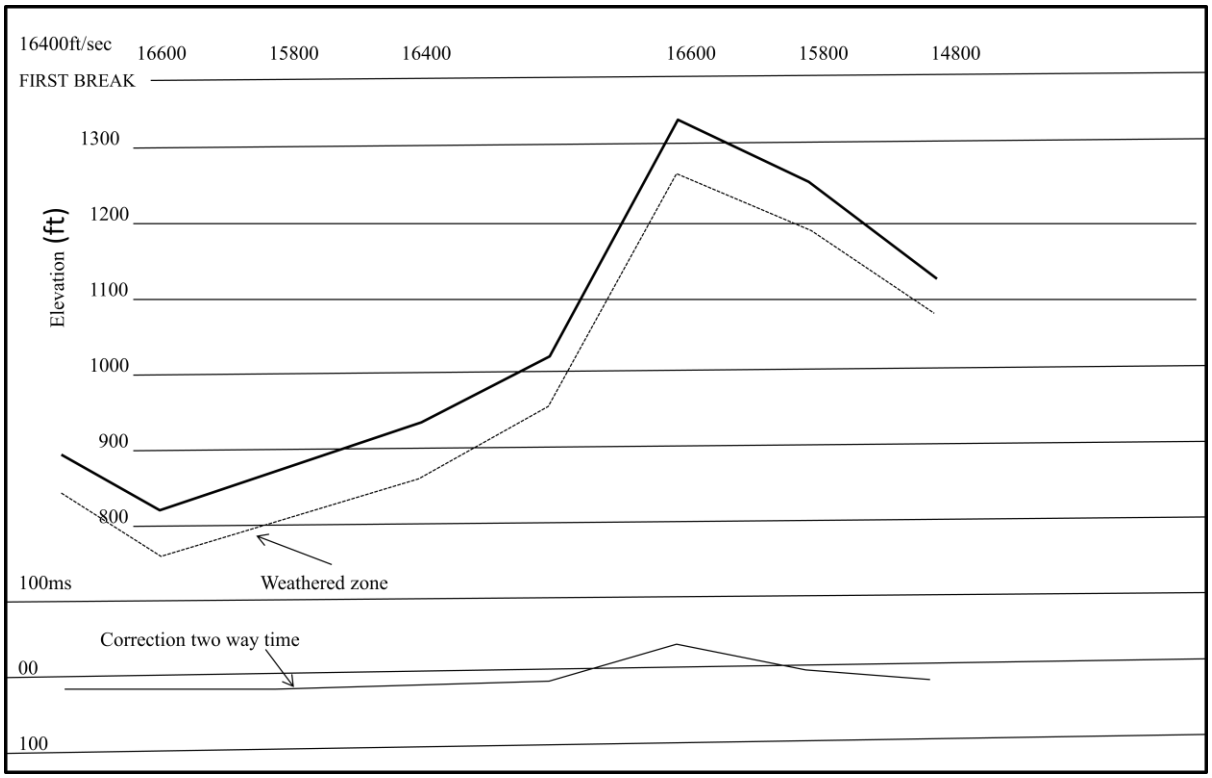

Figure 5- 11: Second weathered zone from line KW-28

With line KW-28 low velocities were found at elevations of approximately 600 ft. (182.88 m) (Figure 5.10), for this same seismic line higher velocities (e.g. 16600 ft./sec or 5,060 m/sec)) correspond with higher elevations (~1350 ft.= 411.5 m). It can be observed from Figures 5.10 and 5.11 that lower velocities are found within elevations between 600 and 800 ft. (183 m and 244 m). Nevertheless the increase in velocity is to a lesser extent related to higher elevations (900-1300 ft. or 274.32- 396.24 m), which may indicate zones prone for groundwater, the weathering being related to percolation of groundwater. King Williams Town, a town from which seismic lines were set, comprises rocks of the Daggaboersnek member, Balfour Formation, Beaufort Group, Karoo Supergroup. The Daggaboersnek member itself is known for its sandstone intercalated with mudstone.

Line KW-29, whose seismic results are presented in Figure 5.12 appears not to display stratigraphic units at all.

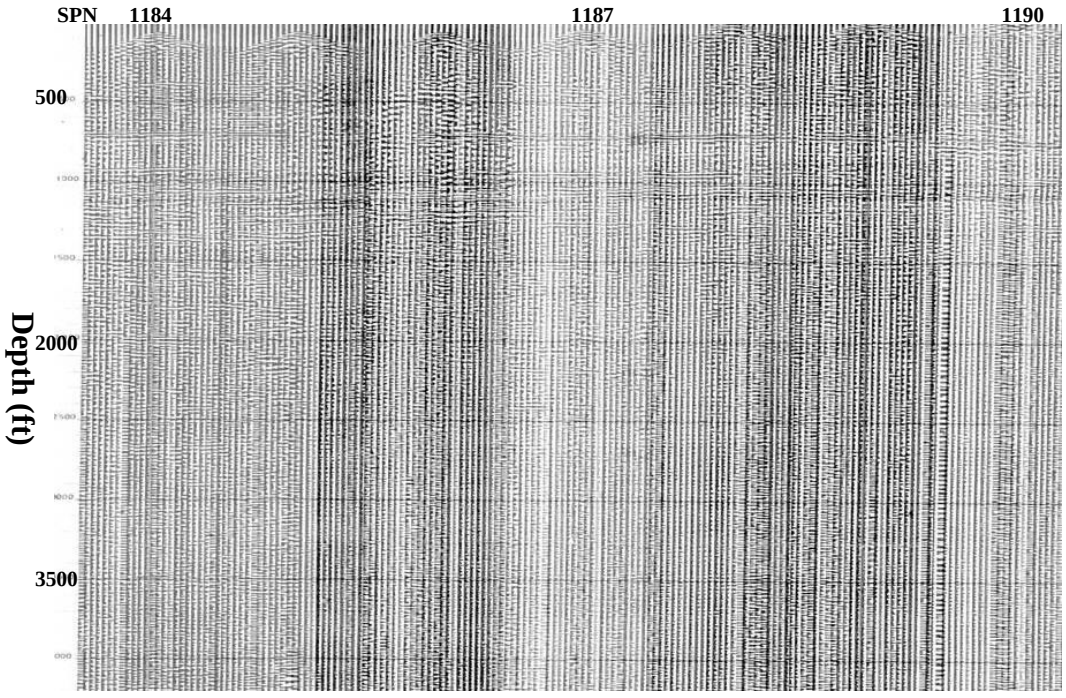

Figure 5- 12: Line KW-29: Three major stratigraphic units on top (source: PetroSA)

The first break in line KW-29 was picked up at a velocity of 16500 ft. /sec or 5,029 m/sec (Figure 5. 13). There is constant velocity decrease from 16800 ft. /sec to 15250 ft. /sec (5,121 - 4648 m/sec). It must be noted that the decrease in velocity is linearly in relation to the increase in elevation. The weathered layer is inclined at an angle of almost 45^{o}. It starts occurring at an elevation of ~700 ft. (213 m) until it reaches ~1500 ft. (457 m). This feature is probably related to a fault that acts as a conduit for groundwater.

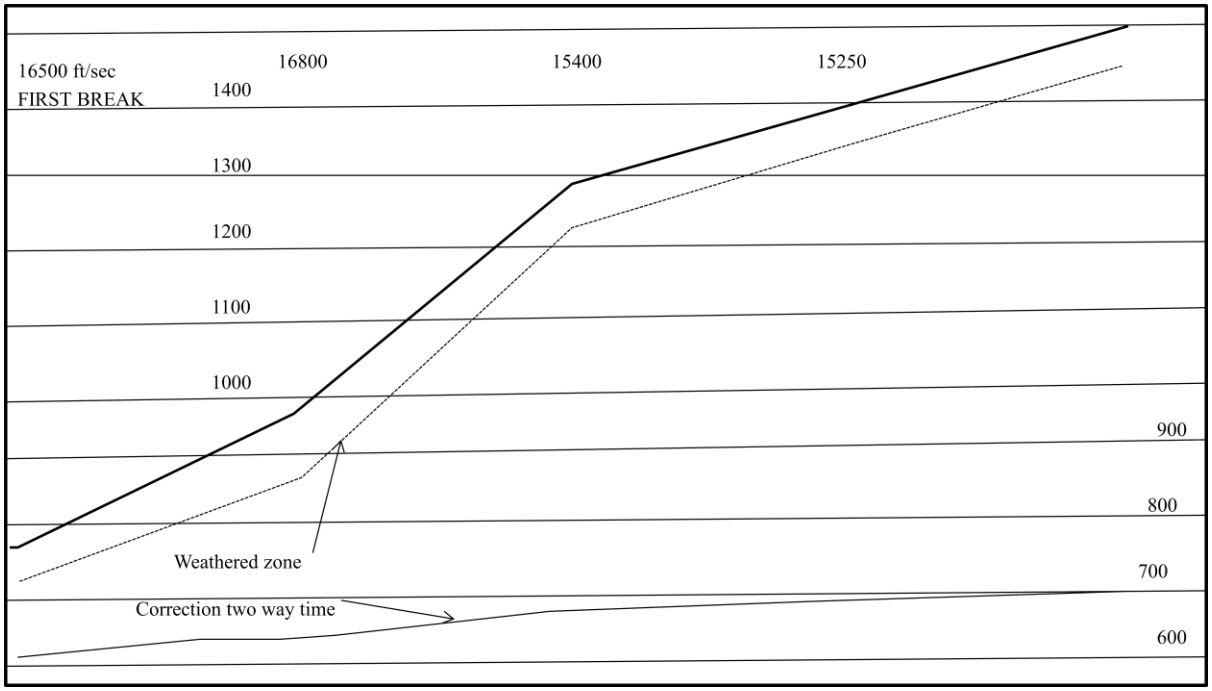

Figure 5- 13: Line KW-29 showing the weathered zone

As for the previous seismic lines, KW-30 and KW-5, show no clear subsurface stratification (Figure 5.14 and Figure 5.16). The weathered layer commences at a very low elevation (300 ft. or 91.4 m) and reaches 900 ft. or 274.3 m. In general, this weathered zone remains below 800 ft. (243.8 m) (Figure 5.15). On the contrary, it starts occurring at very high elevations (1300 ft. or

396.2 m, Figure 5.17). It is clear that the weathered zone of the seismic line KW-5 remains almost at a constant elevation throughout the profile.

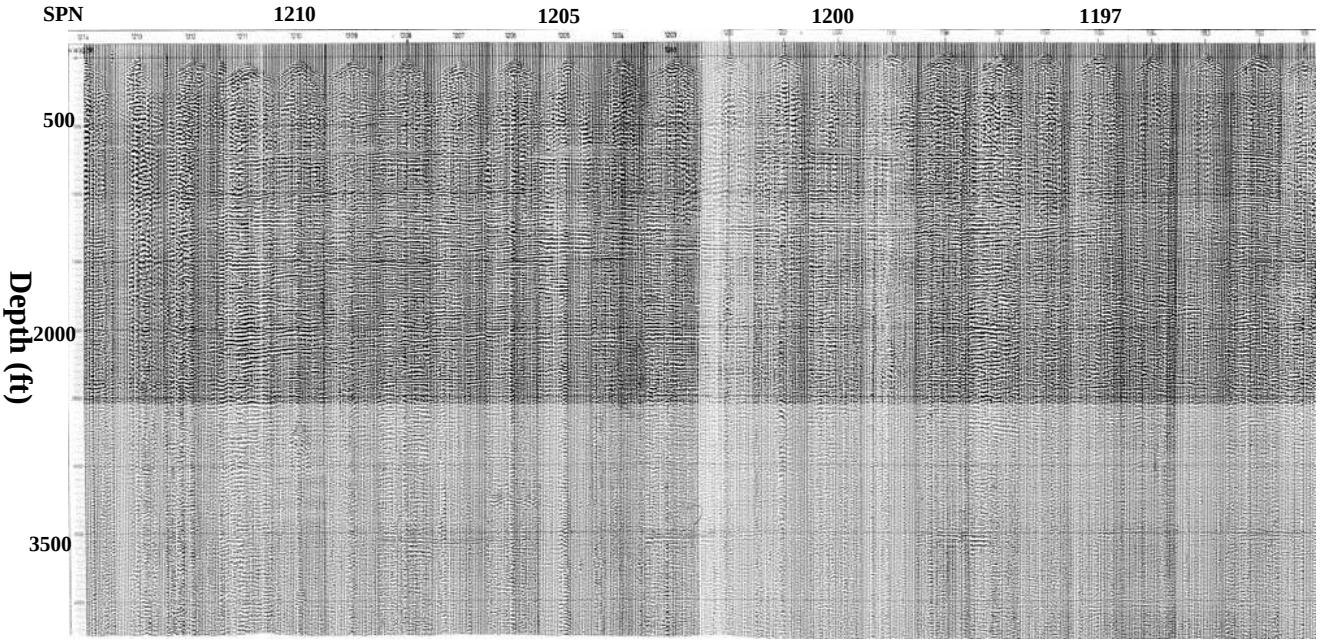

Figure 5- 14: Line KW-30 (reflection free; source: PetroSA)

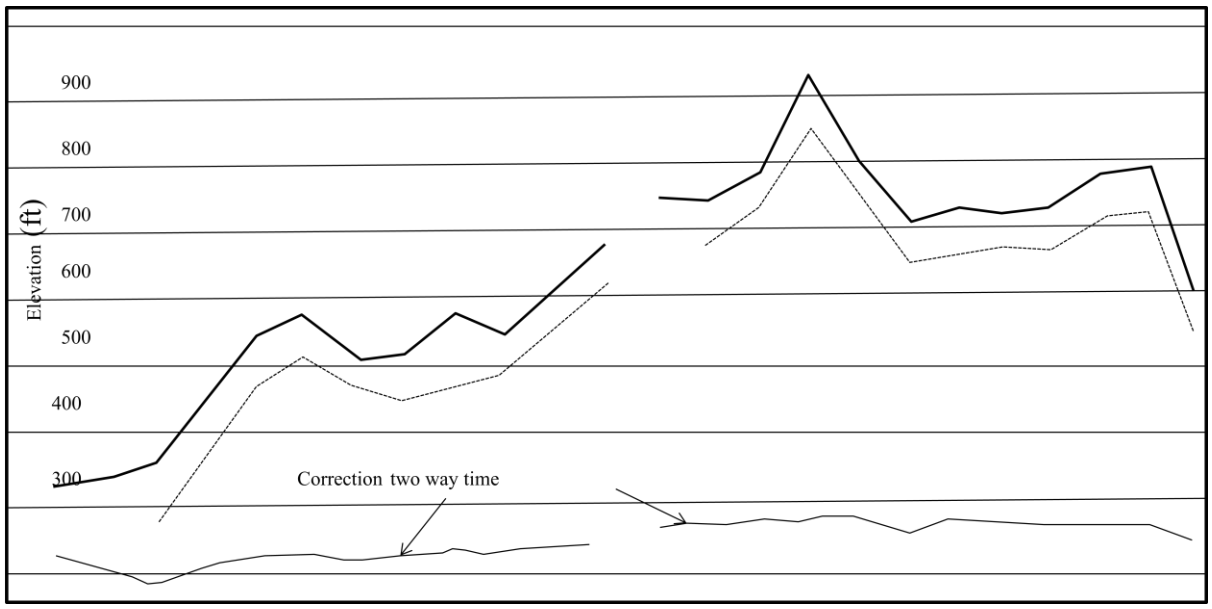

Figure 5- 15: Line KW-30 showing the weathered zone.

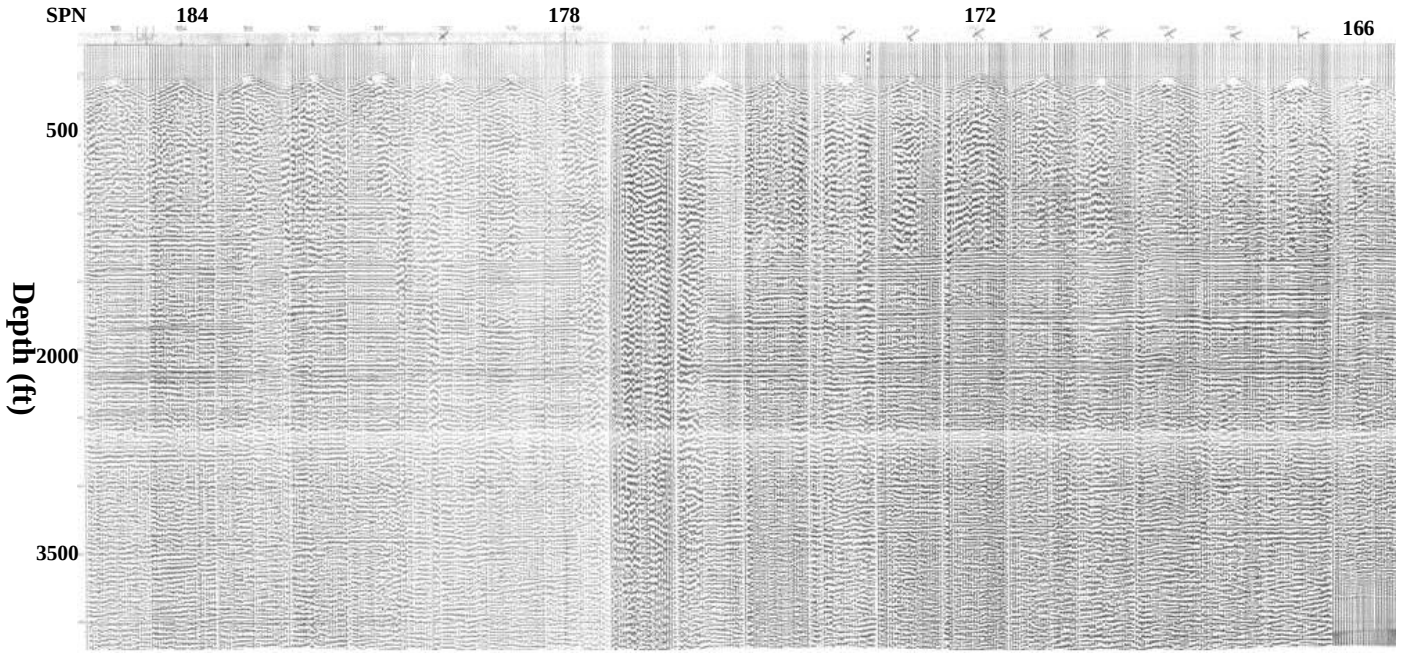

Figure 5- 16: Line KW-5 (reflection free; source: PetroSA)

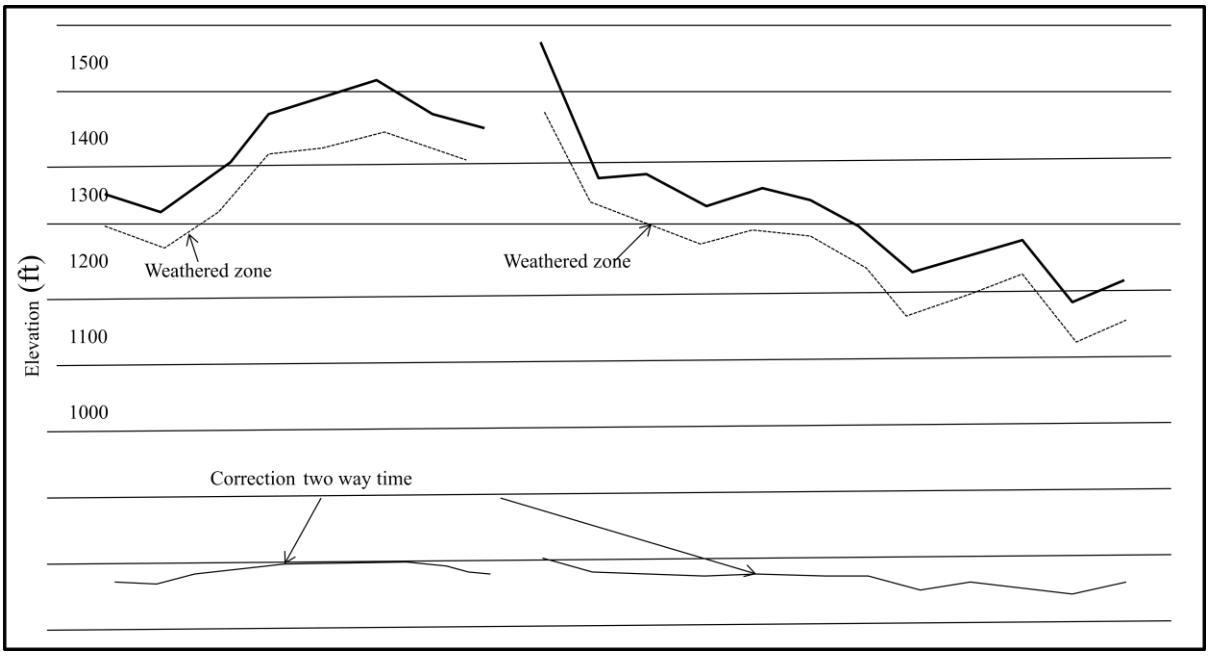

Figure 5- 17: Line KW5 displaying the weathered zone layer.

5.4 Field observations

In King William's Town, a dolerite sill intruded into the sedimentary rocks (mudstones and sandstones of the Daggaboersnek Member of the Balfour Formation, Aldelaide Subgroup, Beaufort Group, Karoo Supergroup) (Figure 5.18). The mudstones are brownish, jointed and show some pencil cleavages. They represent products of the overbank due their very fine grains. The sandstones on top of the mudstones are greyish and jointed. The joints in the sandstones have favoured the percolation of water, which has highly weathered the mudstones. The high degree of weathering has turned the mudstones into soil-like products, in which a structure can be traced to a certain extent, and being classified as a neotectonic fault (Figure 5.18). Different lithologies are well represented in Figure 5.19.

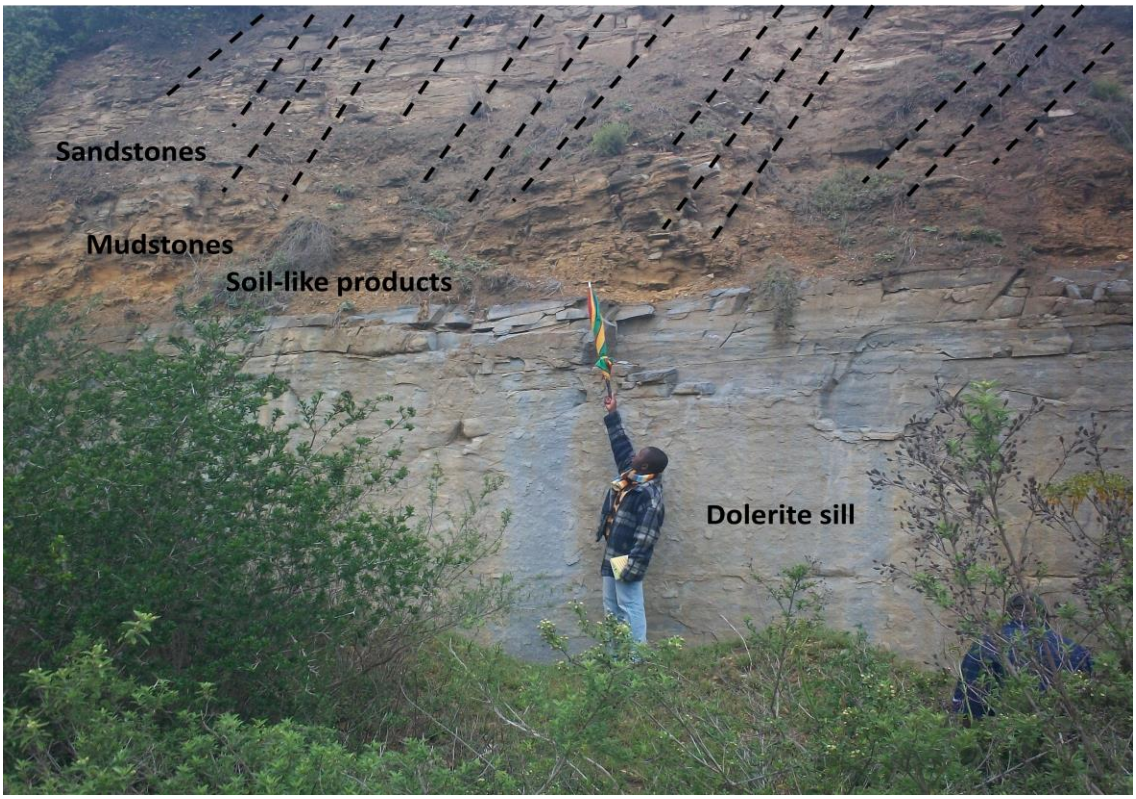

Figure 5- 18: Outcrop showing a dolerite below with mudstones and sandstones on top. The man is pointing at the low angle fault in the soil-like products. Black dashed lines are joints.

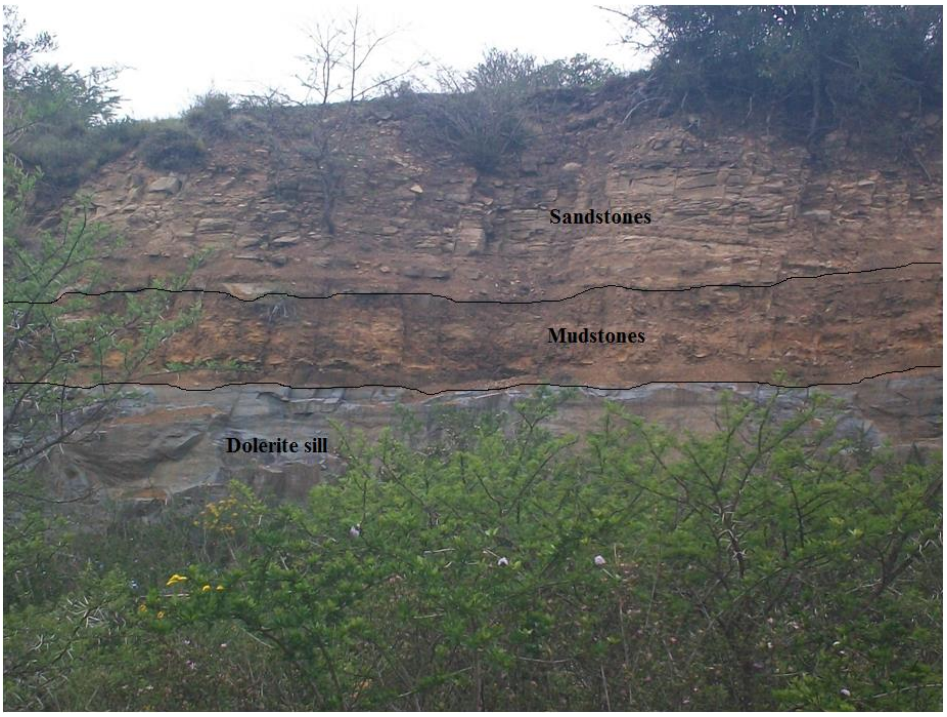

Figure 5- 19: Better view showing the outcrop as seen in Figure 5.18

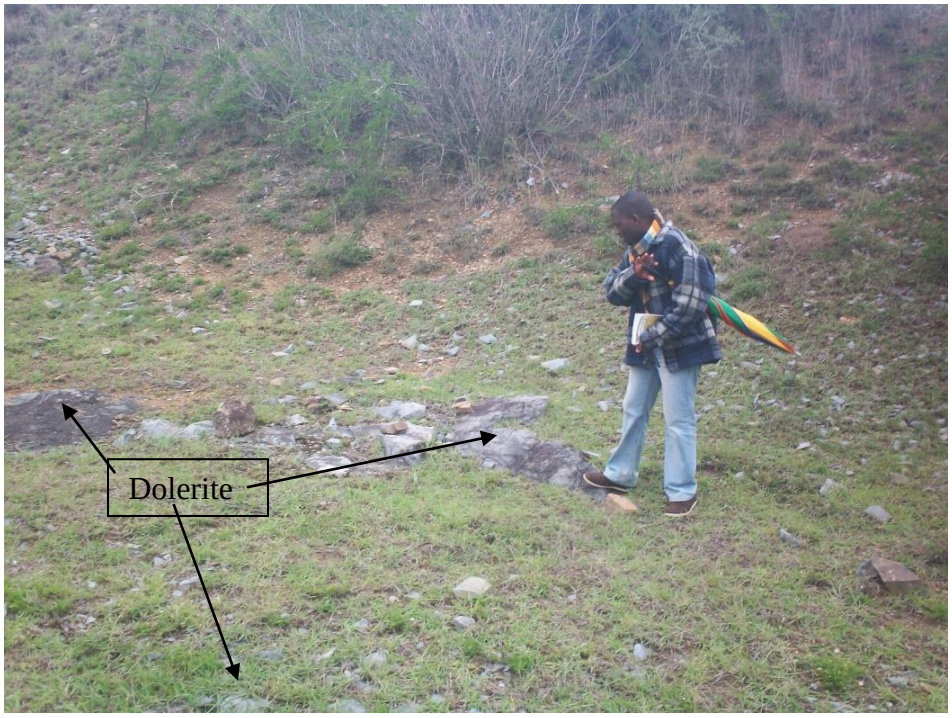

Figure 5- 20: Dolerite few meters below in the footwall.

The outcrop features (dolerite and sedimentary rocks: S 32^{o}. 88195; E 027^{o}37425) present the characteristics of a meso-scale fault oriented N 140^{o}E, which may have resulted from an uplift, probably the Amatole-Swaziland uplift that occurred in the last five millions years. The outcrop (Figure 5.18 and Figure 5.19) is the hanging wall; a few meters below one can see on the earth's surface the same dolerite but in the footwall (Figure 5.20). This is an evidence of an uplift causing a vertical displacement with a dip-slip component.

There is also a river flowing in the same direction parallel to the cliff of the nearby outcrop. The river flows possibly in a zone of weakness as a result of the faulting evidenced by healthy vegetation (Figure 5.22). The dolerite sill was affected by an extensional tectonics, and has both vertical joints (Figure 5.21) and horizontal joints (Figure 5.22). These joints, mainly the horizontal ones, are infilled with quartz veins. These quartz veins mark a late event, and may have filled the joints when the low angle fault seen in Figure 5.18 occurred.

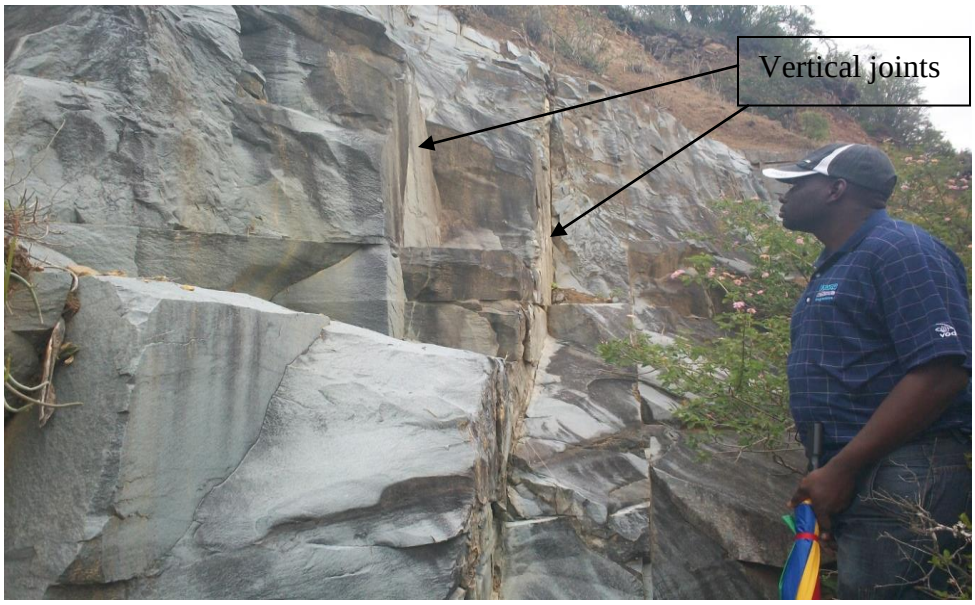

Figure 5- 21: Dolerite with conspicuous vertical joints.

Figure 5- 22: Dolerite sill with horizontal joints infilled with quartz veins.

The vertical joints (Figure 5. 21) will act as conduits for water, and the horizontal joints (Figure 5. 22 will store the water within the dolerite sill.

5.5 Summary

Offshore and on land seismic lines were set in order to visualize the subsurface in certain areas in the Eastern Cape Province eastern neotectonic belt. Seismic shots offshore highlighted few stratigraphic sequences affected by folds and cross cut by few faults. The Amatole-Swaziland uplift, an important and conspicuous neotectonic feature in the Eastern Cape has probably contributed to the noted progressive tilting marked by lateral variations in sediment deposition

rates. There are a number of folding features, but they cannot be clearly defined due to the closure at the end of the profiles. These folding features are the result of compression and are probably related to the NW-SE compressional stress known as the Wegener Stress Anomaly.

On land, weathered layers were found at different elevations varying between 300 and 1500 ft. (91.4 and 457.2 m). These weathered layers have different seismic wave velocities; and they represent porous and permeable rocks. They are probably indicative of intense groundwater circulation and surface water percolation. Straight lines marking the weathered layers seen from the profiles are characteristics of consolidated sediments, unconsolidated sediments always have wavy profiles. On the other hand, as no stratigraphic subdivision was clearly noted, it is concluded that there are thick and massive layers present. Most often thick and massive layers originate from the deposition of sediments during a high flow regime. Unstratified sediments can also indicate seismically homogeneous strata.

The seismic profiles have displayed weathered zones below the surface onland, these weathered zones have been assimilated to fractures that allow the water flow. The above mentioned meso-scale fault and the subsurface fractures may have been generated during the Amatole-Swaziland tectonic uplift. All these characteristics can be taken into consideration while targeting potentially high yield aquifers in the area of King William’s Town.

6. GRAHAMSTOWN KAOLIN FORMATION, STRUCTURAL CONTROL AND GROUNDWATER FLOW

6.1 Introduction

Kaolin deposits may derive from the alteration of various rocks like volcanic rocks, such as trachytes, trachyandesites, andesites, dacites etc. (Papoulis and Tsolis-Katagas, 2008). Field observations in the Grahamstown area suggest that sedimentary rocks are the source of kaolin. Parent rocks are extensively altered either by water of hydrothermal fluids through faults and fractures.

The Grahamstown kaolin deposits (Figure 6.1: image from Google earth) in the southern neotectonic belt originated from the weathering of the Dwyka tillite (Figure 6.2), and the alteration of feldspar possibly in the matrix and in the granite breccias. In Figure 6.1 kaolin deposit appear in white, some few faults highlighted in red in the south west, and some fractures highlighted in blue among which the Grahamstown Fracture characterizes structurally the area.

Groundwater circulation led to the formation of kaolin deposit through fractures. The presence of quartz veins in the more developed kaolin suggests that hydrothermal fluid might have also played a role in the process of alteration.

The kaolin deposits located on the N2 highway displays two distinct zones: a zone which is more weathered (east) associated to more whitish developed kaolin, and a more or less weathered grayish zone (west). The kaolinisation in the eastern zone is more developed due primarily to the presence of fractures that allow water to circulate, and to the presence of subvertical, oblique and subhorizontal quartz veins. Quartz is quasi impermeable and does not allow water flow; the water is trapped and weathers the rocks.

Figure 6- 1: The kaolin deposits and some structures around the Grahamstown area. Blue lines are fractures, and red lines are faults.

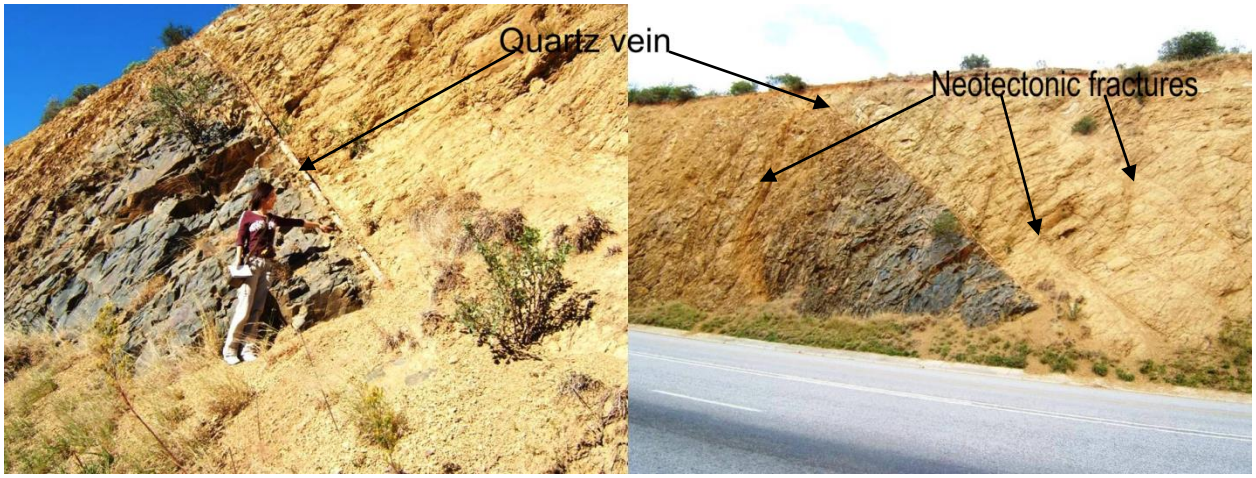

Figure 6- 2: Kaolin deposit showing clearly its genesis from the Dwyka tillite (grey rock).

The western zone is characterized by the absence of hydrothermal quartz veins. White (1957) mentioned that the temperature in hydrothermal fluid is appreciably warmer (e.g. 5^{o}C or more) than the surrounding environment. This zone is more or less weathered, and the old fabric of the rock can still be observed. These fractures and veins were studied in order to infer a possible neotectonic stress regime. The weathering might have occurred without change in volume of the rock. Ollier (1988) stated that the existence of joints, veins and other structures within weathered rock masses shows that weathering has taken place with no change in volume.

6.2 General geological setting

The Grahamstown area is situated in the eastern part of the Cape Fold Belt. Jacobs et al. (2004) indicated that the region is underlain mainly by rocks of the Witteberg Group of the Cape Supergroup, and the Dwyka and Ecca Groups of the Karoo Supergroup. Shales and sandstones of the Weltevrede Formation are the oldest rocks of the Cape Supergroup; they are overlain by quartz arenites of the Witpoort Formation (Figure 6.3).

Fine-grained shales and thin bed sandstones of the Lake Mentz and Kommadaga Subgroups (comprising shales, minor greywacke and arenites sandstone units) overlay the Weltevrede formation. The Witteberg Group rocks are overlain by the rocks of the Dwyka Group of the Karoo Supergroup. The Dwyka Group forms a syncline whose fold axial trace trends ESE, and plunges WNW in the Grahamstown area. Quartzite ridges of the Witpoort Formation north and south of this syncline form the higher-lying hills that enclose the area where the Grahamstown peneplain develops. Generally strata in the Grahamstown area are covered by the Cape Supergroup (Bokkeveld and Witteberg Groups), the Karoo Supergroup (Dwyka, Ecca and Beaufort Groups), the Suurberg, Uitenhage and Algoa Groups, and the Igoda, Grahamstown and

Martindale Formations. Some road cuts have been used for the structural and petrographical analysis.

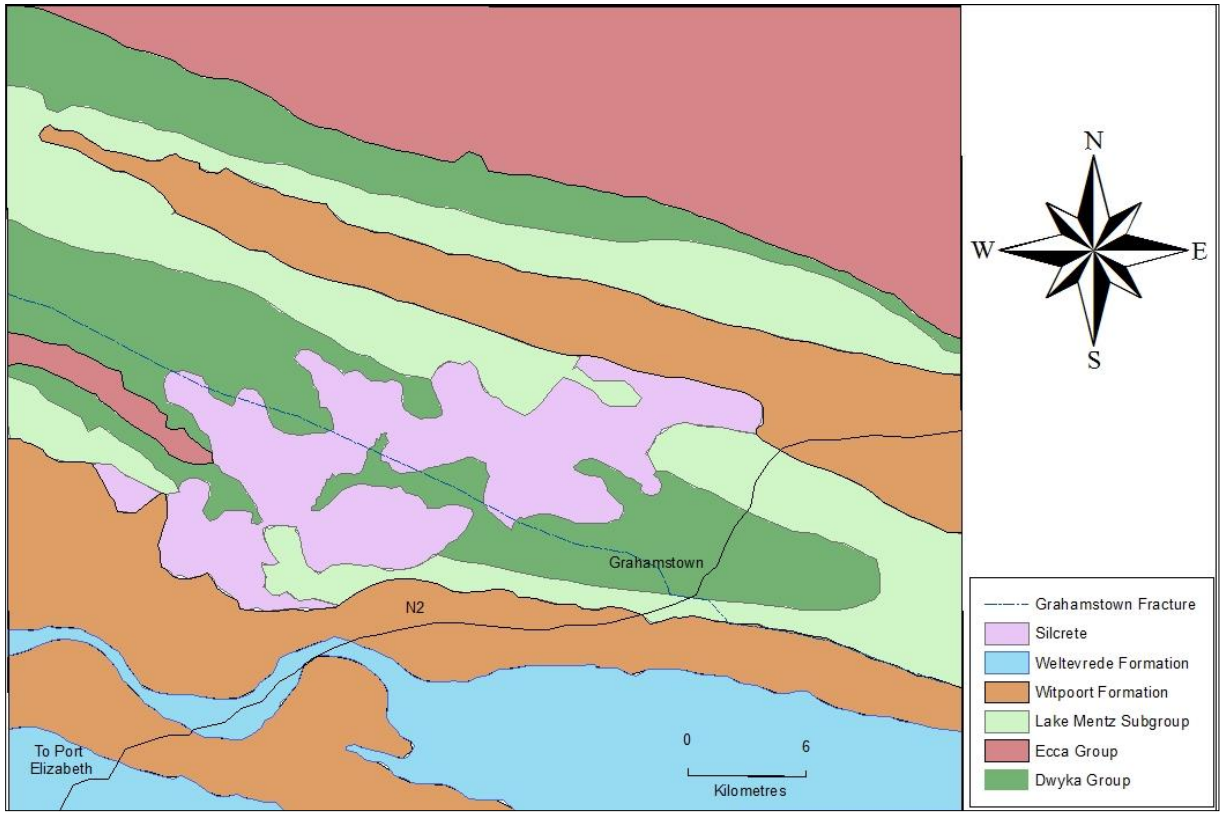

Figure 6- 3: General geological map of the Grahamstown area. (Jacob et al., 2004)

6.3. Outcrop description (from left to right) on the N2 Highway

Many structures are found in the Grahamstown kaolin deposits: faults, fractures without quartz veins, fractures with quartz veins, tension fractures and minor folds. Neotectonic faults and fractures can be seen in Figure 6.4 a, b, and c; fractures are in red, fault in black, and quartz veins in grey.

The outcrop is mainly subdivided in two zones, the eastern zone and the western zone. The two zones differ only in the way weathering occurred in order to produce the kaolin. The east zone

(Figure 6.4 a and b) is more weathered than the west zone (Figure 6. 4 c). In the east zone no fabric of the parent rock is visible. The intensity of weathering effect is marked by the presence of not very well distinguishable fractures, because of advanced alteration. Most of the fractures in this zone are filled with kaolinisation products that seal them.

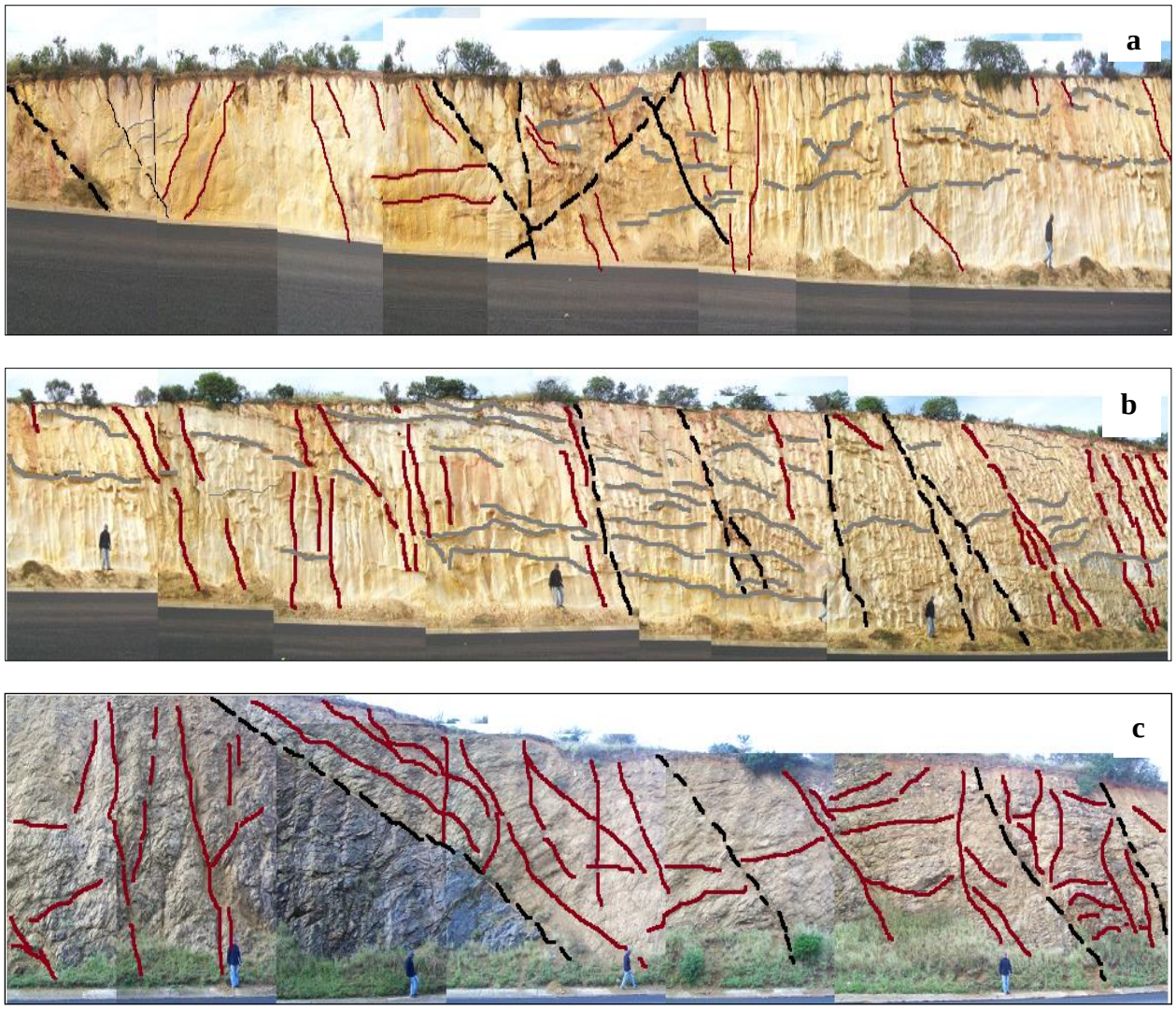

Figure 6- 4: Neotectonic faults and fractures in the Grahamstown kaolin deposit.

These fractures filled with weathered products occur at the extreme part of the east zone. A general and systematic description from left (east zone) to right (west zone) was used in order to

highlight important facts regarding the different structures in the weathering process. However, not all photographs were incorporated. The road cut is described from east to west. At the extreme east, two sets of systematic fractures predominates; one set with a strike varying between 105^{o} and 110^{o}, and a dip varying between 45^{o} and 55^{o}; the second set with a strike varying between 10^{o} and 15^{o} dipping 30^{o}. The first set predates the second one. Some small ferruginised quartz veins are still visible. The weathering occurred possibly in two phases; 1) fracturing occurred first in order to allow water to circulate and to weather the parent rock, and 2) weathering occurred and caused the already developed kaolin to disintegrate and to fill the fractures.

At another place, few subhorizontal fractures oriented 315^{o} dipping 8^{o} filled with quartz veins occur. At this place, the first set of fractures seems to predominate. At a local scale σ_1 (compressional stress) would parallel the above mentioned first set of fractures. After this far left region, a set of 8 fractures dipping 20^{o} and striking 320^{o} terminate in a fault (filled with weathering products) oriented 5^{o} and dipping 50^{o}. Few ferruginised millimetric quartz veins can also be seen in this fault. The set of these few millimetric ferruginised quartz veins (strike 210^{o}, dip 45^{o}) form an angle of 25^{o} with the fault, their number vary by set. These sets of millimetric veins are separated either by twenty or thirty centimeters. The occurrence of these veins indicates that extensional tectonic occurred concomitantly in both directions. This area precedes a fault ($270^{o}/40^{o}$) showing a dip-slip component with a displacement of about 10 cm (Figure 6.5). Above this fault dissolution structures (Figure 6. 6) occur leaving holes. In between these holes quartz veins resisting the alteration are prominent. Some of the quartz veins which are horizontal or subhorizontal show a drag-like fold structures at the right hand side of the above mentioned

fault, they are quasi horizontal at the left hand side of the fault. The fault is bounded far right by a series of small sub-vertical quartz veins and fractures ($25^{o}/80^{o}$).

Another fault zone ($275^{o}/45^{o}$) with a family of small parallel faults filled with millimetric and ferruginised quartz veins is remarkable. This fault zone has a width of almost 15 cm; it is possible that it generated subvertical tensile fractures ($330^{o}/85^{o}$), with an angle difference of 40^{o} between the fault zone and the tensile fractures. Each side of the fault zone hosts quartz veins ($325^{o}/20^{o}$) with a dip direction of 240^{o}. Above the fault zones some folds are present.

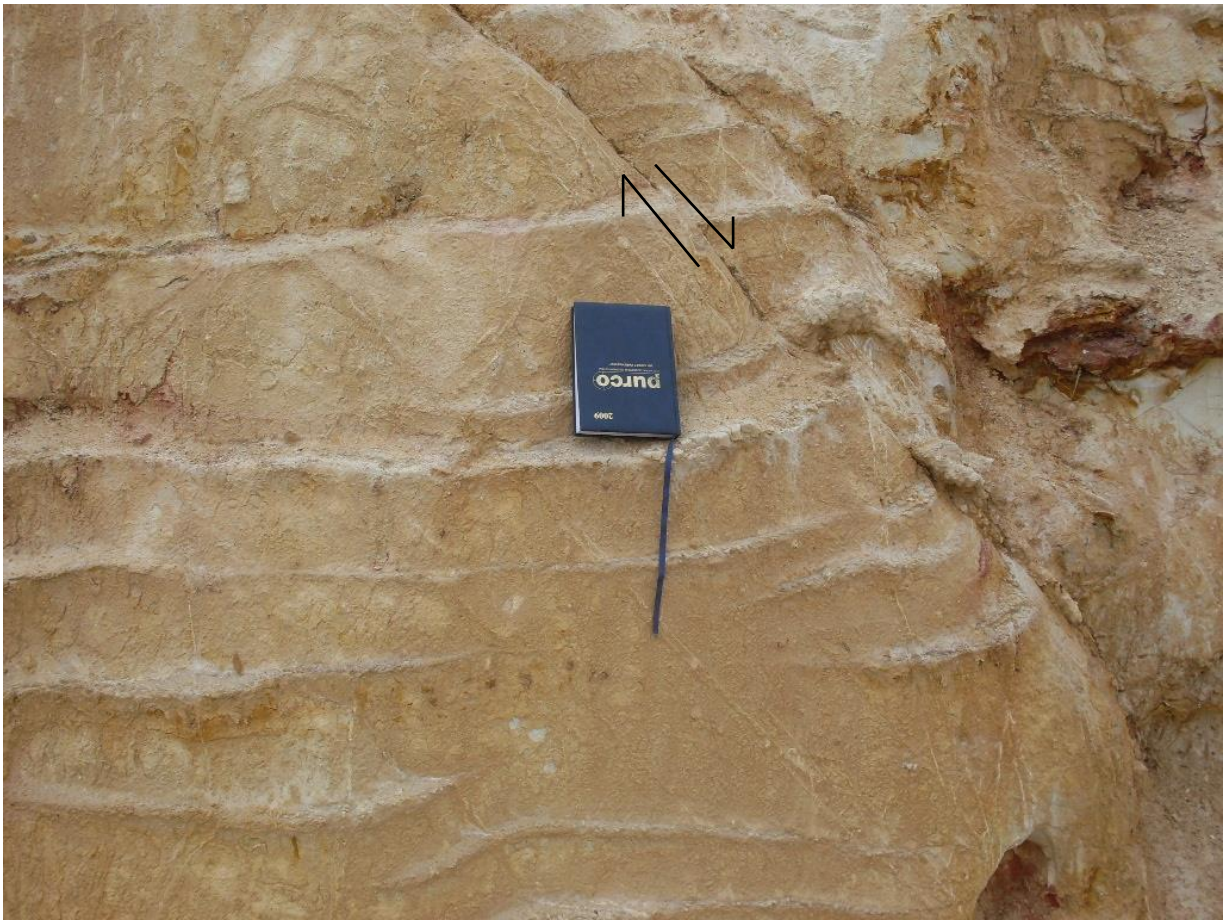

Figure 6- 5: The dip-slip component is apparent where the two arrows are placed.

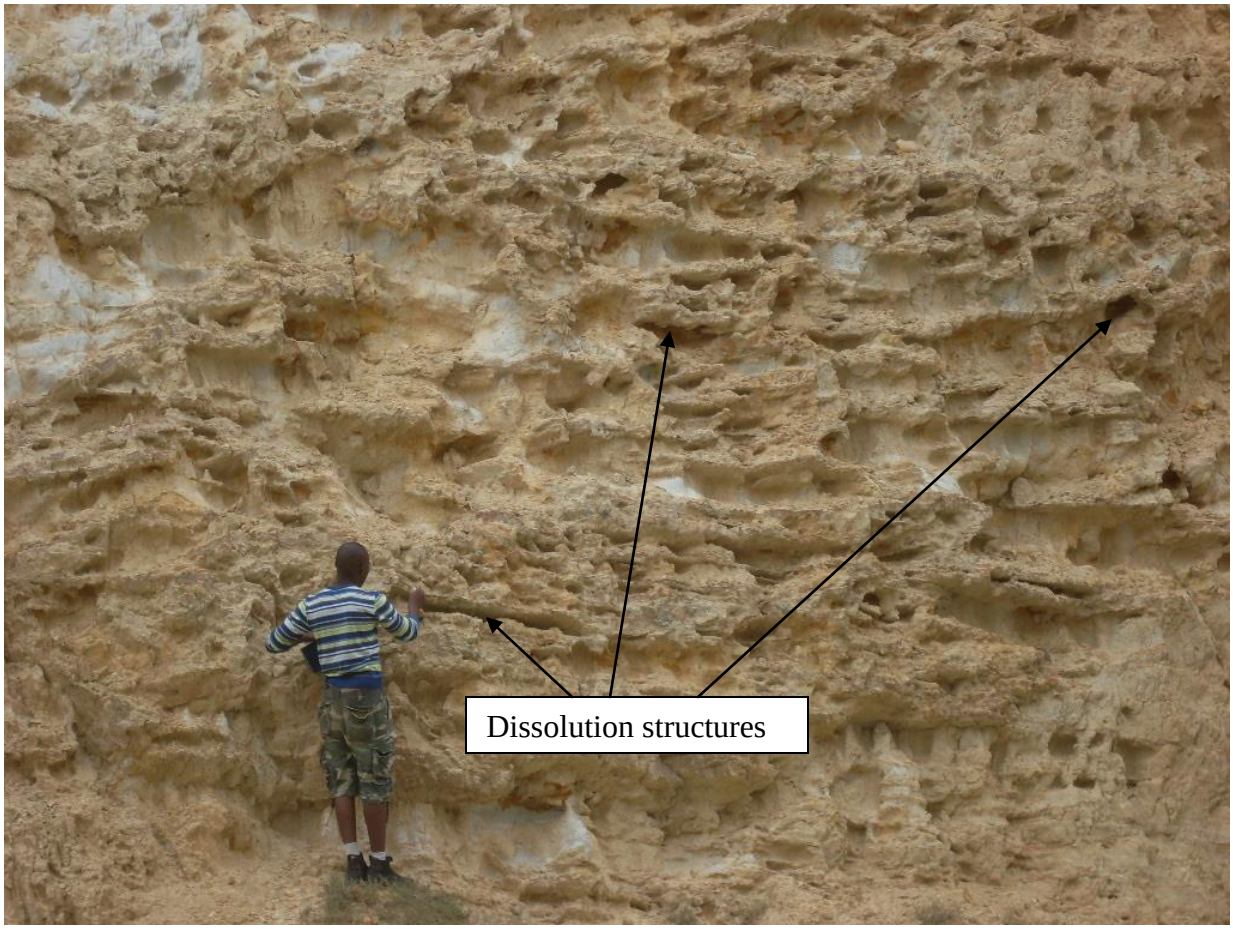

Figure 6- 6: Dissolution structures showing competence differences between quartz veins and the kaolin.

The fault zone precedes a set of 7 fractures ($310^o/85^o$) followed by 11 fractures ($290^o/65^o$) separated by almost a distance of 1cm. These 11 fractures are almost sub-parallel to another major fracture ($330^o/70^o$) at their right hand side. On the surface of this major fracture appear subhorizontal extensional micro-fractures ($330^o/10^o$) (Figure 6.7). In this figure the compressional stress σ_1 is horizontal, and the extensional stress σ_3 is vertical, the direction of stresses is indicated with red arrows. According to the Anderson theory of faulting, the position of σ_1 and σ_3 are characteristics of a reverse faulting.

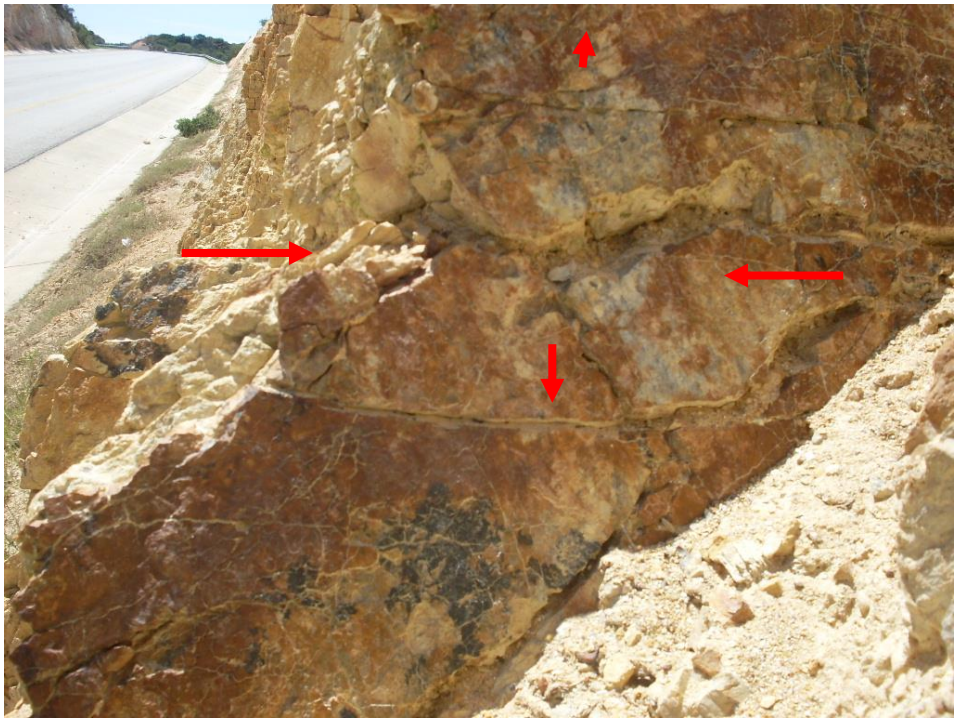

Figure 6- 7: Subhorizontal extension microfractures seen along a fracture surface. Oblique red arrows show the direction of compression, vertical red arrows indicated the direction of the extensional stress.

Other areas are characterized by the presence of quartz veins that alternate with fractures that are not filled. The distance between the fractures is variable, 1.50 m, 80 cm, 70 cm, 50 cm etc.

Another region showing two families of fractures with different attitudes (zone A: $310^{o}/50^{o}$ and zone B: $330^{o}/70^{o}$, Figure 6.8) is prominent. The angle between the two structures is 20^{o}, these pattern is followed by a series of vertical fractures oriented 30^{o}. This zone also hosts some fractures ($290^{o}/60^{o}$) with some antithetic fractures ($45^{o}/75^{o}$) above them; these antithetic fractures are aligned with the fabric of the parent rock. It is also evident that where there is more micro-fractures, kaolinisation is very prominent like in the zone B (Figure 6.8). Some oblique quartz veins in a more or less weathered zone ($10^{o}/25^{o}$) with different thicknesses (4 cm, 2 cm, 1cm, 0.60 cm) show different zones of alteration.

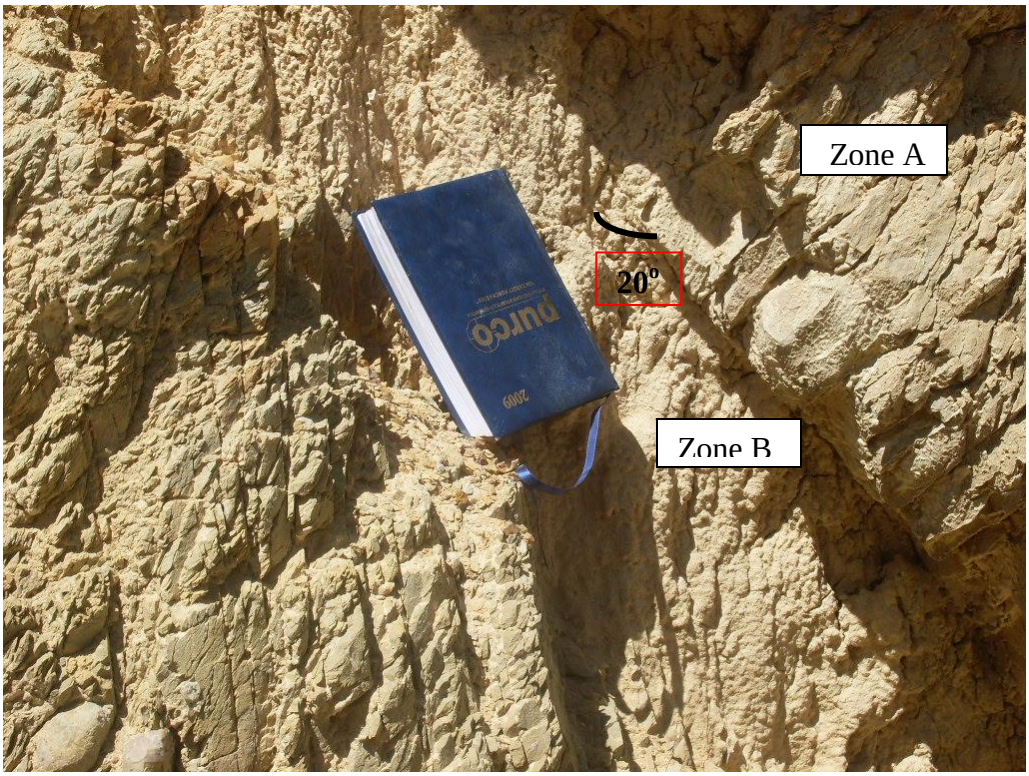

Figure 6- 8: Two families of fracture with different attitudes. Note the intense kaolinisation controlled by microfractures in the zone B.

The outer rims of these quartz veins are ferruginised, reddish to brownish; their inner part is more fresh, whitish in colour. These quartz veins, parallel another big quartz vein which seems to occur earlier than them because of its advanced degree of weathering and ferruginisation. This quartz vein marks a termination for some fractures ($220^{o}/55^{o}$) below it. Another set of quartz veins is followed by a number of fourteen fractures ($210^{o}/65^{o}$) separated between them by an interval of 1,50 m to 50 cm with a dip direction of 300^{o}.

The west zone, in which the alteration is not too much pronounced, is also characterized by brittle deformation. At the left of a fresh Dwyka tillite (Figure 6.2, Figure 6.4 c), a fracture ($285^{o}/60^{o}$) cut across a set of 20 extensional parallel vertical fractures oriented 35^{o}. If in the east zone, fragments or breccias of the parent rock could not be seen because of advanced

weathering, the west zone to the contrary shows evidence of the occurrence of quartzite and granite breccias (Figure 6.9). In this figure the granite breccia is characterised by extensional fractures almost parallel to a major fracture. At the extreme west hand side of the outcrop, the parent rock changes colour from grey to greenish due to the alteration weathering process. This process is seemingly enhanced by the presence of a series of small quartz veins acting as barriers by trapping the water; they are separated by an interval of 30 cm to 50 cm.

Figure 6- 9: Photo displaying two sets of fractures and the granite breccia with extensional fractures almost parallel to the major fracture.

The parent rock appears to be fresh because of the presence of a big hydrothermal quartz vein ($290^{o}/50^{o}$) seen in Figure 6.2, which acts as a barrier. This quartz vein does not allow water flow; the water is then trapped and weathers the rock. This quartz vein occurs near seven fractures having the following attitude ($280^{o}/45^{o}$). Near this set of seven fractures, ten other fractures

occur in a parallel direction that predate a series of antithetic fractures more visible below it oriented 220^{o}and dipping at 70^{o}.

A bit farther from the above prominent quartz vein, a set of parallel fractures (300^{o}/45^{o}) occurs. At the right hand side of these fractures, the parent rock is more or less weathered, with its original fabric more and more visible. The west zone is also characterized by a marked absence of quartz veins despite the presence of fractures.

At another place a set of twenty fractures (290^{o}/65^{o}) occurs, and is followed by another set of fractures (40^{o}/40^{o}). Some slicken lines (plunge 10^{o}, bearing 290^{o}) occur on a pinkish quartzite breccias found on the surface of a fault (290^{o}/ 50^{o}) in a fault zone (Figure 6.10 left).

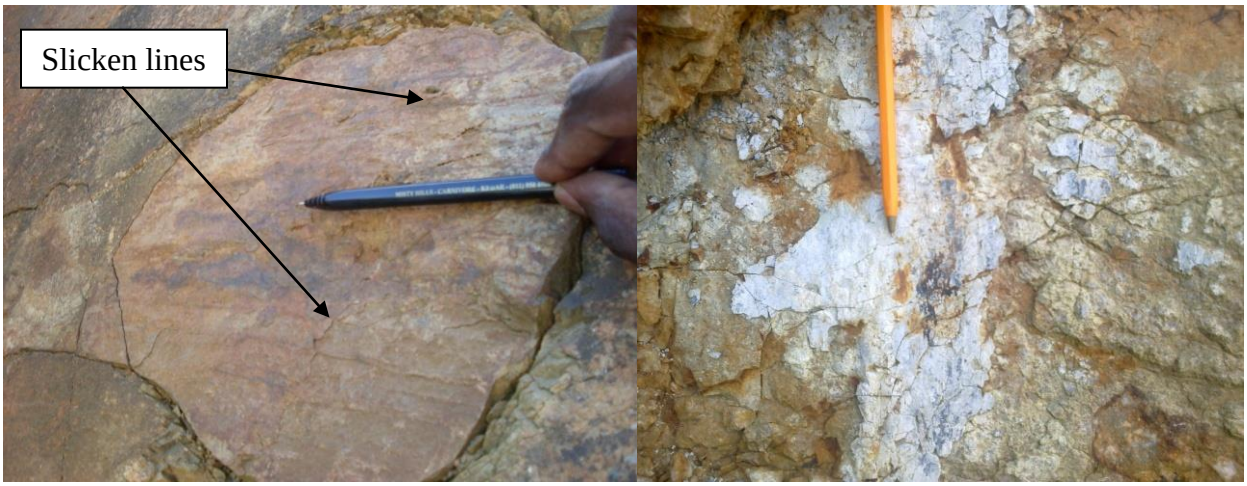

Figure 6- 10: left) Lineation on a quartzite breccias showing horizontal movement; right) dip-slip movement parallel to the pen seen on a coated surface of a reactivated fault.

Other slickenlines showing a dip-slip movement occur on the surface of a fault (Figure 6.10 right). The percolation of water leached weathered products that coated the fault surface on which the displacement is visible.

It can be highlighted that the region of Grahamstown is under continuous extensional tectonics, the slickenlines indicate that there was a reactivation of old fractures. These slickenlines are indicative of a combined srike-slip and dip-slip components. The Grahamstown area is also known for its recurrent seismicity.

6.4. Microscopic observations

Albite crystals are prominent in the tillite, if not fresh; albite weathers by losing its polysynthetic twinning. The alteration is more marked at the edges of albite crystals (Figure 6.11 a, c, d), these greyish and clayey alteration products are fine grained (Figure 6.11 d). These products are similar to the one found in the matrix. The presence of numerous crystals of quartz can be justified by its hardness and resistance to alteration.

6.4.1 Alteration

Muscovitization, albitization and chloritization are the predominant types of alteration affecting the Dwyka tillite.

6.4.1.1 Muscovitization and kaolinization

Muscovite appears as small grain in either sandstone or granite rock fragments found in the tillite. It can be round or slightly elongated; it is being mainly replaced by greenish mineral at the borders, probably chlorite. The size varies from less than 1µm to 10µm. Sometimes it appears very flaky (Figure 6.11 b), and is replacing crystal of plagioclase (albite, Figure 6.11 a) according to the following equation:

$$3\ \text{Albite}\ (NaAlSi_3O_8) + K^+ + 2H^+ \longrightarrow \text{Muscovite}\ (KAl_2(AlSi_3O_{10})(OH)_2) + 6\ SiO_2 + 3\ Na^+$$

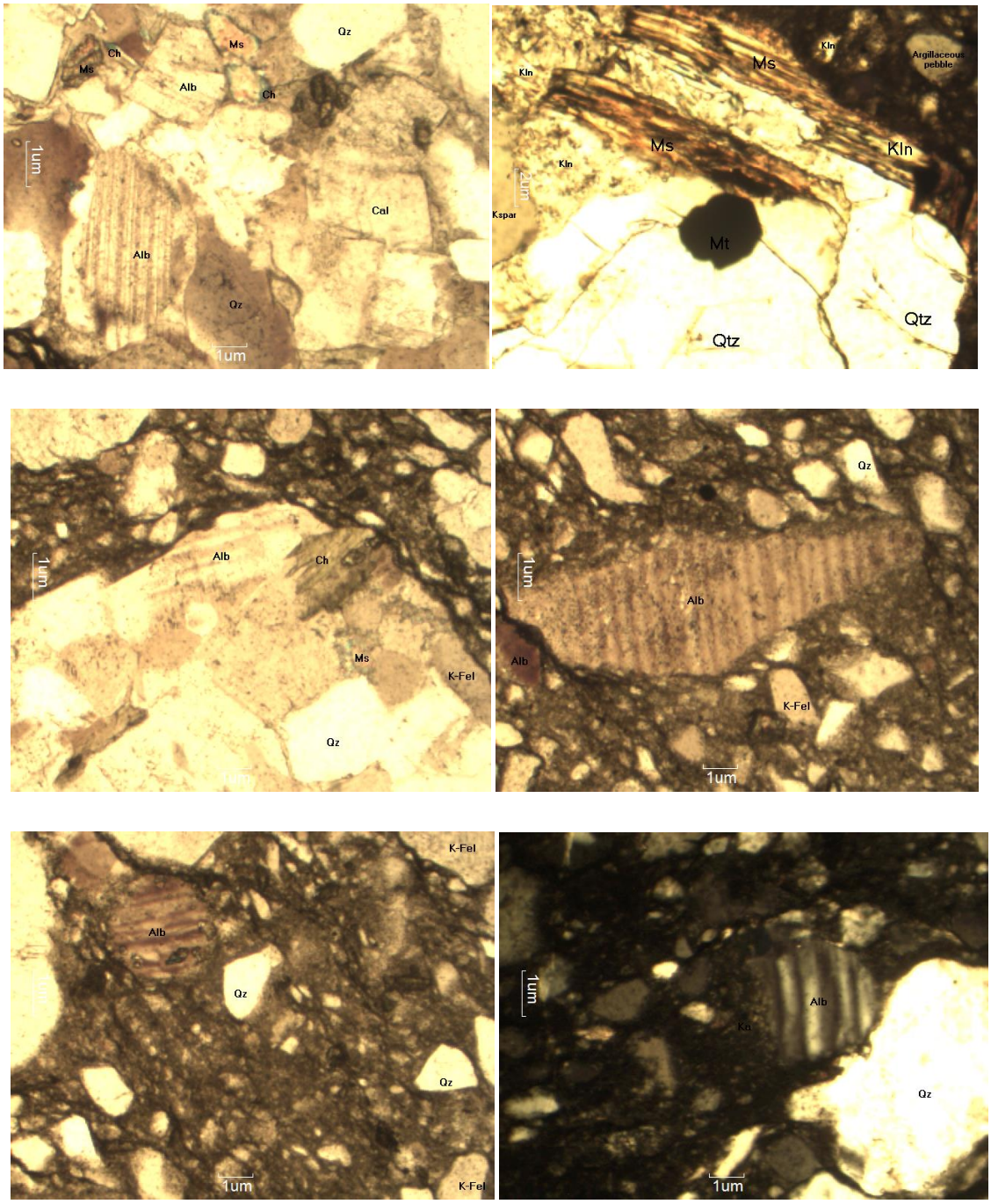

Figure 6- 11: chlorite in green deriving from muscovite, b) muscovite being weathered to kaolin, the grain of magnetite on a fresh quartz; c) fragment of granite with its typical minerals; d) weathered albite; e) albite developing from garnet; f) Dwyka tillite showing weathered albite.

The muscovite at some places is weathered, and altered to kaolinite. This muscovite is from granite breccias. It can also be found along a fractured quartz grain, which has undergone tensile

stresses. Most of these breccias are more brittle than the matrix itself. In these granite breccias appears a magnetite grain as an accessory mineral (Figure 6.11 b).

6.4.1.2 Chloritization

The chlorite was found to be formed in different ways; it was formed as a secondary mineral at the edges of the muscovite, or from the alteration of albite. It might also have been the result of hydrothermal alteration to a lesser extent; the Grahamstown kaolin deposit and the Dwyka tillite have within them numerous quartz veins. The alteration possibly from an albite within granite breccias led to the formation of chlorite. This occurrence characterizes often an alteration mostly found in hydrothermal deposit. It should be noted that the kaolin deposit is supergene; the term hydrothermal in the present context refers only to the occurrence of quartz veins. Chlorite also developed as overgrowth from biotite, the chlorite totally inherited the shape of the biotite with a volume change, a layer of chlorite can replace another layer of biotite with loss of potassium and accumulation of magnesium.

6.4.1.3 Albitization and kaolinisation

Albite is either from granite and sandstone breccias or within the matrix, and is very remarkable. According to microscopic study, the hydrothermal events did not play a part; hydrothermal albite is typically fresh and characterized by albite twinning (Zhao, 2011). Albite at some places derives from the alteration of garnet (Figure 6.11 e); the Dwyka tillite comprises sedimentary, metamorphic and igneous rock fragments. This albite is in turn altered in clayey products at its rims (kaolin) that form the matrix. The garnet from which the albite develops is possibly the grossulaire, few green relics can be seen on top.

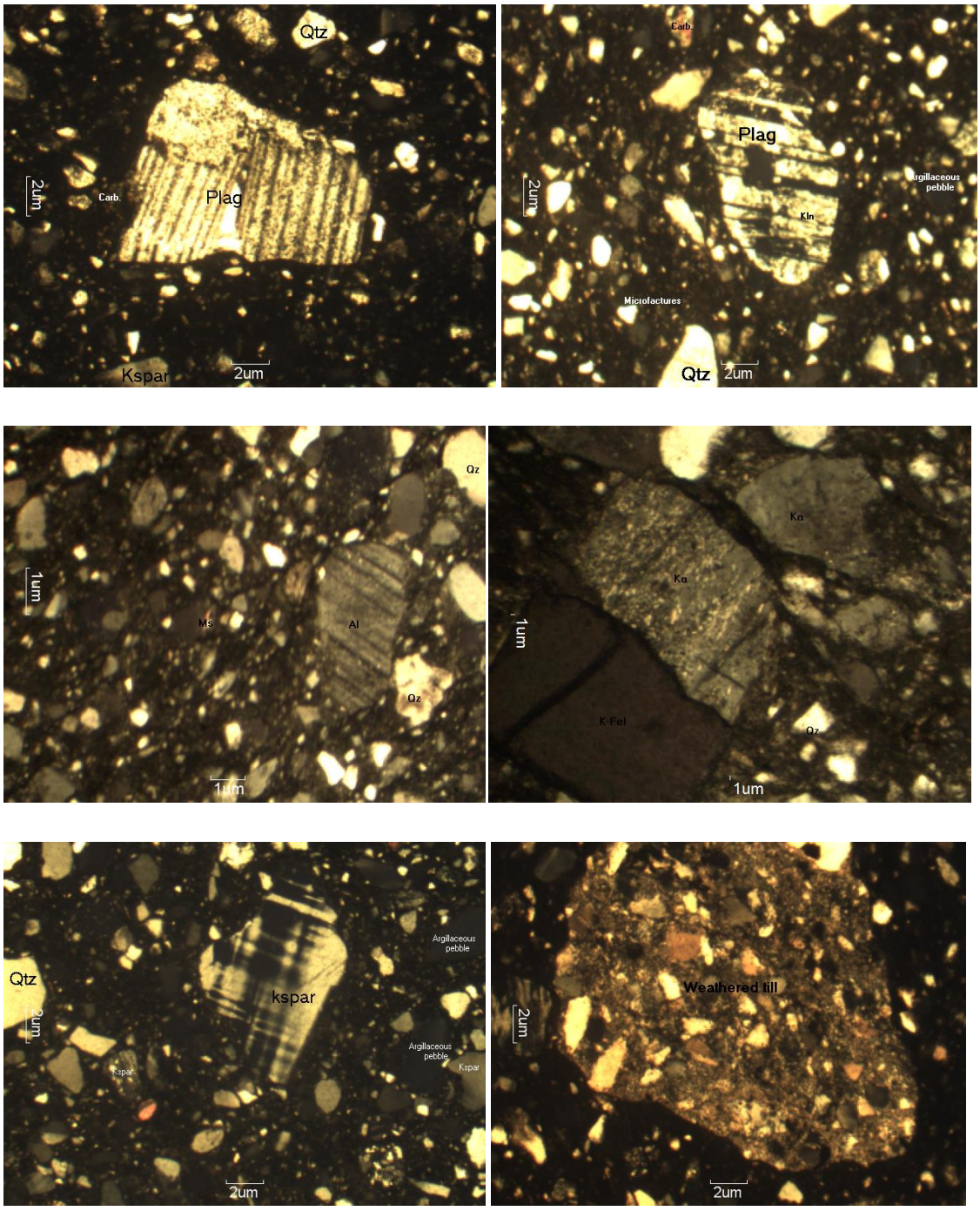

Figure 6- 12: a, b, c, d, feldspar; e) k-feldspar and argillaceous pebbles; f) weathered till

It was observed that besides quartz, the plagioclase albite is the second abundant mineral, which in many cases weathers to produce kaolinite (Figure 6.11 a, c, d, e, f; Figure 6-12 a, b, c,).

Microcline is also present in the matrix (Figure 6. 12 e). Enrichment in albite is a major source to the formation of kaolin. Orthoclase (Figure 6.12 d) is also present.

The Dwyka tillite which is the parent rock that weathered to produce the kaolin is mostly dominated by breccias of granite and quartzite. Microscopic studies revealed the presence of quartz and feldspar crystals in a dark brown matrix (Figure 6.13 left).

Apart from breccias known at present such as the ones of quartzite and granite, the Dwyka tillite contains also tills (Figure 6.12 f), breccias of sandstones with almost 90% of quartz and albite. Other fragments are metamorphic rocks derived from the Cape Fold Belt. These metamorphic rocks are typical of regional metamorphism because they present oriented crystals especially those of quartz showing plastic deformation (Figure 6.13 b).

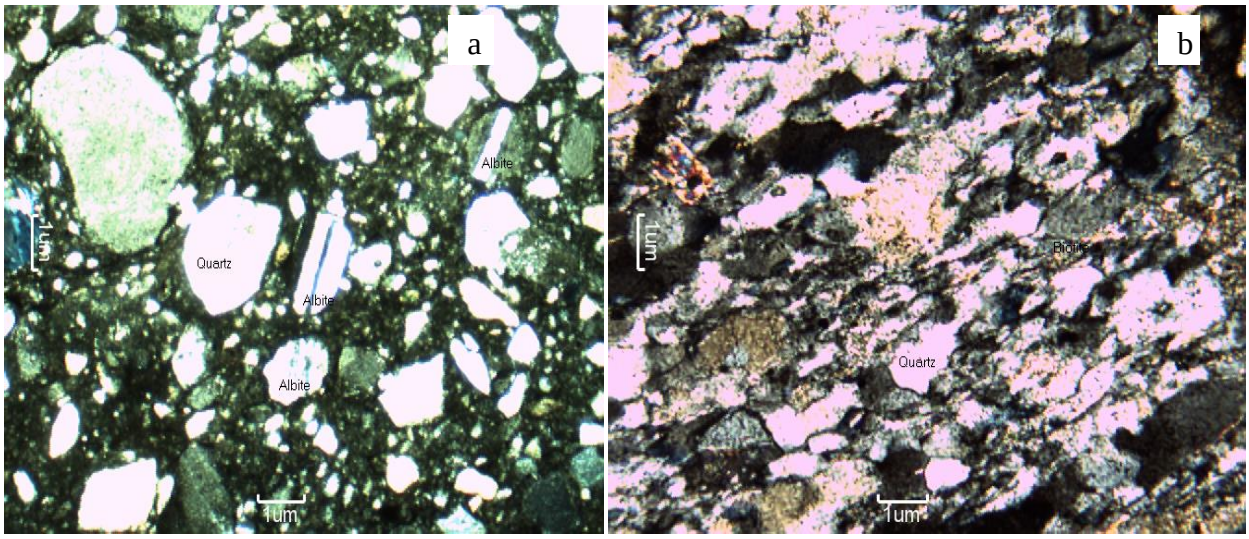

Figure 6- 13: left, quartz and feldspar crystals in a dark brown matrix; right: oriented crystals especially those of quartz showing plastic deformation.

Crystals of albite mainly from granite are present, at some places breccias of granite with minerals in an advanced stage of alteration can still be recognized. The albite in its alteration produces brownish products than can be assimilated to the matrix.

The predominant presence of abundant quartz crystals is an evidence of their resistance to weathering; these quartz crystals sometimes present a rough surface. Other crystals cannot be distinguished clearly because of their advanced stage of alteration and are easily confounded with the matrix.

Crystals of quartz, feldspar can either be found isolated in the matrix (Figure 6.14 left) or within breccias (Figure 6.14 right). This is indicative of two categories of breccias as far as the compaction is concerned; those that are loose and easily broken, and those that are still resisting mechanical and atmospheric weathering.

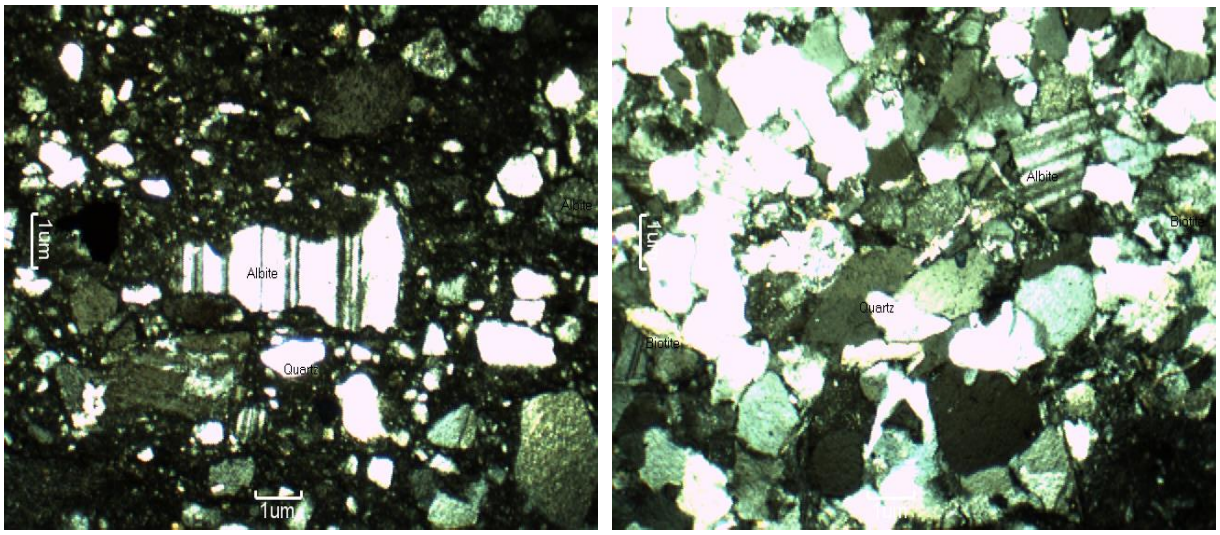

Figure 6- 14: left, Feldspar and quartz crystals in the tillite matrix; right, Feldspar and quartz crystals in breccias.

6.5. Difference of competence between the matrix and breccias

The matrix seen at the macroscopic scale does not present any fracture at all, but microscopic observations have shown that the matrix is affected by micro-fractures. These micro-fractures tend to develop at the contact matrix-grains (Figure 6.11 c, d, e; Figures 6.15 left and right) mostly between the matrix and the grains of quartz and feldspar. This type of fracturing was not seen at the contact matrix-muscovite probably because the muscovite behaves differently on the mechanical point of view from quartz and feldspar.

The difference in mechanical behaviours between the breccias and the tillite matrix is very remarkable (Figure 6.16 a, b, c, d, e and f). The breccias are more brittle and develop extensional fractures, and the tillite matrix is more ductile. Thus the weathering that occurs to produce the kaolin will start first and foremost within the breccias (Figure 6.17 a, b, c, and d) before it continues in the matrix.

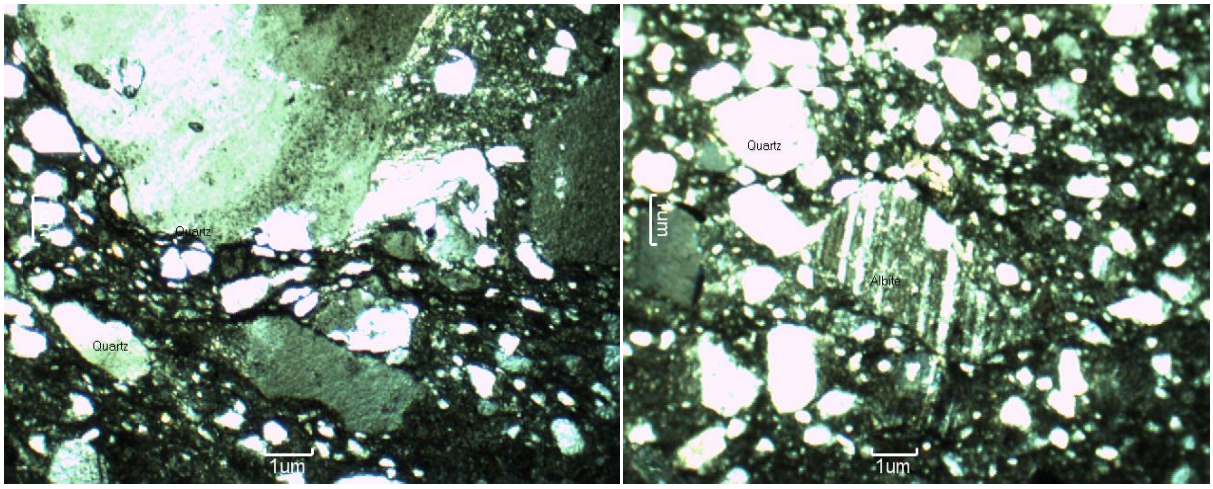

Figure 6- 15: In both these two images (left and right) microfractures tend to develop at the contact matrix-grains

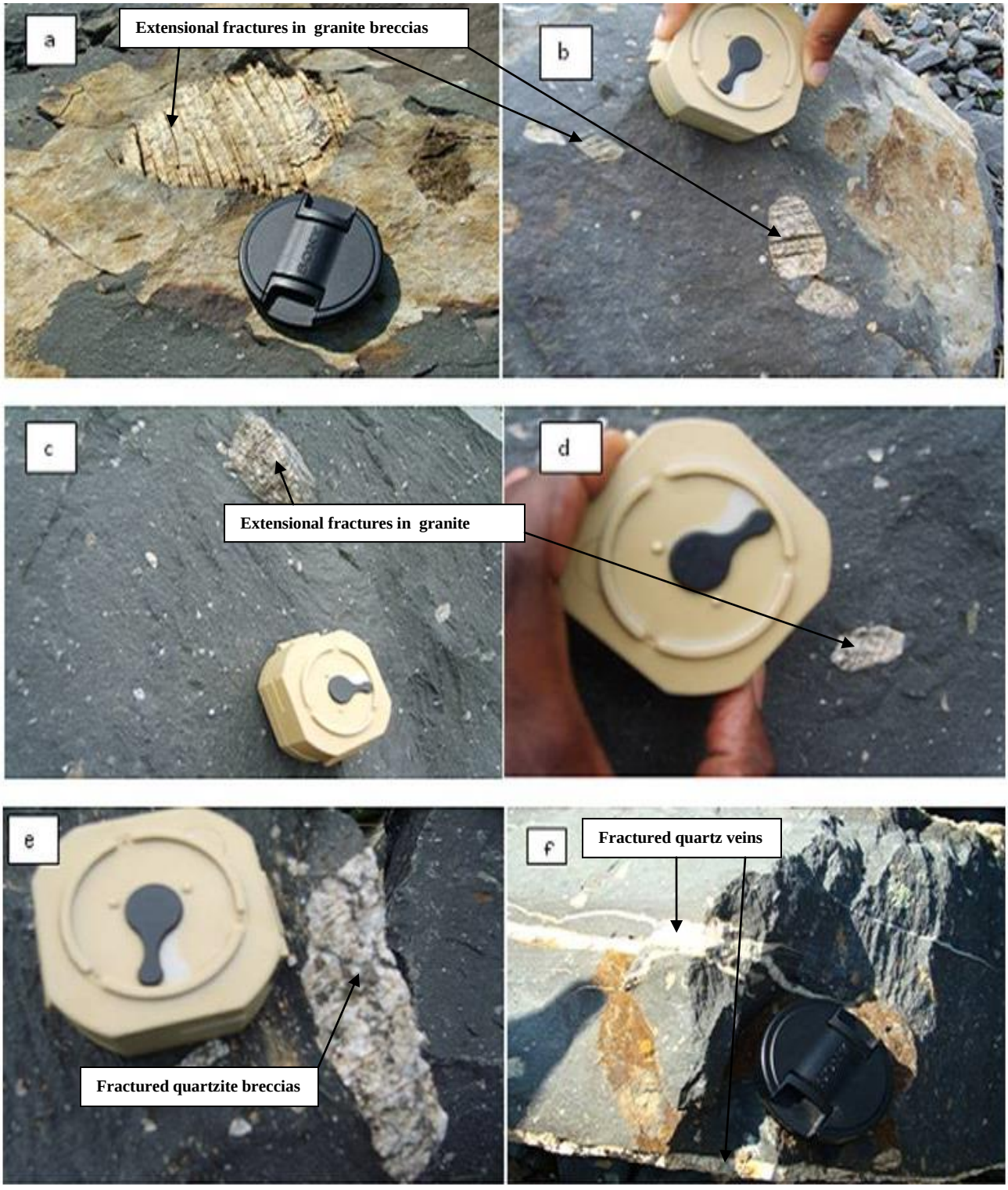

Figure 6- 16: a, b, c, d; extensional fractures in the granite breccias, e: fractured quartzite breccias enclosed in a ductile grey tillite matrix, f: extensional subhorizontal fractures in the tillite filled with fractured quartz veins.

Figure 6- 17: a, b, c, and d; Fractured granite breccias in advanced stage of weathering, the kaolinisation start to develop in the granite breccias (well seen in Figure 6.17 d)

The abundant micro-fractures observed in the matrix allow the circulation of water, which weathers the Dwyka tillite.

Role of foliation in the kaolinisation

It was observed that foliation can accelerate the process of weathering, and accordingly the kaolinisation. The shear zone has shear walls assimilated to C fabrics; in the zone of schistosity (S-fabric or foliation) developed at an angle to the shear walls, the kaolinisation is more pronounced (Figure 6.18). It can once be observed that the more the occurrence of close-spaced

fractures, the more developed is the kaolinisation. This type of structural control (close-spaced fractures) on kaolinisation can also be seen in Figure 6.8 (zone B).

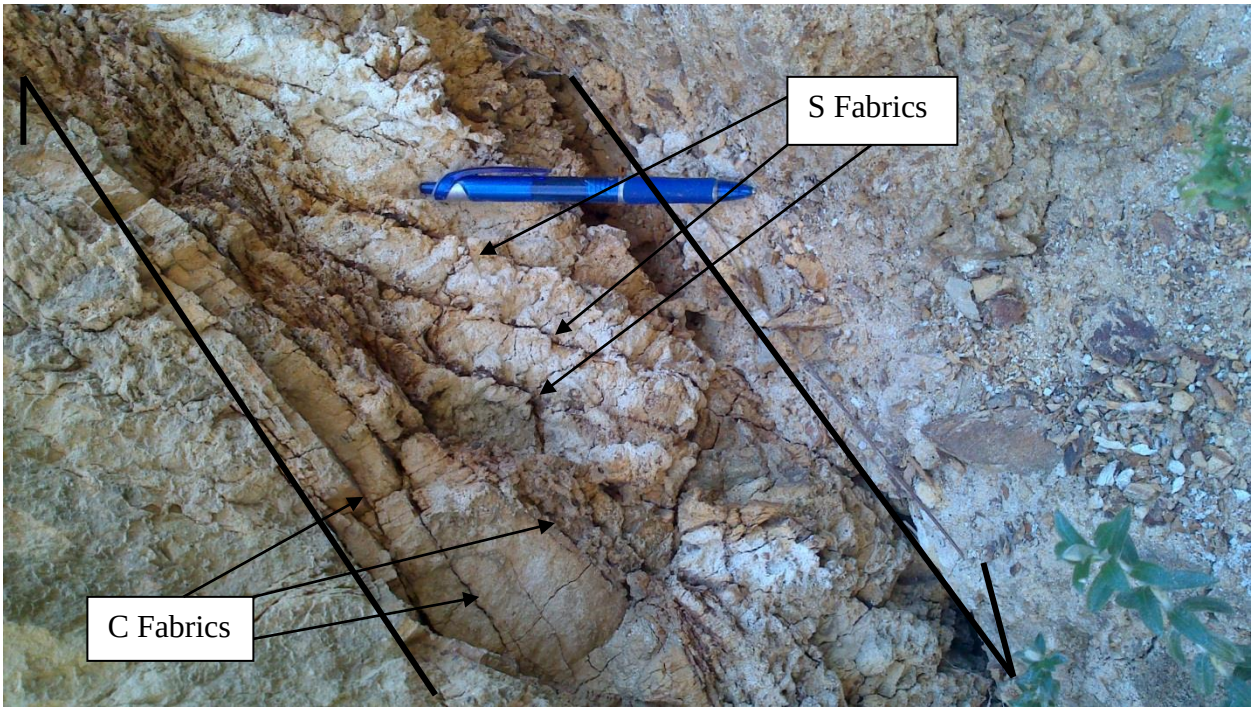

Figure 6- 18: C-S fabrics showing a right-lateral shear movement. Note the more kaolinised rock in the foliated part marked by the S fabrics.

6.6 X ray diffraction analysis

XRD analyses on three different samples collected from three places revealed the presence of albite, clinochlore (chlorite group, Figure 6.19), muscovite (Figure 6.20), orthoclase (Figure 6.21), albite (Figure 6.22) and quartz (Figure 6.23). The presence of muscovite indicates that the kaolin was partly a product from weathered muscovite granite breccia. It can also indicate the advanced stage of weathering as it was also documented in the southern Wisconsin soils (Fanning and Jackson, 1966).

Three places along the kaolin roadcut where samples were collected, were selected according to the degree of weathering. The first place hosts a fresh tillite, greyish in colour; the second place hosts a rock in the process of weathering, greenish to whitish or pinkish. The third place shows that the rock is in an advanced stage of alteration (Figure 6.24).

The three different places where samples were collected have similar XRD patterns, but the intensity differ as can be seen in the the Figures 6.25, 6.26 and 6.27. The fresh Dwyka tillite (zone 1) has its high peak at 2Θ (26.64) and at an intensity of 83633, the rock in the weathering process (zone 2) has its high peak at 2Θ (26.58) and at an intensity of 50769, and the kaolinised rock (zone 3) has its high peak at 2Θ (26.61) and at an intensity of 37281. Thus the more the rock is weathered, the more the counting intensity is lower, the more the fresh is a rock, the more its counting intensity is higher. These three rock showing the same background are reprised in the Figure 6.28., a fresh rock has highest peaks than a more weathered one.

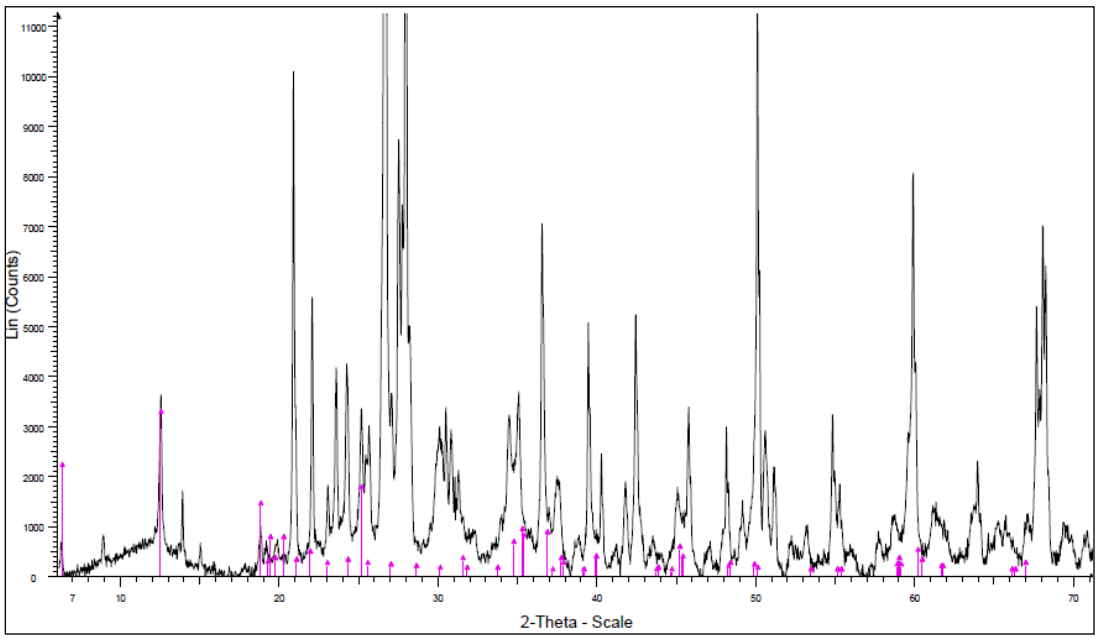

Figure 6- 19: XRD pattern of clinochlore in pink (the black pattern is related to the rock background).

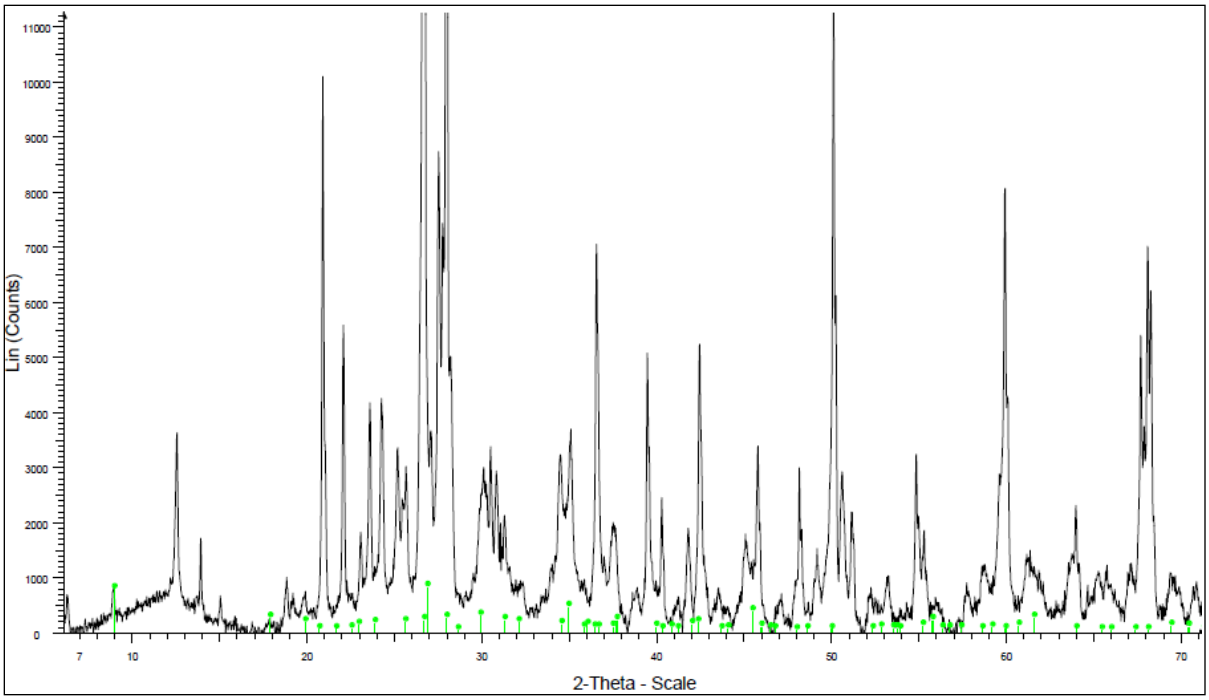

Figure 6- 20: XRD pattern of muscovite in green

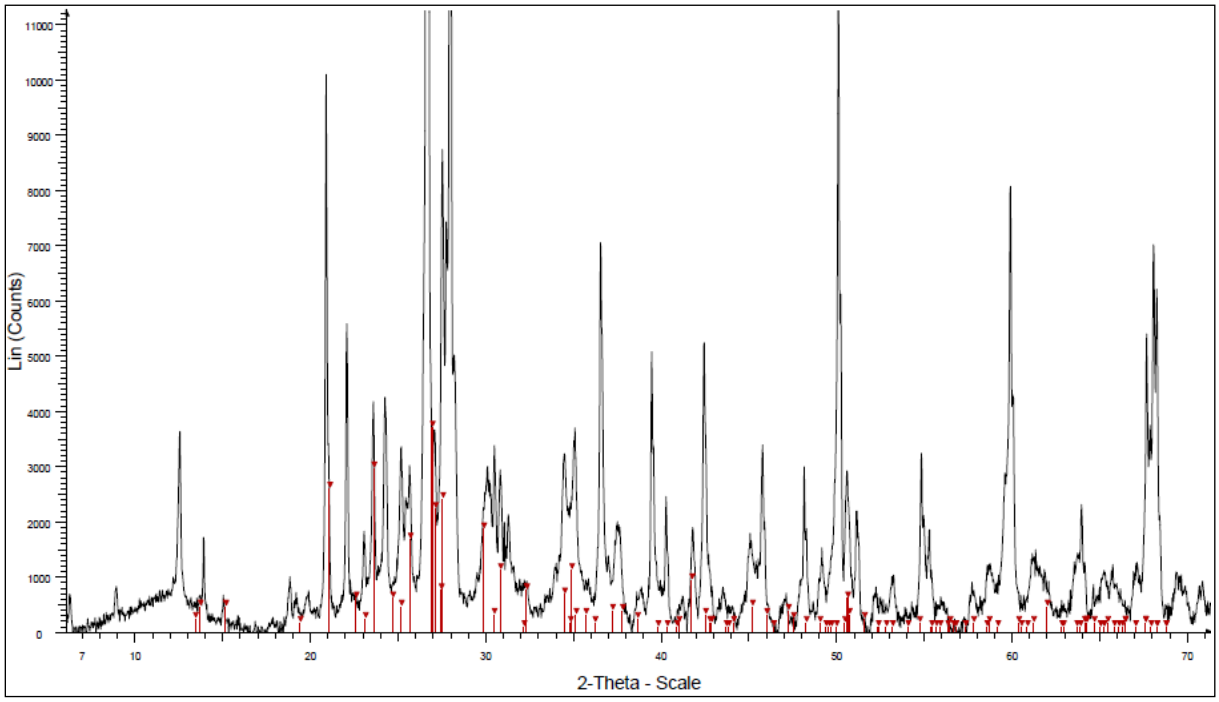

Figure 6- 21: XRD pattern of orthoclase in red

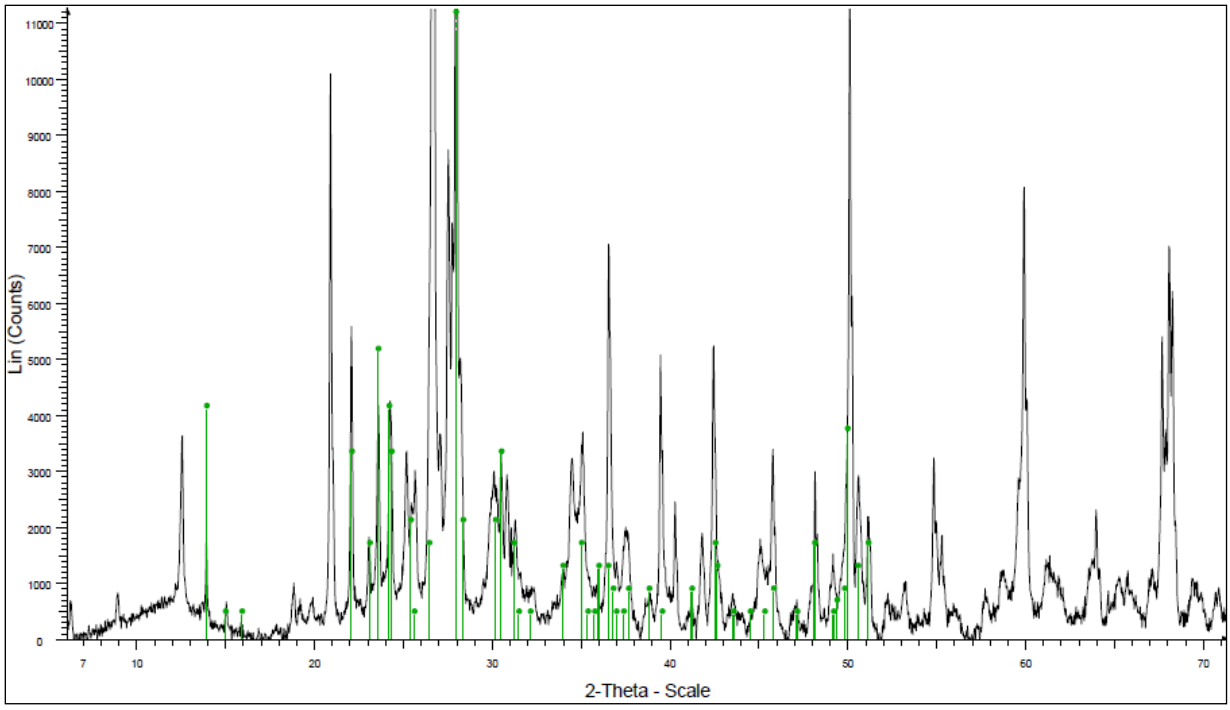

Figure 6- 22: XRD pattern of albite in green

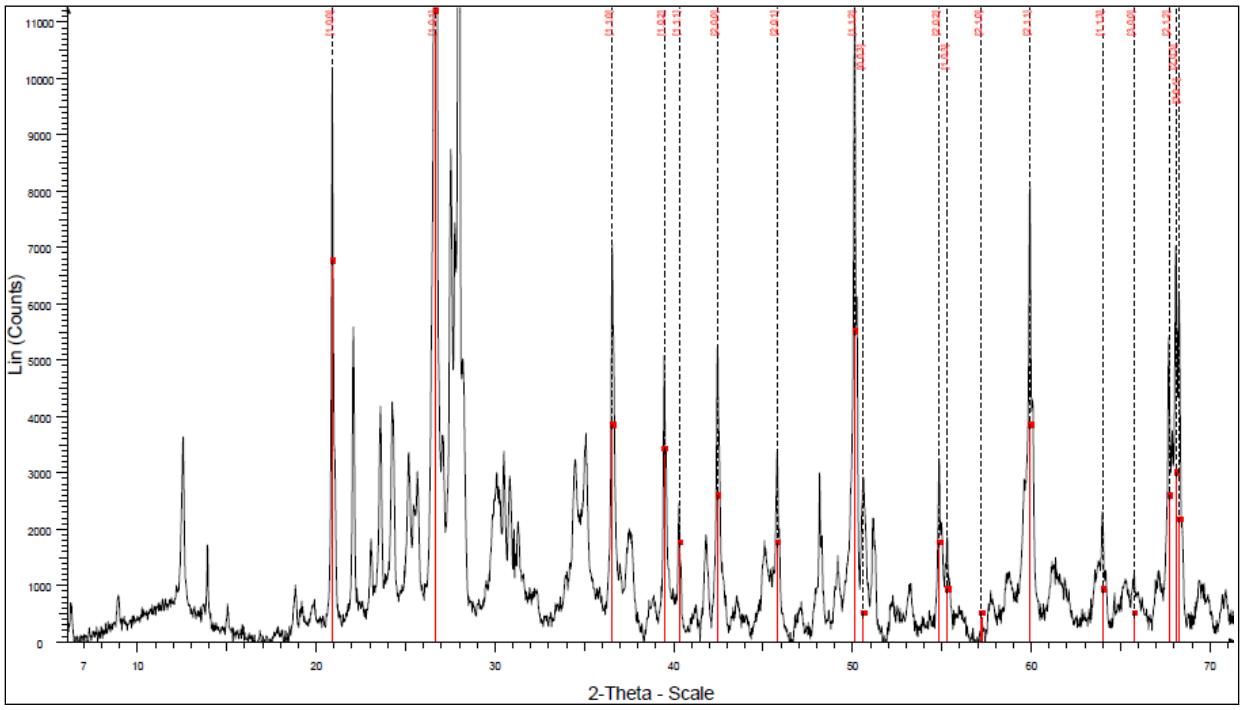

Figure 6- 23: XRD pattern of quartz in red

Figure 6- 24: Sample collection site 1, 2 and 3 used for XRD pattern discriminations

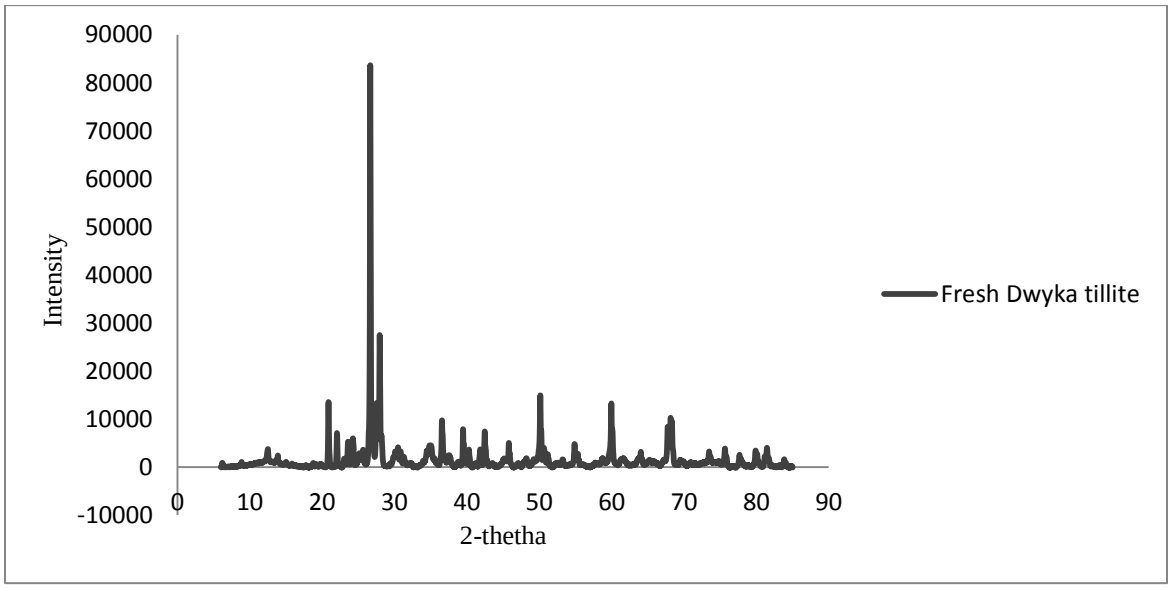

Figure 6- 25: XRD pattern from the fresh Dwyka tillite (zone 1)

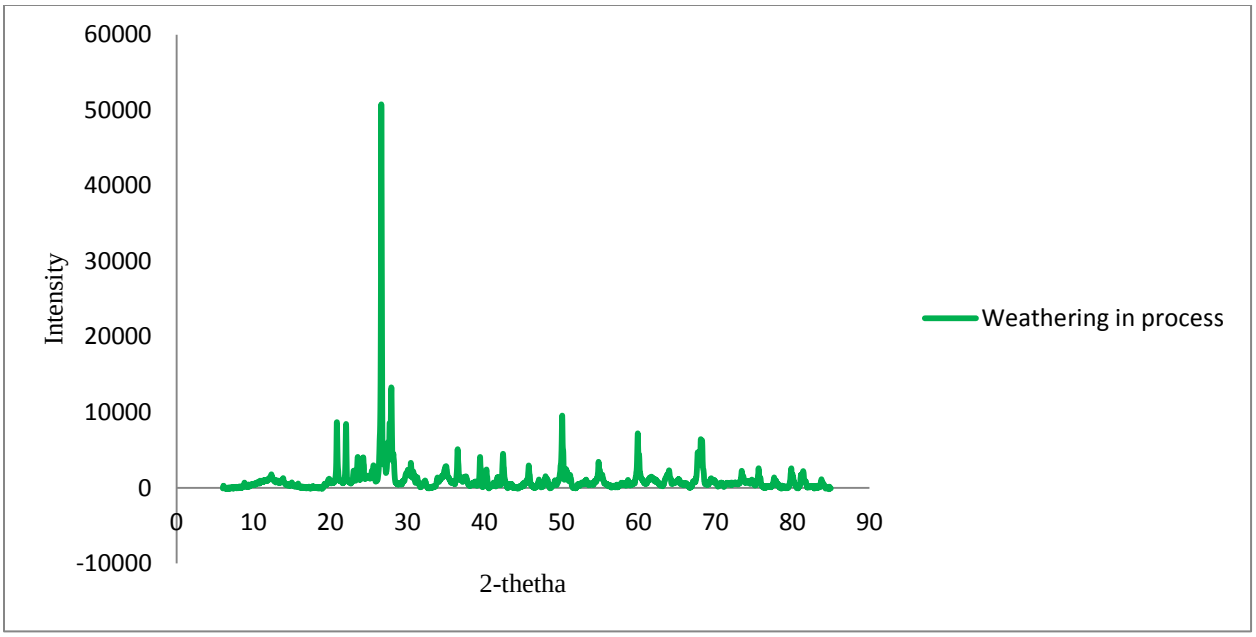

Figure 6- 26: XRD pattern from the rock in the process of weathering (zone 2)

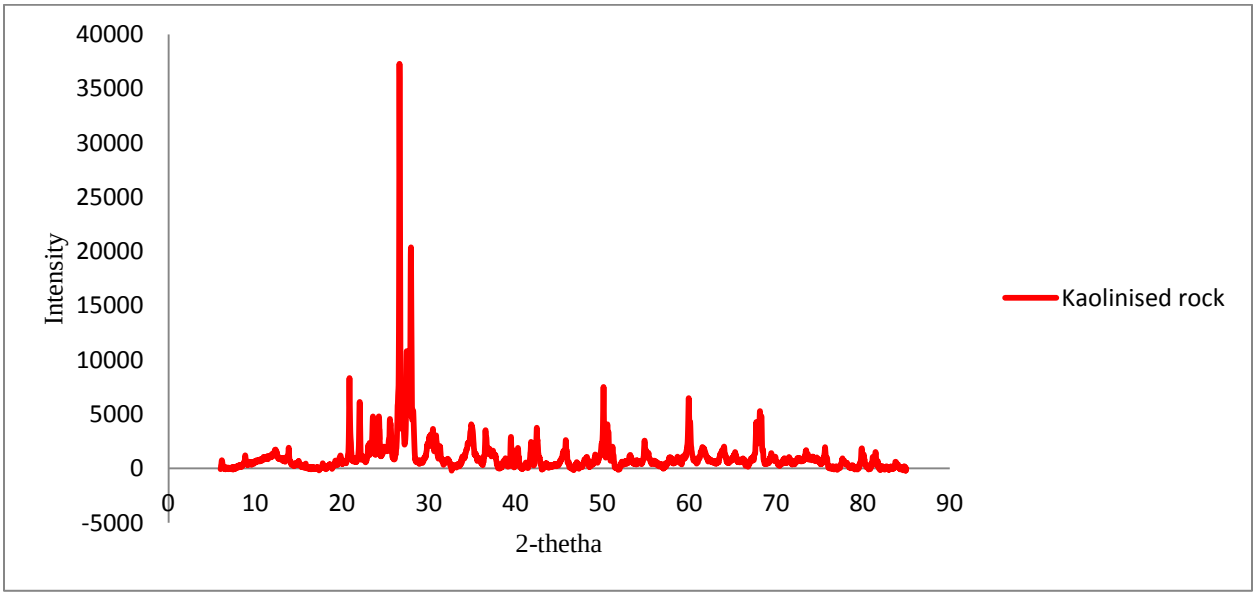

Figure 6- 27: XRD pattern of the kaolinised rock (zone 3)

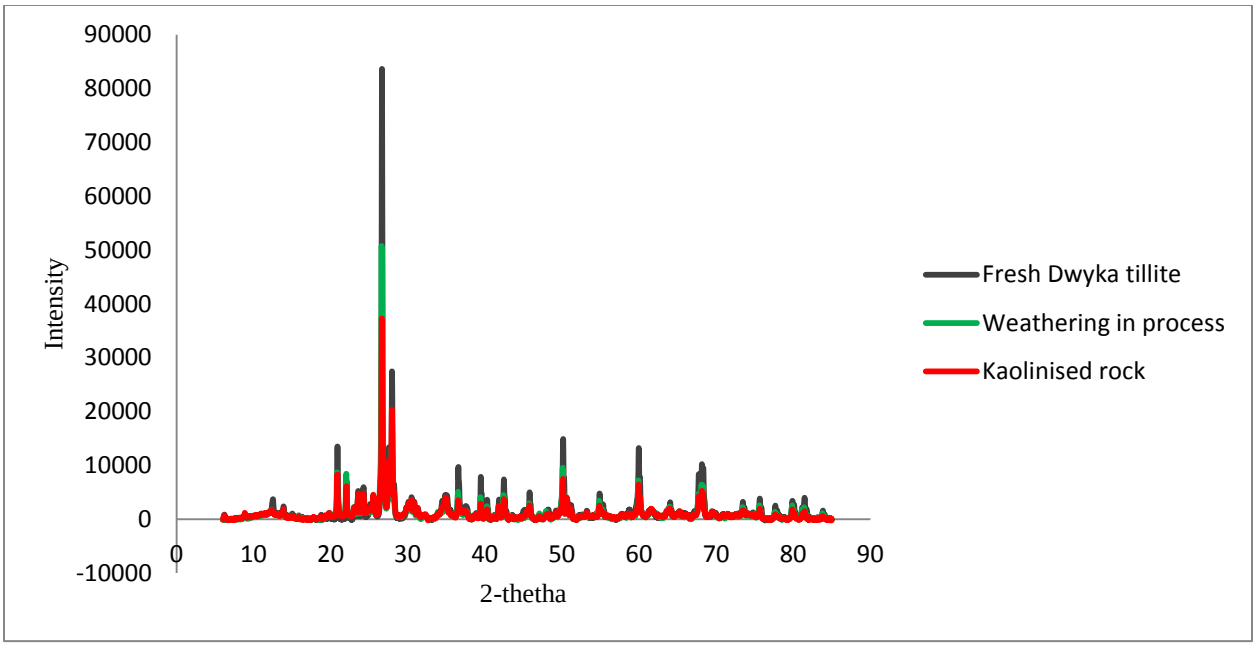

Figure 6- 28: XRD patterns combination of zone 1, zone 2 and zone 3

6.7 XRF results

Eleven samples were collected below the quartz vein in the footwall (Figure 6.2) at 1 m interval. The were analysed using XRF to see the compositions of major elements found in the fresh or moderately weathered Dwyka tillite. The results shown in Table 6.1 indicate that the Dwyka tillite matrix is rich in alumino-silicated materials and iron. The average weight percents of K_2O and Na_2O are 3.20 wt % and 3.19 wt % respectively. These proportions are far less than the average weight percentages of silica and aluminum (66.85 wt % and 13.80 wt % respectively).

From these results it can be indicated that the alkali-feldspars are the abundant minerals undergoing weathering to produce the kaolinite. Their lower proportions relative to the ones of silica and aluminum is related to leaching. These compositions imply that either potassium or sodium, which are more soluble and mobile would have been leached out. Silica and aluminum

which are less mobile will remain in situ to produce the kaolinite [$Al_2Si_2O_5(OH)_4$]. Major elements distribution from these samples can be seen in Figure 6.29. The TiO_2 has lower percentage (0.67-0.73 wt %), the samples are rich in Fe_2O_3 (5.43-6.05 wt %). High silica content as well as high iron content can have an impact on the quality of the kaolin. The iron can enter the kaolinite structure and replace aluminium in the octahedral layer. The MnO, Cr_2O_3 and P_2O_5 have very lower weight percentages (0.06-0.137 wt %, 0.012-0.015, and 0.179-0.215 wt % respectively). The MgO percentages vary between 1.79 and 2.25 wt %.

Table 6.1: Table 6- 1: XRF results from the eleven samples

Sample	S 1	S 2	S 3	S 4	S 5	S 6	S 7	S 8	S 9	S 10	S 11	Average
SiO_2	66.05	68.64	67.83	67.26	68.63	65.05	66.57	66.14	67.18	65.72	66.32	66.85
TiO_2	0.73	0.67	0.69	0.67	0.68	0.69	0.73	0.69	0.67	0.7	0.68	0.69
Al_2O_3	14.65	13.74	13.87	13.51	13.91	13.52	13.8	13.9	13.71	13.6	13.54	13.80
Fe_2O_3(t)	5.94	5.54	5.67	5.8	5.43	6.05	5.89	5.84	5.66	5.7	5.68	5.75
MnO	0.083	0.085	0.087	0.091	0.084	0.12	0.073	0.072	0.066	0.06	0.137	0.09
MgO	2.17	2.09	2.12	2.25	2.05	2.24	2.07	2.12	2.01	1.91	1.79	2.07
CaO	2.01	1.72	1.66	1.65	1.59	1.75	1.6	1.42	1.7	1.41	1.49	1.64
Na_2O	3.18	3.17	3.13	3.12	3.15	3.61	3.12	3.1	3.07	3.3	3.2	3.20
K_2O	3.31	2.88	3.05	3.15	3.01	3.49	3.17	3.34	3.09	3.46	3.25	3.20
P_2O_5	0.206	0.185	0.183	0.179	0.187	0.186	0.215	0.186	0.187	0.197	0.192	0.19
Cr_2O_3	0.015	0.013	0.014	0.014	0.013	0.012	0.015	0.014	0.015	0.015	0.013	0.01
L.O.I.	2.05	1.68	1.83	1.82	1.75	2.04	2.34	2.37	2.32	2.54	2.54	2.12
Total	100.4	100.4	100.13	99.52	100.48	98.76	99.59	99.2	99.67	98.61	98.81	99.60
H_2O^-	0.4	0.24	0.26	0.29	0.21	0.38	0.66	0.62	0.7	0.9	0.95	0.51

Leached major oxides such as MgO, CaO, Na_2O, and K_2O and as well as in situ major oxides such as Al_2O_3, Fe_2O_3 were used in the binary diagrams in order to visualise assorted possible correlations. Leached major oxides were plotted against Al_2O_3, then with Fe_2O_3. The MgO plotted against Al_2O_3 and Fe_2O_3 shows a quasi increasing trend as can be seen in the binary

diagram (Figure 6.29 c, h respectively). This K_2O weight percentage in the binary diagram K_2O-Fe_2O_3 (Figure 6.29 g) is almost constant (2.9-3.5 wt %). Though the silica has higher weight percentages, the binary diagram SiO_2-Fe_2O_3 shows a negative correlation. The silica content is decreasing while the Fe_2O_3 is increasing. However the Grahamstown kaolin deposit is not of very good quality because of high silica content. Likewise, lower percentages of CaO, MgO, Na_2O, and K_2O, indicate that these elements are soluble and mobile. Goldsmith's classification of elements according to their mobility indicates that three groups exist. The first group has elements with $Z/r < 3$ (hydrated and soluble cations: CaO, MgO, Na_2O, K_2O…), the second group has elements with $3 < Z/r < 10$ (insoluble oxides and hydroxides: Fe, Al, Ti, As…), and the third one with $Z/r > 10$ (soluble complex anions: S, C, P, N…). Z is the ionic charge, and r is the ionic radius. The first group has more mobile elements. These elements can be leached out to leave in situ the Al_2O_3 of the second group that forms the kaolin. It was noted in all the samples that Al, Si, and O are preponderant (e.g. Figure 6. 30, a, b, c, and d).

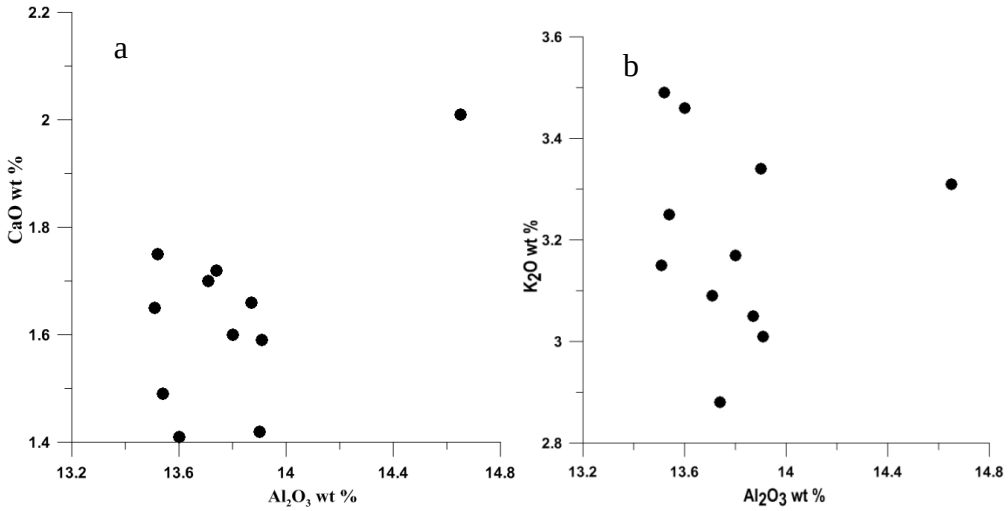

Figure 6.29: Binary diagrams showing leached and in situ oxides vs Al_2O_3 and Fe_2O_3.

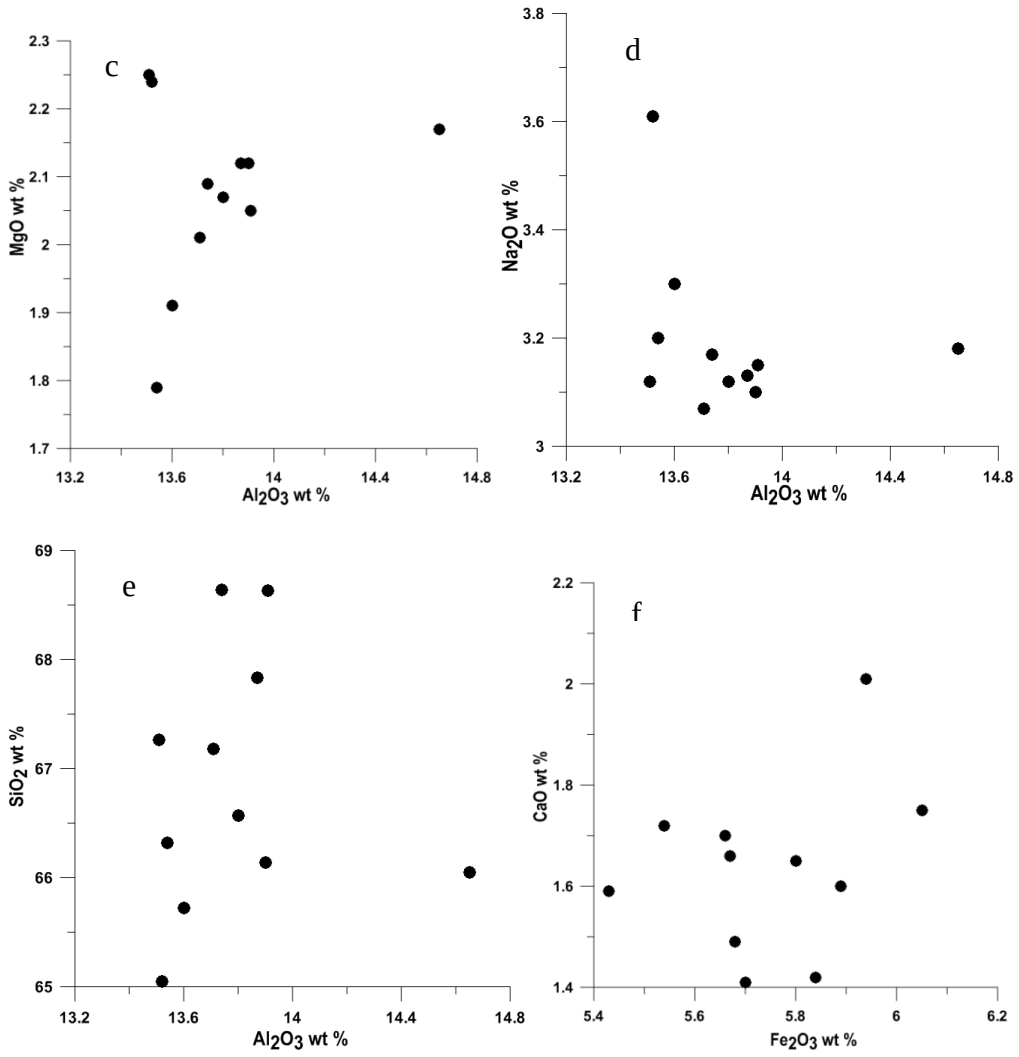

Figure 6- 29: Binary diagrams showing leached and in situ oxides vs Al_2O_3 and Fe_2O_3.

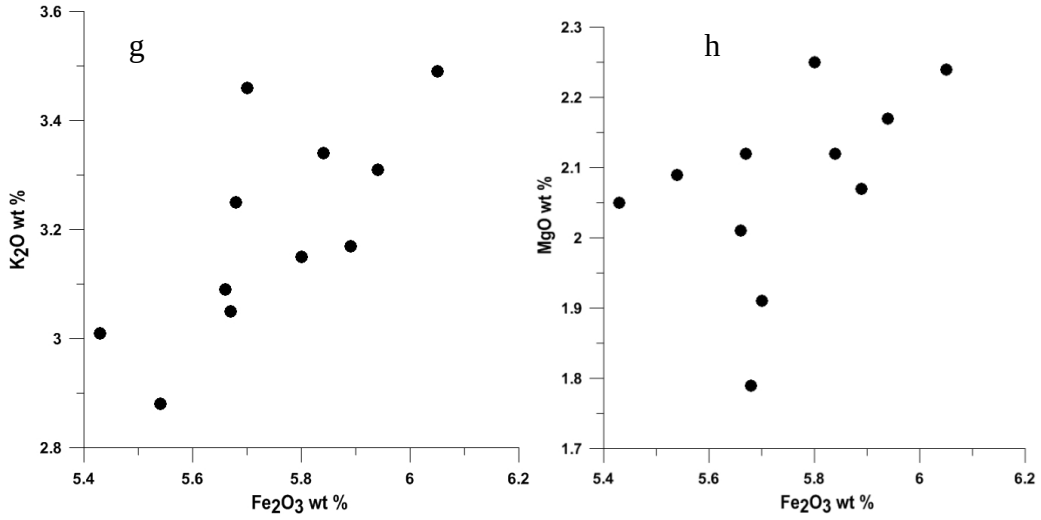

Figure 6-29: Binary diagrams showing leached and in situ oxides vs Al_2O_3

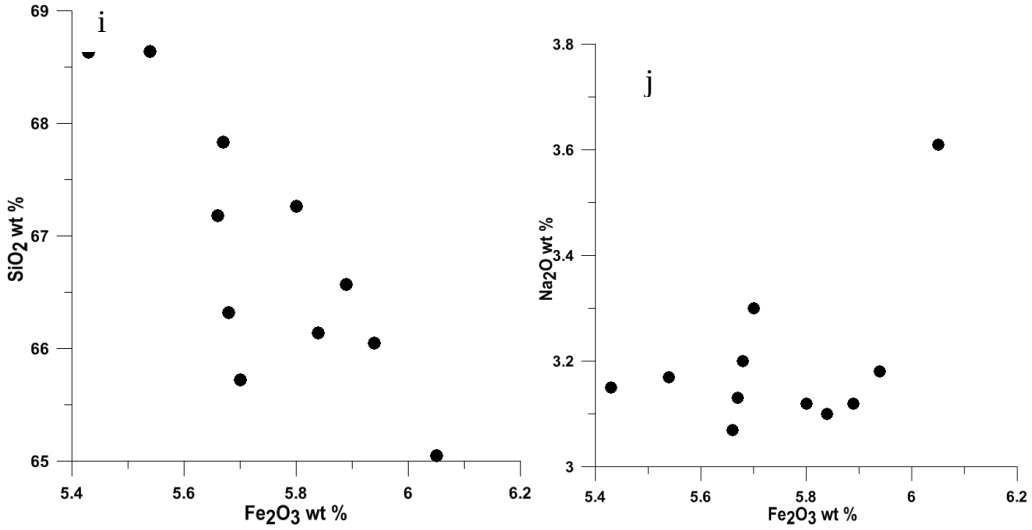

Figure 6- 29 b: Binary diagrams showing leached and in situ oxides vs Al_2O_3 and Fe_2O_3.

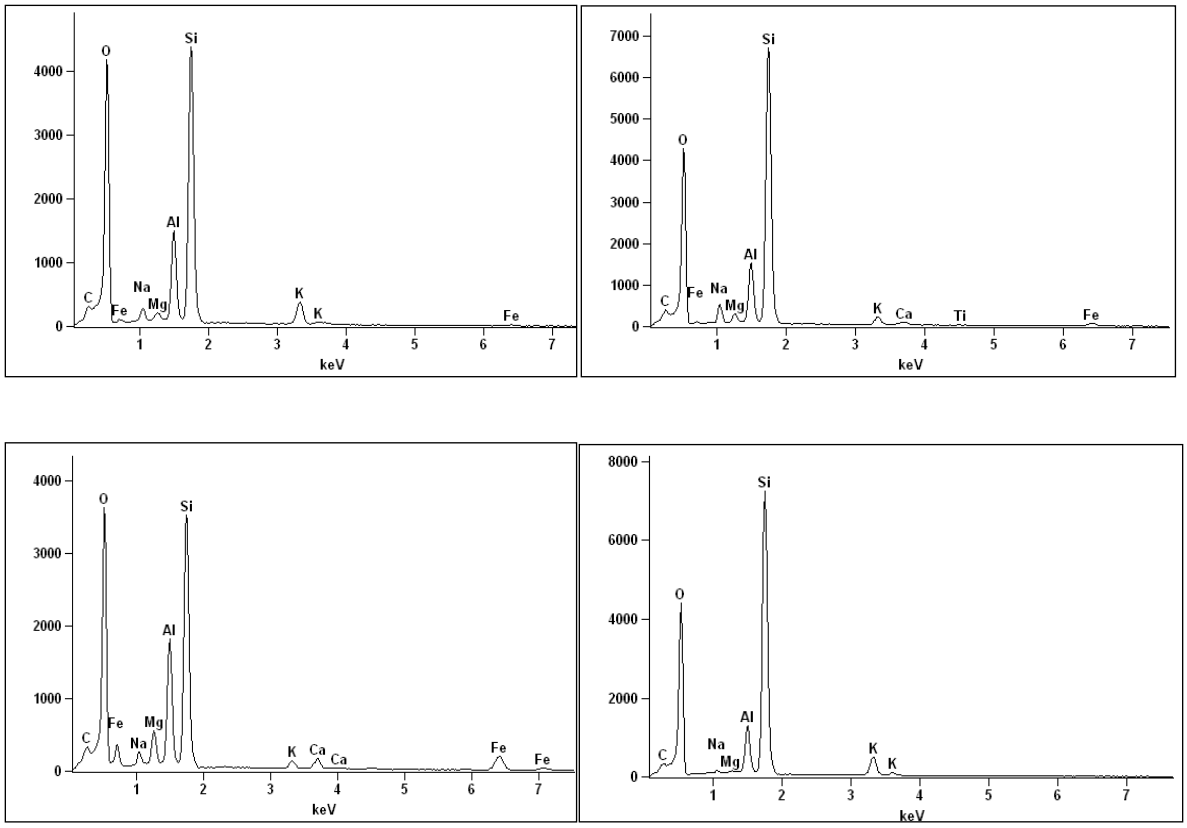

Figure 6- 30: Diagrams showing the preponderance of Si, Al, and O as major components.

6.8 Stress field evaluation

6.8.1 Overview on stress determination

Delvaux and Spener (2003) pointed out that stress analysis consider a certain volume of rocks. This volume of rock must be large enough to sample a sufficient large data set of slips along a variety of different shear surfaces. Bott (1959) assumed that slip on a plane occurs in the direction of the maximum resolved shear stress. The stress state that produced the brittle microstructures can be partly reconstructed knowing the direction and sense of slip on variably oriented fault planes. The slip direction can be derived from slickenlines and grooves. In the inversion methodology for instance, data that are used are: strike and dip of the fault plane, the orientation of the slip line, the shear sense on the fault plane, these are fault slip data. Not only fault data can be used, but also the determination of the palaeostress and neotectonic stress can be derived from other fracture planes. If there is no fault with measurable slip lines or no slickenlines; fractures, joints can be used also as stress indicators (Dunne and Hancock, 1994). Petit (1987) mentioned that for faults, one can measure directly the orientation of the fault plane and slip line and determine the slip sense (normal, inverse, dextral, sinistral).

Reagan (1973) demonstrated that in conjugate fracture systems σ_1 (compressional stress) bisects the acute angle, σ_2 is determined by the intersection between the two fractures, and σ_3 (extensional stress) bisects the obtuse angle. The slip direction on a shear plane without observable slip line can be inferred if tension fractures are associated at an acute angle to shear plane. For shear plane n_s and associated tension fracture n_t, σ_1 is parallel to the tension fracture, σ_2 is determined by the intersection between n_s and n_t, and σ_3 is perpendicular to the tension fracture. Tension fractures (plume joints, tension gashes, mineralized veins, magmatic dykes)

tend to develop perpendicular to σ_3 and parallel to σ_1. Compression fractures (cleavage planes, styloliths) tend to develop perpendicular to σ_1 and parallel to σ_3. Faulting represents a response of rock to shear stress, according to the Anderson's theory of faulting, faults that initiate as Coulomb shear fractures will form at an angle of about 30^o to the σ_1 direction and contain σ_2 direction (Pluijm and Marshak, 2004).

6.8.2. Data sets

Tables containing the different structures and their measurements, categorized by subsets (quartz veins, faults, fractures, etc.) can be seen in appendix (Tables in Appendix).

6.8.2.1 Stress determination from strike and dip measurements

6.8.2.2 Manual determination

As mentioned above, determination of paleostress or current stress can be done using two basic types of brittle structures: faults with slip lines and fractures. The outcrop seems to be dominated by systematic joints. Pluijm and Marshak (2004) stated that systematic joints reflect regional tectonic stress trajectories at the time of fracturing, whereas non-systematic joints reflect local heterogeneities of the stress field. While non-systematic joints may be important for determining rock strength and permeability, they provide no information on regional paleostress or current stress orientation.

6.8.2.3. Stress orientation derived from quartz veins

All the measurements of quartz veins regardless of their dip were plotted in the Kovak rose diagram software to derive the predominant orientation. The rose diagram (Figure 6.31) shows

the general orientation predominating in the kaolin deposit. From these observations, the following statistical analyses were computed; number of Observations: 70; mean: 326.765°; median: 320°; Circular Variance 0.233; Circular Standard Deviation 41.75°. This indicates that from the value of the median, σ_1 is oriented 320^o and σ_3 is perpendicular to it (50^o). Measurements from quartz veins can be seen in Appendix Table A.

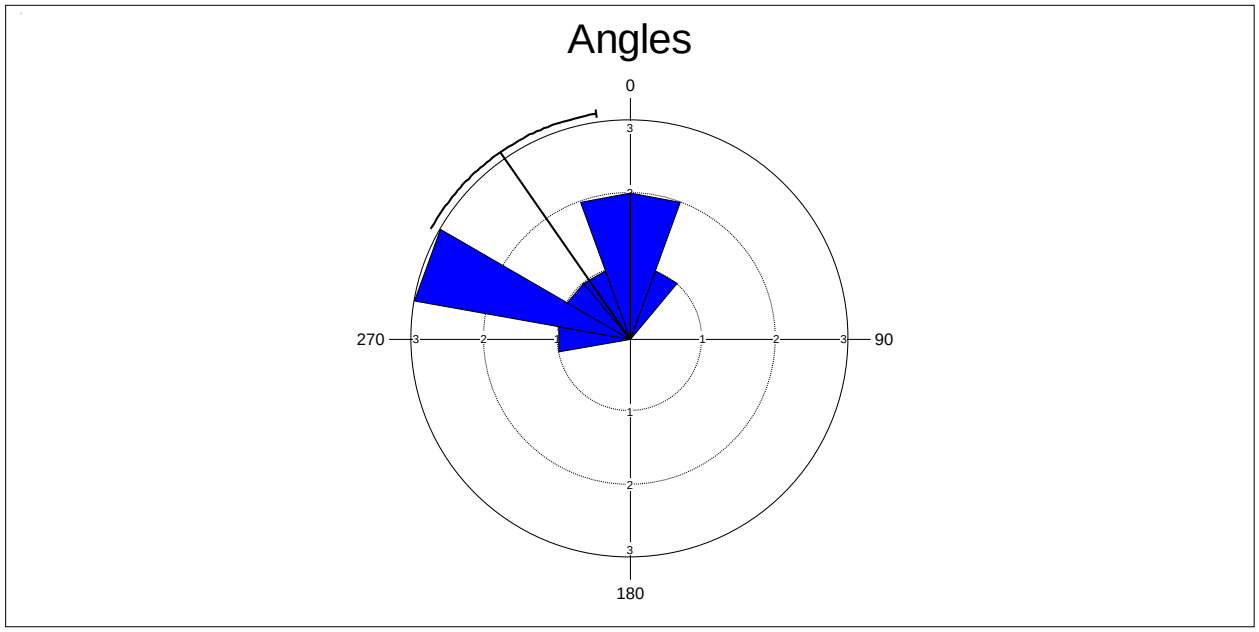

Figure 6- 31: Rose diagram showing the general trend of the quartz veins in the kaolin deposit.

6.8.2.4 Stress orientation derived from faults

From the above field observations it can be concluded that the strike slip and dip-slip regime occurred. Evidence of slickenlines (Figure 6.10 a and b) support this assertion. The rose diagram (Figure 6.32) gives the general trend for all the faults. The following statistical analyses were computed, number of observations: 69; mean value: 287.447^o; median: 285^o; circular variance 0.093; circular standard deviation 25.266°. The value of σ_1 would be 315^o if it is considered that

fault will form at angle 30^{o} to maximum principal stress according to the Anderson theory of faulting. This value of 315^{o} is almost in the same range with the median value found for the quartz veins; if 30^{o} is subtracted from 285^{o}, this will give a value which deviates more (255^{o}) from the one of the median of quartz veins. Measurements from faults can be seen in Appendix Table B.

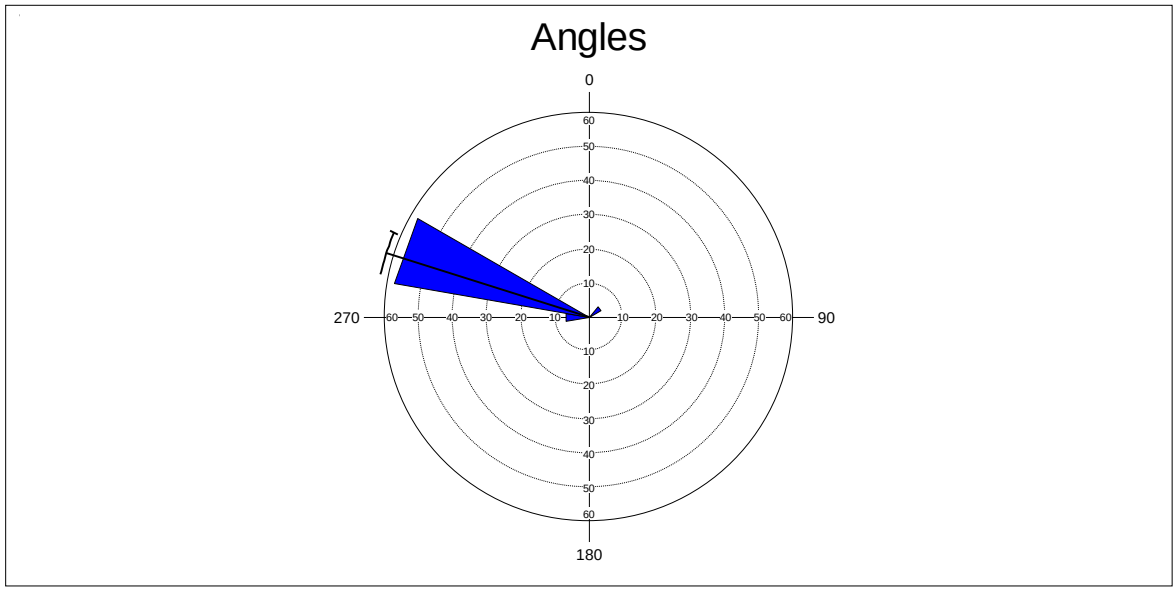

Figure 6- 32: Rose diagram showing the trend of fault in the kaolin deposit.

6.8.2.5 Stress orientation derived from fractures

Dune and Hancock (1994) noted that brittle structures other than the commonly used slickensides can be used as stress indicators, they are known as joints or fractures. The outcrop displays two types of fractures: fractures oriented almost parallel to the general trend of faults were put under the category 1, and fractures at an angle to this trend under the category 2. The rose diagram (Figure 6.33) shows the general trend of all fractures taken as a whole.

Statistical analyses gave the following results: number of observations: 154; mean value: 303.448^{o}, median: 290^{o}; Circular Variance: 0.501; Circular Standard Deviation: 67.592°. From the above results, the general trend is oriented 290^{o} (σ_1). The value 280^{o} was found for the group of category 2. These fractures probably formed during Mode I displacement; this mode stipulates that a crack opens very slightly in the direction perpendicular to the crack surface.

Cracks form parallel to the principal plane of stress σ_1, which is perpendicular to the σ_3 direction. From these observations, joints were formed in a direction perpendicular to the direction 290^{o}, σ_3 would thus be 290^{o}+90^{o}, which is equal to 20^{o}. The mean value of σ_1 for the three types of structures (veins, faults, and fractures would be (230+315+290)/3=308^{o}. Measurements from fractures can be seen in Appendix Table C.

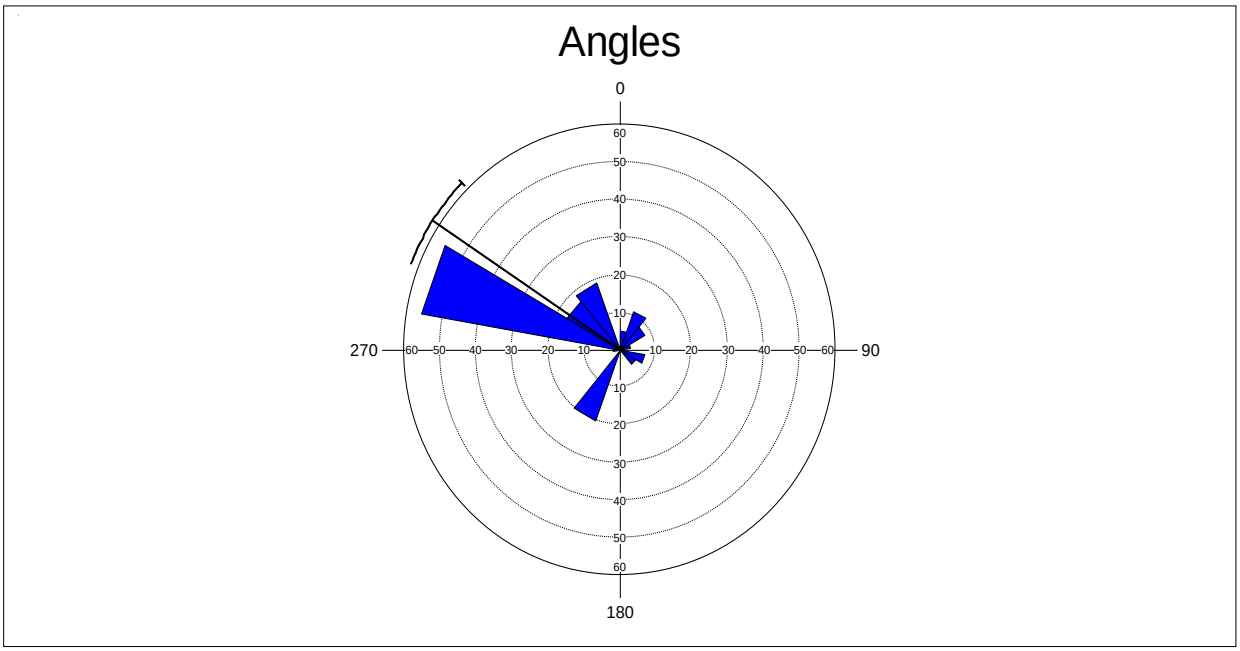

Figure 6- 33: Rose diagram showing the general trend of fractures in the kaolin deposits.

6.8.2.6 Automatic determination using Win Tensor software

Win Tensor uses the Right Dihedron developed first by Angelier and Mechler (1977) as graphical method for the determination of all possible orientation of σ_1 and σ_3. For this study the determination of the principal stresses was done with the improved Right Dihedron Method (Delvaux and Spener, 2003). Right Dihedron Method can also calculate the stress ratio R, and uses other structures like tension and compression fractures. The Right Dihedron of Angelier and Mechler (1977) could only use fault analysis. For this purpose quartz veins were all put in the category of tension fractures, whereas an attempt was made in the manual method to derive the stress differently from quartz veins and fractures respectively.

6.8.2.7 Stress derived from fault analysis

As mentioned above in the section for the outcrop study, some lineations or slickenslines were found on a breccia of quartzite along a fault. Win Tensor is developed in a sense such that different possibilities are envisaged, (fault with striae, with no striae etc.) with confidence levels such as certain, supposed, probable, unknown). The Right Dihedron method gives the last stress orientation after having eliminated incompatible data by iterative procedures. The Figures 6.34 (stereorgraphic projection) and 6.35 (Right Dihedron) show all the fault structural analysis. In the appendix of Tables, faults within a fault zone have the same readings. For a total of 6 faults, after applying the Right Dihedron method, the value of R was 0.80 and the one of R' was 0.80, the mean counting deviation was 19.5+-3.2; Shmax=156 and Shmin=066 in the WSM (World Stress Map) standard format. When $R = \frac{\sigma 2 - \sigma 3}{\sigma 1 - \sigma 3} = R'$ (stress regime index), the fault that generated the seismic activity has an extensional oblique component as can be seen in the inset at

the right bottom corner in Figure 6.35. The oblique component is justified because two types of slicken lines were found; one with a horizontal lateral movement, the other with a dip-slip movement. The combination of dip-slip and lateral movement would result in an oblique trend of slip movement. The extensional stress is oriented SW-NE and the compression stress is oriented NW-SE.

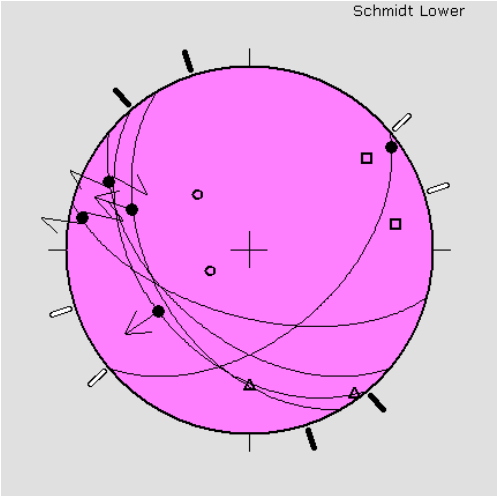

Figure 6- 34: Stereographic projection of all the five faults

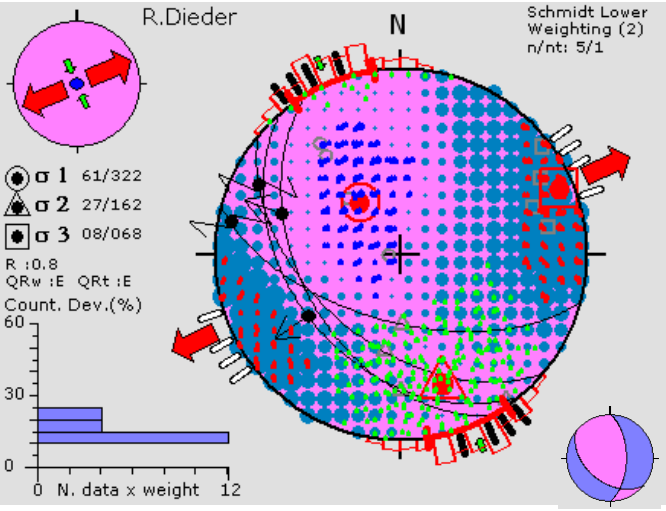

Figure 6- 35: Right Dihedron method iterative procedures for fault data showing the extensional oblique movement (combination of dip slip and strike-slip component)

6.8.2.8 Stress derived from fractures

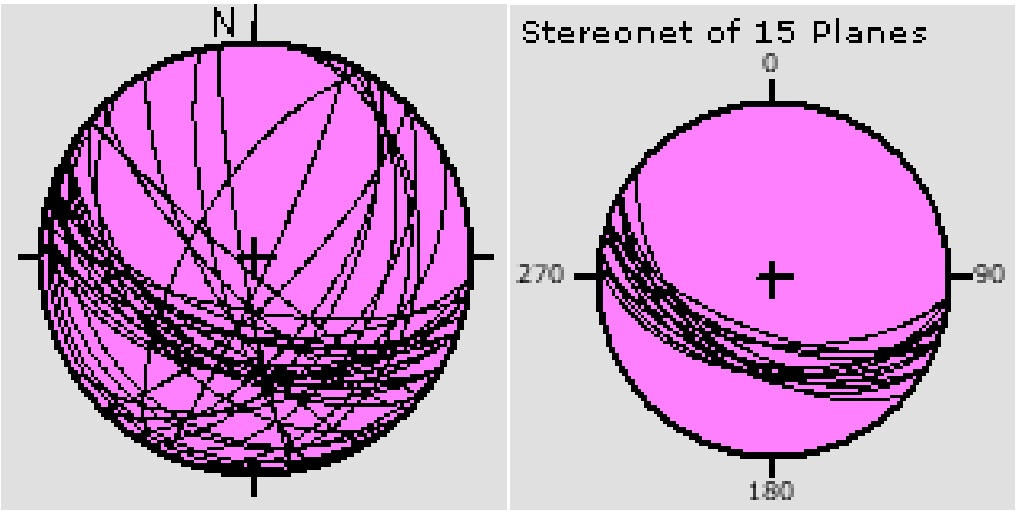

Figure 6- 36: Stereographic projection for all the fractures, on the left, the initial data; on the right after applying the right dihedron method and optimization.

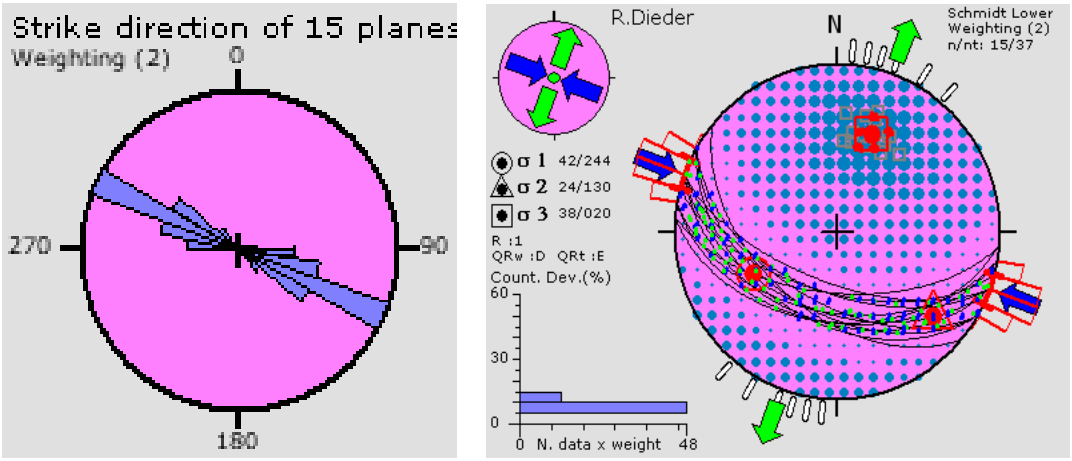

Figure 6- 37: On the left, the strike direction of 15 fracture planes; on the right final representation after applying iterative correction using the right dihedron method.

Quartz veins were assimilated to this category because Win Tensor considers them as tension fractures. Figure 6.36 (left) displays stereographic projections of all the fractures. In Figure 6.36 (right) after optimization, only fifteen fractures were found valid to be used. The strike direction

of these fifteen fracture planes is seen in Figure 6.37 (left) and the final configuration from the Right Dihedron iterative procedures can be seen in Figure 6.37 (right), and as well as the orientation of compressional and extensional stresses.

The mean value of σ_1 for the faults and the fractures: 322+244=546/2=283^o. For the manual method the obtained mean value for σ_1 was 308^o; this gives only a difference of 25^o. In all the cases, the orientation of σ_1 is NW-SE. Delvaux et al. (1997b) defined a stress regime index R' which expresses numerically the stress regime as follows:

R'=R when σ1 is vertical (extensional stress regime or normal faulting), R'=2-R when σ2 is vertical (strike-slip stress regime) and R'=2+R when σ3 is vertical (compressional stress regime). For the above analysed faults it was found that R'=R (0.80), this is typical of the extensional regime.

6.8.3 Rotational optimization and stabilization around stress axis

The works of Delvaux and Spener (2003) on stress inversion methodologies have outlined the importance of Tensor stabilization through Rotational Optimization. This method is based on the testing of a great number of different stress tensors, with the aim of minimizing a misfit function. The whole range of orientations for the three stress axes (σ_1, σ_2 and σ_3) and the stress ratio R has to be tested to find the minimum value of the misfit function. The minimization function has the following form:

$$Fj=\frac{\sum(Fj\ (i))\text{xW(i)}}{n\ X\ \sum W(i)}$$

W(i) is the weight of the individual data

Fj (i) is the function to be minimized

Delvaux and Spener (2003) indicated that the Rotational Optimization procedure consists in a controlled 4D grid search that involves a series of successive rotations of the tensor around the three principal stress axes (σ_1, σ_2 and σ_3: Figure 6.38 a, b, c). In each case, the rotation angle is determined for which the misfit function has its minimum value.

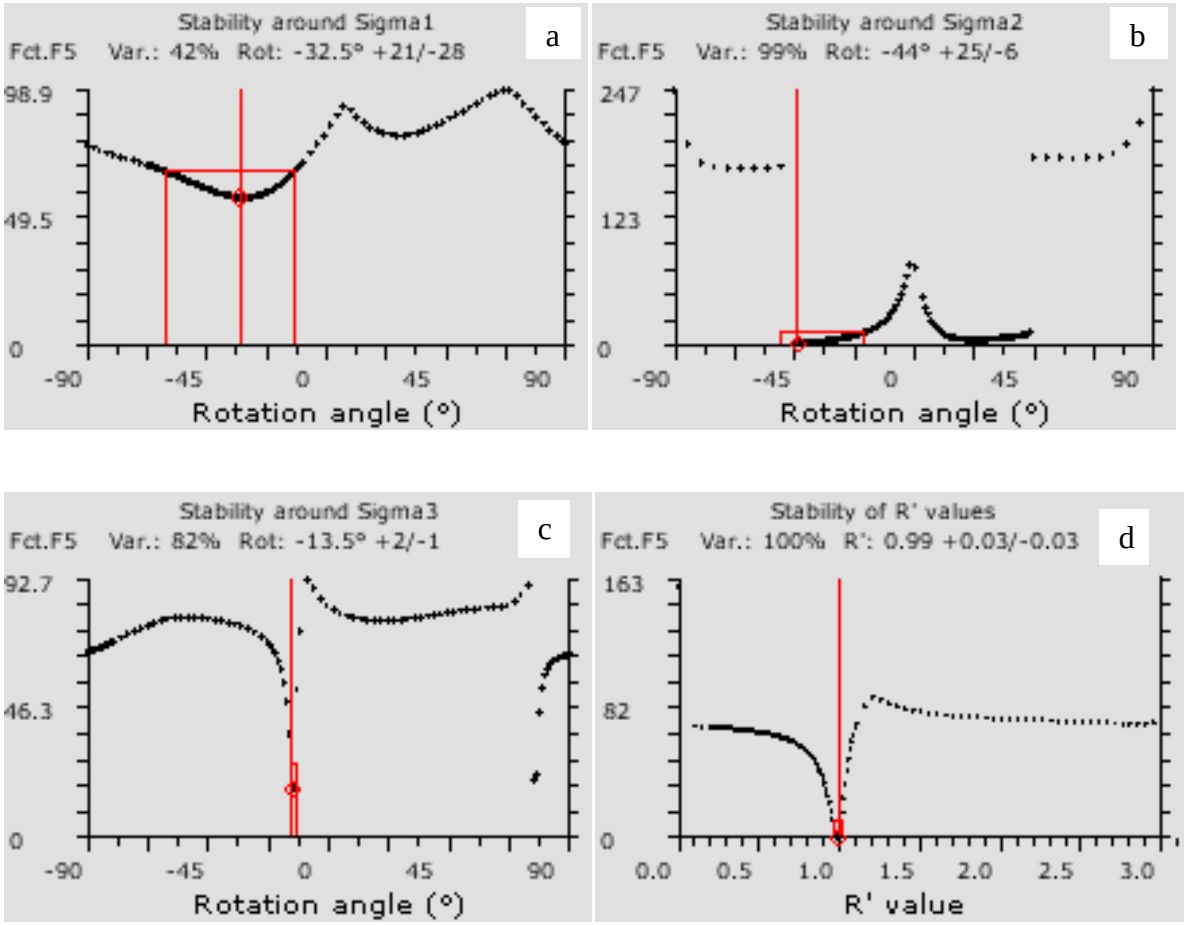

Figure 6- 38: a) rotation around σ1, b) rotation around σ2, c) rotation around σ3, d) stability of R'

The Tensor is rotated each time around one stress axis within a range of more or less 45°, which is verified in Figure 6.38 a, b and c. After rotation around the three stress axis, the process is repeated several times until the tensor is stabilized. Further rotations of the stress axis or modifications of the stress ratio do not improve the results. The tensor itself has been stabilized

because of the value of R' that must vary between 0 and 1, this value is equal to 0.99 (Figure 6.38 d).

Seismic assessment risk

The study of neotectonics in the Eastern Cape can also be used for seismic risk assessment. This is necessary especially in identifying areas which are not good for storing nuclear wastes produced in South Africa. This seismic risk assessment was deduced from the map of seismic epicenters with their magnitudes downloaded from IRIS browser (Figure 6.38).

Seismic epicentres were joined by lineaments, since epicenters of intracontinental earthquakes are concentrated on lineaments (e.g. Meisser and Wever, 1986). It appears that Grahamstown and the entire southern, eastern, and northern part of the Eastern Cape Province is a zone of seismic risk (Figure 6.39). This is an indication that all these zones are not good for nuclear waste storage, avoiding thus groundwater contamination. Figure 6.39 displays seismic epicentres, areas north of Queenstown are best sites if nuclear wastes are to be stored, since these areas are located in a seismically static and inactive zone. Besides the Eastern Cape Great Lineament that was highlighted in Chapter 4, it can also be mentioned that both the Grahamstown Fracture and the Fort Beaufort Fracture are neotectonic domains in the southern neotectonic belt. In Figure 6.39 the alignment of seismic epicentres coincide well with the occurrence of these fractures. They are to be seriously considered regarding neotectonics in the Eastern Cape Province. Most of the seismic events have shallow hypocentral distance, which characterizes better intraplate continental seismicity. It appears from Figure 6.40 that most of the depths from which the earthquakes were generated do not go over 15 km below the earth surface.

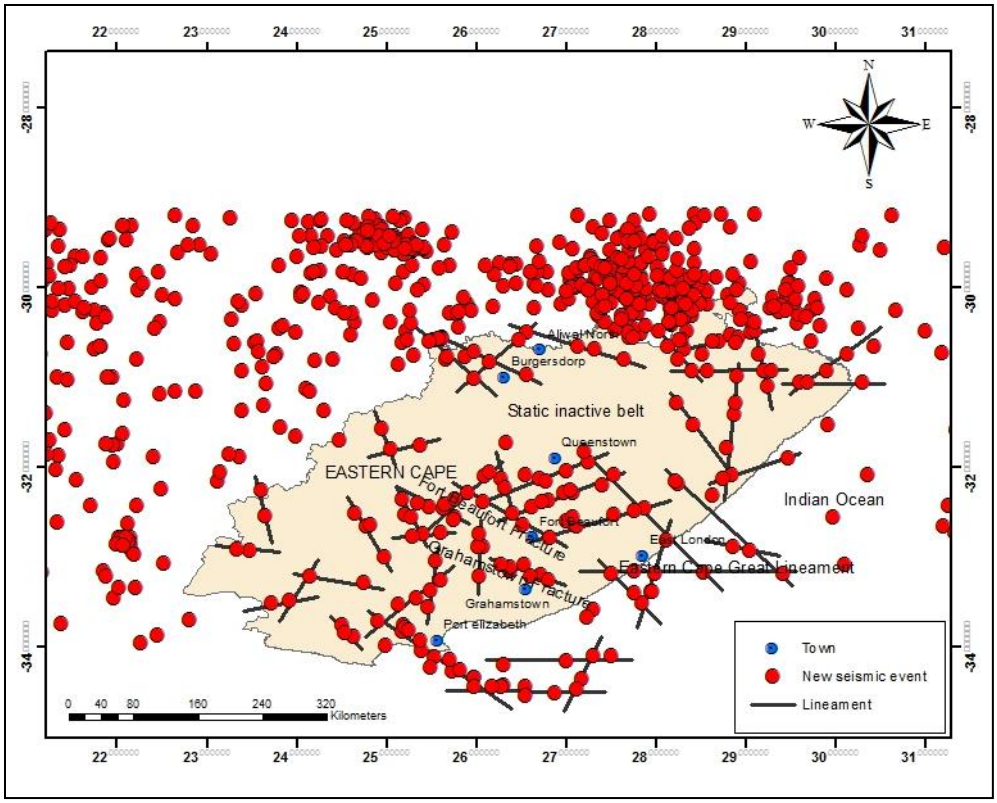

Figure 6- 39: Map of seismic epicentres in South Africa, note the southern part of the Eastern Cape displaying a zone of seismic risk. (Source of epicentres: IRIS Earthquake Browser).

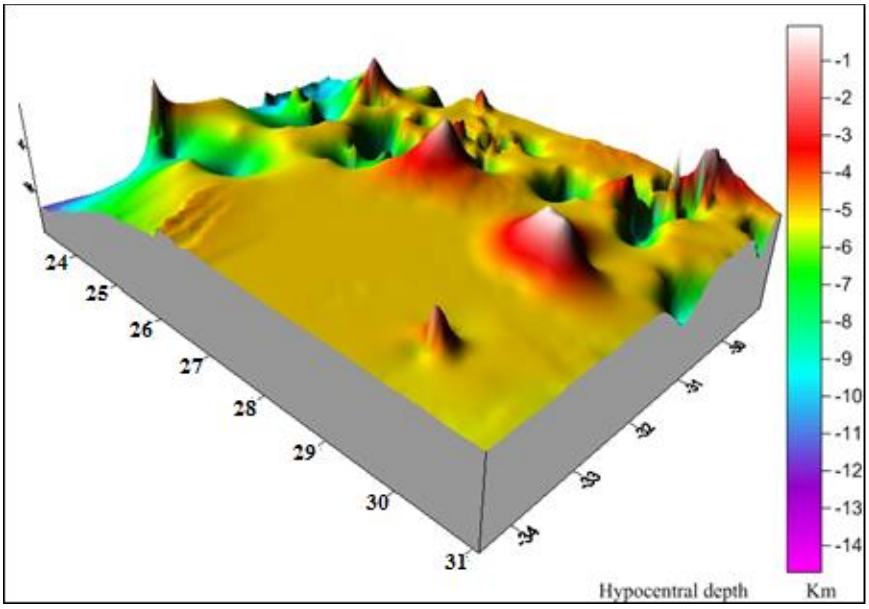

Figure 6- 40: Hypocentral depth of the Eastern Cape and surrounding areas (Source of data: IRIS. The sign – indicates depth below the earth surface)

6.9. Summary

Different rocks such as volcanic rocks may undergo alteration, and this may lead to the kaolin formation. However field observations on the Grahamstown kaolin deposits in the Eastern Cape Province have enabled to conclude that these kaolin deposits derive from the weathering of the Dwyka tillite of the Karoo Supergroup because:

1. Enrichment of granite breccias and feldspar in the Dwyka tillite indicates that a potential source for the formation of kaolin deposit exists;
2. The extensional structures acting as conduits for water migration and quartz veins as barriers accelerate the chemical weathering of feldspars in both matrix and granite breccias, i.e. structures play an important role in kaolin formation;
3. There was a clear horizontal compression and vertical or subvertical extension in the Grahamstown region.
4. It is further suggested that it is important to map out the structures including faults, joints and quartz veins for the exploration of kaolin deposit in the Grahamstown area and other regions with Dwyka tillite in South Africa.

Not only breccias of quartzite and granite are present, but also breccias of quartz sandstone and metamorphic rocks. These rocks possibly derived from the Cape Fold Beld, elongated crystals of quartz showing plastic deformations were seen at the microscope.

XRD analyses have also indicated that other minerals are found within the tillite or the kaolin. Among these minerals one can quote the orthoclase, clinochlore, muscovite; the granitic breccias are probably muscovite granites. The XRD patterns from the fresh tillite, the more or less

weathered rock, and from the kaolinised rock are similar. The difference resides in the intensity counts, the more the rock is weathered the low the intensity is, and vice-versa.

Macroscopic and microscopic observations depict contrasting images. At the macroscopic scale, only breccias within the tillite show extensional fractures, but at the microscopic scale extensional fractures are seen within the tillite matrix. These fractures in the matrix initiate at the contact matrix-breccias. It is clearly appears that breccias are more brittle than the matrix, because the extensional fractures can be only seen with the naked eye in the breccias. This difference in terms of competence between the breccias and the matrix has never been reported.

The weathering differs from east to west; the eastern part is more weathered than the western part. The presence of many fractures allows the water flow, and many quartz veins trap the water, which accordingly, intensify the weathering process. The weathering or alteration is possibly be of two origins; meteoric and hydrothermal. However the meteoric weathering is more predominant.

The neotectonic fractures and faults certainly derive from seismic activity, the Grahamstown area is up to now seismically active. The fractures and faults orientations have been measured, and the measurements were analyzed using Win-Tensor program. All the measurements indicated that the region of Grahamstown is undergoing extensional combined strike-slip and dip-slip components. Discrete horizontal slickenlines were found on a quartzite breccias, and vertical striae showing vertical displacement on a fault surface. A model of kaolinisation is proposed in Figure 6.41.

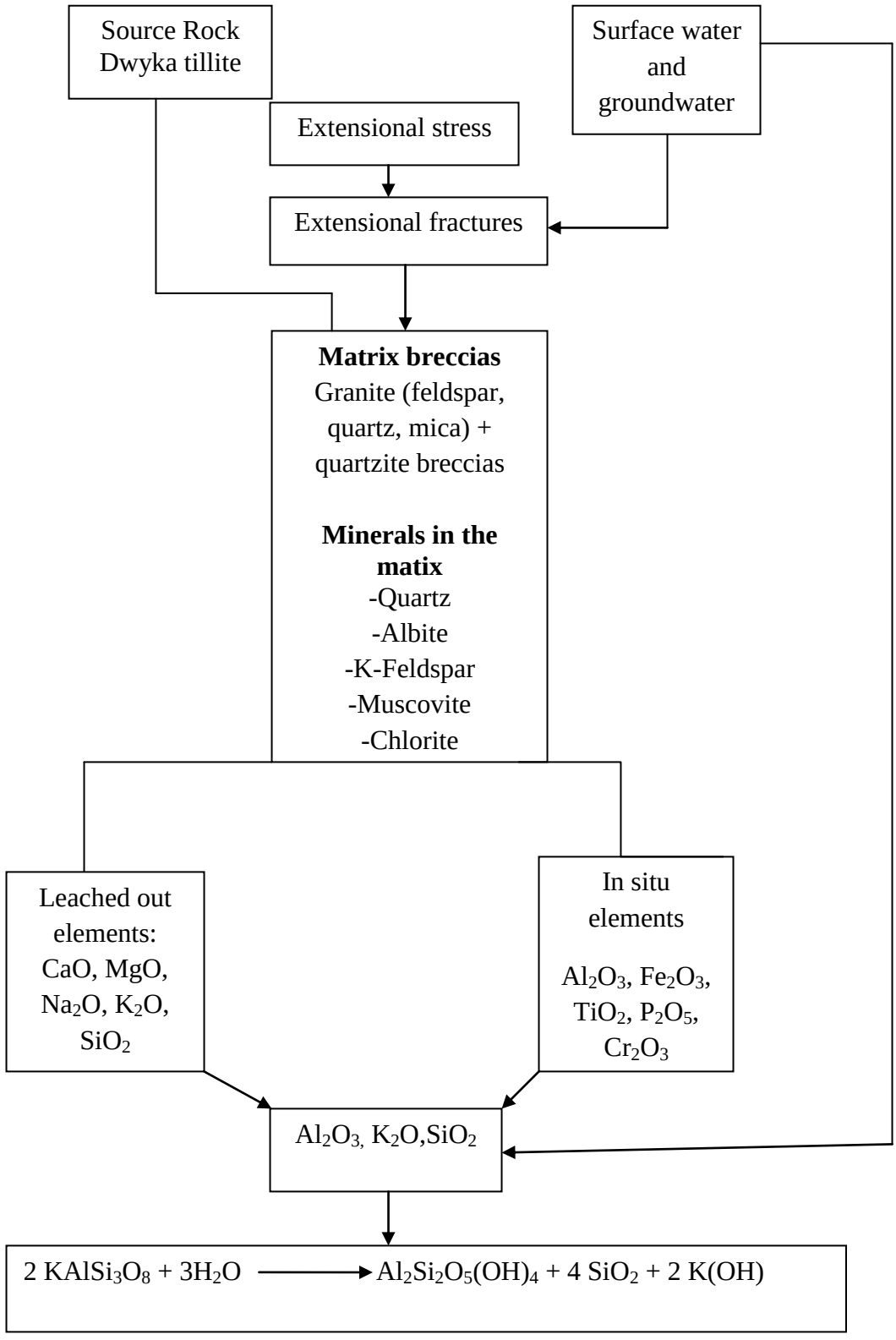

Figure 6- 41: Possible model for transformation of feldspar into kaolin from the Dwyka tillite.

7. THE EASTERN CAPE PROVINCE NORTHERN NEOTECTONIC BELT, HOT SPRINGS GEOPHYSICAL SIGNATURES

7.1 Introduction

As mentioned previously, the Eastern Cape Province is surrounded by three neotectonic belts that almost surround it. The eastern neotectonic belt was qualified as the high level neotectonic domain through remote sensing in terms of abundance of lineaments. However, a careful examination on the term "neotectonics" would undoubtedly indicate that the true neotectonic activity strictly speaking occurs in the northern part of the Eastern Cape Province. First, this region is located in the Kokstad-Koffiefontein seismic belt that runs in an east-west direction; second, seven hot springs (Figure 7.1) are present in this remarkable seismic belt of South Africa, near the border with the country of Lesotho.

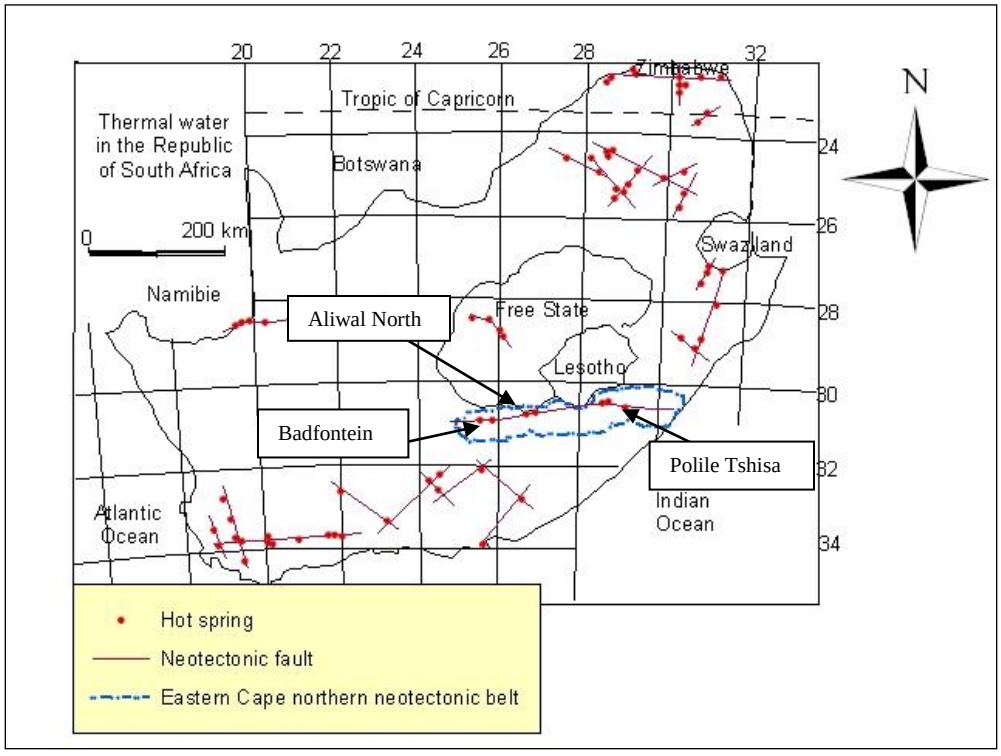

Figure 7- 1: Hot springs in the Republic of South Africa (digitized from Kent, 1949)

Another important thing is that in the Kokstad-Koffiefontein seismic belt, in the town of Smithfield, the local power station might have been built on an active fault (Andreoli pers. comm.). The Orange River tunnel intersected with much pain a huge aquifer that flooded the place. Moreover, this can also be corroborated by the seismic hazard map of South Africa (Figure 7.2) that clearly shows that the area below or south of the country of Lesotho is in a zone characterised by seismic hazards.

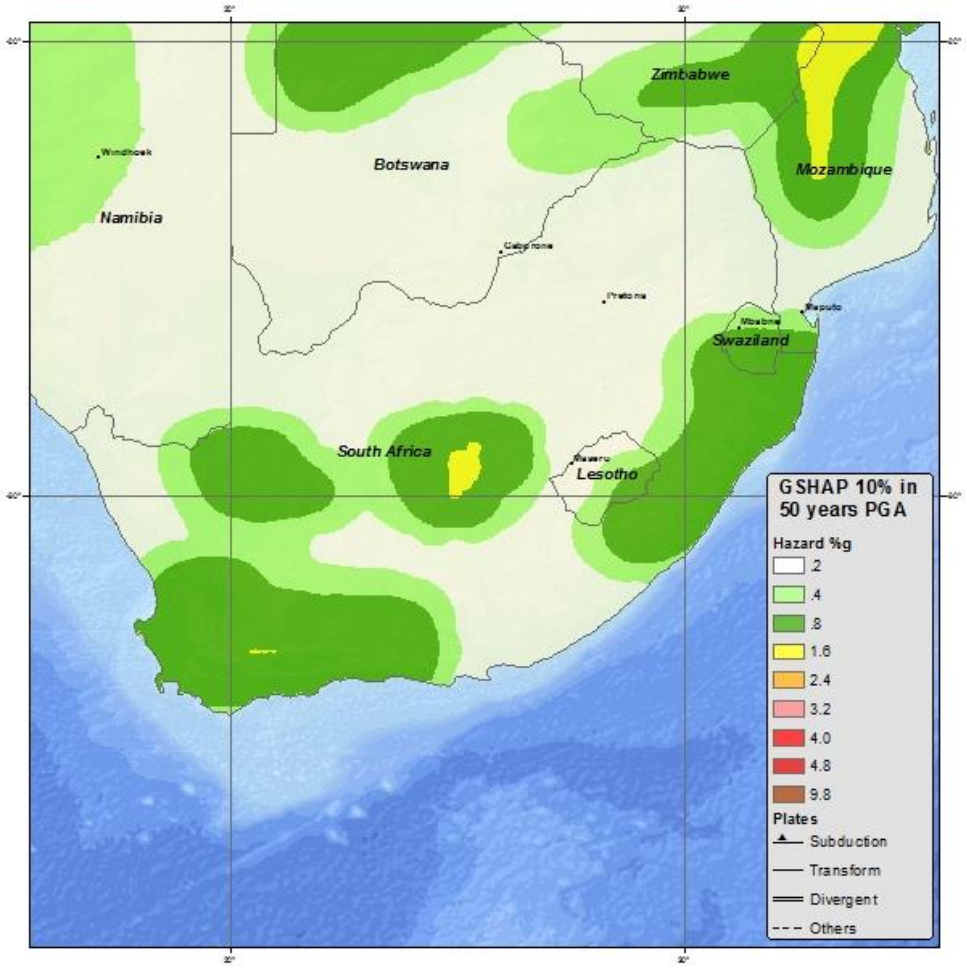

Figure 7- 2: Seismic hazard map of South Africa (http://earthquake.usgs.gov/earthquakes/world/south_africa/gshap.php).

In the Eastern Cape northern neotectonic belt, Olivier (1975) found that in the Orange-Fish tunnel flooding occurred after an abnormally well-developed fissure-zone was intersected approximately 550 m south of the shaft 2. The inrush of water was associated with the collapse of the tunnel roof, as part of the roof major fissure was exposed by the fateful blast. He noted however that influence of earthquakes on the pattern of semi-diurnal tidal fluctuations is of special interest as regards the flooding problem. The flow of the central thermal spring at Badfontein increased markedly for a period of at least 3 months after a local earthquake was felt during August 1956 (Whittingham, 1970).

During the Ceres-Tulbagh earthquake disaster of 1969 in the Western Province, tremors affected the tunnel area; displacements of 3 cm, 4.6 cm, and 7.6 cm on the graphs in some boreholes after some earthquakes of magnitude 6.5 and 6.2 in 1969 and 1970 were noted (Olivier, 1975).

This neotectonic belt is for the above mentioned facts, a zone of potentially high yield wells in the Karoo aquifers in the Eastern Cape Province. For further investigations related to groundwater, three hot springs were chosen to conduct geophysical surveys namely magnetic, electromagnetic, and by radiometric methods.

7.2 Geophysical survey

In a reference guide on geophysical techniques (1993) documented by the Eastern Research Group from Lexington in the U.S.A., it was reported that geophysical techniques are used to assess the physical and chemical properties of soils, rocks and groundwater based on response to either (1) various parts of the electromagnetic (EM) spectrum, including gamma rays, visible light, radar, microwave, and radiowaves, (2) acoustic and/or seismic energy, or (3) other potential fields such as gravity and the Earth’s magnetic field. On the other hand it was indicated

that the greatest benefits of geophysical methods come from using them early in the site characterization, since they are typically non-destructive, less risky, and require less time and cost than using monitoring wells.

7.2.1 Magnetic method

The magnetic survey is a technique that measures the magnetic field of the Earth; this is based on the fact that magnetic variations identify structures and anomalous geological bodies. The presence of ferrous metals can be detected by variations they create in the local magnetic field. Proton precession magnetometers (Figure 7.3) are used by precession of spinning protons after a coil is energized momentarily to measure the Earth's total magnetic field.

Figure 7- 3: Proton precession magnetometer that was used for data acquisition (Polile Tshisa hot spring)

On the hydrological point of view, the magnetometry is used to locate buried metal drums that may be the sources of soil and groundwater contamination (e.g. Benson et al., 1984). Magnetic techniques are not very detailed in groundwater studies because of lack of groundwater magnetic signature. However, it can be highlighted that magnetic surveys have been used to identify faulting and other locations of crustal basement weakness that may represent preferential fluid flow paths. Results of magnetic surveys are usually presented as line profiles or magnetic anomaly maps.

7.2.2 Electromagnetic methods

Electromagnetic techniques are used in groundwater studies mainly for mapping and characterizing lateral and vertical changes in conductivity, using the frequency domain electro-magnetic (FDEM) along line profiles either as single lines or grids of data (e.g. Mc Neill, 1986; Palacky et al., 1981). FDEM geophysical measurements sense the subsurface response to sinusoidal electromagnetic fields at one or more transmitted frequencies. Results of electromagnetic surveys are then presented as contour maps of conductivity and 2-D geoelectric sections showing differences in conductivity along a line profile. Gordio et al. (1998) have indicated that changes in conductivity are often associated with differences between lithological sequences and over disturbed ground such as faulted or mineralized zones. Reynolds (1997) used electrical and electromagnetic surveys in groundwater investigations. It can also be mentioned that electromagnetic methods in groundwater studies are of particular importance since they allow making correlations between some hydrogeological properties such as porosity and permeability to electrical conductivity. EM (electro-magnetic) methods are important because they are able to give signatures that are characteristics of the type of soil and rock, the porosity, saturation, and electrochemistry of the fluids in the pore space (e.g. Benson et al., 1984).

Generally a transmitter coil (Figure 7.4) generates a sinusoidal electromagnetic field that induces eddy currents in the Earth (Figure 7.5). A receiver coil intercepts both the primary and the secondary electromagnetic field created by the eddy current loops and produces an output voltage. This voltage is corrected for the primary field and the loop geometry and spacing. This voltage is then linearly related to subsurface conductivity.

Figure 7- 4: One of the coil (orange circumference) that was used to acquire electro-magnetic data

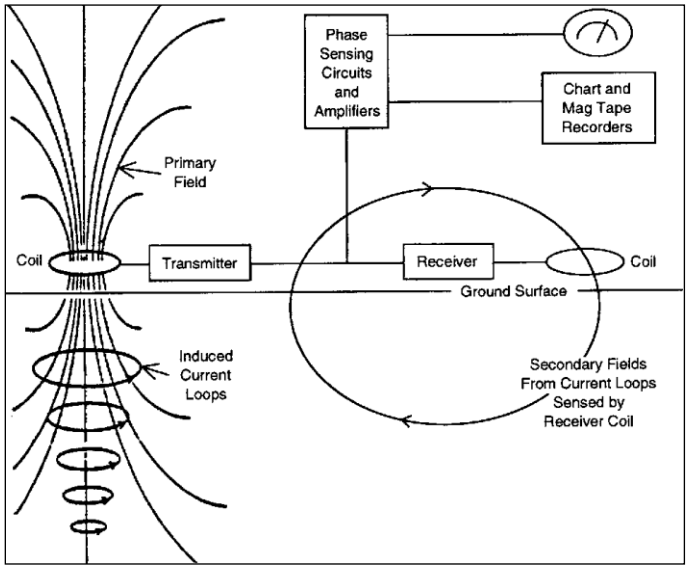

Figure 7- 5: EM principle of operations (from Benson et al., 1984)

7.2.3 Radiometric method

The radiometric method and data acquisition considered here is exclusively for gamma rays. Gamma ray spectrometry surveys detect and map natural radioactive emanations called gamma rays from rocks and soils. Although there are many naturally occurring radionuclides, only those from uranium (U), thorium (Th), and potassium (K) give gamma rays of sufficient energy and intensity to be detected due to the relative abundance of these three elements in crustal rocks. The basic purpose of the surveys is to determine either the absolute or relative amounts of U, Th, and K in the surface rocks and soils.

Potassium is associated with numerous minerals in sedimentary formations, including clays and feldspar. Potassium and sodium are important ions in groundwater, and are used for the assessment of control on quality for samples. They are used in the identification of the groundwater source. Most often thorium is associated with heavy minerals, higher levels are present in certain geological materials such as monazite sands; all naturally occurring thorium is present as thorium 232. Thorium adheres very lightly to soil particles, with concentrations in sandy soil generally more than 3,000 times higher than in interstitial water. It is less mobile in clay soils. Because of its low solubility, thorium is not generally a major contaminant in groundwater (Human Health Fact Sheet, 2005).

Mahesh (2001) indicated that in groundwater uranium is present both in dissolved and particulate form due to minerals such as uraninite, pitchblende and cornalite or as secondary mineral in the form of complex oxides of silicates, phosphates, vanadates etc. Uranium in the earth's crust is found as oxides (UO_2), (U_3O_8). Ebbs et al. (1998) mentioned that in soil uranium is primarily present in the +6 oxidation state as the uranyl cation (UO_2^{2+}). Babu et al. (2007) reported that uranium concentration in groundwater depends on lithology, geomorphology and other

geological conditions of the region. Uranium is much more soluble than K and Th, and because of its solubility, it is found at fractures, oil/water contact. Uranium concentrations in the water depend on some factors such as uranium content in the host aquifer rock, and its chemical constituents, presence of oxygen and its complexion agents, chemical reactions with ions in solution, and nature of the contact between uraniferous minerals in water (e.g. Hess et al., 1985). The recommended World Health Organization guideline value of uranium in drinking water is 0.015 mg/L.

For K, U and Th measurements, the RS-125 gamma ray spectrometer/scintillometer (Figure 7.6) is the state of the art instrument that was used in this project. Gamma ray spectrometer detects gamma rays from all sources in the total count channels, and those which are linked to uranium, thorium and potassium in three channels respectively.

Figure 7- 6: The RS-125 spectrometer

The RS-125 allows the user to produce profiles of the total count data in the Search, Scan or Assay modes. Data can be from a continuous drill core or from a survey with GPS data. In this project the GPS data were used. Data were acquired in assay mode providing the concentrations of K, U and Th with display in ppm of K, U and Th.

7.3 Polile Tshisa hot spring

7.3.1 Field observations

The water of this hot spring wells up at three different places (Figure 7.7 a) separated by a distance of almost thirty centimeter aligned in a direction of N 75^{o} with a quartz vein nearby. The area itself has outcrops of coarse grains sandstones of the Molteno Formation in the Karoo Supergroup. It is characterized by intense weathering (Figure 7.7 b, c, d, e, f) marked by a kaolinisation. This weathering indicates an intensive surface water circulation, which is a major source of recharge. The water possibly goes deep down below, and is discharged through the springs. The high degree of weathering has made some of the original rock to completely alter as can be seen in some photographs in Figure 7.7 e. The sandstone layers have a thickness that varies from 2 cm to 5 cm. A druse of quartz full of impurities colouring them in brown was seen near the spring (Figure 7.8 left) and because of weathering, crystals of quartz are easily being loosed up (Figure 7.8 right).

Two sets of centimetric quartz veins cross cutting each either (Figure 7.9) were found on the bed of a non-perennial river near the hot spring; the first set which is the old one if the cross cutting relation is applied, has a strike of N 320^{o}, and the second one which is the latter one has a strike of N 245^{o}. The two sets are almost perpendicular, they occur in sandstones with few intercalation of shale, both weathered. At this place the beds strike N 250^{o}, dipping 15^{o} and having a dip

direction of N 340^{o}. Similar quartz veins have been found some 10 km north of the Polile Tshisa hot spring near the town of Matatiele (see Figure 4.7).

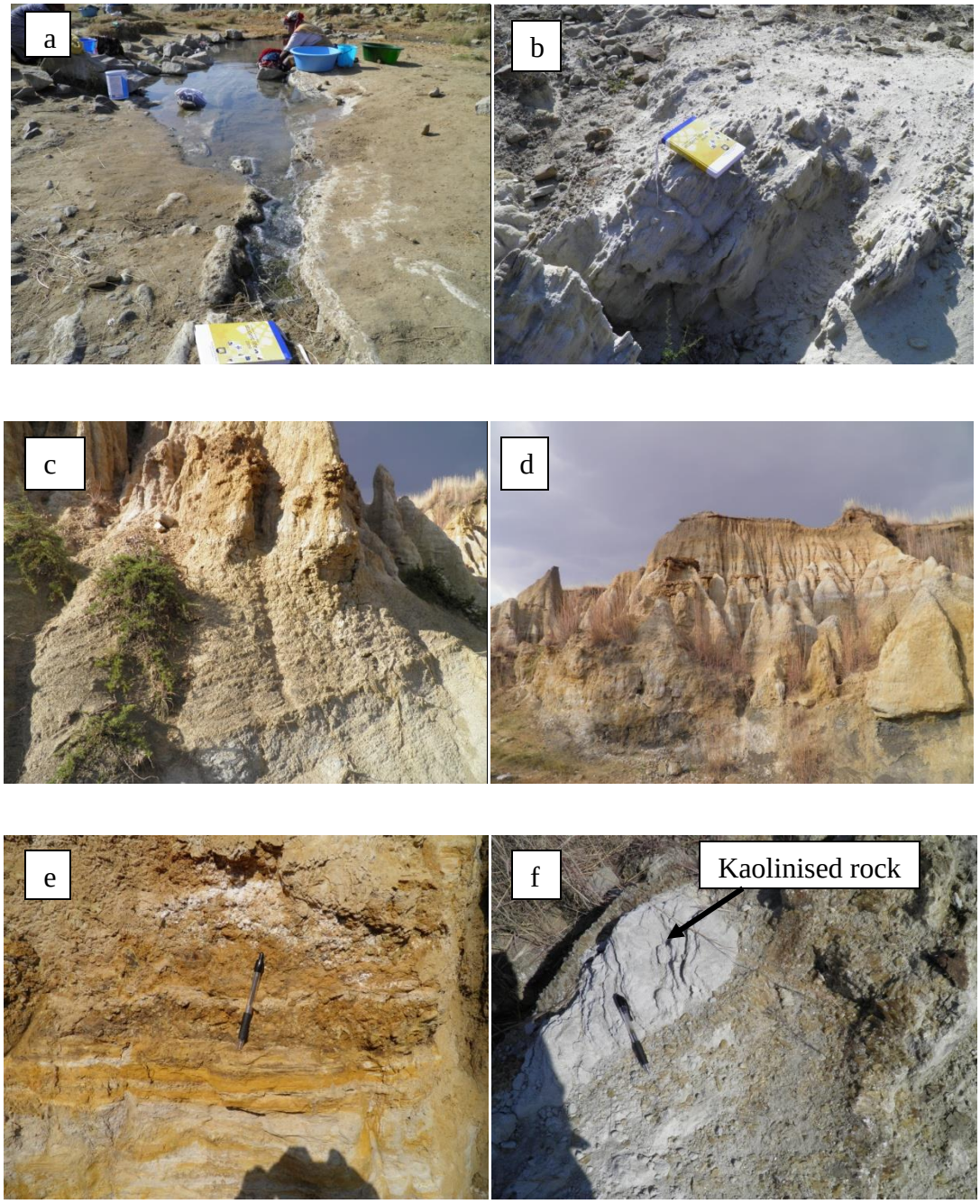

Figure 7- 7: a) Polile Tshisa hot spring; b, c, d, e, and f: highly weathered kaolinised sandstones

Figure 7- 8: left) Druse with quartz crystals; right) loosed quartz crystals due to weathering

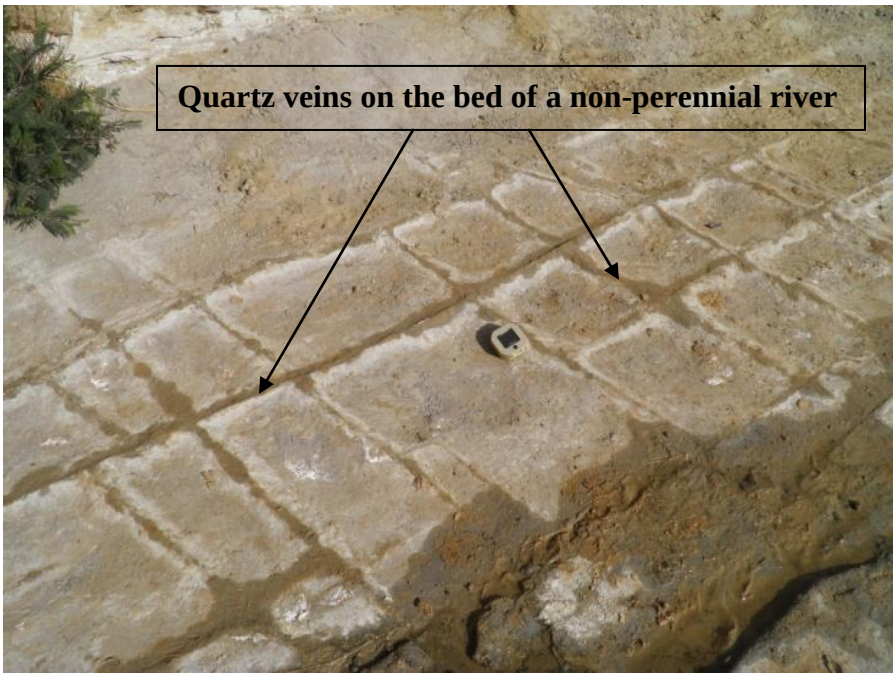

Figure 7- 9: Two set of systematic quartz veins cross cutting each other, occurring in the river bed.

7.3.2 Magnetic survey at Polile Tshisa hot spring

The magnetic survey (see sample in Appendix Table D) was conducted around the Polile Tshisa hot spring. This survey was complicated by uneasy accessibility marked by the presence of gullies (Figure 7.10) and some few constructions in the vicinity. Data acquisition was carried out using a Cesium vapour high precision magnetometer (Geometrics 859) along four lines

(NW-SE, N-S, NE-SW); these lines can be seen in Figure 7.11. The magnetic map was produced first at a grid cell size of 1 m in order to see all the high frequency signals. The grid cell size was then changed to 14 m so that a generalized complete image could be visualized making it easier to give a plausible interpretation (Figure 7.12). The N-S magnetic line at the right hand side has magnetic high values in the southern area. This might be related to the occurrence of a dolerite dyke, which is a good indicator for drilling in order to generate a potential high yield well.

Figure 7- 10: Terrain around the Polile Tshisa hot spring with gullies making difficult data acquisition

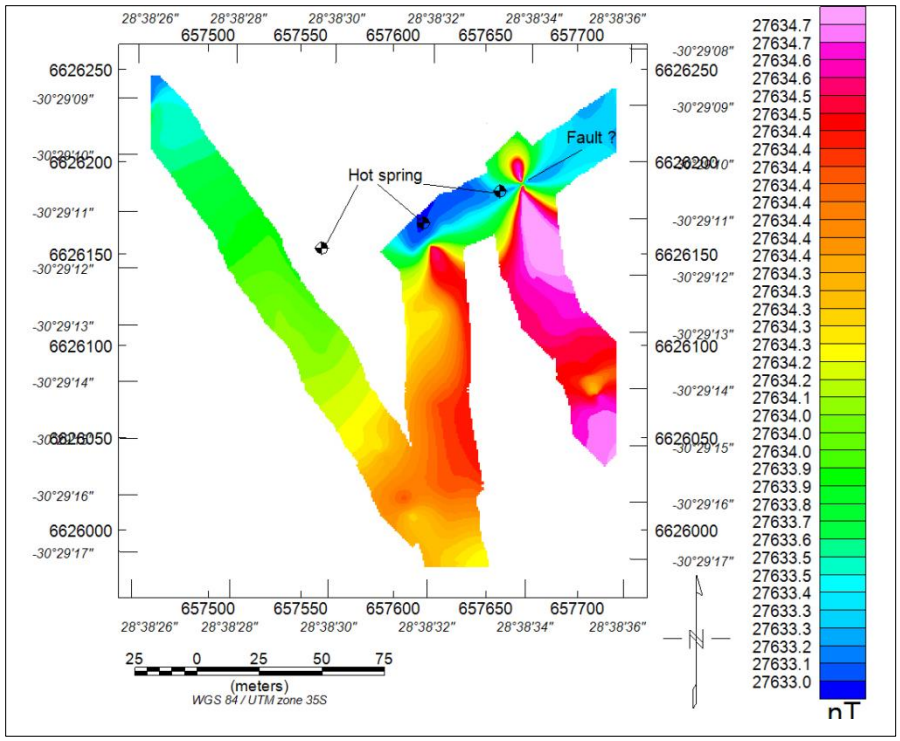

Figure 7- 11: Magnetic map produced at a grid cell size of 1m

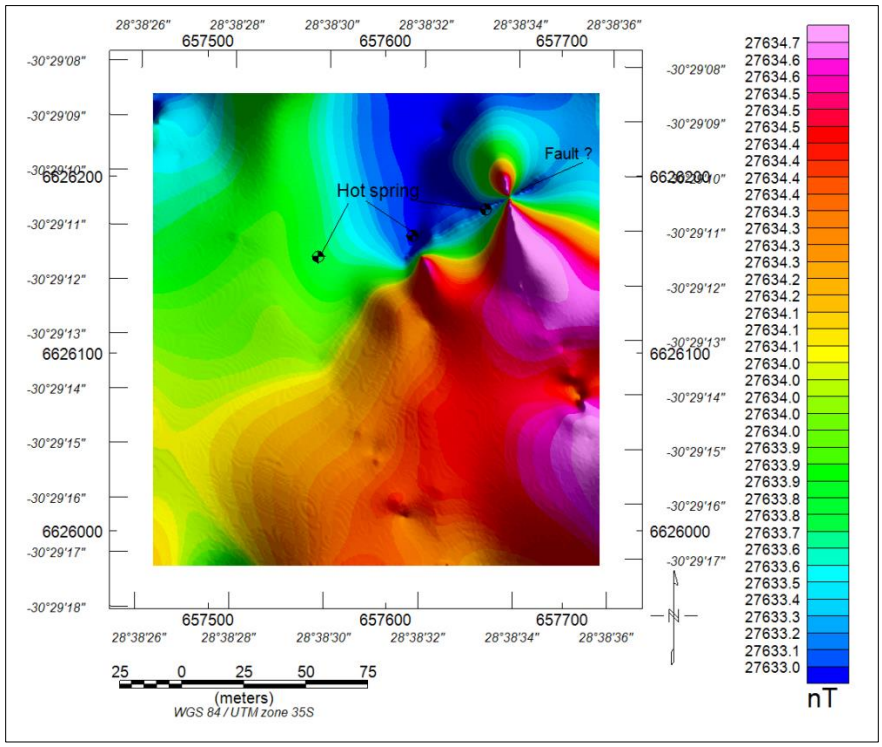

Figure 7- 12: Magnetic map derived from Figure 7.11 but at a grid cell size of 14 m

Three magnetic profiles were extracted from the map in Figure 7.12. The first line SE-NW has a profile that is almost flat at the right side (Figure 7.13). It shows an increase from 10 m reaching more than 27634.4 nT at approximately 28 m. At this point it shows a slight decrease, but in general the profile remains constant up to 200 m. The increase in signal at the left side at approximately 28 m is possibly related to a fault resulting in the block to the right having moved up relative to the other block.

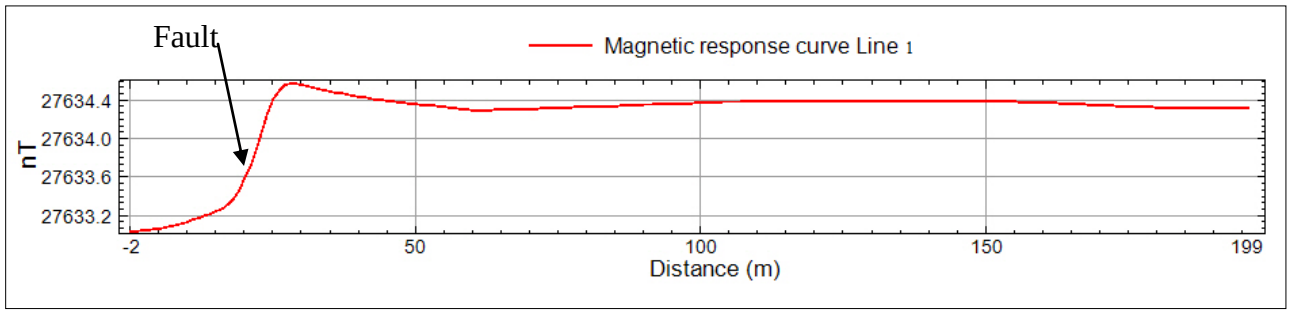

Figure 7- 13: Polile Tshisa magnetic profile in a SE-NW direction.

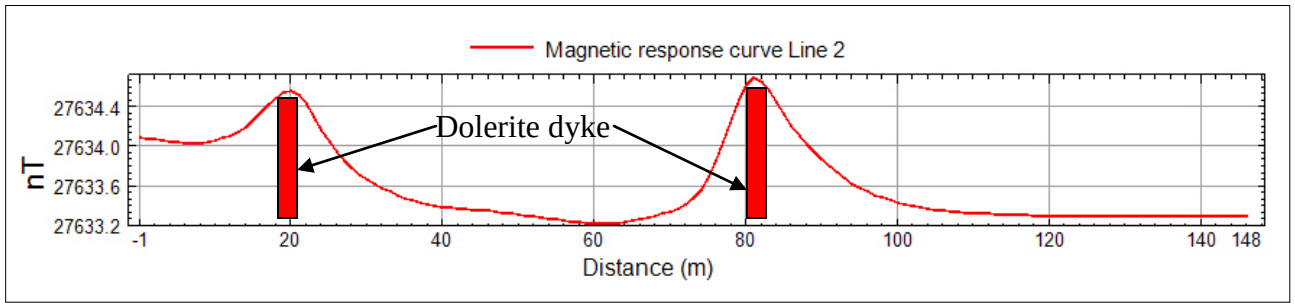

Figure 7- 14: Polile Tshisa magnetic profile in a SW-NE direction.

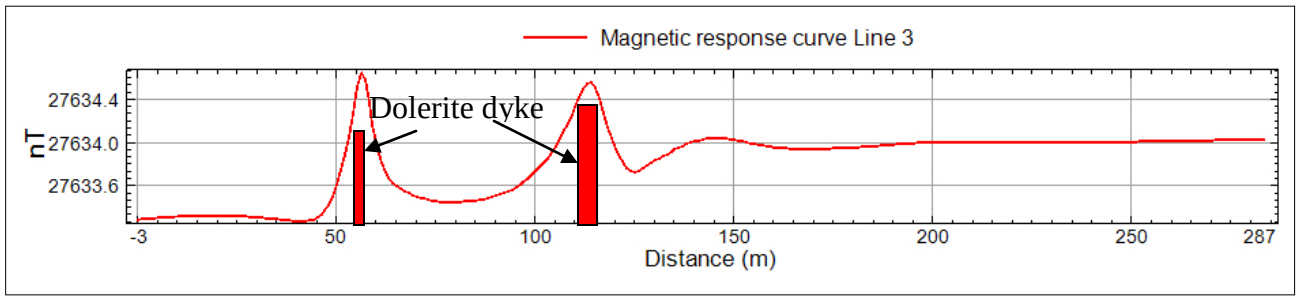

Figure 7- 15: Polile Tshisa second magnetic profile in a SW-NE direction.

The second profile (Figure 7.14) displays two peaks, one at 20 m, and the other 80.5 m. These peaks are possibly due to the presence of a wide dolerite dyke or two narrow dykes located directly beneath the peaks. A similar situation can be observed in Figure 7.15; groundwater can be targeted besides these peaks related to the occurrence of dolerite dykes. Dolerites always cause a chilly margin to occur at the contact with the country rock.

7.4 Aliwal North

7.4.1 Field observations

The measurements (see sample in Appendix Table E) at Aliwal hot springs with its pools were not very easy, because it was during renovation. On the other hand the springs are being used as spa (Figure 7.16 left). Measurements were taken in an outer zone from the spa, only one weathered and jointed greyish mudstone crops out (Figure 7.16 right) at the northwest side of the spa. The area is very humid; there is a lot of surface water coming possibly from the springs.

Figure 7- 16: (left) One of the pools at Aliwal North hot springs; (right) weathered mudstone

7.4.2 Magnetic survey at the Aliwal North hot spring

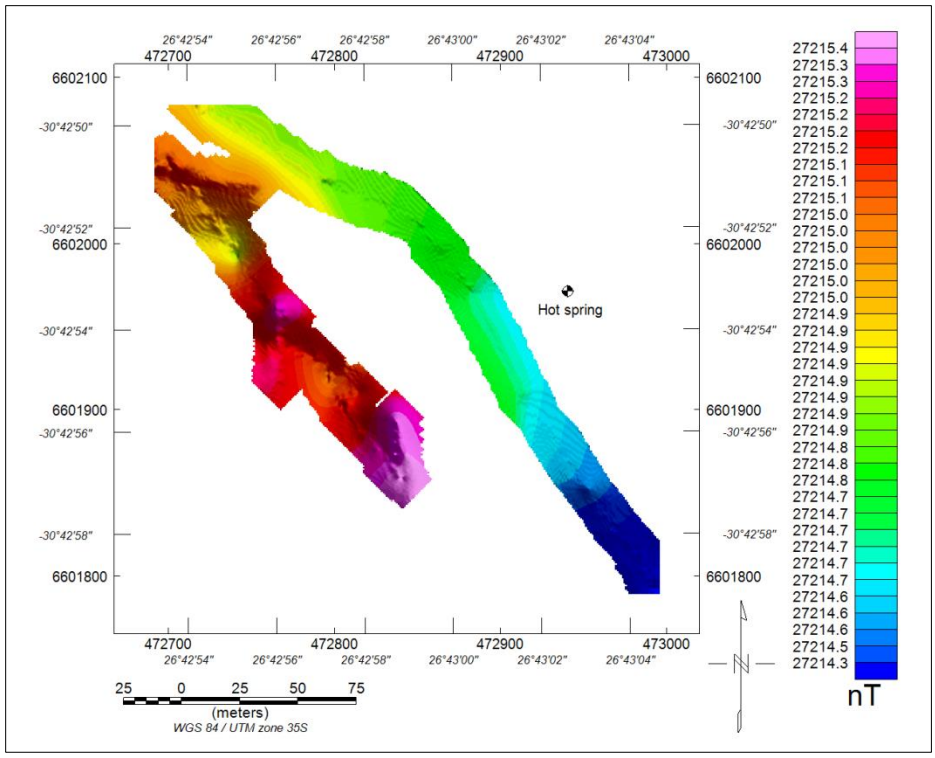

Figure 7- 17: Aliwal North Magnetic map (grid size 1 m)

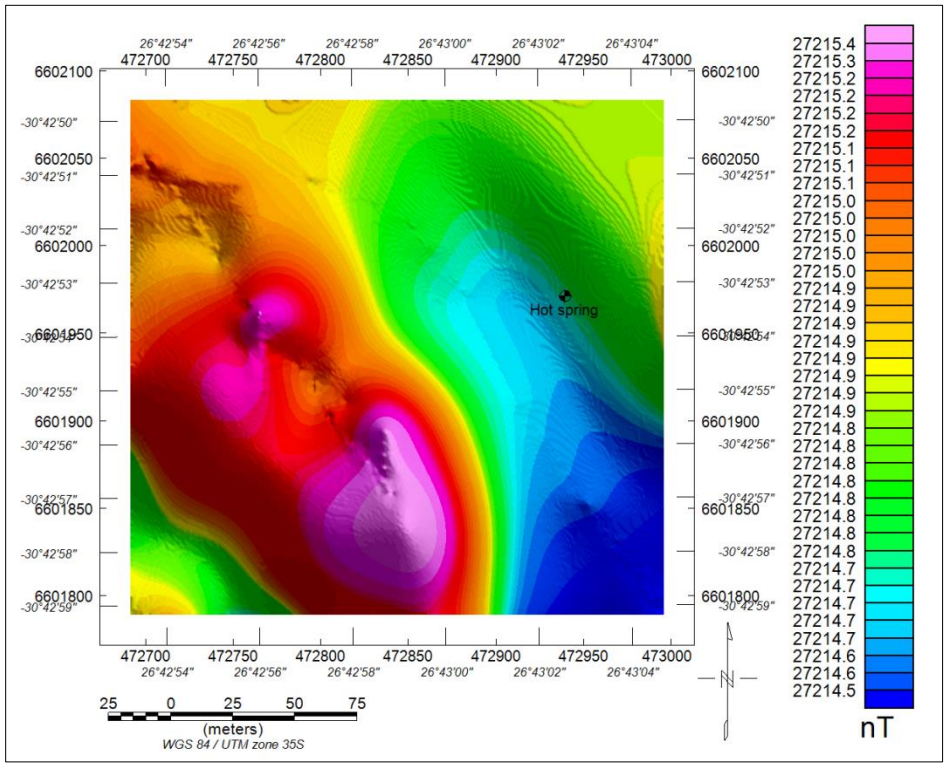

Figure 7- 18: Aliwal magnetic map (grid size 14 m)

Because of the limited area and the renovation around the facilities, only two lines oriented SE-NW could be surveyed. The two lines are separated by a distance of almost 75 m (Figure 7.17). In this figure a grid cell size of 1 m was initially used, and then was expanded to 14 m (Figure 7.18) for a better visualisation.

A profile oriented NW-SE (Figure 7.19) along the Line 1 portrays a general trend characterised by decreases and increases of the magnetic signal. A second profile oriented E-W (Figure 7.20), and a third one oriented NE-SW (Figure 7.21) indicate that the area has at some places a flat-like body, probably a dolerite sill. A great amount of water from beneath wells up on the surface. The flow of this water along the fault can cause a movement, and accordingly neotectonic activity. Hot springs are indicative of circulation of groundwater at great depths.

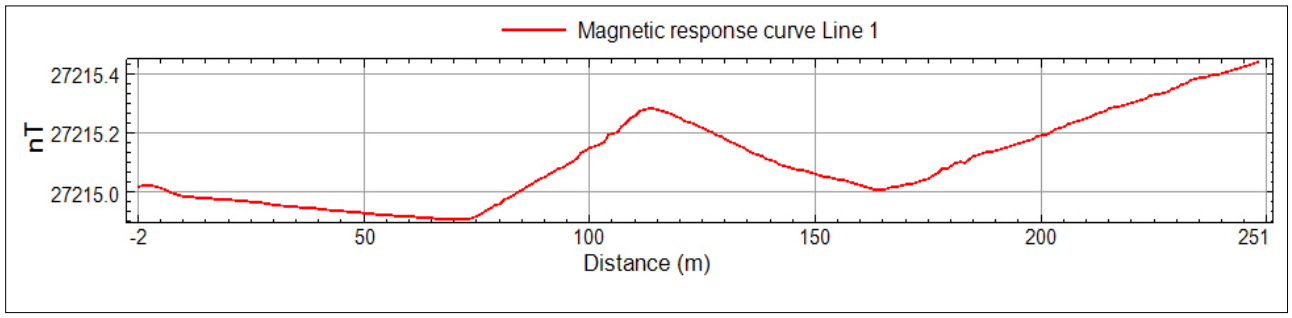

Figure 7- 19: Aliwal magnetic profile in a NW-SE direction.

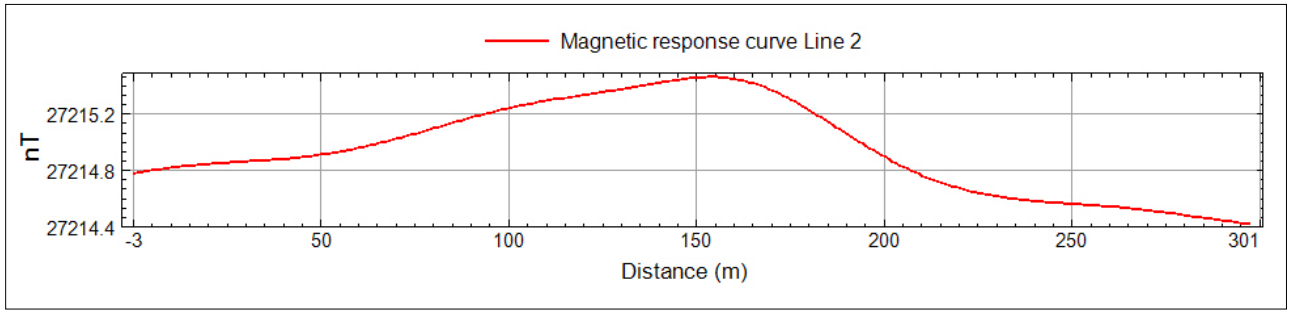

Figure 7- 20: Aliwal magnetic profile in a E-W direction.

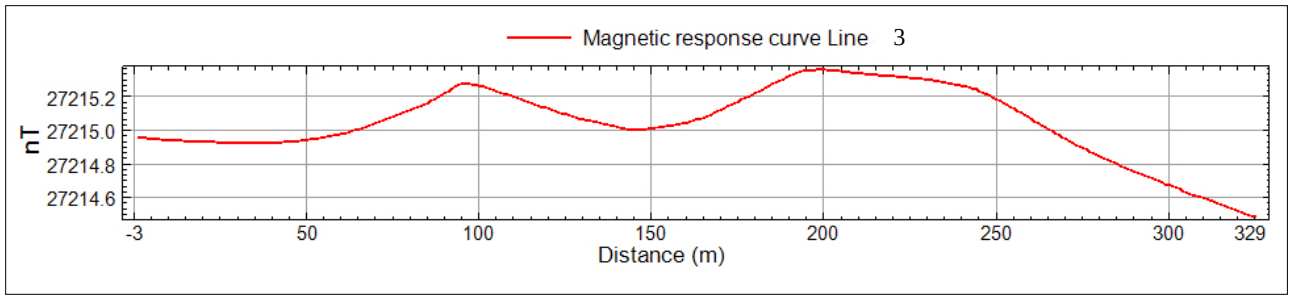

Figure 7- 21: Aliwal magnetic profile in NE-SW direction

7.5 Badfontein hot spring

7.5.1 Field observations

As for Aliwal North, at Badfontein no conspicuous outcrop was encountered, only few extremely weathered types of mounds near the hot springs can be seen (Figure 7.22 right). In this picture one can see that the hot spring discharges a considerable amount of water that flows on the surface due to the slope.

Figure 7- 22: (left) Flat surface at Badfontein farm; (right) mounds created by surface water circulation from the Badfontein hot spring.

In general the area in the farm where the hot spring is located is very flat (Figure 7.22 left). Olivier (1975) made mention of the flooding that occurred during the time when the Orange-Fish tunnel was being dug. This flooding was located some 300 m south of the Badfontein hot spring. This is indicative of neotectonic faults or fractures below the surface.

7.5.1 Magnetic survey around the Badfontein hot spring

Magnetic measurements (see sample in Appendix Table F) were carried out along three lines, two lines oriented NW-SE, and one line oriented SW-NE; first a grid cell size of 1 m was used (Figure 7.23), then expanded to 28 m (Figure 7.24).

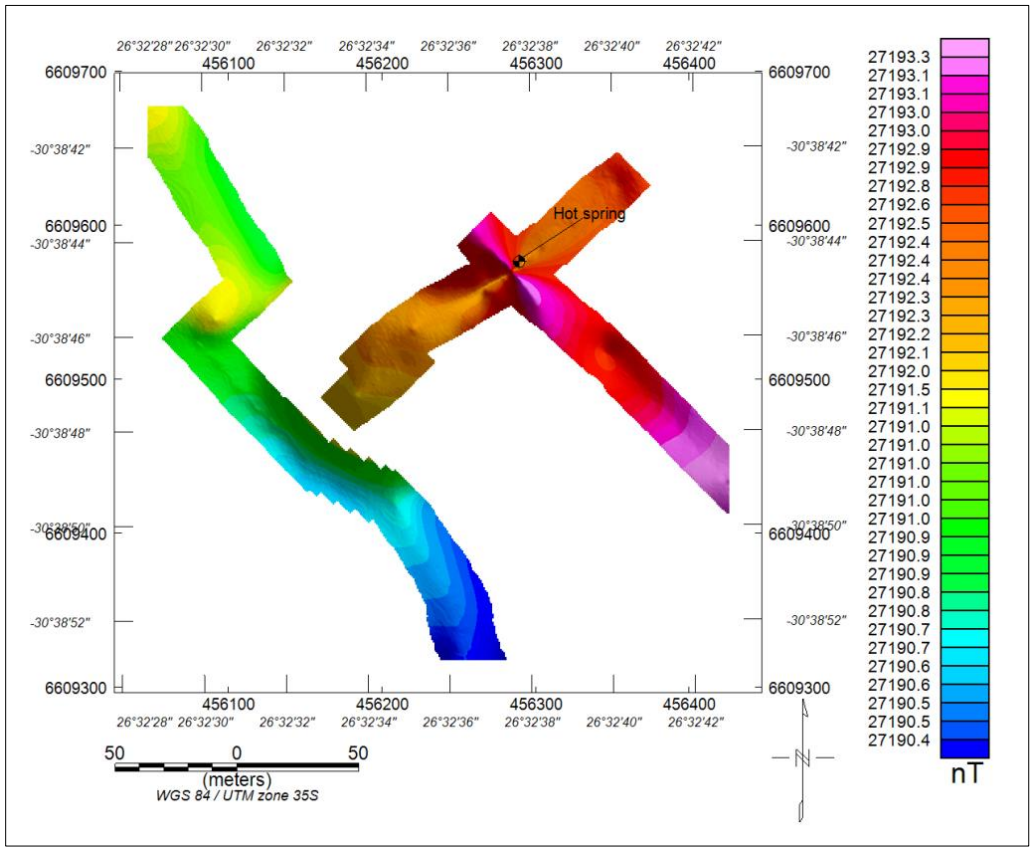

Figure 7- 23: Badfontein magnetic map (cell size 1m) showing the three lines

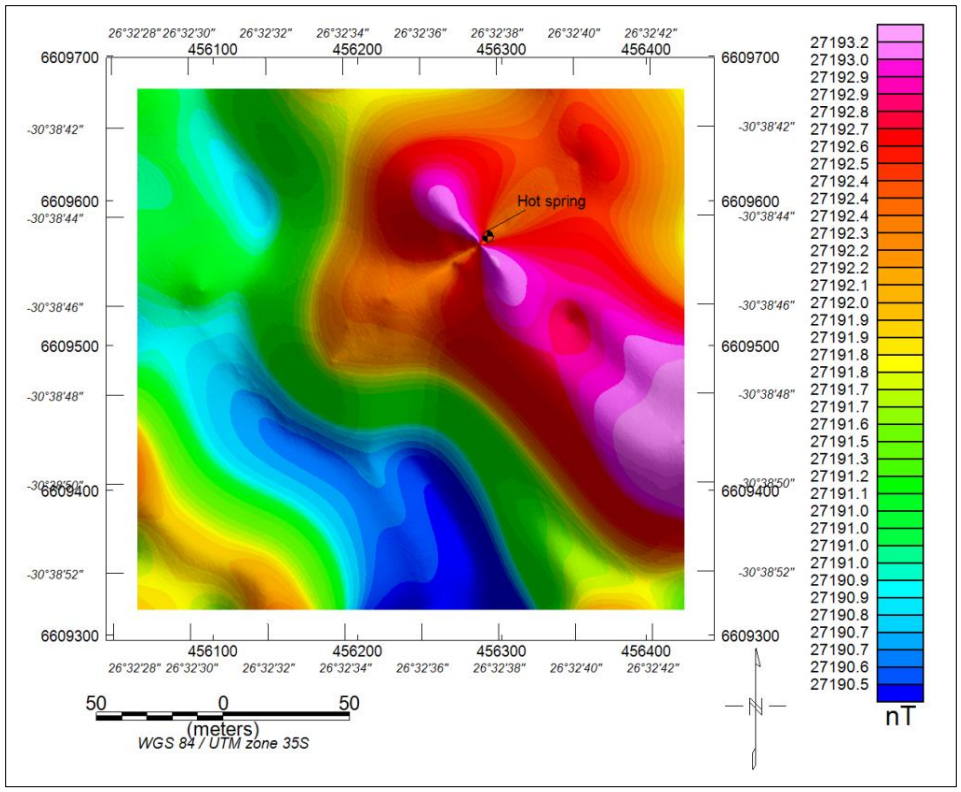

Figure 7- 24: Badfontein magnetic map (cell size 28 m)

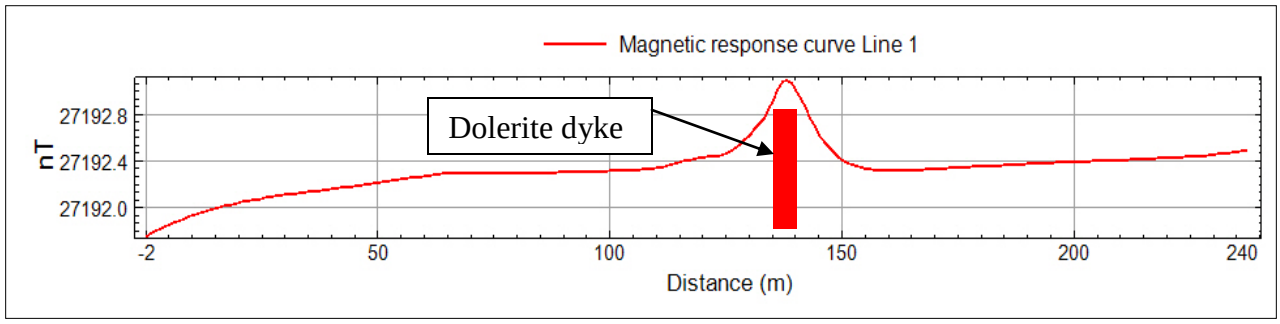

Figure 7- 25: Badfontein magnetic profile in a SW-NE direction

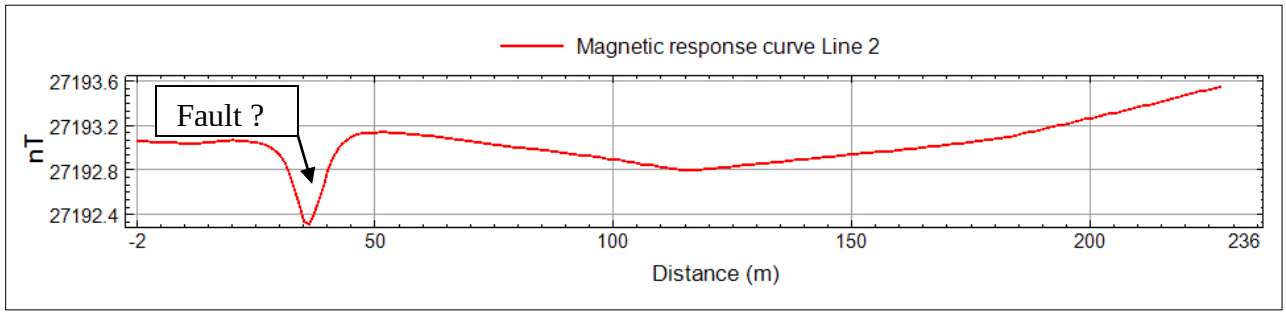

Figure 7- 26: Badfontein magnetic profile in a NW-SE direction

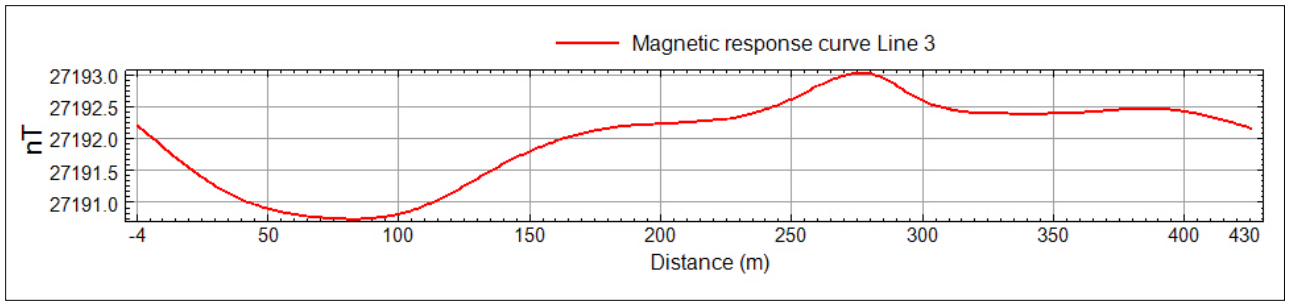

Figure 7- 27: Badfontein second magnetic profile in SW-NE direction

At Badfontein the magnetic response curves indicate that magnetic signals are almost constant (Figure 7.25, Figure 7.26, and to a certain extent in Figure 7.27). However, remarkable features are highlighted in these magnetic response curves. In Figure 7.25 there is a positive peak at 138 m, and this peak is interpreted to be due to a dolerite dyke. Figure 7.26 displays a profile with a negative peak at approximately 31 m, this negative peak is probably related to the occurrence of a fault, which is a conduit for water flow. Figure 7.27 depicts a situation where you might have two bodies of contrasting magnetic properties. The first part of the profile shows that the signal decreases up to 96 m, and the second part shows an increase in the signal from 100 m to reach a maximum at 275 m.

7.6 Electromagnetic survey

In electromagnetic data acquisition one can use either the horizontal magnetic dipole or the vertical magnetic dipole, which describes the orientation of the coils. In the vertical mode, the axis of the coils is perpendicular to the ground while in the horizontal mode the axis of the coils is parallel to the ground. A magnetic dipole is a close circulation of electric current. It is also the limit of either a closed loop of electric current or a pair of poles as the dimensions of the source are reduced to zero while keeping the magnetic moment constant. It is a magnetic analogue of the electric dipole. A magnetic dipole can also be defined as a model of an object that generates a

magmatic field in which the field is considered to emanate from the opposite poles, as in the north and south poles of the magnet.

7.6.1 Polile Tshisa hot spring

The acquisition of data was organized for the survey along profiles oriented SE-NW. Profiles were set so in a quasi-perpendicular direction to the one of hot springs that wells up at three different places separated by a distance of almost thirty centimeter aligned in a direction of N 75^{o} as mentioned above. Another profile NE-SW was also set so that a generalized coverage of the area helps in the visualization and the interpretation.

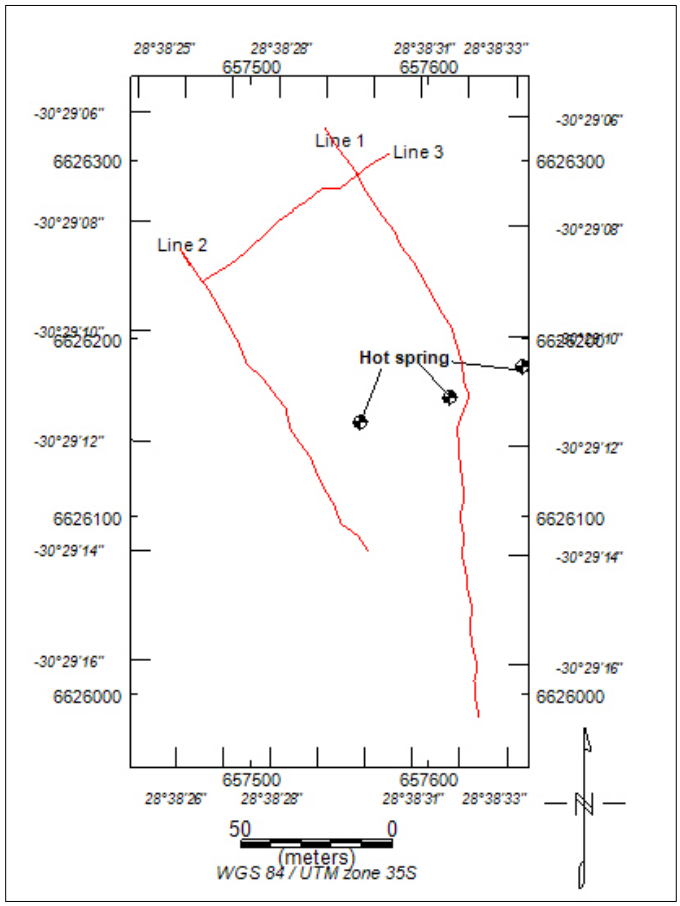

Figure 7- 28: Lines in red were set for data acquisition using the vertical and horizontal dipoles at intercoil spacing of 20 m at the Polile Tshisa hot spring.

Three lines (Line 1, Line 2, and Line 3: Figure 7.28) of combined vertical and horizontal dipole mode were set and data were acquired using an intercoil spacing of 20 m (SE-NW) profiles for line 1 and Line 2), and a third line (Line 3) in an NE-SW profile was set with an intercoil spacing of 20 m. The station spacing was 10 meters. For the first line with 20 m as intercoil spacing (Figure 7.29), it was observed that between 0 and 50 meters, 70 and 130 meters, and from 220 meters to almost 270 meters, the horizontal dipole is higher than the vertical dipole, this might be indicative of a conductance that decreases with depth, and that the regolith is shallow.

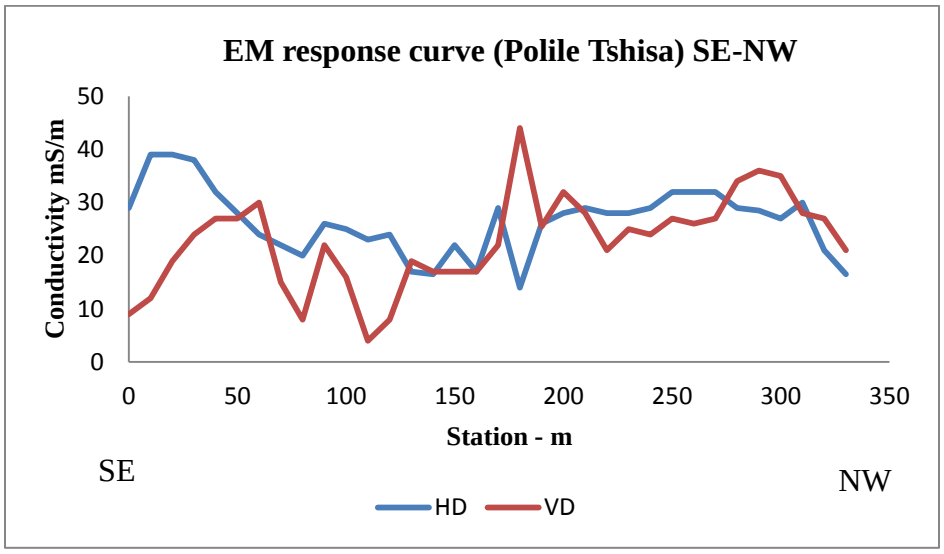

Figure 7- 29: Line 1 oriented SE-NW (intercoil spacing: 20 m)

Two contrasting anomalies can be seen around 170 m; the vertical dipole showing a positive peak might be indicative of a weathered and fractured zone, and the horizontal dipole showing a low peak at the same place can be interpreted as a vertical dyke. Dykes in the Karoo aquifers are good indicators for groundwater exploration. This area may have two structures favourable for groundwater. Between 60 m and 130 m, the vertical dipole displays two remarkable low separated by a high. The two peaks can be related to dolerite dykes with a fracture in between

them. Thus the potential of finding a productive well is high in this area. There is a quite good variation in conductivity for the horizontal dipole (~40 mS/m to 13 mS/m), whilst for the vertical dipole the variation is a bit high (9 mS/m to 44 mS/m). The complete set of data is presented in Appendix Table G.

For Line 2 (see Table H in Appendix) with 20 m as intercoil spacing (Figure 7.30), there is no remarkable variation in the conductivity for the horizontal dipole (26-30 mS/m). This may signify that there is no much variation either in mineralogy or porosity. The vertical dipole (Figure 7.30) has higher variation (16.5-32 mS/m) than the horizontal dipole. It is quite clear that between 0 and 40 m and between 42 and 70 m the response of the horizontal dipole is higher than that of the vertical one. This is indicative of a shallow regolith. Between 0 and 30 m, both the horizontal and vertical dipole signatures almost dovetail.

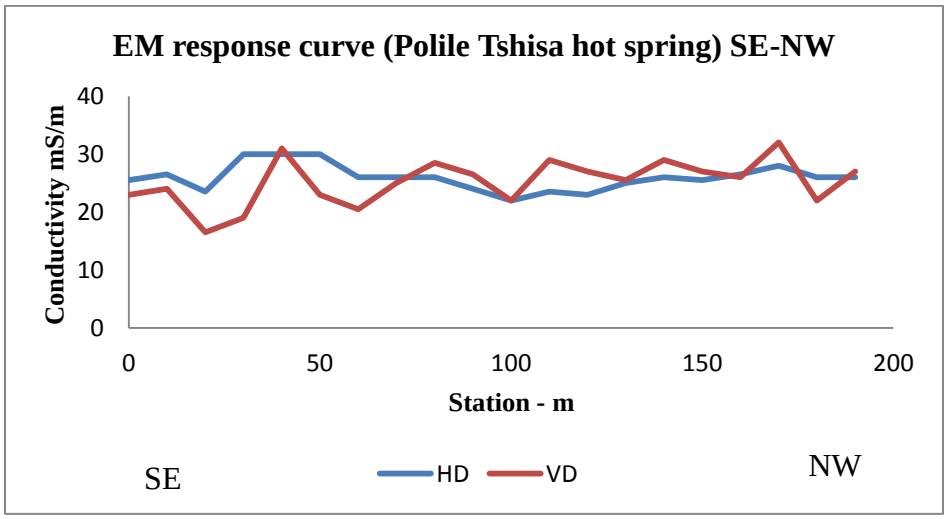

Figure 7- 30: Line 2 (intercoil spacing: 20 m)

For Line 3 (see Table I in Appendix) with intercoil spacing of 20 m (Figure 7.31), the vertical dipole response seems higher than that of the horizontal dipole from 0 to 70 m. The signatures of

the dipoles (HD and VD) almost dovetail between 15 and 36 m. On this profile the survey may have intersected a dyke. It may imply that there is a change in the physical properties of the rocks because of the similar responses for the vertical and the horizontal dipoles.

As for Line 2 in Figure 7.30 (20 m intercoil spacing), there is similarity in horizontal dipole patterns. It can be seen that from 50 m to 110 m, the profile is almost flat like in Figure 7.30, and not showing much variations.

The vertical dipole shows high conductivities at two points at 40 m and 60 m (> 40 mS/m), with lower conductivities of 18.5 and 24.5 mS/m at 30 and 80 m. These high conductivities from the vertical dipole indicate a possible fault or fracture below the surface. For Line 1 oriented SE-NW with an intercoil spacing of 10 m (Figure 7.32, Table J in Appendix), the horizontal dipole shows high conductivity of 49 to 50 mS/cm between 10 and 20 m, which is possibly related to a weathered zone.

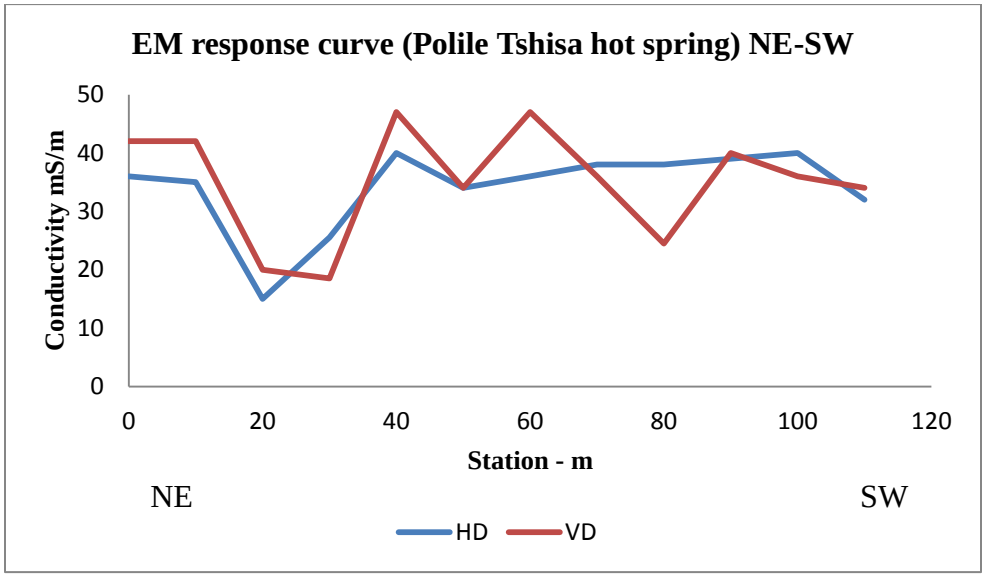

Figure 7- 31: Line 3 (intercoil spacing: 20)

There is a quite remarkable variation in conductivity ranging from 16 to 50 mS/m in Figure 7.32. From 20 m to 60 m there is a steadfast decrease in conductivity. From 60 to 300 m the conductivity does not show remarkable variations, which could be indicative of low porosity.

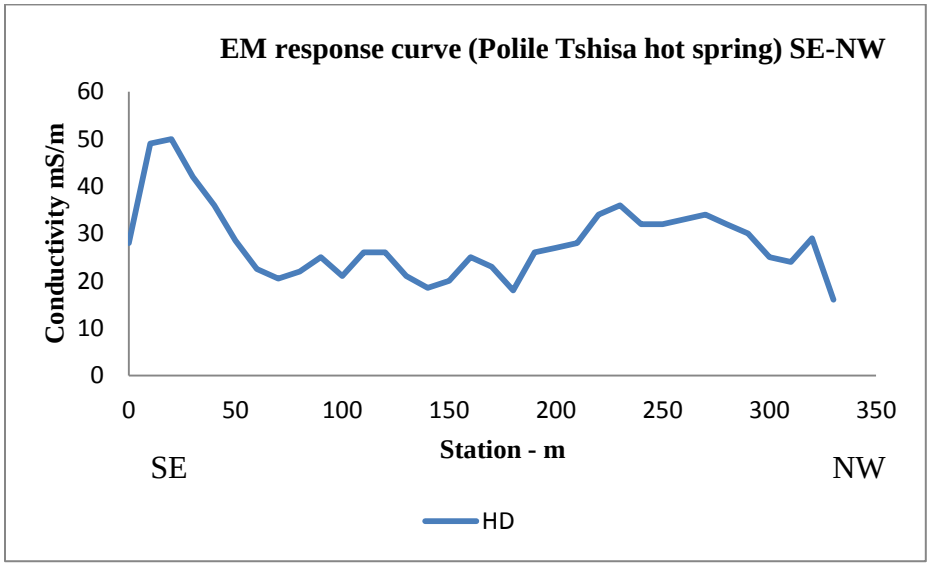

Figure 7- 32: Line 1 (intercoil spacing 10 m)

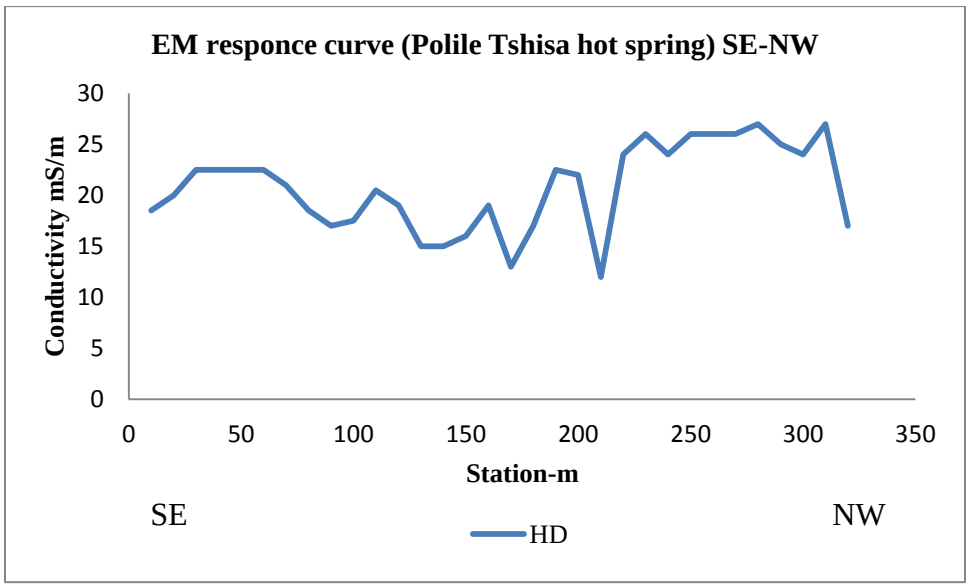

Figure 7- 33: Line 1 (intercoil spacing 40 m)

For Line 1 with an intercoil spacing of 40 m and HD only (Figure 7.33 and Table K in Appendix) the conductivity is almost constant from 10 m to 140 m. The conductivity varies between 150 m and 200 m showing two negative peaks. The area between these negative peaks can be related to a weathered rock or rock of high porosity. From 200 m the conductivity increases to reach 26 mS/m, then remains almost constant. The lowest observed conductivity is 12 mS/cm and the highest is 18.5 mS/cm.

The depth-conductivity model (Figure 7-34) from Line 1 data at the Polile Tshisa hot spring shows two high conductivity zones (e.g ≥ 30 mS/m) at the southeastern end of the profile and from about 175 m to the northern end of the profile. Both zones of high conductivity extend from surface to about 8 m depth.

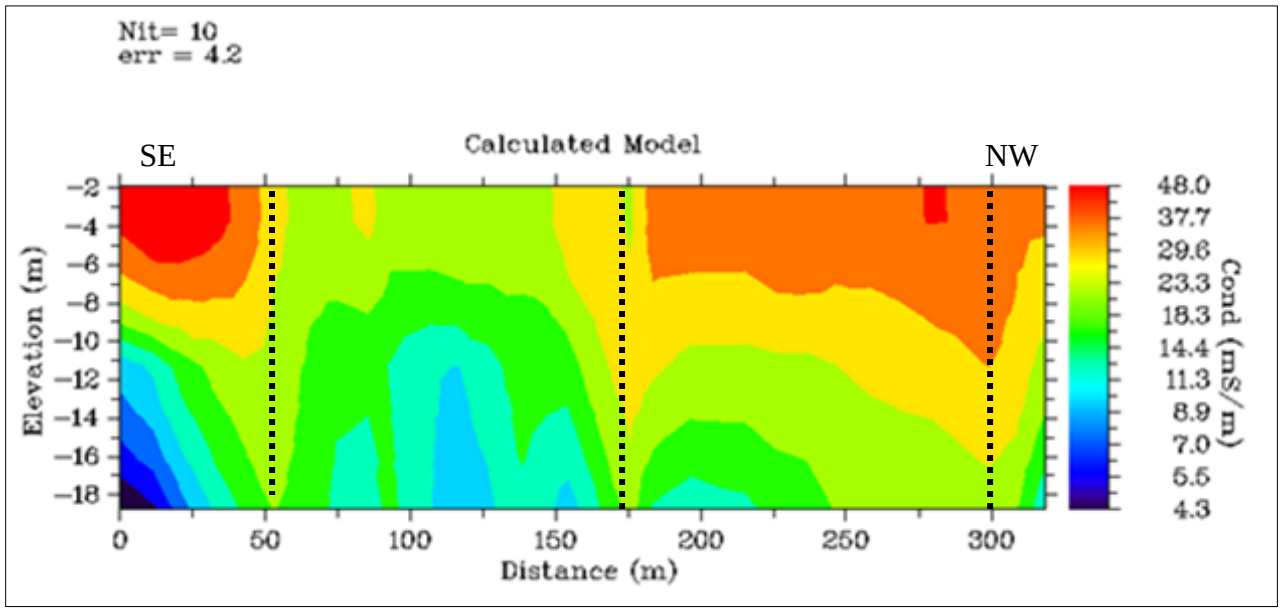

Figure 7- 34: Polile Tshisa hot spring conductivity-depth model. The dotted lines mark positions of inferred faults. Nit is the number of iterations, and err is the least squares error between calculated and observed conductivities.

The high conductivity zones can be interpreted as highly weathered sandstones. The area of the Polile Tshisa hot spring was observed to have sandstones that are weathered, leaving loosed particles of sand and whitish kaolinised material. The dashed lines marked in Figure 7.34 are inferred to be either large faults or fractures along which water can migrate upwards easily. Generally, it transpires from the depth modelling that the conductivity is decreasing with depth for the maximum investigated depth (≈ 20 m).

7.6.2 Aliwal North hot spring

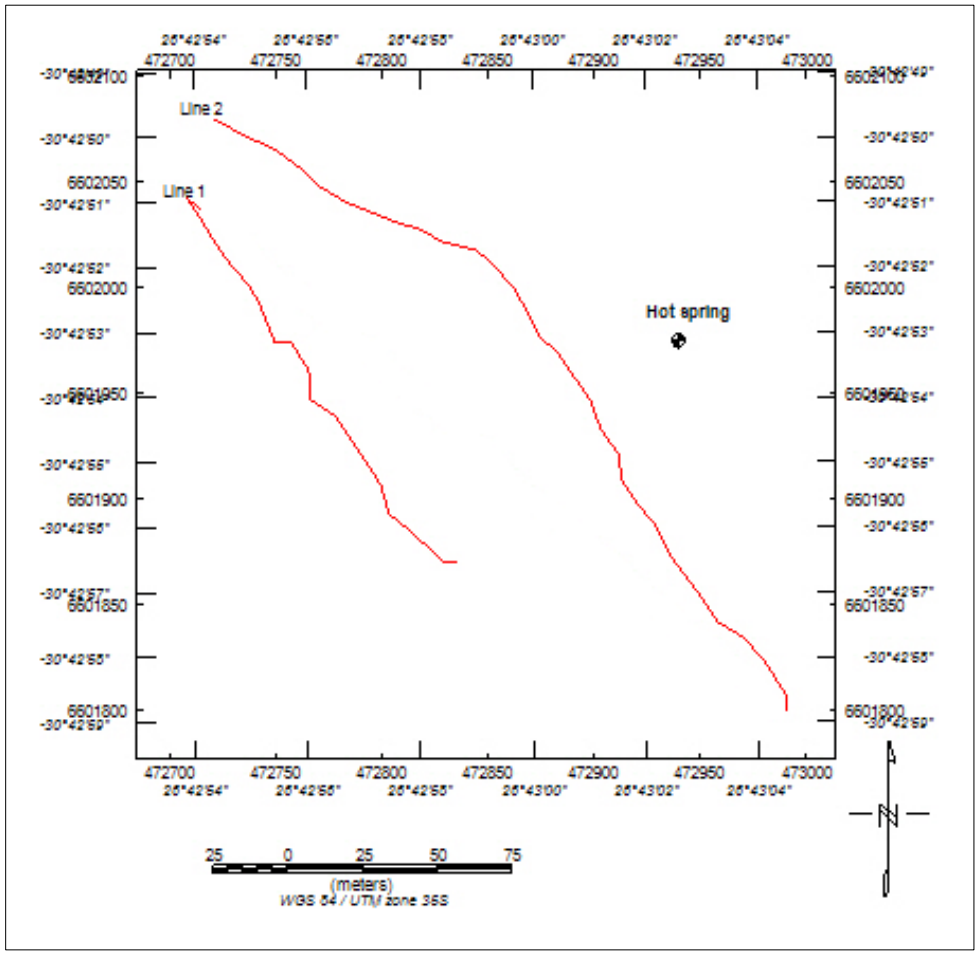

Figure 7- 35: Line 1 and Line 2 set for data acquisition using the horizontal dipole at intercoil spacing of 10, 20, and 40 m at Aliwal North.

At the Aliwal North hot springs, due to the limited accessibility and the position of the building facilities, only two lines (Figure 7.35) oriented SE-NW were set with intercoil spacing of 10, 20 and 40 m using the horizontal dipole (see Tables L, M, N, O, P and Q in Appendix). At Aliwal North, there is considerable amount of water that flows on the surface, which indicates zones of seepage.

Unlike at Polile Tshisa the Line 1 profile with an intercoil spacing of 10 m (Figure 7.36) displays a wide variation in conductivity values, at position 0 m the conductivity is 170 mS/m whilst at 170 m, the conductivity is only 30 mS/m. The conductivity decreases from position 0 m to 30 m, and remains almost constant between 30 m and 80 m. There is a peak of conductivity between 80 and 120 m, which could be due to the occurrence of a fault or a zone of high porosity. After 100 m, the decreasing conductivity may be due to an unweathered rock, which is less permeable and could probably be a shale or any very fine grain rock. According to hydrogeological and sedimentological studies, a coarse grain rock would have a good porosity. A fine grain rock would be characterised by low porosity.

For the intercoil spacing of 20 m (Figure 7.37), it can be depicted that the same peak appears at around 100 m. As it was observed for the intercoil spacing of 10 m, there is wide variation in conductivity (19-130.5 mS/m).

This can be related to variations in physical properties of the bedrock. For Line 1 at all the intercoil spacings, (e.g. Figure 7.36, Figure 7.37, Figure 7.38) the southeast side in this line is highly conductive than the northwest side. A peak is seen at around 100 m for the intercoil spacings of 10 m and 20 m.

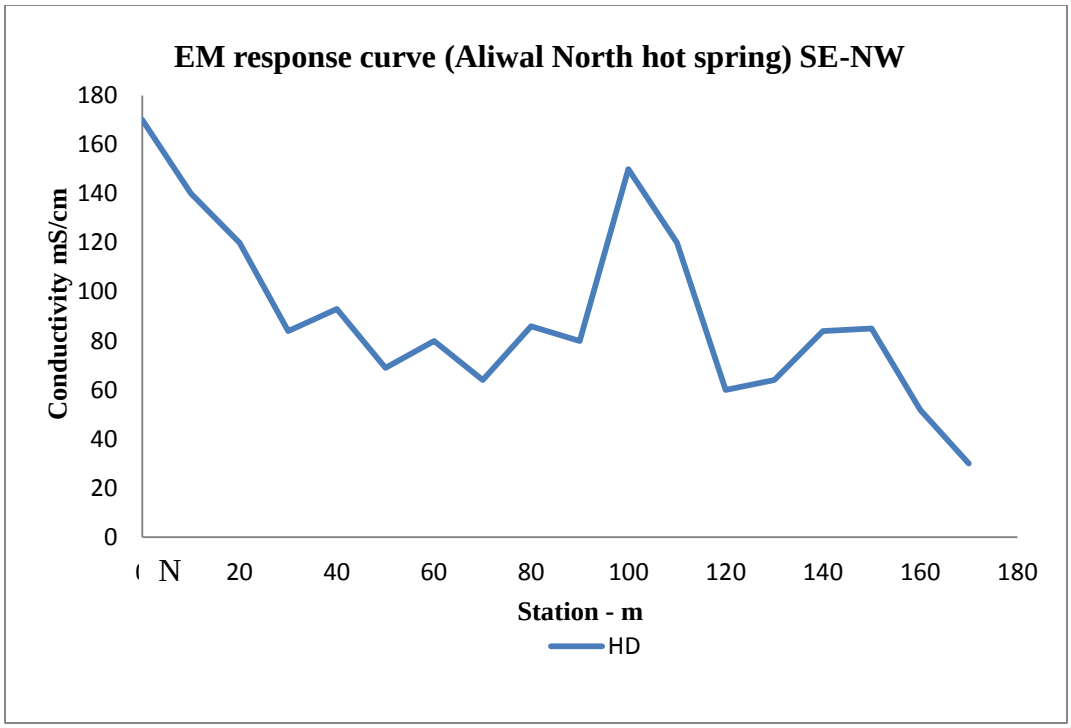

Figure 7- 36: Aliwal North Line 1 (intercoil spacing 10).

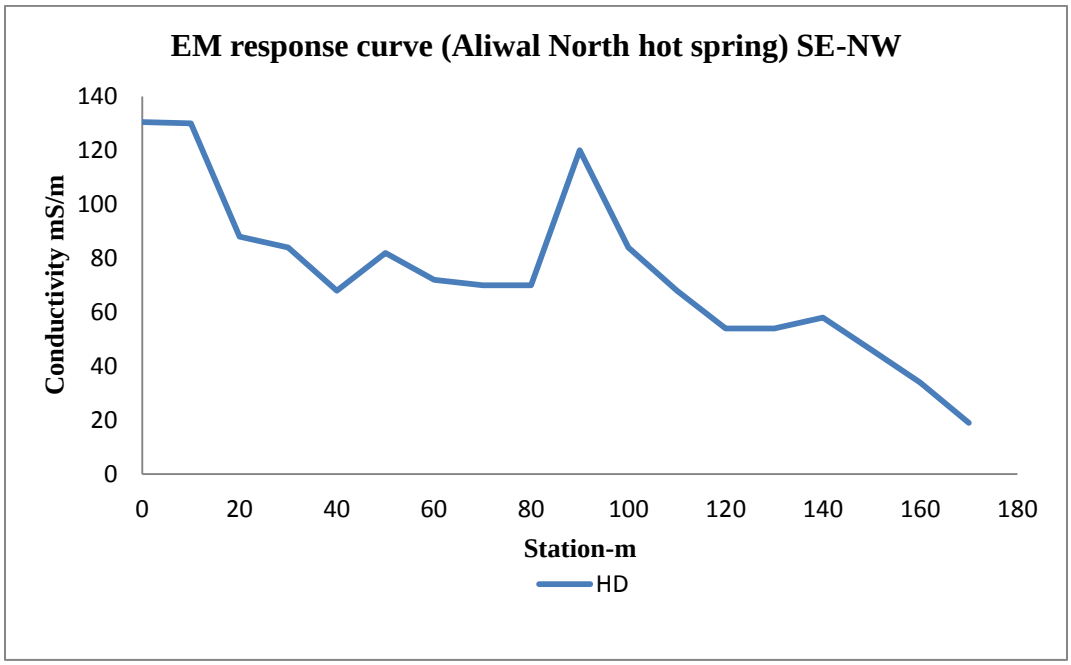

Figure 7- 37: Aliwal North Line 1 (intercoil spacing 20 m)

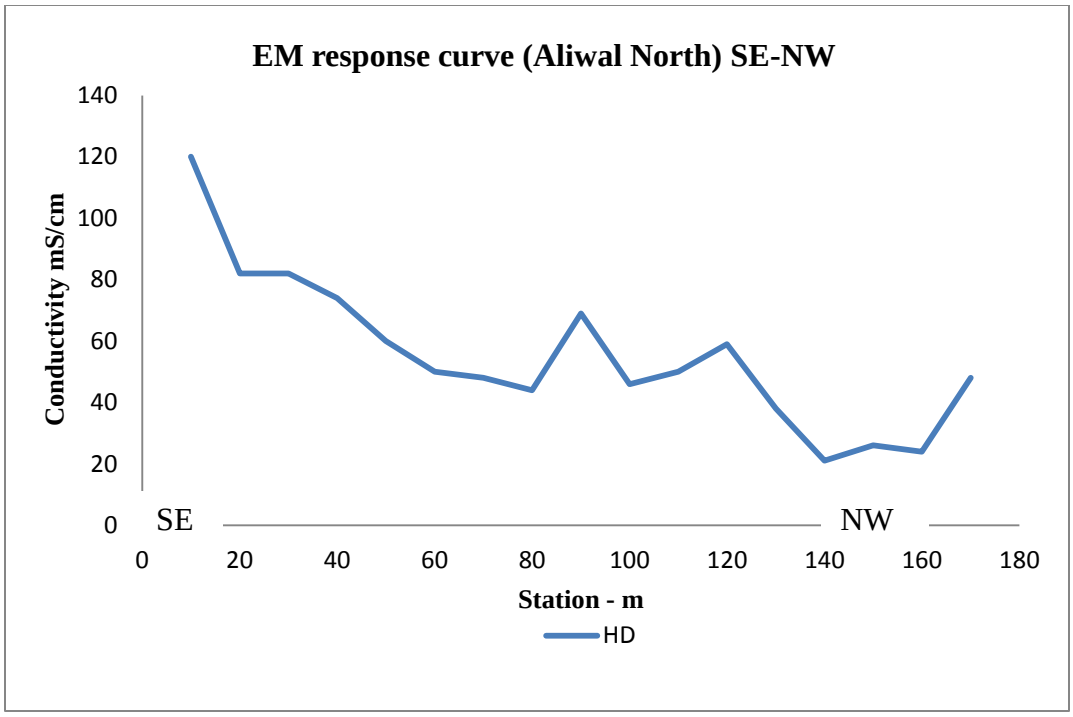

Figure 7- 38: Aliwal North line 1 (intercoil spacing 40 m)

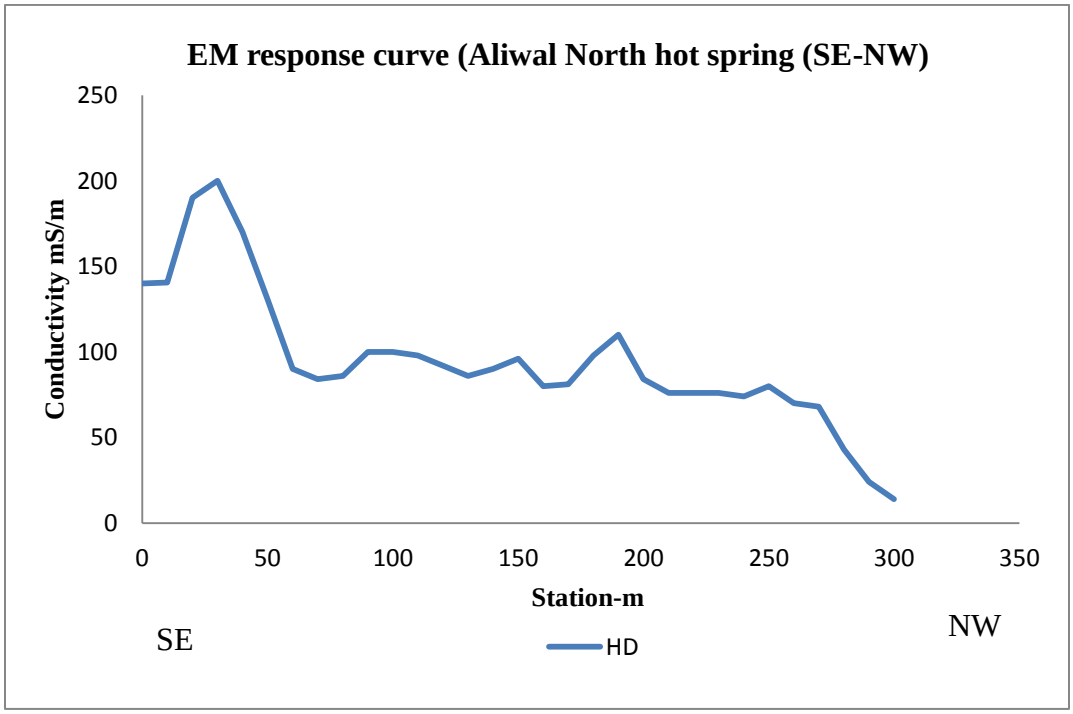

Figure 7- 39: Aliwal North Line 2 intercoil spacing 10 m.

Figure 7.39 shows the Aliwal North Line 2 profile of 10 m intercoil spacing. The conductivity increases from position 0 m to 30 m where it reaches a maximum of 200 mS/m. This increase can be related to a fractured or weathered zone. It then decreases to reach 90 mS/m at 60 m. From 60 m it remains fairly constant up from 275 m in a small interval (68-90 mS/m). Thereafter it decreases sharply, reaching a minimum of 14 mS/m at 300 m.

At Aliwal North the conductivity can have negative values (Figure 7.40). At exactly 150 m, there is a negative conductivity of – 21 mS/m. This feature is typical of a dolerite dyke EM signature. This dolerite dyke has disturbed the bedrock, creating varied values of conductivity after 150 m. For the whole profile the conductivity varies between 36 mS/m to 180 mS/m.

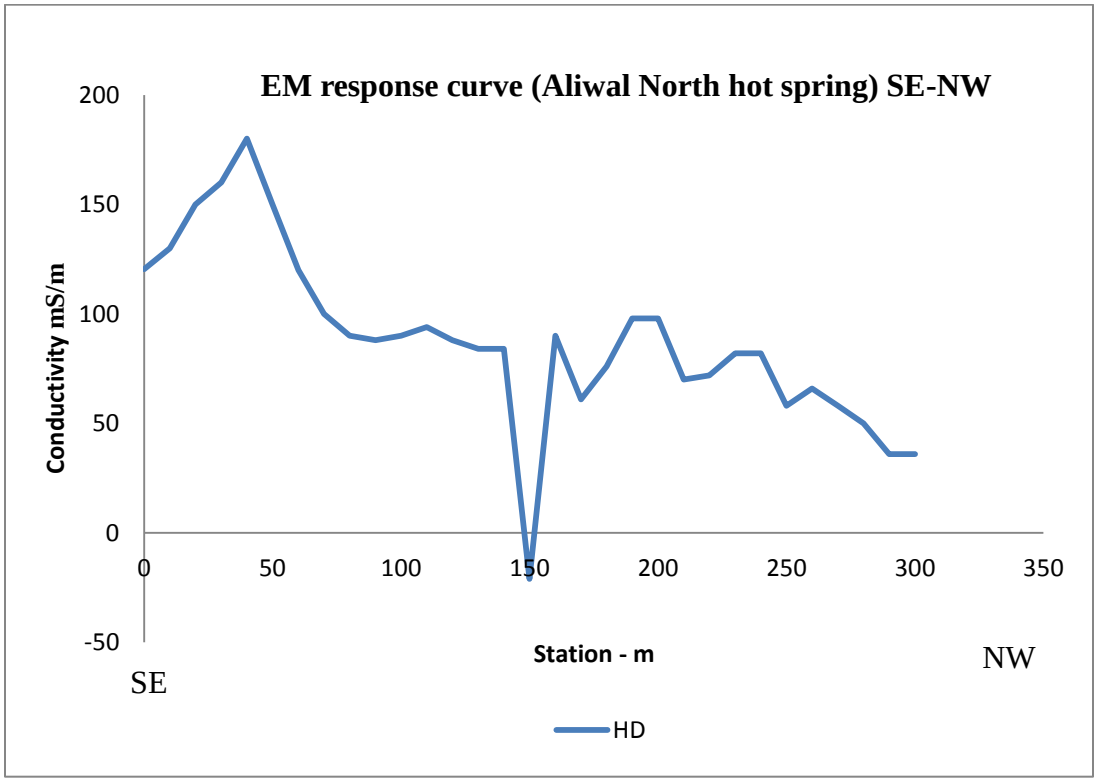

Figure 7- 40: Aliwal North Line 2 (intercoil spacing 20)

The 40 m intercoil spacing profile (Figure 7.41) shows a slightly decreasing conductivity zone between 0 m and 120 m. From 120 m this conductivity sharply decreases, this may be due to a dolerite or a fresher or less porous rock in the substratum. The conductivity increases from positions 150 m to 160 m and from 190 m to 200 m where it reaches 200 mS/m. The peaks at 160 m and 220 m are indicative of faults or very weathered and porous rock with high permeability. But as the profile goes to the north, the conductivity decreases as has been observed in almost all the profiles.

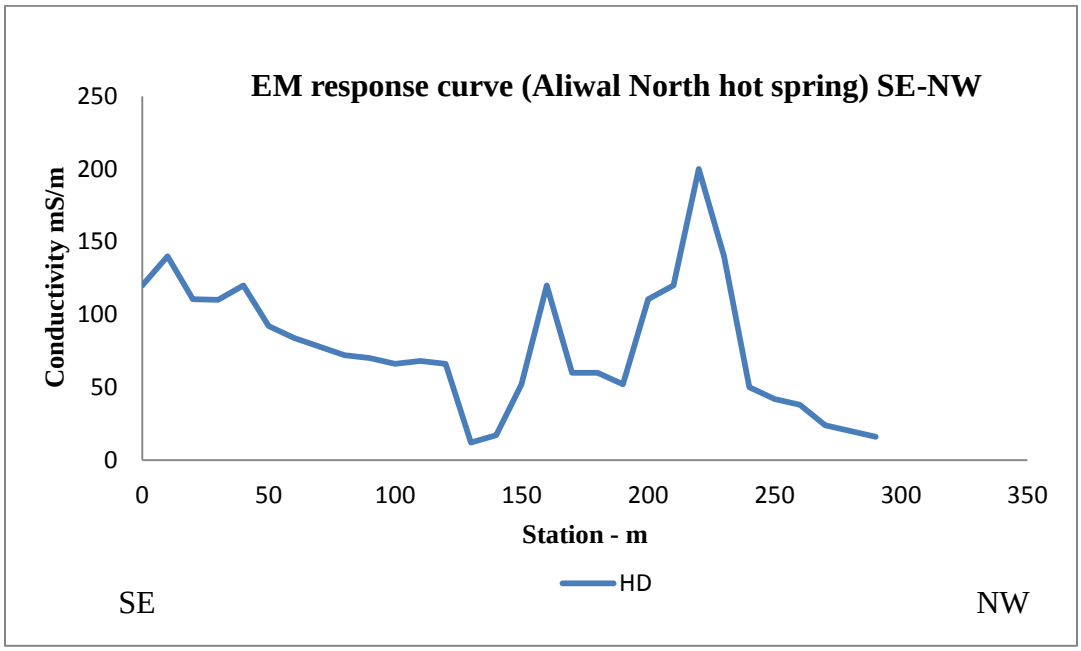

Figure 7- 41: Aliwal North Line 2 (intercoil spacing 40 m)

The depth-conductivity model at the Aliwal North hot spring shows for the Line 1 (Figure 7.42) high conductivities (e.g. ≥ 130 mS/m) from southeast to northwest. The model shows values of conductivities up to almost 20 m below the Earth surface. Between 2 m and 11 m as depth interval over a distance between 0 and 175 m, the survey line is characterised by higher conductivities.

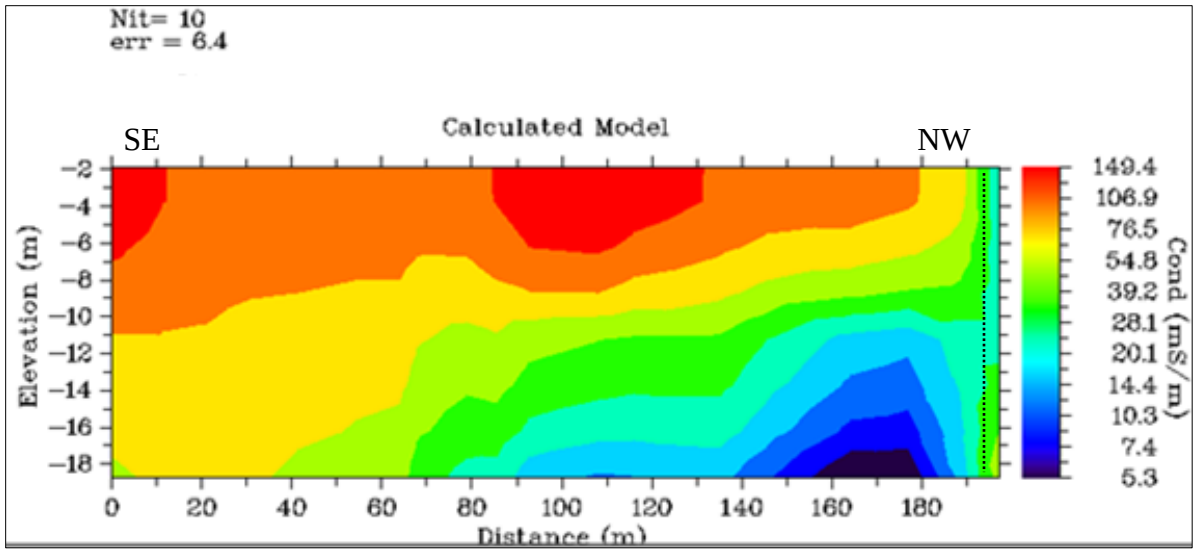

Figure 7- 42: Depth-conductivity model for Aliwal North Line 1. The dashed line at the end of the profile indicates an inferred fault.

This is corroborated with field observations; lot of water is being gushed out from the spring. As for the Polile Tshisa hot spring, one can note the decrease of conductivity with depth.

The depth-conductivity model for Line 2 at Aliwal North (Figure 7.43) is mainly characterised by zones of high conductivities ($\geq$ 200 mS/m). At some places the conductivity decreases with depth, at others it does not. For instance, between 262.5 and 312.5 m, there is a higher conductivity zone visible from 14 m below the earth surface. This zone is possibly connected to a fault below. Most often, hot springs are indicative of groundwater circulation at greater depths inducing neotectonics. The zone between 150 and 200 m is characterized by a decrease in conductivity, possibly a dolerite dyke separating adjacent zones of higher conductivities. This sharp decrease of conductivity was observed while using the intercoil spacing of 20 m at 150 m along the survey line (Figure 7.40). It can be highlighted that the Aliwal North hot spring has more conductive zones than the Polile Tshisa hot spring. Faults at Aliwal North must be widely

opened, allowing thus lot of water flow, which increases the conductivity values. This conductivity increase can be also related to high salinity. Dashed lines in Figure 7.43 are inferred faults.

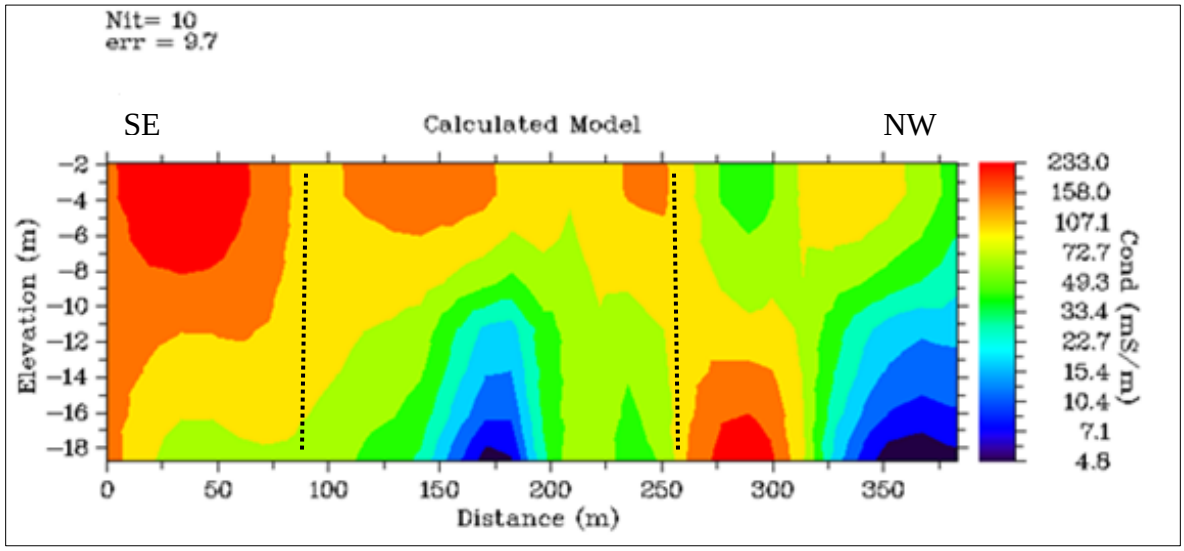

Figure 7- 43: Depth-conductivity model for Aliwal North Line 2

7.6.3 Badfontein hot spring

The Badfontein spring is located near the town of Aliwal North. The hot spring is being used as a spa and is sulphurous. One line only was set with two intercoil spacings of 10 m and 20 m in a southeast-northwest direction (Figure 7.44). For the intercoil spacing of 10 m (Figure 7.45) there are two areas of increasing conductivity (between 30 m and 110 m and between 200 m and 230 m). The first area may indicate higher permeability whilst the second one with a remarkable peak at 230 meters (210 mS/m) may indicate a fault. The variation of conductivity is also notable from 68 mS/m at the start of the profile to 210 mS/m at 240 m.

The Figure 7.46 displays a SE-NW profile, which does not show too much variation in conductivity from 50 to 300 m. However the peaks at 50 m and 220 m are indicative of fault

zones. As for the intercoil spacing of 10 m, the intercoil spacing of 20 m show similar trend with an increase in conductivity in the first 50 m. The variation in conductivity is remarkable, the lowest value is 90 mS/m at 300 m, and the highest value is 260 mS/m at 50 m. The two profiles indicate possible faulting in the area.

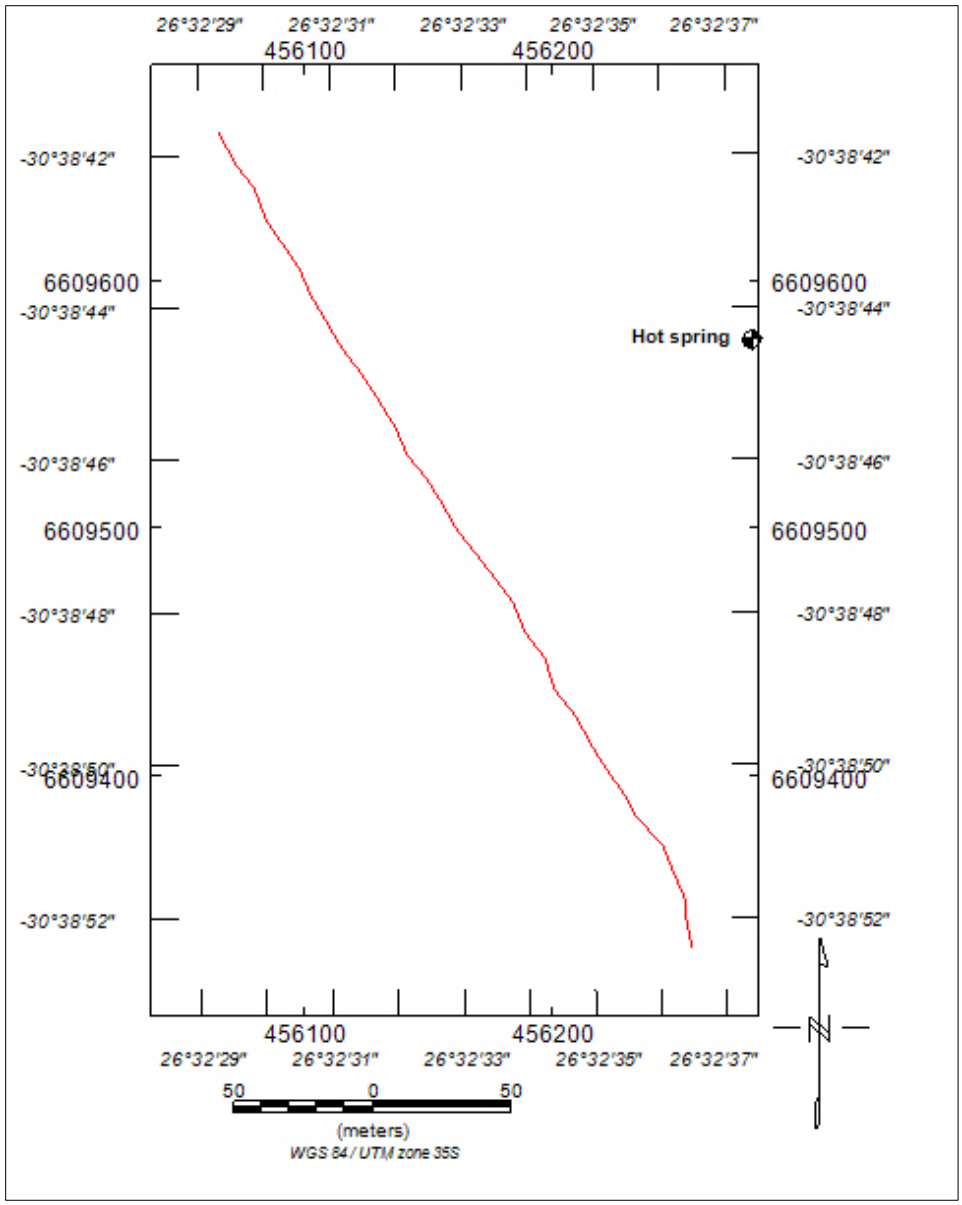

Figure 7- 44: The only line adopted for the horizontal dipole at intercoil spacing of 10, 20 at Badfontein hot spring.

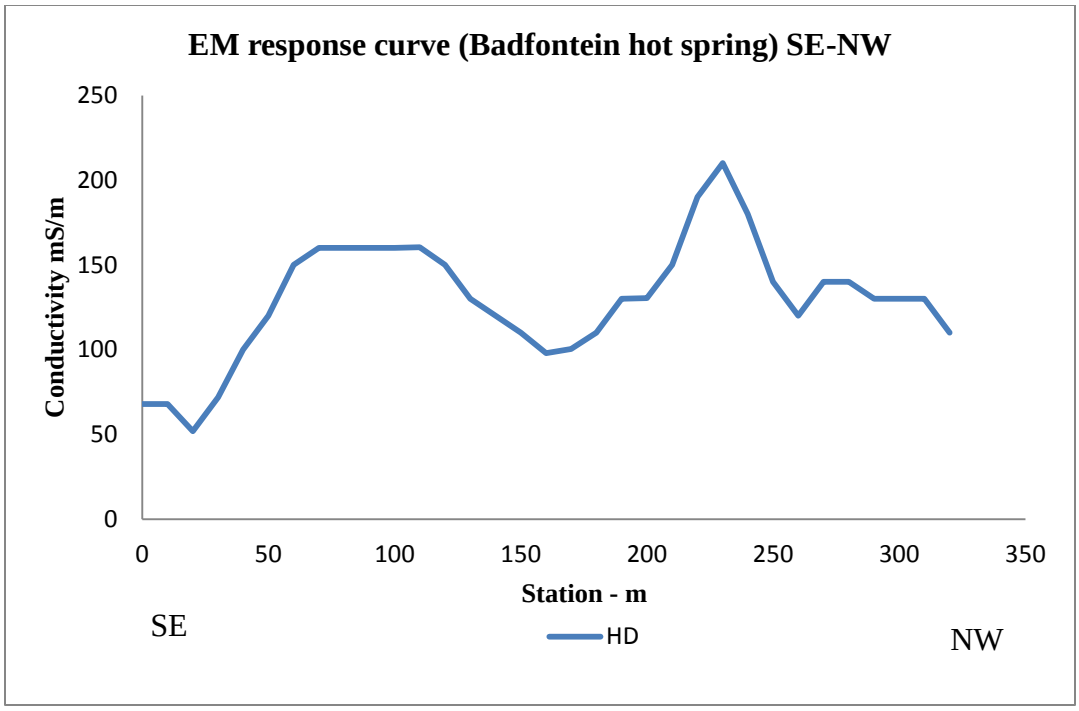

Figure 7- 45: Badfontein line (intercoil spacing 10 m)

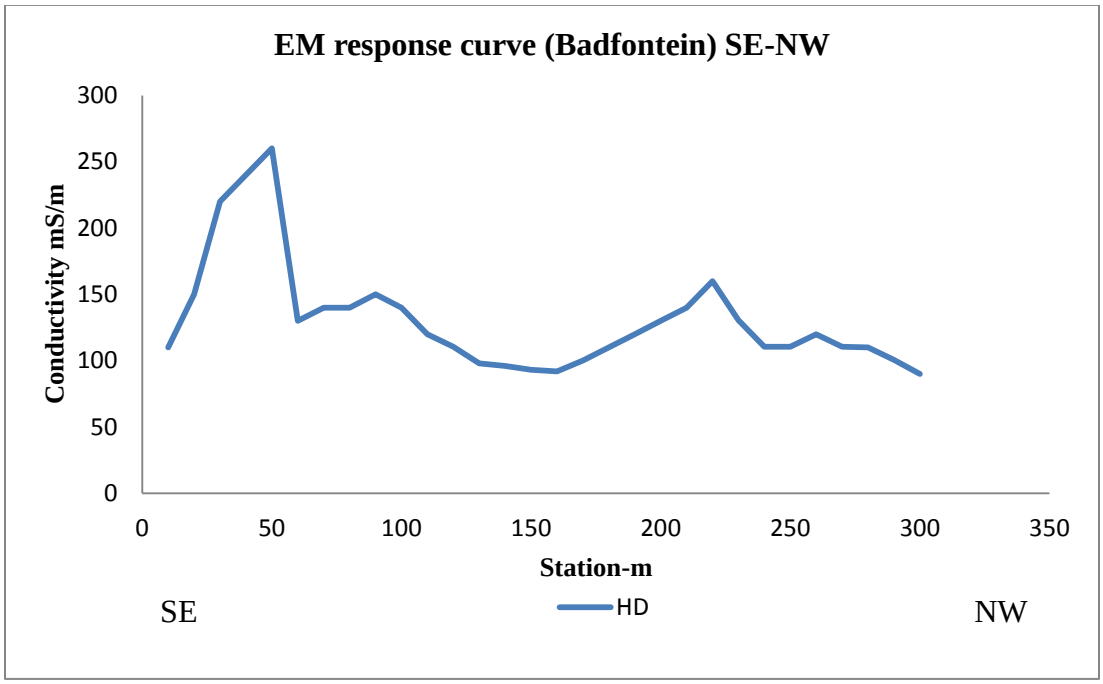

Figure 7- 46: Badfontein line (intercoil 20 m)

The Badfontein hot spring (Figure 7.47 left) seems to discharge a lot of water too, evidence of flow structure was seen around the spring with intense weathering (Figure 7.47 right).

Figure 7- 47: (left) the Badfontein spa; (right), flow channels near the spring

7.7 Radiometric survey

108 samples were collected at Polile Tshisa, 66 samples at Aliwal North, and 82 samples at Badfontein. Their statistical representation can be seen in Table 7.1 below.

Table 7- 1: Statistical representation of Potassium, Uranium and Thorium in the three hot springs

	Polile Tshisa			**Aliwal North**			**Badfontein**		
	K[ppm]	U[ppm]	Th[ppm]	K[ppm]	U[ppm]	Th[ppm]	K[ppm]	U[ppm]	Th[ppm]
Minimum	0.0	0.0	3.30	0.30	0.00	0.30	0.30	0.0	0.30
Maximum	1.8	11.4	21.10	1.70	3.20	12.60	1.70	3.2	12.60
Mean	0.6	2.3	8.96	0.95	1.16	5.44	0.95	1.2	5.44
Median	0.6	2.0	7.65	0.90	1.00	5.35	0.90	1.0	5.35
Standard deviation	0.4	2.1	4.17	0.29	0.86	2.28	0.29	0.9	2.28
Variation coefficient	0.6	0.9	0.47	0.30	0.74	0.42	0.30	0.7	0.42
Skewness	0.7	1.4	0.72	0.38	0.45	0.81	0.38	0.5	0.81
Kurtosis	0.2	3.1	-0.38	-0.24	-0.65	1.05	-0.24	-0.6	1.05

K shows an arithmetic mean of less than 1 ppm for all the three springs. At Polile Tshisa the uranium is a bit higher (2.3 ppm) compared to the two springs of Aliwal North and Badfontein.

The maximum values of thorium show that for all the three springs, the concentrations are higher comparatively to potassium and uranium. This might be explained by the fact that thorium is not easily dissolved in contact with groundwater.

For each spring, the mean values of K, U and Th have been represented in pie charts (Figure 7.48, 7.49 and 7.50). The thorium in soil has a proportion of 75, 69 and 72 % at Polile Tshisa, Aliwal and Badfontein respectively.

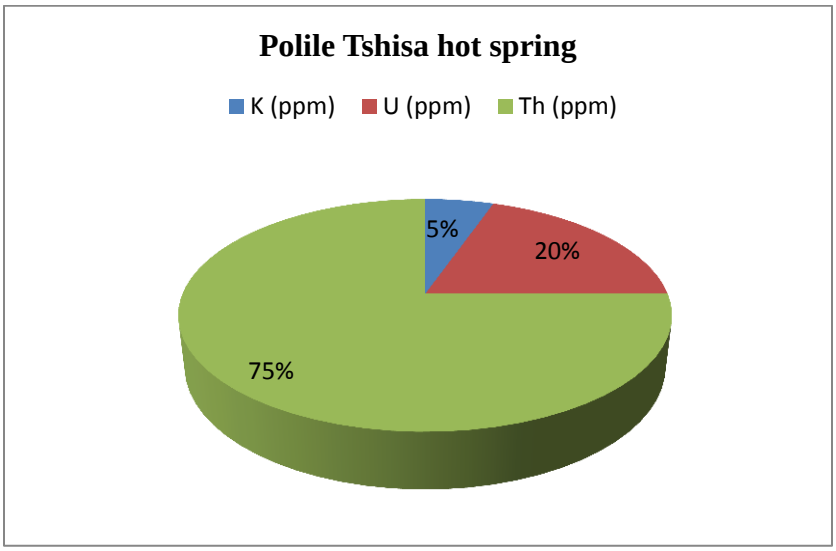

Figure 7- 48: Percentage proportions of K, U and Th at Polile Tshisa

The uranium has a proportion of 20, 18 and 15 % and the potassium has a proportion of 5, 13 and 13 % at Polile Tshisa, Aliwal North and Badfontein respectively. Some monazite has been seen 20 km from the Polile Tshisa hot spring (Figure 4.12 d). Knowing that 1 µg/g is equal to 1 ppm, the arithmetic mean values for the three springs are U (2.3 ppm, 1.16 ppm and 1.2 ppm) and Th

(8.96 ppm, 5.44 ppm and 5.44 ppm). It can be mentioned that the uranium values are below the world average concentration of U = 2.8 µg/g as well as the thorium, the world average of thorium is 7.4 µg/g (UNCSEAR, 2000).

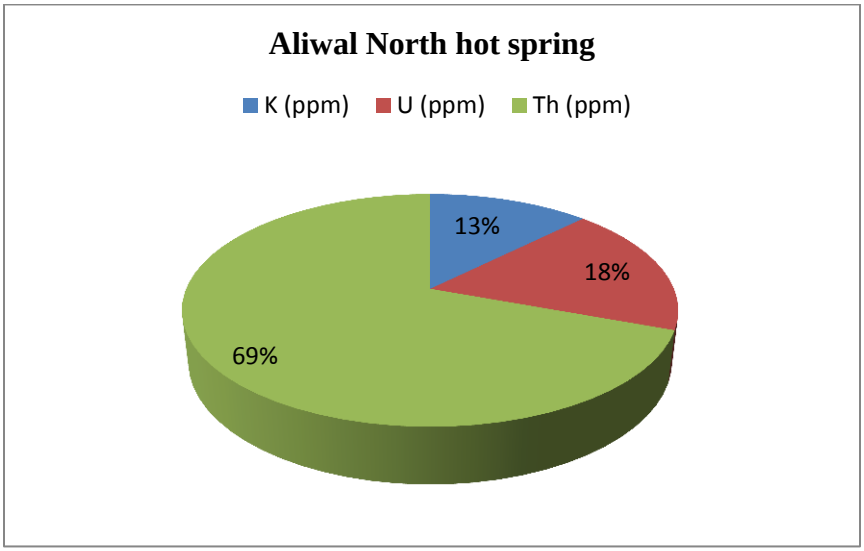

Figure 7- 49: Percentage proportions of K, U and Th at Aliwal North

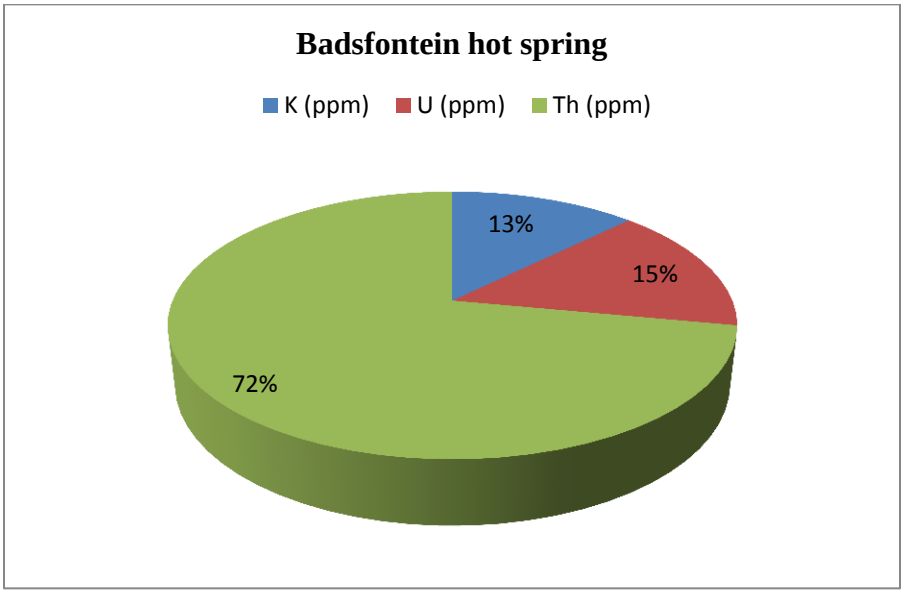

Figure 7- 50: Percentage proportions of K, U and Th at Badsfontein

At Polile Tshisa concentrations of K vary between 0 and 1.8 ppm with a predominant compositional range between 0.4 and 0.7 ppm (Figure 7.51 a), the concentrations of U vary between 0 and 11.4 ppm, a large part is covered by lower values (0 to 2 ppm: Figure 7.51 b), and concentrations of Th vary between 3.30 and 21 ppm. There seems to be equal distribution in concentration ranges of Th (0-7 ppm, 7-13 ppm, and 13-21 ppm: Figure 7.51 c).

The Polile Tshisa U/K ratio varies from 0 to 60 (Figure 7.51 d), signifying an increase in uranium relative to potassium; the uranium elemental concentration can only reach 10 ppm. This can also be explained by the fact that intense weathering occurred and potassium in K-bearing minerals have been leached out. There is not too much depletion in Th, the ratios U/Th (Figure 7.51 e) and K/Th (Figure 7.51 f) are very low (-0.2 to 1.2 and 0.01 to 0.22 respectively). At the Aliwal North hot spring the concentration in K varies between 0 and 1.6 ppm (Figure 7.52 a), but a vast area of the mapped zone is dominated by values of K in the interval of 0.5 to 0.8 ppm.

If at Polile Tshisa the concentration of uranium could reach 11.4 ppm, at Aliwal North the elemental uranium concentration (Figure 7.52 b) is very low (0 to 3.8 ppm). Compositional ranges between 1 and 1.7 ppm seems to predominate. The concentration of thorium (Figure 7.52 c) is also low compared to the one of Polile Tshisa. A great part of the area is dominated by concentrations of thorium varying between 4 and 7 ppm. The U/K (Figure 7.52 d) ratio reaches 38 implying an increase in uranium relative to potassium, 90 % of the mapped area has this ratio varying between 0 to 8. There is little decrease in Th, the U/Th (Figure 7.52 e) and K/Th (Figure 7.52 f) show values which are a little bit higher (0.2 to 4.6 and 0 to 2.8).

At Badfontein there are similarities in concentration regarding the potassium (Figure 7.53 a) as it was observed both at Aliwal North and Polile Tshisa (1.7, 1.7 and 1.8 ppm). The concentration

of uranium varies between 0 and 3 ppm (Figure 7.53 b). A great part has uranium concentration in the interval 0.7 and 1.3 ppm.

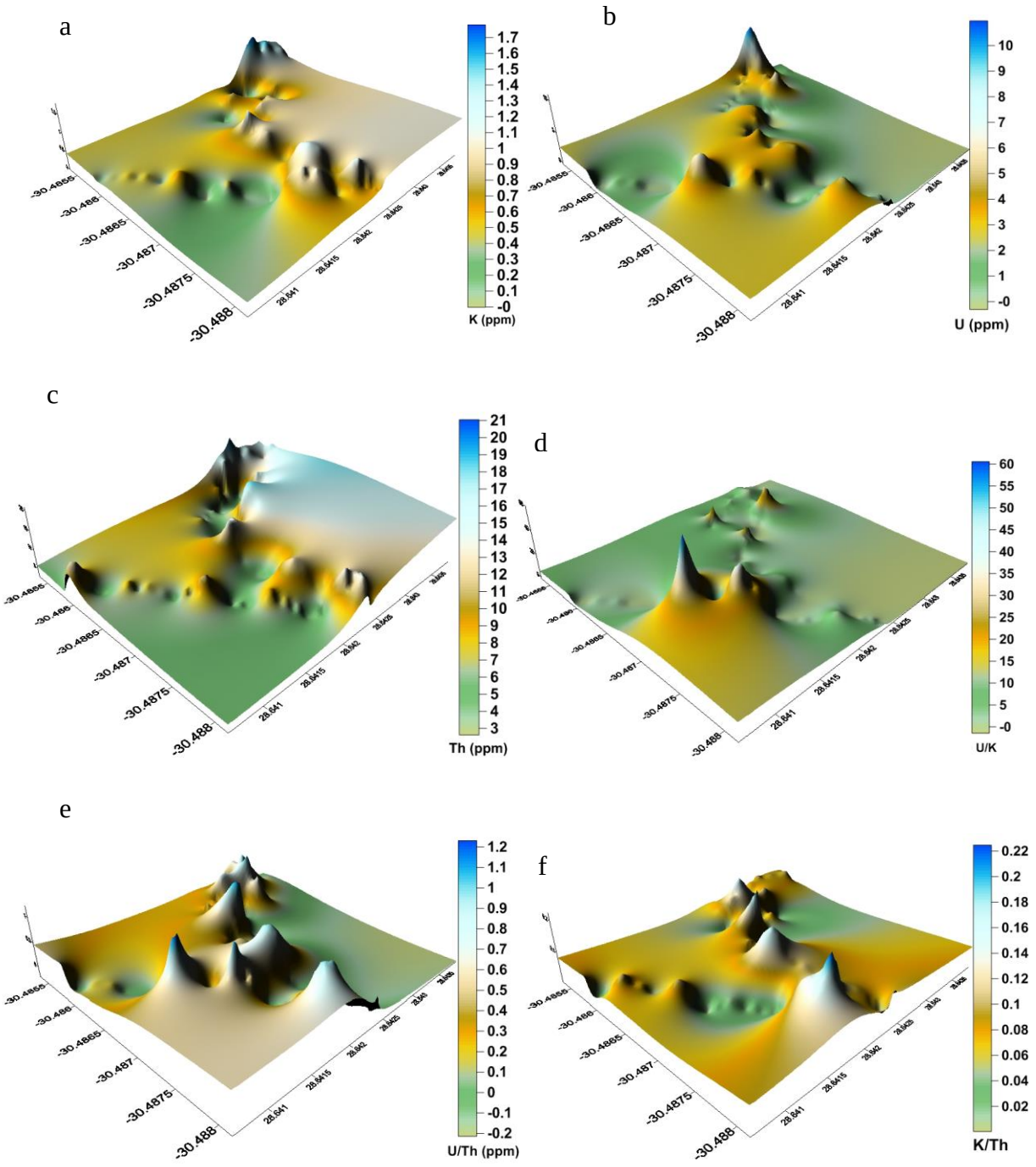

Figure 7- 51: Polile Tshisa; a, b, c: K, U and Th spatial distribution; d, e, f: ratio U/K, U/Th and K/Th

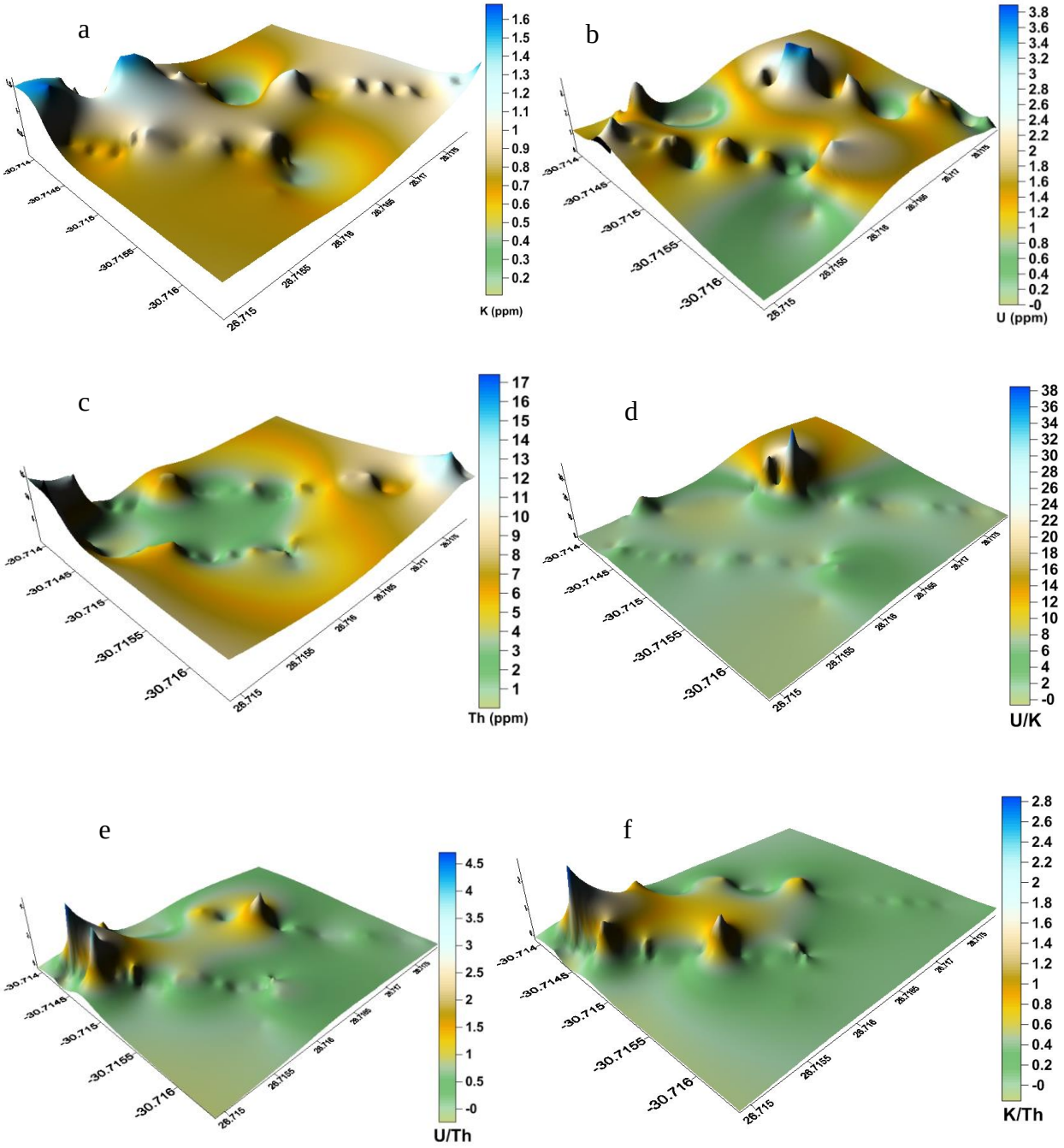

Figure 7- 52: Aliwal North; a, b, c: K, U and Th spatial distribution; d, e, f: ratio of U/K, U/Th and K/Th

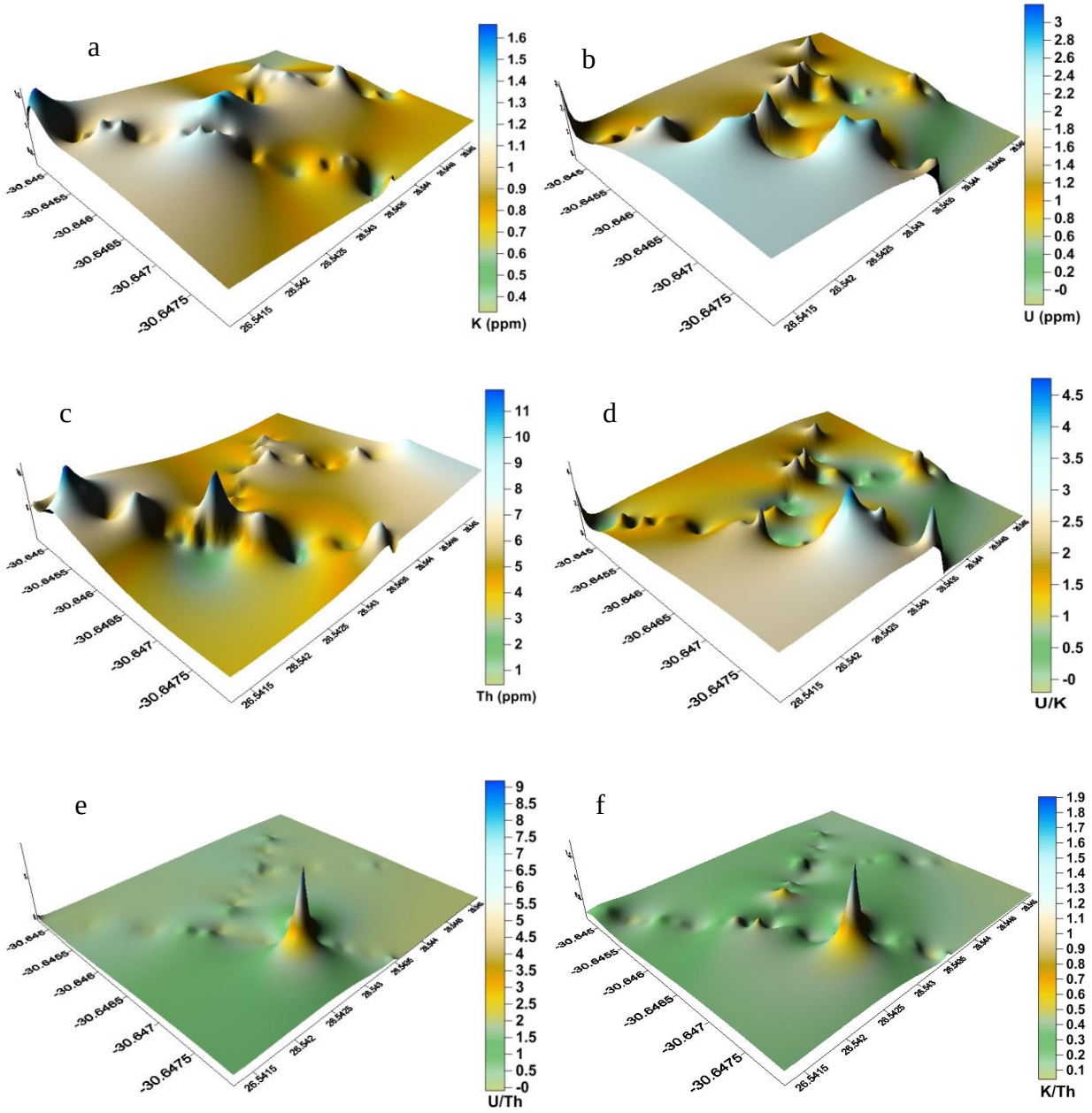

Figure 7- 53: Badfontein; a, b, c : K, U, Th spatial distribution; d, e, f: ratio of U/K, U/Th and K/Th

The thorium concentration is low compared to the two previous springs (0 to 11.5 ppm: Figure 7.53 c). Eighty percent of the area is dominated by elemental thorium concentrations in the interval between 3.5 and 5.5 ppm. The U/K ratio is limited (-0.2-4.6, Figure 7.53 d), the U/Th is a bit higher and can reach 9 (Figure 7.53 e) only on one percent of the total area. This can also be applied to K/Th (Figure 7.53 f), ninety-five percent of the mapped are is covered by K/Th ratios between 0 and 0.4.

For all the three hot springs, concentrations of uranium, potassium and thorium can be seen in Table R (Polile Tshisa), S (Aliwal North), and T (Badfontein) in Appendix B.

7.8 Summary

This project targeted neotectonic zones in the Eastern Cape Province. Three hot springs in the northern neotectonic belt were selected for geophysical characterization using the magnetic, electromagnetic and radiometric data. These three hot spring are controlled by a regional neotectonic fault oriented E-W. Their selection was motivated by the induced neotectonic activity by the circulation of groundwater at great depths, and seismicity of the belt.

Magnetic highs like those observed at the Polile Tshisa hot springs are related to the occurrence of dolerite dykes, which are always good indicators for groundwater target in the Karoo aquifers. The negative peaks in the magnetic profiles (Badfontein) may be related to lower susceptibilities minerals, but it can possibly be related to the occurrence of a fault. The profiles derived from magnetic lines at Aliwal North show that there may be a dolerite sill below. Badfontein magnetic profile show that the magnetic signal does not vary much, but depicted positive and negative peaks point in favour of a dolerite dyke and a fault respectively.

The electromagnetic response curves show that all features can be found in this three hot springs: dolerite dykes, faults or fractures, weathered and unweathered rocks, seepages, disturbed bedrock.

Radiometric data indicate high concentration of thorium relative to potassium and uranium in all the three springs. The increasing uranium derived from the U/K ratios is related to the leaching of potassium; to the contrary the U/Th ratios indicate no significant variation, the thorium is not easily dissolved by groundwater.

8. DISCUSSION

Neotectonics is still occurring in the Eastern Cape, this province used to be considered as one of the quiescent in South Africa; the map of earthquakes from 1620 to 2008 as reported in the South African Seismological Database (SANSD) and re-assessed by Singh et al. (2009) confirms this idea, which is a bit contrary to the findings in this study. Seismic epicenters of the southern Africa region downloaded in 2011 from the IRIS website as can be seen in Figure 4.38, and Figure 6.39, indicate that the Eastern Cape is seismically active. In continental intraplate configuration like the case of South Africa, seismic epicenters are located on lineaments (e.g. Meisser and Wever, 1986). These lineaments can be targeted for potentially high yield aquifers. It was found that the three major structures have seismic epicenters aligned along them. These three structures are the Fort Beaufort Fracture, Grahamstown Fracture (e.g. Figure 6.39) and the Eastern Cape Great Lineament (e.g. Figure 4. 38). Madi and Zhao (2010) made mention of recurrence of seismic activities in the area of Grahamstown in the south as recorded by the Council for Geoscience from 1850 to 2007. Seismic risk assessment is a potential tool to predict areas where nuclear wastes can be stored in order to avoid groundwater contamination. In the Eastern Cape only a small area located south of the big seismic belt near the country of Lesotho and north of the southern neotectonic belt is free from seismic activities (Figure 6.39). This is the unique place, which comprises the town of Queenstown that can be used for storing nuclear wastes.

The Sobel operator has been proved to be an efficient technique in remote sensing to extract lineaments. From lineament extraction, the eastern neotectonic belt can be considered as the second neotectonic domain of the province because of the intensity of lineaments. Kumanan (2001) has found that lineament density maxima zones and lineament intersections were buffered

out as possible neotectonics zones. This can be a good highlight from the present project, which can help to target productive aquifers. On the other hand the normalized difference vegetation index (NDVI) performed on some satellite images clearly indicate that the quality of chlorophyll is high. This can only be related to healthy vegetation, which is in turn connected to more groundwater percolation favoured by the occurrence of lineaments as surface expression of brittle structures below. Moreover, what has been called as the Eastern Cape Great Lineament (ECGL) north of the town of Grahamstown has a geomorphology that is highly favourable to be considered as a major catchment. Seismic epicenters present within it have possibly reactivated faults and fractures, and thus contribute to the circulation of groundwater. The Grahamstown fracture is considered as a splay of the ECGL, which displays a graben-like morphology.

On the geomorphologic point of view, the modelling of surface topography has indicated that elevations in grid 3327 towards the west do not exceed 450 m. To the contrary the grid 3228, which is more in the east, has elevations that can reach 1020 m. Though the elevations are not uniform in this grid, the higher surface topography of 1020 m can be related to Cenozoic uplift (e.g. Esthuizen, 2008). In the northern neotectonic belt near the country of Lesotho the elevation can reach 2000 m. This higher topography is the source of increasing stress in the lithosphere triggering earthquakes (e.g Steinberger et al., 2001). The east-west big seismic belt that stretches from the east coast to Koffiefontein is located in this area. It belongs to the Senqu seismotectonic belt or Kokstad-Koffiefontein seismic belt (e.g. Hartnady, 1998; Fernandez and Du Plessis, 1992).

Seismic lines offshore that were used for the characterization of the subsurface have revealed the presence of some faults. These faults probably underwent neotectonic activity, and may be

related to the major fracture offshore known as the Agulhas Falkland Fractured Zone (AFFZ) along the east coast in the Indian Ocean. In early Oligocene times the Agulhas Ridge was tectono-magmatically reactivated (e.g. Uenzelmann-Nieben and Gohl, 2004). Parsiegla et al. (2007) found that the tectonic motion seems to be sub vertical instead of strike-slip along the re-activated part of the fracture zone, thus this subvertical motion can then be related to the Quaternary uplift along the eastern neotectonic belt. Offshore in the south west Indian Ocean, Ben-Avraham (1995) has indicated that renewal of tectonic activity probably took place along several segments of the AFFZ. The lateral thickening of sediments in a wedge-shape style, which is interpreted as deriving from a progressive tilting, can also be related to the Amatole-Swaziland uplift that took place during the Quaternary. Few fold structures can also be seen, these folds are the result of compressional stress, probably the Wegener Stress Anomaly. Andreoli et al. (2006) reported that neotectonics activity in southern Africa is also related to the Wegener Stress Anomaly, which stretches from south Angola to South Africa in a NW-SE direction. The Wegener Stress Anomaly orientation dovetails the seismic lines that were set offshore. On land the seismic lines KW have depicted weathered layers, related possibly to zones of higher permeability such as faults, in which groundwater percolates easily to intensify the weathering. The profile of the weathered layers is typical of consolidated sediments; Lawton (1989) has found a very wavy profile, typical of unconsolidated material in the Canadian Rocky Mountain. The Amatole Swaziland uplift is possibly the origin of the meso-scale fault observed on a dolerite sill overlain by sedimentary rocks in King Williams Town. Andreoli (pers. comm.) indicated that this uplift may have generated new fractures in the Karoo aquifers.

The structural orientation in this study indicates clearly that horizontal or subhorizontal structures are predominant in the tillite quarry. These structures are caused by northwest

compression and horizontal or subhorizontal extension according to the interpretation of the data from the Schmidt net. This trend is in agreement with the NW structural control in the Eastern Cape Province of South Africa as postulated by Lewis (2008). Microscopic study further evidences fractures developed along the contact of breccias and matrix. Mechanically, the breccias fragments are competent while the matrix is more ductile.

Field observation clearly shows that the extensional fractures were found in the granite and quartzite breccias, but rather closed fractures in the tillite matrix. The difference in mechanical behaviour when fracturing occurs to allow water circulation indicates that the breccias of granite and quartzite are the first to undergo brittle deformation, followed by the tillite. The tillite is more ductile despite the fact that microscopic fractures can be seen in the matrix. The mineralization time is most probably Quaternary, which is an important factor to control the Grahamstown kaolin deposit. This study is the first to report on this phenomenon.

On the other hand, quartz veins were developed along joints and faults, which were observed in the kaolin deposit and tillite. A quartz vein as a conduit directed water to underground, and also served as traps, i.e. fractured reservoir to allow water to chemically weather materials for longer time. Quartz veins also prevent water from being lost through the footwall. The evidence is that fresh tillite below a quartz vein is well preserved in its footwall.

According to the methods of Delvaux and Spener (2003), rotational optimization confirms the NW-SE compressional stress, which has generated more of the fractures and faults that occur in the kaolin deposit in Grahamstown.

Geological occurrences of kaolin minerals formed by weathering of non-layer silicate particularly of feldspars products have been documented in modern weathering products in the

southern Appalachian region (Sand, 1956). Enrichment of granite breccias and albite in the matrix proves that the tillite contains materials such as feldspar to produce kaolin. The geochemical analysis of samples by Makhado (2007) indicated there is a clear evolution of fresh, weathered tillite to kaolin through a chemical weathering process. Enrichment of quartz in the tillite matrix was identified in this study. In addition, quartz veins, specifically micro veins occur in the kaolin deposit. This is well in line with the low quality of kaolin due to high concentration of SiO_2 in the Grahamstown tillite.

The neotectonics belt near the country of Lesotho is also known for the occurrence of many hot springs, which are indicative of circulation of groundwater at great depths, the occurrence of these springs indicate that they are connected by a major neotectonic fault that stretches from west (Aliwal North) to east (Polile Tshisa). The flooding that occurred in an abnormally well-developed fissure zone, through which lot of water gushed out during the construction of the Orange-Fish tunnel (Olivier, 1975) is a proof that neotectonics is at work in the northern neotectonic belt. Whittingan (1970) noted that the flow of the thermal spring at Badfontein increased markedly for a period of at least three months after a local earthquake.

Strongest magnetic values at the three hot springs can indicate the presence of dolerite dykes or sills, or even unweathered solid geological basement (e.g. Street et al., 2002), and movement along fault. At Polile Tshisa the magnetic profile in Figure 7.13 is typical of a fault that has moved two blocks with a dip-slip component. The water at Polile Tshisa wells up at three different places, which are connected by a fault that has possibly cut across a dolerite dyke (Figure 7.12). The Karoo rocks were intruded by dolerite dykes and sills. Electromagnetic profiles in all the three hot springs are indicative of faults or fractures at some places and dolerite

dykes at others. These profiles also show that the weathering process is underway. At Polile Tshisa combined profiles of both horizontal and vertical dipole show that the horizontal dipole is higher than the vertical one at some places, this is always an indication for a shallow regolith (e.g. Barry et al., 2010). Negative electromagnetic values like the one observed at Aliwal North (-21 mS/m) may be showing that there is a dolerite dyke below the surface, dolerite dykes are always used for targeting groundwater in the Karoo. The concentrations of thorium in all the three hot springs is very high (69-75%) compared to uranium (15-20%) and potassium (5-13%). High levels of thorium are normally related to minerals such as monazite, which is hardly dissolved in water. Some monazites have been observed in the area of the Polile Tshisa hot spring. The ratios of U/Th, U/K and K/Th as indicated in this study are indicative of depletion or enrichment radioisotopes (e.g. Tzortzis and Tsertos, 2004). At Polile Tshisa for instance U/K ratio varies from 0 to 60, at Aliwal North from 0 to 38, and at Badfontein this ratio is very limited. There is considerable enrichment of uranium at Polile Tshisa and Aliwal North, this trend is not applicable to Badfontein. This might be related to the increased flow of water as noted by Wittingham (1970), which has contributed to the dissolution of thorium.

9. CONCLUSIONS

Neotectonics is active in the Eastern Cape Province as can be seen from the recent map of seismic epicenters. It is an important tool in targeting potentially high yield aquifers for two reasons: 1) it can reactivate old fractures or faults; 2) it can create new fractures or faults. All these two reasons imply more opportunities for the circulation of groundwater in the aquifers.

This study has also helped not only to find and characterize targets favourable for groundwater, but also to propose or predict areas that can be used for environmental purposes. In fact nuclear wastes in the Eastern Cape can be stored in the area of Queenstown south of the Senqu Seismotectonic belt (Kokstad-Koffiefontein seismic belt),which is inactive and scarcely affected by lineaments.

Surface topography modelling in this study has highlighted the flow direction of surface water, it was found that most vectors are oriented in the E-W direction; this can be taken into consideration during groundwater target and exploration. The eastern neotectonics belt is a good target for groundwater, it is characterized by a high density of lineaments, and most of them are oriented northwest-southeast.

Seismic lines have helped characterize the subsurface, offshore neotectonics faults and folds occur. On land some weathered layers in consolidated sediments are a good indication for groundwater target, the weathered layers can only be in structures where there is great circulation of groundwater.

In the southern neotectonic belt, field observations have clearly indicated that the kaolinisation is controlled by extensional structures and quartz veins while the parent rock is the Dwyka tillite. Fractures allow water to penetrate into the Dwyka tillite and accelerate chemical weathering.

Parts of the more kaolinised tillite are extensively jointed, and fractured. Rotational optimisation used in this study has indicated that the compressional stress is oriented NW-SE, and the extentional stress is oriented NE-SW.

The quartz veins indicate that the Grahamstown kaolin deposits are of two categories. The first ones developed due to weathering of the parent sedimentary rock by the percolation of water through fractures with no presence of quartz at all. The second ones are deposits in which quartz veins played an important part in the kaolinisation process by trapping the water. It is worthwhile noting that there have been unreported thermal and neotectonic events in this region although not on a large scale.

The hot springs in the Eastern Cape northern neotectonic belt are connected or occur along an east-west neotectonic fault that is a regional structure. The magnetic and electromagnetic data have helped to identify fractured or faulted zones with different degrees of weathering, with in some places the presence of dolerite dykes, known for their potential to localise groundwater in the Karoo. High conductances are mainly related to clayey soils and lower conductances to sandy soils.

This project has given fundemental highlights to characterize the major and potential good yield aquifers by using remote sensing, by examining the seismicity, the structures, the subsurface offshore and onland, and the geophysical data. This project is important since it has also brought in the environmental impact through examination of seismic risk assessment. This can help in targetting places for storing nuclear wastes so that the groundwater may not be contaminated in the Eastern Cape Province, South Africa.

It is recommended that the Eastern Cape Great Lineament (ECGL) and the Eastern Cape northern neotectonic belt be surveyed by airbone gravity and magnetic methods. In the case of the northern neotectonic belt, geophysical survey can help depicting the regional east-west oriented inferred fault connecting the seven hot springs, among which the Polie Tshisa, Aliwal North, and Badfontein hot springs. The geophysical survey can also give detailed structures of the ECGL.

10. REFERENCES

Al-amri, S. S. et al (2010). A Comparative Study of Removal Noise from Remote Sensing Image. *Int. J. of Computer Science Issues*,7, no. 1, pp. 32 - 35.

Al-Bakri, J.T. and Al-Jahmany, Y.Y. (2013). Application of GIS and Remote Sensing to Groundwater Exploration in Al-Wala Basin in Jordan. *Journal of Water Resource and Protection*, vol. 5, 962-971

Ali E. A. , El Khidir, S. O. , Babikir, I. A. A., Abdelrahman, E. M. (2012). Landsat ETM+7 Digital Image Processing Techniques for Lithological and Structural Lineament Enhancement: Case Study Around Abidiya Area, Sudan. *Open Rem. Sens*.J.5:83-89

Andersen, N. J. B., and Ainslie, L. C., (1994). Neotectonic reactivation-an aid to the location of groundwater. *African Geoscience Review*, 1, pp. 1-10.

Andreoli, M.A.G.; Norman, N.G.; van der Vlugt, R.; von Veh, M.; Andersen, N.J.B. and Hambleton-Jones, B.B. (1989). Geology of the coastal strip between Gansbaai and Waenhuiskrans, Volume 1: Geological description of the project area. Eskom Southern Cape Project. Investigations for the siting of nuclear power stations. Progress Report no. 10. PIN: 1133 GEA 845.

Andreoli, M.A.G., Hambleton-Jones, B.B., Andersen, N.J.B., Faurie, J.M., Raubenheimer, E., Von Veh, M., Antoine, L. And McMillan, L.K. (1990). Continental margins neotectonics in South Africa: a nuclear siting perspective. *Abstr. Vol. 23rd Congr. Geol. Soc. S. Afr*., Cape Town, pp. 12-15 (extended abstract).

Andreoli, M.A.G., Doucouré, M., Van Bever Donker, J., Faurie, J.N. and Fouché, J. (1995). The Ceres-Prince Edward Fabric (CPEF). an anomalous neotectonic domain in the southern sector of the African plate. *Absr. Vol. 25th Congr. Geol. Soc. S. Afr.*, Johannesburg, Vol. 1, 434-437 (extended abstract).

Andreoli, M. A. G., M. Doucoure, J. Van Bever Donker, D. Brandt, and N. J. B. Andersen (1996). Neotectonics of southern Africa: A review. *Africa Geoscience Review* 3 (1), 1–16.

Andreoli, M.A.G., Hart, R.J., Ashwal, L.D. and Coetzee, H. (2006). Correlation between U, Th content and metamorphic grade in the Western Namaqualand belt, South Africa, with implications for radioactive heating of the crust. *Journal of Petrology*, 47, pp.1095–1118.

Angelier, J., and Mechler P. (1977), Sur une method graphique de recherche des contraintes principales egalement utilisable en tectonique et en seismologie: La methode des diedres droites, Bull. Soc. Geol. Fr., 7(19), 1309 – 1318.

Anhaeusser, C. R., and Wilson, J. F. (1981). The granitic gneiss-greenstone shield *in* Precambrian of the southern hemisphere (D.R. Hunter, ed.) Elsevier, Amsterdam, pp. 423-494.

Babu, M. N. S., Somashekar, R. K., Kumar, S. A., Shivanna, K., Krishnamurthy, V., Eappen, K. P. (2007). Concentration of uranium levels in groundwater, *Int. J. Environ. Sci. Tech*., 5 (2), pp. 263-266.

Ballard, D., and Brown, C. (1982). Computer vision, Prentice-Hall Inc., New York.

Barry, B., Kortatsi, B., Forkuor, G., Gumma, M. K., Namara, R., Rebelo, L-M., van den Berg, J., and Laube,W. (2010). Shallow groundwater in the Atankwidi Catchment of the White Volta Basin: Current status andfuture sustainability. Colombo, Sri Lanka: International Water Management Institute. 30p. (IWMI ResearchReport 139). doi:10.5337/2010.234

Barth, A., Reinecker, J., and Heidbach, O. (2008). Stress derivation from earthquake focal mechanisms, Guidelines: Focal mechanisms, World Stress Map Project, Postdam, 8 p.

Beijachund, M., Kijko, A., and Durrheim, R., (2009). Seismotectonic models for South Africa: synthesis of geoscientific information, problems, and their way forward. *Seismological Reasearch Letters*, vol. 80, pp. 33-65

Ben-Avraham, Z. (1995). Neotectonic activity offshore southeast Africa and its implications. *S.Afr.Tydskr.Geol*, 1995, 98(2), 202-207.

Benson, R.C., Glaccum, R.and Noel M. (1984). Geophysical techniques for sensing buried wastes and waste migration (NTIS PB84-198449). Prepared for U.S. EPA Environmental Monitoring Systems Laboratory, Las Vegas, 236 p.

Bird,P., Ben-Avraham, Z., Schubert, G., Andreoli, M. A. G., and Viola, G., (2006). Patterns of stress and strain rate in southern Africa. *J. Geophys. Res*., vol.111, B08.

Boggs, J. S. (2001). Principles of sedimentology and stratigraphy. Upper Saddle River: Prentice-Hall, Inc.

Botha,J.F., Verwey,J.P., Van der Voort, I., Vivier, J.J.P., Buys, J., Colliston, W.P. and Lock, J.C., (1998). Karoo aquifers, their geology, geometry and physical properties. WRC Report N^{o} 487/1/98.

Bott, M. H. P. (1959). The mechanism of oblique-slip fulting. *Geological Magazine*, 96, pp. 109-117.

Brandt, M. (2000). A review of the reservoir induced seismicity at the Katse Dam, Kingdom of Lesotho, November 1995 to March 1999. Cant. Scient. diss., University of Bergen, Norway.

Burke, K. (1996). The African Plate. *South African Journal of Geology*, 99 (4), pp. 341–409.

Burke, K., and Gunnell, Y. (2008). The African Erosion Surface: A continental-scale synthesis of geomorphology, tectonics, and environmental change over the past 180 million years: Geological Society of America Memoir 201, pp. 66.

Burnett, D.O. (2011). Use of Remote Sensing for Groundwater Mapping in Haiti. Earthzine, Fostering Earth Observation & Global Awareness.

Catuneanu, O., Hancox, P. J., and Rubidge, B. S. (1998). Reciprocal flexural behavior and contrasting stratigraphies: a new basin development model for the Karoo retroarc foreland system, South Africa, *Basin Research*, 10, pp. 417-439.

Catuneanu, O., Abreu, V., Bhattacharya, J.P., Blum, M.D., Dalrymple, R.W., Eriksson, P.G., Fielding, C.R., Fisher, W.L., Galloway, W.E., Gibling, M.R., Giles, K.A., Holbrook, J.M., Jordan, R., Kendall, C.G.St.C., Macurda, B., Martinsen, O.J., Miall, A.D., Neal, J.E., Nummedal, D., Pomar, L., Posamentier, H.W., Pratt, B.R., Sarg, J.F., Shanley, K.W., Steel, R.J., Strasser, A., Tucker, M.E., Winker, C. (2009). Towards the standardization of sequence stratigraphy. *Earth-Science* Reviews 92, pp.1–33.

Cheriyadat, A., and Bruce, L. (2003). Decision Level Fusion with Best Bases for Hyperspectral Classification, Proceedings of the IEEE Workshop on Advances in Techniques for Analysis of Remotely Sensed Data, pp. 399:406.

Contes, A.and Carla A. (2011). Lineament mapping for groundwater exploration using remotely sensed imagery in a karstterrain: Rio Tanama and Rio de Arecibo basins in the northern karst of Puerto Rico. Michigan Technol. Univ.77:1505814

Cook S.E., Corner, R.J., Gravoes, P.R. & Grealish, G.J. (1996). Use of gamma radiometric data for soil mapping: *Australian Journal of Soil Research* 34, pp. 183-194.

Cracknell, A.P., and Hayes, L.W.B. (1993). Introduction to Remote Sensing. Taylor and Francis, London.

Daley, T. M., McEvilly, T. V., and Majer, E. L. (1988). Analysis of P and S waves for vertical seismic profile data from the Salton sea scientific drilling project, *Journal of Geopghysical Research*, vol. 93, 11, pp. 13,025-13,036

De Beer, C. H., (1990). Similtaneous folding in the western and southern branches of the Cape Fold Belt: *South African Journal of Geology*, 93, pp. 583-591.

De Beer, J. H. (1983). Geophysical studies in the southern Cape Province and models of the lithosphere in the Cape Fold Belt (A. P. G. Söhnge and I. W. Hälbisch, eds): Special Publication, *Geological Society of South Africa*, 12, pp. 57-64.

Delvaux, D., Moeys, R., Stapel, G. (1997). Paleostress reconstructions and geodynamics of the Baikal region, Central Asia. Part II: Cenozoic tectonic stress and fault kinematics. *Tectonophysics*, 282(1-4), pp. 1-38.

Delvaux, D., and Spener, B. (2003). New aspects of tectonic stress inversion with reference to the Tensor program, Annal Royal Museum for Central Africa, department of Geology-Mineralogy, Tervuren, Belgium.

Delvaux, D.A.S., Macheyeki, A.S., Kervyn, F., Petermans, T., Verbeeck, K., Temu, E.B., 2007. Earthquake geology of the Kanda fault system (Tanganyika – Rukwa rift, SW highlands of Tanzania). EGU General Assembly 2007, Vienna, Session TS3.3/ NH4.4 — Earthquake Geology. *Geophys. Res*. Abstr. 9, 09129.

De Swardt, A. M. J. and Rowsell, D. M. (1974). Note on the relationship between diagenesis and deformation in the Cape Fold Belt: Transactions, *Geological Society of South Africa*, 77, pp. 239-245

De Villiers, J. (1994). A review on the Cape orogeny: Annals, University of Stellenbosch, 22A, pp. 183-208.

Dingle, R.V. and Robson, S. (1985). Slumps, canyons and related features on the continental margin of East London, SE Africa (SW Indian Ocean). *Mar Geology*, 67, pp. 37-54.

Dobson, K. J., McDonald, R., Brown, R. W., Gallagher, K. S., and Finlay, M. (2010).Dating the emergence of the Africa Superswell: A window into mantle processes using combined (U-Th)/He and AFT thermochronology. EGU General Assembly, Vienna, Austria, pp.5167

Dunne, W. M., and Hancock, P. L. (1994). Paleostress analysis of small-scale brittle structures. In: Hancock, P. L. (ed.) Continental deformation. Pergamon, Oxford, pp. 101-120.

Ebbs, S.D., Brady, D. J., Kochian, L.V. (1998). Role of uranium speciation in the uptake and translocation of uranium by plants. *J. Exp. Bot*., 49 (324), 1183-1190.

Elmahdy. S. I. and Mohamed, M. M.(2012). Geological Lineament Detection, Characterization and Association with Groundwater Contamination in Carbonate Rocks of Musandam Peninsular Using Digital Elevation Model (DEM). *The Open Hydrology Journal*, 2012, 6, (Suppl 1-M3) 45-51

Esterhuizen, A. (2008). Mineral sands deposits of Africa. In: Africa Uncovered: Mineral Resources for the Future. *SEG-GSSA 2008 Conference*, Johannesburg, South Africa.

Fanning, D. S., and Jackson, M. L. (1966). Clay mineral weathering in Southern Wisconsin soils developed in loess and in shale-derived till: *Clays and Clay Minerals* 13, pp. pp.175-191. [Pergamon Press, New York].

Fernández, L. M. and du Plessis, A. (1992). Seismic Hazard Maps for Southern Africa, Council for Geoscience, *Geological Survey of South Africa*, Pretoria.

Flint, S.S., Hodgson, D.M, Sprague, A.R., Brunt, R.L., Van der Merwe, W.C., Figueiredo, J., Prélat, A., Box, D., Di Celma, C. and Kavanagh, J.P. (2011). Depositional architecture and sequence stratigraphy 41 of the Karoo basin floor to shelf edge succession, Laingsburg depocentre, South Africa. *Marine and Petroleum Geology*, 28, pp. 658-674.

Frankel, J. J., and Kent, L. E. (1937). Grahamstown surface quartzites: Trans. Geol. Soc. S. Afr., 11, pp. 1-42.

Friese, A.E.W., Swartz, H.G., Titus, R., Fielies, A., Davids, S., Domonay, R. (2006). Geomechanical modeling as a tool for groundwater exploration on fractured rock aquifers in the Namaqualand region, South Africa. WRC Report N^{o} 1117/1/06.

Godio, A., Chiara, P. Gaill, C. C. and Naldi, M. (1998). A Combined Geophysical Survey for Hydrogeological Purposes in North-Eastern Italy. *Proceedings of IV Meeting Environmental and Engineering Geophysial Society*, pp. 209-212.

Goedhart, M.L. (1997). Neotectonic control on drainage evolution in the Algoa Basin, southeastern Cape Province. *S. Afr. J. Geol*. 1997, 100(1), pp. 43-52.

Goedhart, M.L. and Booth, P.W.K. (2009). Early Holocene extensional tectonics in the south-eastern Cape Fold Belt, South Africa. Short Paper in the proceedings CD of the 11th South African Geophysical Association (SAGA). *Biennial Technical Meeting and Exhibition, and Inkaba ye Afrika*, Phase II workshop, 13-18, Swaziland.

Gonzalez, R., and Woods, R. (1992). Digital Image Processing, Addison-Wesley Publishing Company.

Guo, G., and Carroll, H. B. (1995). A New Methodology for Oil and Gas Exploration Using Remote Sensing Data and Surface Fracture Analysis. *DOE Report* No. NIPER/BDM-0163.

Hälbisch, I. W. and Swardt, J. (1983). Structural zoning and dynamic history of the cover rocks in the Cape Fold Belt *in* Geodynamics of the Cape Fold Belt (A. P. G. Söhnge and I. W. Hälbisch, eds): Special Publication, *Geological Society of South Africa*, 12, pp. 75-100.

Hälbisch, I. W., Fitch, F. J. and Miller, J. A., (1983). Dating the Cape orogeny *in* Geodynamics of the Cape Fold Belt (A. P. G. Söhnge and I. W. Hälbisch, eds): Special Publication, *Geological Society of South Africa*, 12, p. 149-164.

Hardage, B. A., 1985, Vertical seismic profiling, Part A, principles (2d ed.): Amsterdam, Elsevier, 509 p

Harris, C., Marsh, J.S., Duncan, A.R., and Erlank, A.J., (1990). The petrology of the Kirwan Basalts of Dronning Maud Land, Antarctica, *Petrol*., 31, pp. 341-369.

Hartnady, C.J.H., (1998). Lesotho seismotectonics: SE African SCR in transition. Amer. Geophys. Un. Chapman Conference on Stable Continental Region (SCR) Earthquakes, *National Geophysical Research Institute*, Hyderabad, India (January 25-29), Abstract, Volume, pp. 23

Herman, J., Etzler, P. J., Wilson, M. L. and Vincent, R. K. (1986). Remote sensing Study of the Mid-continent Geophysical Anomaly in Iowa. *Paper presented at the Society of Mining Engineering Fall Meeting*, St. Louis, Missouri.

Hess, C. T., Michel, J., Harton, T. R., Procured, H. M. and Coniglio, W. A., (1985). The occurrences of radioactivity in public water supplies in United States., *Health Phys*., 48 (5), pp. 553-86

Hill, R.S. (1988). Quaternary faulting in the south-eastern Cape Province. *S.Afr.J.Geol*.1988, 91(3), pp. 399-403.

Illgner, P. M. (1995). The morphology and sedimentology of two unconsolidated quaternary debris slope deposits in the Alexandria district, Cape Province.

Isiorho, S.A. (1985). 'The significance of lineaments mapped from remotely sensed images of the 1:250 000 Lau Sheet in the Benue trough of Nigeria', *International Journal of Remote Sensing*, 6 (6), pp. 911-918.

Jacob, R.E., Mitha, V.R. and MacPherson, D. (2004). The kaolinitic clay deposits of Beaconsfield, north of Grahamstown. *South Africa Journal of Science*, November/ December 2004.

Johnson, M. R. (1990). Provenance and tectonic setting of the Cape-Karoo Basin in the Eastern Cape Province: Abstracts, Geocongress, 90, Cape Town, *Geological Society of South Africa*, pp. 690-693.

Johnson, M. R., Anhaeusser, C.R. and Thomas, R. J. (2006). The Geology of South Africa. *Geological Society of South Africa* Johannesburg*/ Council for Geoscienc,* Pretoria. 691pp.

Joubert, P. (1986). Namaqualand – a model of Proterozoic accretion: Transactions, *Geological Society of South Africa*, 89 (2), pp. 79-86.

Joubert, A., Beukes G. J., Visser J. N. J., and de Bruin, H. (1991). A note on fluorite in Late Pleistocene thermal spring deposits at Florisbad, Orange Free State. *South African Journal of Geology* 94, 174–177.

Karnieli, A., Meisels, A., Fisher, L., and Arkin, Y. (1996). Automatic extraction and evaluation of geological linear features from digital remote sensing data using a Hough transform, *Photographic Enginnering and Remote Ssensing*, vol. 62 (5), pp. 525-531.

Kent, L. E. (1949). The thermal waters of the Union of South Africa and South West Africa. *Trans. Geol. Soc. S.Afr*, vol. 52, pp. 231-264.

Kent, L. E. (1981). The thermal springs of south-eastern Transvaal and northern Natal. *Annals of the Geological Survey of South Africa* **15**, 51–67

Khattri, K., (1973). Earthquake focal mechanism studies─A review, Earth Sci. Rev., 9, pp.19-63.

Kisslinger, C., Bowman, J.R., and Koch, K. (1981). Procedures for computing focal mechanisms from local (SV/P) data, *Bull. Seism. Soc. Am.*, 71, pp. 1719–1729.

Kumanan, C.J. (2001). Remote sensing revealed morphotectonic anomalies as a tool to neotectonic mapping – experience from South India. In Proceedings of the *22nd Asian Conference on Remote Sensing*.

Lachaal, F., Mlayah, A., Anane, M., Bédir, M., Tarhouni, J., and Leduc, C. (2013). Comprehension and hydrogeological conceptualizationof aquifer in arid and semi-arid regions using integrated hydrogeological information system: case of the deep aquifer of Zéramdine-Béni Hassen (east-central Tunisia). *Arab J Geosci*, 6, pp. 2655–2671.

Lawton, D. C. (1989). Computation of refraction static corrections using first-break traveltime differences, Geophysics, vol. 54, 10, pp. 1289-1296

Lewis, C.A. (2008). Glaciations and glacial features. In: Lewis, C.A., (2008). Geomorphology of the Eastern Cape.

Lock, B. E. (1978). The Cape Fold Belt of South Africa: tectonic control of sedimentation: Proceedings, *Geological Association*, 89, pp. 263-281.

Lock, B. E. (1980). Flat-plate subduction and the Cape Fold Belt of South Africa: *Geology*, 8, pp. 35-39

Madi, K. and Zhao, B. (2010). Neotectonics and its applications for the exploration of groundwater in the Karoo fractured aquifers in the Eastern Cape, South Africa. MSc dissertation, University of Fort Hare, South Africa.

Maged. M., Mansor, S. and Hashim M (2009). Geologic mapping of United Arab Emirates using multispectral remotely sensed data. *Amer. J. Eng. Appl. Sci.,* 2, pp. 476-480.

Makhado, M. (2007). Geological resource assessment towards economic and social development in the Eastern Cape Province, South Africa. (unpubl.) MSc dissertation, University of Fort Hare, pp. 229.

Mahesh, H. M., Avadhani, D. N., Someshekarappa, H. M., Karunakara, N., Narayana, Y. and Siddappa, K. (2001). Uranium concentration in water samples in the environment of coastal Karnataka and Kaiga. *Proc. Nat. Sem. Atom. Energ. Ecol Environ*., pp. 113-116.

Marghany, M., and Hashim, M. (2010). Lineament mapping using multispectral remote sensing satellite data. *International Journal of the Physical Sciences* Vol. 5(10), pp. 1501-1507.

Maud, R.R. (1996). The macro-geomorphology of the Eastern Cape. In The Geomorphology of the Eastern Cape, South Africa, ed. C.A. Lewis, pp. 1–18. Grocott and Sherry Publishers, Grahamstown.

Maxwell, O., Ibrahim, N., and Uguwoke, P. E. (2012). Gamma ray assessment of subsurface water-rock interaction in Abuja from geological background and its effects in groundwater, Nigeria (Review article), *Advances in Life Science and Technology*, vol. 6.

McNeill, J.D. (1986). Electromagnetic Geophysical Mehods Applied to Ground Water Exploration and Evalution, *Developing World Water*, pp. 60

Meisser, R. and Wever, T. (1986). Intracontinental seismicity, strength of crustal units and the seismic signature of fault zones. Institüt für Geophysik, Neue Universitat, Oslhausentrasse, pp. 40-60, 2300 Kiel, F.R.G.

Mogaji, K. A., Aboyeji, O. S. and Omosuyi, G. O. (2011). Mapping of lineaments for groundwater targeting in basement complex area of Ondo State using remote sensed data. *International Journal of Water Resources and Environmental Engineering* Vol. 3(7), pp. 150-160.

Mohamed, A. (2010). Significance of surface lineaments for gas and oil exploration in part of Sabatayn Basin-Yemen, *Journal of Geography and Geology*, vol. 2 (1).

Newton, A. R. (1973). A gravity folding model for the Cape Fold Belt: Transactions, *Geological Society of South Africa*, 76(2), pp. 145-152.

Nton, M. E. and Easn, T. B. (2010). Sequence Stratigraphy of EMI Field, OFFSHORE Eastern Niger Delta, Nigeria, *European Journal of Scientific Research*, Vol.44, 1, pp.115-132.

Ölgen, M. K., (2004). Determining lineaments and geomorphic features using landsat 5-TM data on the Lower Bakircay Plain, Western Turkey. *Aegean Geographical Journal*, *13*, pp. 47-57, Izmir—TURKEY

Olivier, H. J. (1975). Geohydrological investigation of the flooding at shaft 2, Orange-Fish tunnel, North-Eastern Cape Province. *Transactions of the Geological Society of South Africa*, vol. 75, pp. 197-224.

Ollier, C. D. (1988). Deep weathering, groundwater and climate, Geografiska Annaler 70, A.

Pallacky, G. J., Ritsema, I. L., and De Jong, S. J. (1981). Electromagnetic prospecting for groundwater in precambrien terrains in the Republic of Upper Volta (Benin). *Geopghysical Prospecting*, vol. 29, pp. 932-955.

Papoulis, D. and Tsoli-Katagas, P. (2008): *Clay minerals*; volume 43 No.4, abstract.

Parsiegla, N., Gohl, K., and Uenzelmann-Neben, G. (2007). Deep crustal structure of the sheared South African continental margin: first results of the Agulhas-Karoo Geoscience Transect. *South African Journal of Geology*, v. 110, pp. 393-406.

Pethick, J. (1984) An Introduction to Coastal Geomorphology, Edward Arnold, London, 260 pp.

Petit, J. P. (1987). Criteria for the sense of movement on fault surfaces in brittle rocks. *Journal of Structural Geology*, 9, pp. 597-608.

Pluijm, B. A. and Marshak, S. (2004). Earth Structure, and introduction to structural geology and tectonics. *Library of Congress Cataloguing-in-Publication Data.* Norton & Company, Inc.

Pysklywec, R. N. And Mitrovica, J. X. (1999). The role of subduction-induced subsidence in the evolution of the Karoo Basin. *Journal of Geology*, 107: pp.155–164.

Reagan, D. M. (1973). Structural Geology. An introduction to geometrical techniques (second edition). John Wiley & Sons, Chichester.

Reuter, H. I., Nelson, A., and Jarvis, A. (2007). An evaluation of void filling interpolation methods for SRTM data. Institute for Environment and Sustainability – Land Management and Natural Hazards 8 Unit, European Commission - DG Joint Research Centre, TP 280, Via Fermi 1, pp.1- 9 21020 Ispra (VA) Italy.

Reynolds, J.M. (1997). An Introduction to Applied and Environmental Geophysics. John Wiley and Sons Inc.

Rust, I.C.and Theron, J. N. (1964). Some aspects of the Table Mountain Series near Vanhrynsdorp. *Trans. Geol. Soc. S. Afr*., 62, pp. 131-136.

Salama, R.B., Farrington, P., Bartle, G. A. and Watson, G. D. (1993). The role of geological structures and relict channels in the development of dry land salinity in the wheat-belt of western Australia. *Aust. J. Earth Sci*.,40, pp. 45-56.

Sand, L. B. (1956) On the genesis of residual kaolins. *Am. Mineral*, 41, pp. 28-40.

Shaoqing, Z., and Lu, X. (2008). The comparative study of three methods of remote sensing image change detection. School of Resource and Environment Science, Wuhan University,129 Luoyu Road,Wuhan,China ,430079.

Sheppard, T. (1912). The Lost Towns of the Yorkshire Coast and Other Chapters Bearing Upon

the Geography of the District, A. Brown and Sons, London, 329 + xviii pp.

Singh, M., Kijko, A., and Durrheim, R. (2009). Seismotectonic Models for South Africa. Synthesis of Geoscientific Information, Problems and Way Forward, *Seismological Research Letters*, 80, 65-33.

M. Singh, A Kijko, and R. Durrheim (2011). First-order regional seismo-tectonic models for South Africa, *Natural Hazards*, **59**, 1, 383-400.

Stein, S. and Wysession, M. (2003). An introduction to seismology, earthquakes, and earth structure, Blackwell Publishing.

Steinberger, B.M., Schmeling, B.M.H., and Marquart, G. (2001). Large-scale lithospheric stress field induced by global mantle circulation, *Earth Planet.Sci.Lett*., 186, pp.75-91

Street, G.J., Pracilio, G., and Anderson-Mayes, M. (2002). Interpretation of geophysical data for salt hazard identification and catchment management in southwest Western Australia. *Exploration Geophysics* 33, pp. 65-72.

Tankard, A.J., Jackson, M.P.A., Eriksson, K.A., Hobday, D.K., Hunter, D.R. and Minter, W.E.L. (1982). Crustal evolution of southern Africa: *Springer-Verlag*, New York, pp. 14-45

Tankard, A., Welsink, H., Aukes, P., Newton, R., and Stettler, E. (2009). Tectonic evolution of the Cape and Karoo basins of South Africa, *Marine and Petroleum Geology*, 26, p. 1379-1412.

Thamm, A. G. and Johnson, M. R. (2006). The Cape Supergroup. In Johnson et al., (2006). The Geology of South Africa. Published by the Geological Society of South Africa and the Council for Geoscience.

Theron, J.N. (1972). An analysis of the Cape folding in the district of Willowmore, C.P: Annuals, University of Stellenbosch, 37, pp. 347-421.

Titus, R., Friese, A., Adams, S (2009). A tectonic and geomorphic framework for the development of basement aquifers in Namaqualand – a review. The basement aquifers of south Africa: Water Research Commission, TT428/09.

Tsai, F., Lin, E. K., and Yoshino, K. (2006). Spectrally segmented principal component analysis of hyperspectral imagery for mapping invasive plant species, *Internal Journal of Remote Sensing.*

Tzortzis, M. and Tsertos, H. (2004). Determination of thorium, uranium and potassium elemental concentrations in surface soils in Cyprus. *Journal of Environmental Radioactivity*, pp. 27, 325-338.

Uenzelmann-Nieben, G. and Gohl, K. (2004). The Agulhas Ridge, South Atlantic: The Peculiar Structure of a Fracture Zone (2004). *Marine Geophysical Researches*, vol 25(3) pp. 305-319.

Van Dongen, P. and Woodhouse, M. (1994). Finding groundwater: a project manager's guide to techniques and how to use them. UNDP-WB Technical Report.

Van Wagoner, J. C., Mitchum Jr., R. M., Campion, K. M., Rahmanian, V. D. (1990). Siliciclastic sequence stratigraphy in well logs, core, and outcrops: concepts for highresolution correlation of time and facies. *American Association of Petroleum Geologists Methods in Exploration*, Series 7, 55 pp.

Vearnacombe, J.R. (1998). Shear zones, fault networks and Archaean gold. *Geology*, 26(9) pp. 855-858.

Viola, G., M.A.G. Andreoli, Z. Ben-Avraham, I. Stengel, and M. Reshef, 2005. Offshore mud volcanoes and on land faulting in southwestern Africa: neotectonic implications and constraints on the regional stress field. *Earth and Planetary Science Letters,* 231, 147-160.

Visser, J. N. J. (1990). The age of the late Paleozoic glacigene deposits in southern Africa: *South African Journal of Geology*, 93, pp. 366-375.

Visser, J. N. J. (1992). Basin tectonics in southwestern Gondwana during the Carboniferous and Permian *in* Inversion tectonics of the Cape Fold Belt, Karoo and Cretaceous basins of southern Africa (M. J. de Wit and I. G. Ransome, eds): Balkema, Rotterdam, pp. 109-115.

Vincent, O. R. and Folorunso O. (2009). A Descriptive Algorithm for Sobel Image Edge Detection. Proceeding of the Information Science and Information technology Education Joint Conference, Macon, Georgia USA, 97-107.

Viola, G., Andreoli, M.A.G., Ben-Avraham, Z., Stengel,I., Reshef, M. (2005). Offshore mud volcanoes and onland faulting in southwestern Africa: neotectonic implications and constraints on the regional stress field.

White, D.E. (1957). Thermal waters of volcanic origin, *Geological Society of America Bulletin*, 68 (1957), pp. 1637–1658

Wilford, J. (2002). Airborne gamma ray spectrometry, Geophysical and remote sensing methods for regolith exploration, CRCLEME Open File Report 144, CRCLEME, Canberra.

Wittingham JK (1970) Report of geophysical investigations along the route of the Orange-Fish tunnel. Cape Prov Rep Geol Surv S Afr (Unpublished).

Woodford, A.C. and Chevallier, L. (2002). Hydrogeology of the main Karoo basin: current knowledge and future research needs: WRC Report N^{o} TT179/02.

Zhao, B. (2011). The Witwatersrand conglomerate gold deposits in South Africa: The Ventersdorp Contact Reef. Northeast Normal University Press, Changchun.

Zoback, M.L., Zoback, M.D., Adams, J., Assumcâo, M., Bells, S., Bergman, E.A., Blümling, P., Brereton, N.R., Denham, D., Ding, J., Fuchs, K., Gay, N., Gregersen, S., Gupta, H.K., Gvishiani, A., Jacob, K., Klein, R., Knoll, P., Magee, M., Mercier, J.L., Müller, B.C., Paquin, C., Rajerdran, K., Stephansson, O., Suarez, G., Suter, M., Udias, A., Xu, Z.H. and Zhizhin, M. (1989). Global patterns of tectonic stresses. *Nature* 341, pp 291-298.

APPENDIX

APPENDIX A: Tables of data

Table A. Quartz veins, the number between brackets is the quantity of quartz veins

	Strike (º)	Dip (º)	Dip Direction (º)
1	315	8	225
2 (7)	350	85	260
3 (8)	5	45	135
4 (6)	320	5	230
5 (7)	25	85	115
6 (6)	275	45	185
7 (3)	345	75	255
8	280	50	190
9 (9)	10	25	100
10	290	50	200
11 (6)	285	60	185

Table B. Faults (Normal=N, Reverse=I, Dextral=D, Sinistral=S).

	Strike (º)	Dip (º)	Dip Direction (º)	Slip Sense
1	270	40	230	N,dip slip:10cm
2 (6)	275	45	240	D
3 (8)	290	50	220	D
4	50	50	140	
5 (50)	285	60	195	D

Table C. Dip and strikes of fractures in the Grahamstown Kaolin deposit

	Strike (°)	Dip (°)	Dip Direction (°)
1 (4)	105	55	210
2 (5)	15	30	105
3	110	45	200
4 (5)	290	50	200
5 (3)	60	35	150
6 (7)	320	20	225
7 (2)	270	40	230
8 (7)	310	85	220
9 (10)	290	65	200
10	330	70	240
11	345	75	255
12 12 (11)	310 330	50 70	220 240
13 (6)	300	50	210
14 (6)	30	90	120
15 (2) 15 (8)	290 280	60 70	200 190
16 (2)	45	75	135
17 (6)	210	55	120
18 (5)	120	15	210
19 (14)	210	65	300
20 (7) 21 (6)	285 350	60 90	195
22 (6)	280	45	190
23 (10)	290	50	200
24 (5)	35	60	125
25 (3)	300	45	210
26 (8)	290	65	200
27 (6)	40	40	130

Table D: Sample of magnetic readings at Polile Tshisa

X (^{O})	Y(^{O})	GPS_HEIGHT (m)	READING_1 (nT)	DIURNAL_1(nT)	CORRECTED (nT)	TIME	DATE
28.64212	-30.4866	1360.789	27616.876	-16.424	27633.3	13:49:59.80	05/29/12
28.64212	-30.4866	1360.735	27623.534	-9.766	27633.3	13:49:59.60	05/29/12
28.64212	-30.4866	1360.681	27623.96	-9.34	27633.3	13:49:59.40	05/29/12
28.64212	-30.4866	1360.628	27621.513	-11.787	27633.3	13:49:59.20	05/29/12
28.64212	-30.4866	1360.574	27618.573	-14.727	27633.3	13:49:59.00	05/29/12
28.64212	-30.4866	1360.54	27621.324	-11.976	27633.3	13:49:58.80	05/29/12
28.64212	-30.4866	1360.527	27624.978	-8.322	27633.3	13:49:58.60	05/29/12
28.64213	-30.4866	1360.514	27632.037	-1.263	27633.3	13:49:58.40	05/29/12
28.64213	-30.4866	1360.501	27635.632	2.332	27633.3	13:49:58.20	05/29/12
28.64213	-30.4866	1360.488	27633.31	0.01	27633.3	13:49:58.00	05/29/12
28.64213	-30.4866	1360.47	27630.625	-2.675	27633.3	13:49:57.80	05/29/12
28.64214	-30.4866	1360.449	27632.072	-1.228	27633.3	13:49:57.60	05/29/12
28.64214	-30.4865	1360.428	27634.68	1.38	27633.3	13:49:57.40	05/29/12
28.64214	-30.4865	1360.406	27638.985	5.685	27633.3	13:49:57.20	05/29/12
28.64214	-30.4865	1360.385	27640.587	7.287	27633.3	13:49:57.00	05/29/12
28.64214	-30.4865	1360.354	27637.336	4.036	27633.3	13:49:56.80	05/29/12
28.64215	-30.4865	1360.315	27634.981	1.681	27633.3	13:49:56.60	05/29/12
28.64215	-30.4865	1360.276	27634.591	1.291	27633.3	13:49:56.40	05/29/12
28.64215	-30.4865	1360.238	27635.551	2.251	27633.3	13:49:56.20	05/29/12
28.64215	-30.4865	1360.199	27638.56	5.26	27633.3	13:49:56.00	05/29/12
28.64215	-30.4865	1360.166	27640.662	7.362	27633.3	13:49:55.80	05/29/12
28.64216	-30.4865	1360.141	27636.606	3.306	27633.3	13:49:55.60	05/29/12
28.64216	-30.4865	1360.115	27633.287	-0.013	27633.3	13:49:55.40	05/29/12
28.64216	-30.4865	1360.089	27632.014	-1.286	27633.3	13:49:55.20	05/29/12
28.64216	-30.4865	1360.064	27634.284	0.984	27633.3	13:49:55.00	05/29/12
28.64216	-30.4865	1360.036	27637.53	4.23	27633.3	13:49:54.80	05/29/12
28.64217	-30.4865	1360.007	27642.044	8.744	27633.3	13:49:54.60	05/29/12
28.64217	-30.4865	1359.978	27639.692	6.392	27633.3	13:49:54.40	05/29/12
28.64217	-30.4865	1359.949	27636.889	3.589	27633.3	13:49:54.20	05/29/12
28.64217	-30.4865	1359.92	27636.167	2.867	27633.3	13:49:54.00	05/29/12
28.64217	-30.4865	1359.892	27639.147	5.847	27633.3	13:49:53.80	05/29/12
28.64218	-30.4865	1359.867	27643.981	10.681	27633.3	13:49:53.60	05/29/12
28.64218	-30.4865	1359.842	27649.235	15.935	27633.3	13:49:53.40	05/29/12
28.64218	-30.4865	1359.816	27648.192	14.892	27633.3	13:49:53.20	05/29/12
28.64218	-30.4865	1359.791	27647.845	14.545	27633.3	13:49:53.00	05/29/12
28.64218	-30.4865	1359.774	27651.505	18.205	27633.3	13:49:52.80	05/29/12
28.64219	-30.4865	1359.767	27656.119	22.819	27633.3	13:49:52.60	05/29/12
28.64219	-30.4865	1359.76	27662.603	29.303	27633.3	13:49:52.40	05/29/12
28.64219	-30.4865	1359.752	27668.121	34.821	27633.3	13:49:52.20	05/29/12

28.64219	-30.4865	1359.745	27667.763	34.463	27633.3	13:49:52.00	05/29/12
28.6422	-30.4865	1359.739	27668.977	35.677	27633.3	13:49:51.80	05/29/12
28.6422	-30.4865	1359.734	27676.68	43.38	27633.3	13:49:51.60	05/29/12
28.6422	-30.4865	1359.729	27680.699	47.399	27633.3	13:49:51.40	05/29/12
28.6422	-30.4865	1359.724	27688.957	55.657	27633.3	13:49:51.20	05/29/12
28.6422	-30.4865	1359.719	27691.569	58.269	27633.3	13:49:51.00	05/29/12
28.64221	-30.4865	1359.717	27690.99	57.69	27633.3	13:49:50.80	05/29/12
28.64221	-30.4865	1359.716	27694.13	60.83	27633.3	13:49:50.60	05/29/12
28.64221	-30.4865	1359.716	27698.642	65.342	27633.3	13:49:50.40	05/29/12
28.64221	-30.4865	1359.716	27703.999	70.699	27633.3	13:49:50.20	05/29/12
28.64222	-30.4865	1359.715	27709.518	76.218	27633.3	13:49:50.00	05/29/12
28.64222	-30.4865	1359.727	27709.386	76.086	27633.3	13:49:49.80	05/29/12
28.64222	-30.4865	1359.751	27713.465	80.165	27633.3	13:49:49.60	05/29/12
28.64222	-30.4865	1359.775	27722.623	89.323	27633.3	13:49:49.40	05/29/12
28.64223	-30.4865	1359.799	27727.628	94.328	27633.3	13:49:49.20	05/29/12
28.64223	-30.4865	1359.823	27737.051	103.751	27633.3	13:49:49.00	05/29/12
28.64223	-30.4865	1359.837	27740.421	107.121	27633.3	13:49:48.80	05/29/12
28.64223	-30.4865	1359.842	27741.883	108.583	27633.3	13:49:48.60	05/29/12
28.64223	-30.4865	1359.847	27746.097	112.797	27633.3	13:49:48.40	05/29/12
28.64223	-30.4865	1359.851	27749.984	116.684	27633.3	13:49:48.20	05/29/12
28.64224	-30.4865	1359.856	27751.505	118.205	27633.3	13:49:48.00	05/29/12
28.64224	-30.4865	1359.855	27760.037	126.737	27633.3	13:49:47.80	05/29/12
28.64224	-30.4865	1359.85	27765.333	132.033	27633.3	13:49:47.60	05/29/12
28.64224	-30.4865	1359.844	27767.607	134.307	27633.3	13:49:47.40	05/29/12
28.64224	-30.4865	1359.838	27771.036	137.736	27633.3	13:49:47.20	05/29/12
28.64224	-30.4865	1359.833	27778.494	145.194	27633.3	13:49:47.00	05/29/12
28.64225	-30.4865	1359.83	27785.487	152.187	27633.3	13:49:46.80	05/29/12
28.64225	-30.4865	1359.83	27792.654	159.354	27633.3	13:49:46.60	05/29/12
28.64225	-30.4865	1359.83	27804.345	171.045	27633.3	13:49:46.40	05/29/12
28.64225	-30.4865	1359.831	27808.339	175.039	27633.3	13:49:46.20	05/29/12
28.64225	-30.4865	1359.831	27811.176	177.876	27633.3	13:49:46.00	05/29/12
28.64225	-30.4865	1359.831	27817.256	183.956	27633.3	13:49:45.80	05/29/12
28.64225	-30.4865	1359.831	27826.289	192.989	27633.3	13:49:45.60	05/29/12
28.64226	-30.4865	1359.831	27831.112	197.812	27633.3	13:49:45.40	05/29/12
28.64226	-30.4865	1359.83	27837.302	204.002	27633.3	13:49:45.20	05/29/12
28.64226	-30.4865	1359.83	27837.878	204.578	27633.3	13:49:45.00	05/29/12
28.64226	-30.4865	1359.825	27834.249	200.949	27633.3	13:49:44.80	05/29/12
28.64226	-30.4865	1359.816	27836.724	203.424	27633.3	13:49:44.60	05/29/12
28.64226	-30.4864	1359.807	27840.916	207.616	27633.3	13:49:44.40	05/29/12
28.64226	-30.4864	1359.798	27838.404	205.104	27633.3	13:49:44.20	05/29/12
28.64226	-30.4864	1359.789	27842.434	209.134	27633.3	13:49:44.00	05/29/12

28.64227	-30.4864	1359.79	27845.238	211.938	27633.3	13:49:43.80	05/29/12
28.64227	-30.4864	1359.802	27840.98	207.68	27633.3	13:49:43.60	05/29/12
28.64227	-30.4864	1359.815	27846.563	213.263	27633.3	13:49:43.40	05/29/12
28.64227	-30.4864	1359.827	27858.536	225.236	27633.3	13:49:43.20	05/29/12
28.64227	-30.4864	1359.839	27868.502	235.202	27633.3	13:49:43.00	05/29/12
28.64227	-30.4864	1359.834	27877.287	243.987	27633.3	13:49:42.80	05/29/12
28.64228	-30.4864	1359.813	27891.319	258.019	27633.3	13:49:42.60	05/29/12
28.64228	-30.4864	1359.792	27898.842	265.542	27633.3	13:49:42.40	05/29/12
28.64228	-30.4864	1359.77	27905.877	272.577	27633.3	13:49:42.20	05/29/12
28.64228	-30.4864	1359.749	27922.575	289.275	27633.3	13:49:42.00	05/29/12
28.64228	-30.4864	1359.727	27945.254	311.954	27633.3	13:49:41.80	05/29/12
28.64228	-30.4864	1359.706	27962.899	329.599	27633.3	13:49:41.60	05/29/12
28.64229	-30.4864	1359.685	27991.921	358.621	27633.3	13:49:41.40	05/29/12
28.64229	-30.4864	1359.664	28014.035	380.735	27633.3	13:49:41.20	05/29/12
28.64229	-30.4864	1359.643	28013.811	380.511	27633.3	13:49:41.00	05/29/12
28.64229	-30.4864	1359.611	28024.038	390.738	27633.3	13:49:40.80	05/29/12
28.6423	-30.4864	1359.569	28042.894	409.594	27633.3	13:49:40.60	05/29/12
28.6423	-30.4864	1359.527	28035.862	402.562	27633.3	13:49:40.40	05/29/12
28.6423	-30.4864	1359.485	28014.74	381.44	27633.3	13:49:40.20	05/29/12

Table E: Sample of magnetic readings at Aliwal North

X(°)	Y(°)	GPS_HEIGHT(m)	READING_1(nT)	DIURNAL_1(nT)	CORRECTED (nT)	TIME	DATE
26.71794	-30.7164	1327.653	27176.434	-37.766	27214.2	15:17:07.90	06/01/12
26.71794	-30.7164	1327.652	27176.48	-37.72	27214.2	15:17:07.70	06/01/12
26.71794	-30.7164	1327.651	27176.908	-37.292	27214.2	15:17:07.50	06/01/12
26.71794	-30.7164	1327.65	27176.936	-37.264	27214.2	15:17:07.30	06/01/12
26.71794	-30.7164	1327.649	27177.053	-37.147	27214.2	15:17:07.10	06/01/12
26.71794	-30.7164	1327.632	27177.523	-36.677	27214.2	15:17:06.90	06/01/12
26.71794	-30.7164	1327.596	27177.66	-36.54	27214.2	15:17:06.70	06/01/12
26.71794	-30.7164	1327.562	27177.327	-36.873	27214.2	15:17:06.50	06/01/12
26.71794	-30.7164	1327.526	27177.326	-36.874	27214.2	15:17:06.30	06/01/12
26.71794	-30.7164	1327.492	27177.303	-36.897	27214.2	15:17:06.10	06/01/12
26.71794	-30.7164	1327.528	27177.611	-36.589	27214.2	15:17:05.90	06/01/12
26.71794	-30.7164	1327.636	27177.861	-36.339	27214.2	15:17:05.70	06/01/12
26.71794	-30.7164	1327.744	27178.018	-36.182	27214.2	15:17:05.50	06/01/12
26.71794	-30.7164	1327.851	27178.098	-36.102	27214.2	15:17:05.30	06/01/12
26.71794	-30.7164	1327.959	27178.23	-35.97	27214.2	15:17:05.10	06/01/12
26.71794	-30.7164	1328.049	27178.167	-36.033	27214.2	15:17:04.90	06/01/12
26.71794	-30.7164	1328.122	27177.974	-36.226	27214.2	15:17:04.70	06/01/12
26.71794	-30.7164	1328.194	27177.679	-36.521	27214.2	15:17:04.50	06/01/12

26.71794	-30.7164	1328.267	27177.4	-36.8	27214.2	15:17:04.30	06/01/12
26.71794	-30.7164	1328.34	27177.299	-36.901	27214.2	15:17:04.10	06/01/12
26.71794	-30.7164	1328.372	27177.807	-36.393	27214.2	15:17:03.90	06/01/12
26.71794	-30.7164	1328.365	27178.853	-35.347	27214.2	15:17:03.70	06/01/12
26.71794	-30.7164	1328.358	27180.092	-34.108	27214.2	15:17:03.50	06/01/12
26.71794	-30.7164	1328.35	27180.825	-33.375	27214.2	15:17:03.30	06/01/12
26.71794	-30.7164	1328.343	27180.969	-33.231	27214.2	15:17:03.10	06/01/12
26.71794	-30.7164	1328.3	27180.873	-33.327	27214.2	15:17:02.90	06/01/12
26.71794	-30.7164	1328.223	27181.03	-33.17	27214.2	15:17:02.70	06/01/12
26.71794	-30.7164	1328.145	27181.468	-32.732	27214.2	15:17:02.50	06/01/12
26.71794	-30.7164	1328.067	27183.274	-30.926	27214.2	15:17:02.30	06/01/12
26.71794	-30.7164	1327.99	27186.407	-27.793	27214.2	15:17:02.10	06/01/12
26.71794	-30.7164	1327.94	27189.22	-24.98	27214.2	15:17:01.90	06/01/12
26.71794	-30.7164	1327.919	27189.364	-24.836	27214.2	15:17:01.70	06/01/12
26.71794	-30.7164	1327.898	27186.928	-27.272	27214.2	15:17:01.50	06/01/12
26.71794	-30.7164	1327.877	27184.099	-30.101	27214.2	15:17:01.30	06/01/12
26.71794	-30.7164	1327.856	27180.818	-33.382	27214.2	15:17:01.10	06/01/12
26.71794	-30.7164	1327.819	27177.765	-36.435	27214.2	15:17:00.90	06/01/12
26.71794	-30.7164	1327.766	27175.145	-39.055	27214.2	15:17:00.70	06/01/12
26.71794	-30.7164	1327.713	27173.023	-41.177	27214.2	15:17:00.50	06/01/12
26.71794	-30.7164	1327.66	27171.188	-43.012	27214.2	15:17:00.30	06/01/12
26.71794	-30.7164	1327.607	27169.321	-44.879	27214.2	15:17:00.10	06/01/12
26.71794	-30.7164	1327.698	27166.87	-47.33	27214.2	15:16:59.90	06/01/12
26.71794	-30.7164	1327.931	27164.479	-49.721	27214.2	15:16:59.70	06/01/12
26.71794	-30.7164	1328.165	27164.942	-49.258	27214.2	15:16:59.50	06/01/12
26.71794	-30.7164	1328.399	27167.409	-46.791	27214.2	15:16:59.30	06/01/12
26.71795	-30.7164	1328.632	27168.57	-45.63	27214.2	15:16:59.10	06/01/12
26.71795	-30.7164	1328.756	27167.117	-47.083	27214.2	15:16:58.90	06/01/12
26.71795	-30.7164	1328.769	27162.893	-51.307	27214.2	15:16:58.70	06/01/12
26.71795	-30.7164	1328.783	27157.605	-56.595	27214.2	15:16:58.50	06/01/12
26.71794	-30.7164	1328.797	27148.779	-65.421	27214.2	15:16:58.30	06/01/12
26.71794	-30.7164	1328.725	27138.867	-75.333	27214.2	15:16:57.90	06/01/12
26.71794	-30.7164	1328.541	27136.081	-78.119	27214.2	15:16:57.70	06/01/12
26.71794	-30.7164	1328.357	27133.673	-80.527	27214.2	15:16:57.50	06/01/12
26.71794	-30.7164	1328.173	27130.176	-84.024	27214.2	15:16:57.30	06/01/12
26.71794	-30.7164	1327.989	27127.949	-86.251	27214.2	15:16:57.10	06/01/12
26.71793	-30.7164	1327.872	27126.503	-87.697	27214.2	15:16:56.90	06/01/12
26.71793	-30.7164	1327.821	27124.87	-89.33	27214.2	15:16:56.70	06/01/12
26.71793	-30.7164	1327.771	27123.299	-90.901	27214.2	15:16:56.50	06/01/12
26.71793	-30.7164	1327.721	27123.048	-91.152	27214.2	15:16:56.30	06/01/12
26.71793	-30.7164	1327.67	27123.068	-91.132	27214.2	15:16:56.10	06/01/12

26.71793	-30.7164	1327.694	27123.48	-90.72	27214.2	15:16:55.90	06/01/12
26.71793	-30.7164	1327.793	27124.756	-89.444	27214.2	15:16:55.70	06/01/12
26.71793	-30.7164	1327.892	27125.549	-88.651	27214.2	15:16:55.50	06/01/12
26.71793	-30.7164	1327.99	27125.659	-88.541	27214.2	15:16:55.30	06/01/12
26.71793	-30.7164	1328.089	27126.312	-87.888	27214.2	15:16:55.10	06/01/12
26.71793	-30.7164	1328.372	27127.084	-87.117	27214.201	15:16:54.90	06/01/12
26.71793	-30.7164	1328.842	27127.77	-86.432	27214.202	15:16:54.70	06/01/12
26.71793	-30.7164	1329.311	27076.113	-138.09	27214.203	15:16:54.50	06/01/12
26.71794	-30.7164	1330.203	27131.379	-82.828	27214.207	15:16:53.90	06/01/12
26.71793	-30.7164	1329.643	27134.118	-80.091	27214.209	15:16:53.70	06/01/12
26.71793	-30.7164	1329.083	27135.063	-79.147	27214.21	15:16:53.50	06/01/12
26.71792	-30.7164	1328.523	27136.361	-77.85	27214.211	15:16:53.30	06/01/12
26.71792	-30.7164	1327.963	27138.293	-75.92	27214.213	15:16:53.10	06/01/12
26.71792	-30.7164	1327.861	27139.147	-75.067	27214.214	15:16:52.90	06/01/12
26.71792	-30.7164	1328.216	27140.03	-74.185	27214.215	15:16:52.70	06/01/12
26.71792	-30.7164	1328.572	27141.332	-72.885	27214.217	15:16:52.50	06/01/12
26.71792	-30.7164	1328.928	27142.442	-71.776	27214.218	15:16:52.30	06/01/12
26.71792	-30.7164	1329.283	27143.464	-70.755	27214.219	15:16:52.10	06/01/12
26.71792	-30.7164	1329.454	27145.366	-68.855	27214.221	15:16:51.90	06/01/12
26.71792	-30.7164	1329.439	27146.478	-67.744	27214.222	15:16:51.70	06/01/12
26.71792	-30.7164	1329.425	27146.949	-67.274	27214.223	15:16:51.50	06/01/12
26.71792	-30.7164	1329.411	27148.085	-66.14	27214.225	15:16:51.30	06/01/12
26.71792	-30.7164	1329.396	27148.952	-65.274	27214.226	15:16:51.10	06/01/12
26.71792	-30.7164	1329.376	27149.523	-64.704	27214.227	15:16:50.90	06/01/12
26.71791	-30.7164	1329.349	27150.708	-63.521	27214.229	15:16:50.70	06/01/12
26.71791	-30.7164	1329.322	27151.508	-62.722	27214.23	15:16:50.50	06/01/12
26.71791	-30.7164	1329.295	27151.927	-62.304	27214.231	15:16:50.30	06/01/12
26.71791	-30.7164	1329.268	27152.25	-61.983	27214.233	15:16:50.10	06/01/12
26.71791	-30.7163	1329.219	27152.827	-61.407	27214.234	15:16:49.90	06/01/12
26.71791	-30.7163	1329.148	27153.056	-61.179	27214.235	15:16:49.70	06/01/12
26.71791	-30.7163	1329.076	27153.718	-60.519	27214.237	15:16:49.50	06/01/12
26.7179	-30.7163	1329.004	27154.492	-59.746	27214.238	15:16:49.30	06/01/12
26.7179	-30.7163	1328.933	27154.806	-59.433	27214.239	15:16:49.10	06/01/12
26.7179	-30.7163	1328.929	27155.44	-58.801	27214.241	15:16:48.90	06/01/12
26.7179	-30.7163	1328.994	27156.839	-57.403	27214.242	15:16:48.70	06/01/12
26.7179	-30.7163	1329.059	27158.441	-55.802	27214.243	15:16:48.50	06/01/12
26.7179	-30.7163	1329.123	27160.486	-53.759	27214.245	15:16:48.30	06/01/12
26.71789	-30.7163	1329.188	27163.154	-51.092	27214.246	15:16:48.10	06/01/12
26.71789	-30.7163	1329.154	27164.472	-49.775	27214.247	15:16:47.90	06/01/12
26.71789	-30.7163	1329.021	27165.597	-48.652	27214.249	15:16:47.70	06/01/12

Table F: Sample of magnetic readings at Badfontein

X(°)	Y(°)	GPS_HEIGHT(m)	READING_1(nT)	DIURNAL_1(nT)	CORRECTED (nT)	TIME	DATE
26.54522	-30.647	1292.205	27286.971	93.344	27193.627	15:44:44.70	06/02/12
26.54522	-30.647	1292.199	27284.542	90.917	27193.625	15:44:44.50	06/02/12
26.54522	-30.647	1292.195	27282.147	88.524	27193.623	15:44:44.30	06/02/12
26.54522	-30.647	1292.19	27250.499	56.878	27193.621	15:44:44.10	06/02/12
26.54522	-30.647	1292.181	27276.631	83.014	27193.617	15:44:43.70	06/02/12
26.54522	-30.647	1292.18	27278.641	85.026	27193.615	15:44:43.50	06/02/12
26.54522	-30.647	1292.179	27278.679	85.066	27193.613	15:44:43.30	06/02/12
26.54522	-30.647	1292.178	27279.026	85.415	27193.611	15:44:43.10	06/02/12
26.54522	-30.647	1292.177	27279.493	85.884	27193.609	15:44:42.90	06/02/12
26.54522	-30.647	1292.179	27279.386	85.779	27193.607	15:44:42.70	06/02/12
26.54522	-30.647	1292.184	27279.725	86.12	27193.605	15:44:42.50	06/02/12
26.54522	-30.647	1292.189	27279.905	86.302	27193.603	15:44:42.30	06/02/12
26.54522	-30.647	1292.194	27279.895	86.294	27193.601	15:44:42.10	06/02/12
26.54521	-30.647	1292.199	27279.947	86.348	27193.599	15:44:41.90	06/02/12
26.54521	-30.647	1292.196	27279.661	86.064	27193.597	15:44:41.70	06/02/12
26.54521	-30.647	1292.184	27279.623	86.028	27193.595	15:44:41.50	06/02/12
26.54521	-30.647	1292.172	27279.38	85.787	27193.593	15:44:41.30	06/02/12
26.54521	-30.647	1292.16	27279.327	85.736	27193.591	15:44:41.10	06/02/12
26.54521	-30.647	1292.148	27278.925	85.336	27193.589	15:44:40.90	06/02/12
26.54521	-30.647	1292.149	27278.795	85.208	27193.587	15:44:40.70	06/02/12
26.54521	-30.647	1292.164	27278.709	85.124	27193.585	15:44:40.50	06/02/12
26.54521	-30.647	1292.178	27278.692	85.109	27193.583	15:44:40.30	06/02/12
26.54521	-30.647	1292.192	27278.724	85.143	27193.581	15:44:40.10	06/02/12
26.5452	-30.647	1292.207	27278.831	85.252	27193.579	15:44:39.90	06/02/12
26.5452	-30.647	1292.213	27278.819	85.242	27193.577	15:44:39.70	06/02/12
26.5452	-30.647	1292.21	27278.818	85.243	27193.575	15:44:39.50	06/02/12
26.5452	-30.647	1292.208	27278.713	85.14	27193.573	15:44:39.30	06/02/12
26.5452	-30.647	1292.206	27278.6	85.029	27193.571	15:44:39.10	06/02/12
26.5452	-30.6469	1292.203	27278.557	84.988	27193.569	15:44:38.90	06/02/12
26.5452	-30.6469	1292.203	27278.507	84.94	27193.567	15:44:38.70	06/02/12
26.5452	-30.6469	1292.205	27278.564	84.999	27193.565	15:44:38.50	06/02/12
26.54519	-30.6469	1292.207	27278.521	84.958	27193.563	15:44:38.30	06/02/12
26.54519	-30.6469	1292.208	27278.395	84.834	27193.561	15:44:38.10	06/02/12
26.54519	-30.6469	1292.21	27278.327	84.768	27193.559	15:44:37.90	06/02/12
26.54519	-30.6469	1292.21	27278.322	84.765	27193.557	15:44:37.70	06/02/12
26.54519	-30.6469	1292.207	27278.263	84.708	27193.555	15:44:37.50	06/02/12
26.54519	-30.6469	1292.205	27278.138	84.585	27193.553	15:44:37.30	06/02/12
26.54519	-30.6469	1292.203	27278.063	84.512	27193.551	15:44:37.10	06/02/12
26.54518	-30.6469	1292.2	27278.062	84.513	27193.549	15:44:36.90	06/02/12

26.54518	-30.6469	1292.213	27277.859	84.312	27193.547	15:44:36.70	06/02/12
26.54518	-30.6469	1292.24	27277.663	84.118	27193.545	15:44:36.50	06/02/12
26.54518	-30.6469	1292.267	27277.404	83.861	27193.543	15:44:36.30	06/02/12
26.54518	-30.6469	1292.294	27277.249	83.708	27193.541	15:44:36.10	06/02/12
26.54518	-30.6469	1292.321	27277.181	83.642	27193.539	15:44:35.90	06/02/12
26.54518	-30.6469	1292.338	27277.052	83.515	27193.537	15:44:35.70	06/02/12
26.54518	-30.6469	1292.347	27276.875	83.34	27193.535	15:44:35.50	06/02/12
26.54517	-30.6469	1292.355	27276.372	82.839	27193.533	15:44:35.30	06/02/12
26.54517	-30.6469	1292.363	27276.002	82.471	27193.531	15:44:35.10	06/02/12
26.54517	-30.6469	1292.372	27275.472	81.943	27193.529	15:44:34.90	06/02/12
26.54517	-30.6469	1292.388	27275.295	81.768	27193.527	15:44:34.70	06/02/12
26.54517	-30.6469	1292.412	27275.398	81.873	27193.525	15:44:34.50	06/02/12
26.54517	-30.6469	1292.436	27275.34	81.817	27193.523	15:44:34.30	06/02/12
26.54517	-30.6469	1292.46	27275.004	81.483	27193.521	15:44:34.10	06/02/12
26.54516	-30.6469	1292.484	27274.766	81.247	27193.519	15:44:33.90	06/02/12
26.54516	-30.6469	1292.5	27274.757	81.24	27193.517	15:44:33.70	06/02/12
26.54516	-30.6469	1292.508	27274.102	80.587	27193.515	15:44:33.50	06/02/12
26.54516	-30.6469	1292.516	27274.07	80.557	27193.513	15:44:33.30	06/02/12
26.54516	-30.6469	1292.523	27274.1	80.589	27193.511	15:44:33.10	06/02/12
26.54516	-30.6469	1292.531	27274.138	80.629	27193.509	15:44:32.90	06/02/12
26.54516	-30.6469	1292.538	27273.929	80.422	27193.507	15:44:32.70	06/02/12
26.54516	-30.6469	1292.545	27273.689	80.184	27193.505	15:44:32.50	06/02/12
26.54516	-30.6469	1292.552	27273.69	80.187	27193.503	15:44:32.30	06/02/12
26.54516	-30.6469	1292.559	27273.491	79.99	27193.501	15:44:32.10	06/02/12
26.54516	-30.6469	1292.566	27273.489	79.99	27193.499	15:44:31.90	06/02/12
26.54516	-30.6469	1292.568	27273.44	79.943	27193.497	15:44:31.70	06/02/12
26.54516	-30.6469	1292.565	27273.184	79.689	27193.495	15:44:31.50	06/02/12
26.54516	-30.6469	1292.562	27272.991	79.498	27193.493	15:44:31.30	06/02/12
26.54515	-30.6469	1292.559	27272.795	79.304	27193.491	15:44:31.10	06/02/12
26.54515	-30.6469	1292.556	27272.61	79.121	27193.489	15:44:30.90	06/02/12
26.54515	-30.6469	1292.564	27272.566	79.079	27193.487	15:44:30.70	06/02/12
26.54515	-30.6469	1292.581	27272.566	79.081	27193.485	15:44:30.50	06/02/12
26.54515	-30.6469	1292.599	27272.443	78.96	27193.483	15:44:30.30	06/02/12
26.54515	-30.6469	1292.617	27272.199	78.718	27193.481	15:44:30.10	06/02/12
26.54515	-30.6469	1292.634	27271.826	78.347	27193.479	15:44:29.90	06/02/12
26.54515	-30.6469	1292.646	27271.73	78.253	27193.477	15:44:29.70	06/02/12
26.54515	-30.6469	1292.652	27271.812	78.337	27193.475	15:44:29.50	06/02/12
26.54514	-30.6469	1292.658	27271.703	78.23	27193.473	15:44:29.30	06/02/12
26.54514	-30.6469	1292.663	27271.529	78.058	27193.471	15:44:29.10	06/02/12
26.54514	-30.6469	1292.669	27271.48	78.011	27193.469	15:44:28.90	06/02/12
26.54514	-30.6469	1292.669	27271.2	77.733	27193.467	15:44:28.70	06/02/12

26.54514	-30.6469	1292.664	27270.835	77.37	27193.465	15:44:28.50	06/02/12
26.54514	-30.6469	1292.658	27270.812	77.349	27193.463	15:44:28.30	06/02/12
26.54514	-30.6469	1292.652	27270.826	77.365	27193.461	15:44:28.10	06/02/12
26.54514	-30.6469	1292.647	27270.681	77.222	27193.459	15:44:27.90	06/02/12
26.54514	-30.6469	1292.645	27270.487	77.03	27193.457	15:44:27.70	06/02/12
26.54513	-30.6469	1292.647	27270.208	76.753	27193.455	15:44:27.50	06/02/12
26.54513	-30.6469	1292.65	27270.075	76.622	27193.453	15:44:27.30	06/02/12
26.54513	-30.6469	1292.652	27269.758	76.307	27193.451	15:44:27.10	06/02/12
26.54513	-30.6469	1292.654	27269.464	76.015	27193.449	15:44:26.90	06/02/12
26.54513	-30.6469	1292.654	27269.285	75.838	27193.447	15:44:26.70	06/02/12
26.54513	-30.6469	1292.653	27269.146	75.701	27193.445	15:44:26.50	06/02/12
26.54513	-30.6469	1292.651	27268.983	75.54	27193.443	15:44:26.30	06/02/12
26.54513	-30.6469	1292.65	27268.787	75.346	27193.441	15:44:26.10	06/02/12
26.54513	-30.6469	1292.649	27268.311	74.872	27193.439	15:44:25.90	06/02/12
26.54513	-30.6469	1292.65	27268.24	74.803	27193.437	15:44:25.70	06/02/12
26.54512	-30.6469	1292.653	27268.067	74.632	27193.435	15:44:25.50	06/02/12
26.54512	-30.6469	1292.657	27267.773	74.34	27193.433	15:44:25.30	06/02/12
26.54512	-30.6469	1292.66	27267.558	74.127	27193.431	15:44:25.10	06/02/12
26.54512	-30.6469	1292.663	27267.465	74.036	27193.429	15:44:24.90	06/02/12

Table G: Polile Tshisa hot spring L1_20, horizontal and vertical dipole

Sta (m)	HD (mS/m)	VD (mS/m)	X (m)	Y (m)	Z (m)	DIRECTION SE-NW
0	29	9	657629	6625987	1355	SE
10	39	12	657627	6625996	1355	
20	39	19	657626	6626008	1356	
30	38	24	657628	6626016	1357	
40	32	27	657625	6626027	1349	
50	28	27	657623	6626039	1350	
60	24	30	657625	6626048	1350	
70	22	15	657622	6626059	1349	
80	20	8	657621	6626069	1349	
90	26	22	657619	6626080	1351	
100	25	16	657620	6626087	1352	
110	23	4	657618	6626101	1354	
120	24	8	657620	6626110	1355	
130	17	19	657619	6626121	1357	
140	16.5	17	657618	6626132	1358	
150	22	17	657618	6626141	1359	
160	17	17	657616	6626148	1360	
170	29	22	657619	6626157	1360	
180	14	44	657623	6626168	1361	

190	26	25.5	657620	6626175	1361	
200	28	32	657619	6626188	1363	
210	29	28	657613	6626206	1365	
220	28	21	657607	6626216	1366	
230	28	25	657602	6626224	1367	
240	29	24	657598	6626233	1368	
250	32	27	657592	6626243	1369	
260	32	26	657585	6626252	1370	
270	32	27	657581	6626260	1370	
280	29	34	657575	6626268	1371	
290	28.5	36	657569	6626277	1372	
300	27	35	657564	6626285	1372	
310	30	28	657559	6626294	1373	
320	21	27	657547	6626310	1374	
330	16.5	21	657542	6626319	1376	NW

Table H. Polile Tshisa hot spring line 2: L2-20, horizontal and vertical dipole

Sta (m)	X_Dist	HD (mS/m)	VD (mS/m)	X (m)	Y (m)	Z (m)	DIRECTIO N-S
190	0	26	27	657566	6626081	1359	SE
180	10	26	22	657561	6626089	1360	
170	20	28	32	657551	6626096	1361	
160	30	26.5	26	657547	6626106	1362	
150	40	25.5	27	657542	6626115	1364	
140	50	26	29	657538	6626123	1366	
130	60	25	25.5	657533	6626134	1367	
120	70	23	27	657533	6626134	1367	
110	80	23.5	29	657528	6626141	1367	
100	90	22	22	657522	6626149	1370	
90	100	24	26.5	657520	6626161	1371	
80	110	26	28.5	657520	6626161	1370	
70	120	26	25	657512	6626170	1371	
60	130	26	20.5	657507	6626178	1371	
50	140	30	23	657498	6626186	1372	
40	150	30	31	657493	6626198	1373	
30	160	30	19	657477	6626227	1375	
20	170	23.5	16.5	657470	6626235	1376	
10	180	26.5	24	657460	6626251	1378	
0	190	25.5	23	657466	6626241	1377	NW

Table I: Polile Tshisa line 3: L3_20, horizontal and vertical dipole

Sta (m)	X-Dist	HD (mS/m)	VD (mS/m)	X (m)	Y (m)	Z (m)	D IRECTION
110	0	32	34	657472	6626232	1377	NE
100	10	40	36	657491	6626244	1376	
90	20	39	40	657499	6626250	1376	
80	30	38	24.5	657509	6626259	1376	
70	40	38	36	657515	6626266	1377	
60	50	36	47	657524	6626272	1376	
50	60	34	34	657524	6626273	1376	
40	70	40	47	657531	6626277	1374	
30	80	25.5	18.5	657540	6626284	1374	
20	90	15	20	657551	6626285	1374	
10	100	35	42	657567	6626298	1372	
0	110	36	42	657578	6626304	1373	SW

Table J: Polile Tshisa line 1 (L1_10), horizontal dipole

Sta (m)	HD (mS/m)	X (m)	Y (m)	Z (m)	Dir
0	28	657629	6625987	1355	SE
10	49	657627	6625996	1355	
20	50	657626	6626008	1356	
30	42	657628	6626016	1357	
40	36	657625	6626027	1349	
50	28.5	657623	6626039	1350	
60	22.5	657625	6626048	1350	
70	20.5	657622	6626059	1349	
80	22	657621	6626069	1349	
90	25	657619	6626080	1351	
100	21	657620	6626087	1352	
110	26	657618	6626101	1354	
120	26	657620	6626110	1355	
130	21	657619	6626121	1357	
140	18.5	657618	6626132	1358	
150	20	657618	6626141	1359	
160	25	657616	6626148	1360	
170	23	657619	6626157	1360	
180	18	657623	6626168	1361	
190	26	657620	6626175	1361	
200	27	657619	6626188	1363	
210	28	657613	6626206	1365	
220	34	657607	6626216	1366	

230	36	657602	6626224	1367	
240	32	657598	6626233	1368	
250	32	657592	6626243	1369	
260	33	657585	6626252	1370	
270	34	657581	6626260	1370	
280	32	657575	6626268	1371	
290	30	657569	6626277	1372	
300	25	657564	6626285	1372	
310	24	657559	6626294	1373	
320	29	657547	6626310	1374	
330	16	657542	6626319	1376	NW

Table K: Polile Tshisa line 1 (L1_40), horizontal dipole

Sta (m)	HD (mS/m)	X (m)	Y (m)	Z (m)	Dir
320	18.5	657627	6625996	1355	S
310	20	657626	6626008	1356	
300	22.5	657628	6626016	1357	
290	22.5	657625	6626027	1349	
280	22.5	657623	6626039	1350	
270	22.5	657625	6626048	1350	
260	21	657622	6626059	1349	
250	18.5	657621	6626069	1349	
240	17	657619	6626080	1351	
230	17.5	657620	6626087	1352	
220	20.5	657618	6626101	1354	
210	19	657620	6626110	1355	
200	15	657619	6626121	1357	
190	15	657618	6626132	1358	
180	16	657618	6626141	1359	
170	19	657616	6626148	1360	
160	13	657619	6626157	1360	
150	17	657623	6626168	1361	
140	22.5	657620	6626175	1361	
130	22	657619	6626188	1363	
120	12	657613	6626206	1365	
110	24	657607	6626216	1366	
100	26	657602	6626224	1367	
90	24	657598	6626233	1368	
80	26	657592	6626243	1369	
70	26	657585	6626252	1370	
60	26	657581	6626260	1370	
50	27	657575	6626268	1371	
40	25	657569	6626277	1372	

30	24	657564	6626285	1372	
20	27	657559	6626294	1373	
10	17	657547	6626310	1374	N

Table L: Aliwal North line 1 (L1_10), horizontal dipole

Sta (m)	HD (mS/m)	X (m)	Y (m)	Z (m)	Dir
0	170	472835	6601870	1285	SE
10	140	472828	6601871	1289	
20	120	472812	6601886	1294	
30	84	472803	6601893	1295	
40	93	472799	6601907	1296	
50	69	472778	6601939	1301	
60	80	472775	6601941	1301	
70	64	472766	6601947	1302	
80	86	472765	6601961	1303	
90	80	472765	6601961	1302	
100	150	472757	6601974	1304	
110	120	472749	6601974	1306	
120	60	472742	6601992	1308	
130	64	472737	6602001	1308	
140	84	472725	6602015	1309	
150	85	472718	6602026	1310	
160	52	472712	6602036	1310	
170	30	472707	6602043	1313	NW

Table M: Aliwal North line 1 (L1_20), horizontal dipole

Sta (m)	X_Dist	HD (mS/m)	X (m)	Y (m)	Z (m)	Dir
170	0	130.5	472835	6601870	1285	SE
160	10	130	472828	6601871	1289	
150	20	88	472812	6601886	1294	
140	30	84	472803	6601893	1295	
130	40	68	472799	6601907	1296	
120	50	82	472778	6601939	1301	
110	60	72	472775	6601941	1301	
100	70	70	472766	6601947	1302	
90	80	70	472765	6601961	1303	
80	90	120	472765	6601961	1302	
70	100	84	472757	6601974	1304	
60	110	68	472749	6601974	1306	
50	120	54	472742	6601992	1308	
40	130	54	472737	6602001	1308	
30	140	58	472725	6602015	1309	
20	150	46	472718	6602026	1310	
10	160	34	472712	6602036	1310	

0	170	19	472707	6602043	1313	NW

Table N: Aliwal North line 1 (L1_40), horizontal dipole

Sta (m)	HD (mS/m)	X (m)	Y (m)	Z (m)	Dir
10	120	472835	6601870	1285	SE
20	82	472828	6601871	1289	
30	82	472812	6601886	1294	
40	74	472803	6601893	1295	
50	60	472799	6601907	1296	
60	50	472778	6601939	1301	
70	48	472775	6601941	1301	
80	44	472766	6601947	1302	
90	69	472765	6601961	1303	
100	46	472765	6601961	1302	
110	50	472757	6601974	1304	
120	59	472749	6601974	1306	
130	38	472742	6601992	1308	
140	21	472737	6602001	1308	
150	26	472725	6602015	1309	
160	24	472718	6602026	1310	
170	48	472712	6602036	1310	NW

Table O: Aliwal North line 2 (L2_10), horizontal dipole

Sta (m)	X_Dist	HD (mS/m)	X (m)	Y (m)	Z (m)	Dir
300	0	140	472991	6601800	1334	SE
290	10	140.5	472990	6601808	1334	
280	20	190	472980	6601824	1334	
270	30	200	472970	6601835	1334	
260	40	170	472958	6601842	1333	
250	50	130.5	472951	6601853	1334	
240	60	90	472942	6601865	1334	
230	70	84	472936	6601873	1334	
220	80	86	472928	6601889	1334	
210	90	100	472920	6601898	1335	
200	100	100	472913	6601909	1334	
190	110	98	472911	6601922	1333	
180	120	92	472903	6601933	1333	
170	130	86	472898	6601947	1333	
160	140	90	472891	6601957	1333	
150	150	96	472883	6601969	1333	
140	160	80	472874	6601977	1333	
130	170	81	472868	6601989	1334	
120	180	98	472862	6602000	1334	
110	190	110	472851	6602012	1333	
100	200	84	472844	6602018	1333	

90	210	76	472828	6602022	1334	
80	220	76	472817	6602028	1333	
70	230	76	472807	6602031	1333	
60	240	74	472794	6602036	1333	
50	250	80	472782	6602041	1333	
40	260	70	472770	6602048	1334	
30	270	68	472762	6602056	1334	
20	280	43	472750	6602065	1334	
10	290	24	472735	6602072	1334	
0	300	14	472720	6602080	1335	NW

Table P: Aliwal North line 2 (L2_20), horizontal dipole

Sta (m)	HD (mS/m)	X (m)	Y (m)	Z (m)	Dir
0	120.5	472991	6601800	1334	SE
10	130	472990	6601808	1334	
20	150	472980	6601824	1334	
30	160	472970	6601835	1334	
40	180	472958	6601842	1333	
50	150	472951	6601853	1334	
60	120	472942	6601865	1334	
70	100	472936	6601873	1334	
80	90	472928	6601889	1334	
90	88	472920	6601898	1335	
100	90	472913	6601909	1334	
110	94	472911	6601922	1333	
120	88	472903	6601933	1333	
130	84	472898	6601947	1333	
140	84	472891	6601957	1333	
150	-21	472883	6601969	1333	
160	90	472874	6601977	1333	
170	61	472868	6601989	1334	
180	76	472862	6602000	1334	
190	98	472851	6602012	1333	
200	98	472844	6602018	1333	
210	70	472828	6602022	1334	
220	72	472817	6602028	1333	
230	82	472807	6602031	1333	
240	82	472794	6602036	1333	
250	58	472782	6602041	1333	
260	66	472770	6602048	1334	
270	58	472762	6602056	1334	
280	50	472750	6602065	1334	
290	36	472735	6602072	1334	
300	36	472720	6602080	1335	NW

Table Q: Aliwal North line 2 (L2_40), horizontal dipole

Sta (m)	HD (mS/m)	X (m)	Y (m)	Z (m)	Dir
0	120	472991	6601800	1334	SE
10	140	472990	6601808	1334	
20	110.5	472980	6601824	1334	
30	110	472970	6601835	1334	
40	120	472958	6601842	1333	
50	92	472951	6601853	1334	
60	84	472942	6601865	1334	
70	78	472936	6601873	1334	
80	72	472928	6601889	1334	
90	70	472920	6601898	1335	
100	66	472913	6601909	1334	
110	68	472911	6601922	1333	
120	66	472903	6601933	1333	
130	12	472898	6601947	1333	
140	17	472891	6601957	1333	
150	52	472883	6601969	1333	
160	120	472874	6601977	1333	
170	60	472868	6601989	1334	
180	60	472862	6602000	1334	
190	52	472851	6602012	1333	
200	110.5	472844	6602018	1333	
210	120	472828	6602022	1334	
220	200	472817	6602028	1333	
230	140	472807	6602031	1333	
240	50	472794	6602036	1333	
250	42	472782	6602041	1333	
260	38	472770	6602048	1334	
270	24	472762	6602056	1334	
280	20	472750	6602065	1334	
290	16	472735	6602072	1334	NW

Table R: Polile Tshisa radio-elements and their concentrations

K[ppm]	K[cpm]	U[ppm]	U[cpm]	Th[ppm]	Th[cpm]	Dose	Dose units	Latitude (°)	Longitude (°)
0.6	52.9	2.5	18.1	3.4	7.5	37.3	nSv/h	-30.488137	28.642378
0.5	50.8	3.1	22.3	4.4	9.6	42.2	nSv/h	-30.488137	28.642378
0.9	71.7	1.3	18.1	8.5	17.9	51.1	nSv/h	-30.488143	28.64238
0.8	59.1	0.1	11.8	8.6	17.9	41.9	nSv/h	-30.488115	28.642377
0.6	71.7	2.7	32.7	14.5	30.5	74.5	nSv/h	-30.488028	28.64235
0.6	59.1	1.5	20.2	9.5	20	51.2	nSv/h	-30.487965	28.642312
0.7	50.8	0	9.7	10.7	22.1	46.1	nSv/h	-30.488085	28.642372
0.6	54.9	1.5	20.2	9.5	20	50	nSv/h	-30.488112	28.642368

0.7	63.3	0.3	20.2	14.7	30.5	60.8	nSv/h	-30.488093	28.64235
0.9	75.8	0.7	22.3	14.6	30.5	66.2	nSv/h	-30.488003	28.642342
1.3	86.3	0	13.9	15.8	32.6	71.4	nSv/h	-30.48791	28.642297
1.1	80	0.6	18.1	11.6	24.2	58.5	nSv/h	-30.487827	28.642277
0.7	63.3	2	20.2	7.5	15.8	48.9	nSv/h	-30.487707	28.642292
0.7	57	0.8	13.9	7.6	15.8	41.5	nSv/h	-30.487603	28.642263
1.1	69.6	0	7.6	10.7	22.1	52.3	nSv/h	-30.487498	28.642237
1.2	82.1	0	13.9	12.7	26.3	60.3	nSv/h	-30.487375	28.642203
1.1	86.3	2	24.4	10.5	22.1	64.3	nSv/h	-30.487248	28.642188
0.5	63.3	4.5	30.6	5.3	11.7	55	nSv/h	-30.487153	28.642185
0.5	61.2	4.3	28.5	4.3	9.6	50.8	nSv/h	-30.487037	28.64218
0.7	65.4	3.9	26.4	4.3	9.6	50.1	nSv/h	-30.48694	28.64217
1	75.8	2	18.1	5.4	11.7	47.2	nSv/h	-30.486848	28.642155
1	82.1	3	24.3	6.4	13.7	56.3	nSv/h	-30.486748	28.64215
0.8	90.5	4.8	39	10.3	22.1	78.7	nSv/h	-30.486633	28.642157
0.8	73.8	1.1	24.4	14.6	30.5	67.6	nSv/h	-30.486538	28.642162
1.1	96.7	3	30.6	11.4	24.2	74.6	nSv/h	-30.486492	28.642187
1	82.1	1.8	24.4	11.5	24.2	64.8	nSv/h	-30.486432	28.642247
0.5	57	3.2	26.4	7.4	15.8	52.9	nSv/h	-30.486397	28.642353
0.2	42.3	4.2	26.4	3.3	7.5	41.9	nSv/h	-30.486323	28.642483
0.7	65.3	3.7	24.3	3.3	7.5	46.4	nSv/h	-30.486232	28.64255
0.7	65.3	3	24.3	6.4	13.7	51.5	nSv/h	-30.48616	28.64261
0.6	59.1	2.1	22.3	8.5	17.9	51.4	nSv/h	-30.486097	28.642712
0.6	48.7	0	11.8	10.7	22.1	44.7	nSv/h	-30.486035	28.642817
0.6	52.9	1.6	18.1	7.5	15.8	44.1	nSv/h	-30.485935	28.64291
0.5	59.1	3.4	26.4	6.4	13.7	51.7	nSv/h	-30.48586	28.643012
0.5	59.1	4.7	30.6	4.2	9.6	52.1	nSv/h	-30.485783	28.643112
0.5	59.1	3.7	26.4	5.3	11.7	50	nSv/h	-30.4857	28.64318
0.5	75.9	6.2	41.1	6.2	13.7	69.7	nSv/h	-30.485592	28.643208
0.8	111.5	8.2	60	13.1	28.4	108.8	nSv/h	-30.48549	28.643207
1.4	170.2	11.4	80.9	15.9	34.7	149.3	nSv/h	-30.485382	28.643258
1.7	178.6	9.3	76.7	21.1	45.2	156.4	nSv/h	-30.485333	28.64333
1.8	153.4	5.1	49.5	17.3	36.8	117.8	nSv/h	-30.485357	28.643405
1.3	113.6	3.6	39	15.4	32.6	93.7	nSv/h	-30.485388	28.643462
1.6	107.3	0	18.1	16.8	34.7	79.3	nSv/h	-30.48543	28.643547
1.3	101	1	24.4	14.6	30.5	75.2	nSv/h	-30.48547	28.643643
1.3	94.6	1.1	22.3	12.6	26.3	68.1	nSv/h	-30.485523	28.643763
1	84.2	0.7	26.4	17.7	36.7	77.4	nSv/h	-30.485567	28.64385
0.4	54.9	4.3	28.5	4.3	9.6	49.1	nSv/h	-30.487827	28.642122
0.5	65.4	4.9	32.7	5.2	11.7	57.5	nSv/h	-30.487802	28.642083
0.8	75.8	4.3	28.5	4.3	9.6	54.9	nSv/h	-30.487765	28.642045
1	80	3.1	22.3	4.3	9.6	50.4	nSv/h	-30.487715	28.641993
1.1	82.1	1.8	18.1	6.5	13.7	50.6	nSv/h	-30.487658	28.641963

0.8	63.3	2	18.1	5.4	11.6	43.6	nSv/h	-30.487612	28.641935
1.1	77.9	0.7	13.9	7.5	15.8	47.3	nSv/h	-30.487565	28.641908
0.9	63.3	0.6	11.8	6.6	13.7	39.6	nSv/h	-30.487508	28.641873
0.8	52.8	0	5.5	9.7	20	44.9	nSv/h	-30.487433	28.641837
0.3	27.8	0	7.6	7.7	15.8	30.2	nSv/h	-30.487367	28.641793
0.1	25.7	1.7	16	5.5	11.6	31.2	nSv/h	-30.487312	28.641752
0.1	27.8	2.4	18.1	4.4	9.6	31.9	nSv/h	-30.487258	28.641705
0.1	27.8	2.1	18.1	5.5	11.6	33.7	nSv/h	-30.4872	28.641673
0.1	34	4.2	26.4	3.3	7.5	39.6	nSv/h	-30.487127	28.641645
0.1	36.1	3.5	26.4	6.4	13.7	45.3	nSv/h	-30.48706	28.641608
0.3	48.7	3	26.4	8.4	17.9	52.2	nSv/h	-30.48699	28.641558
0.5	46.6	0.2	16	11.7	24.2	47.2	nSv/h	-30.48695	28.641507
0.3	44.5	2.1	24.3	10.5	22.1	52.5	nSv/h	-30.486913	28.64145
0.2	44.5	4.3	30.6	6.3	13.7	51.4	nSv/h	-30.486867	28.641387
0	48.7	6.2	43.2	8.2	17.9	67.6	nSv/h	-30.486815	28.64135
0.1	52.9	6.5	41.1	5.1	11.7	61.5	nSv/h	-30.486762	28.641315
0.2	54.9	5.7	36.9	5.2	11.7	58.3	nSv/h	-30.486698	28.641278
0.6	59.1	3	24.3	6.4	13.7	49.8	nSv/h	-30.48665	28.641238
0.7	50.7	0.6	11.8	6.6	13.7	36.1	nSv/h	-30.486575	28.641195
0.5	38.2	0	7.6	7.7	15.8	33.3	nSv/h	-30.486493	28.641157
0.3	23.6	0	3.4	5.7	11.6	23.9	nSv/h	-30.486428	28.641098
0.4	27.7	0	5.5	8.7	17.9	34.3	nSv/h	-30.486363	28.641045
0.5	34	0	3.4	6.7	13.7	30.3	nSv/h	-30.486302	28.640992
0.4	38.2	0.9	11.8	5.5	11.6	30.9	nSv/h	-30.486233	28.640935
0.5	40.3	0.7	9.7	4.5	9.6	27.9	nSv/h	-30.486165	28.640877
0.4	38.2	0.9	11.8	5.5	11.6	30.9	nSv/h	-30.486087	28.640807
0.4	42.4	0	16	12.7	26.3	47.8	nSv/h	-30.48602	28.640745
0.3	29.8	0	11.8	12.8	26.3	45.7	nSv/h	-30.485945	28.640688
0.4	44.5	2.3	18.1	4.4	9.6	36.7	nSv/h	-30.485875	28.64064
0.3	40.3	2	20.2	7.5	15.8	42.5	nSv/h	-30.485878	28.64233
0.2	29.9	1.2	16	7.6	15.8	35.8	nSv/h	-30.485848	28.642405
0.1	27.8	2.5	20.2	5.4	11.7	35.6	nSv/h	-30.485813	28.642462
0.4	40.3	1.4	16	6.5	13.7	37	nSv/h	-30.485792	28.642515
0.7	61.2	2.1	18.1	5.4	11.7	43	nSv/h	-30.485765	28.642587
0.8	61.2	1.4	16	6.5	13.7	42.9	nSv/h	-30.485727	28.642682
0.6	50.8	2.6	18.1	3.4	7.5	36.7	nSv/h	-30.485695	28.642777
0.5	46.6	2.6	18.1	3.4	7.5	35.5	nSv/h	-30.48565	28.642852
0.3	44.5	3.3	24.3	5.4	11.7	44	nSv/h	-30.485592	28.642905
0.4	46.5	1.8	20.1	8.5	17.9	45.9	nSv/h	-30.485555	28.642925
0.2	42.3	1.8	24.3	11.5	24.2	53.6	nSv/h	-30.485545	28.642943
0.2	36.1	1.7	22.2	10.5	22.1	48.2	nSv/h	-30.485543	28.642945
0	32	3.7	28.5	7.4	15.8	48.1	nSv/h	-30.485523	28.642985
0	29.9	2.8	24.3	7.4	15.8	43.3	nSv/h	-30.485487	28.64308

0.6	69.6	2.2	32.7	16.6	34.6	77.4	nSv/h	-30.485478	28.6431
0.7	73.8	2.1	28.5	13.5	28.4	69.6	nSv/h	-30.485908	28.643223
0.3	61.2	3	36.9	16.5	34.6	78.8	nSv/h	-30.485952	28.643168
0.2	63.3	6.6	45.3	8.2	17.9	73.4	nSv/h	-30.485992	28.643083
0.4	61.2	4.1	34.8	10.4	22.1	66.7	nSv/h	-30.48605	28.642995
0.9	67.5	0.4	16	10.6	22.1	51.4	nSv/h	-30.486117	28.642887
0.8	63.3	0	13.9	16.8	34.6	67.9	nSv/h	-30.486172	28.642805
0.9	69.6	0	18.1	17.8	36.7	71.5	nSv/h	-30.486222	28.642718
1	71.7	0	13.9	14.8	30.5	63.8	nSv/h	-30.486275	28.64262
0.7	63.3	1.5	20.2	9.5	20	52.3	nSv/h	-30.486307	28.642553
0.3	42.4	2.8	24.3	7.4	15.8	46.9	nSv/h	-30.486342	28.642463
0.3	48.7	3.4	28.5	8.4	17.9	54.1	nSv/h	-30.486393	28.642378
1.1	86.3	0.2	20.2	14.7	30.5	67.3	nSv/h	-30.486442	28.64228
1.5	103	0	16	14.7	30.5	72.2	nSv/h	-30.4865	28.642187

Table S: Aliwal North radio-elements and their concentrations

K[ppm]	K[cpm]	U[ppm]	U[cpm]	Th[ppm]	Th[cpm]	Dose	Dose units	Latitude (^{o})	Longitude (^{o})
0.4	40.2	2.6	16	1.4	3.3	28.4	nSv/h	0	0
0.4	40.3	2.6	18.1	3.4	7.5	33.7	nSv/h	-30.715888	26.716107
0.7	44.4	0	5.5	4.6	9.6	26	nSv/h	-30.71599	26.715805
0.7	48.6	1.4	9.7	1.4	3.3	25.1	nSv/h	-30.715715	26.716197
0.5	40.3	0.7	9.7	4.5	9.6	27.9	nSv/h	-30.715712	26.716192
0.4	40.3	1.5	13.9	4.5	9.6	31.7	nSv/h	-30.7157	26.716255
0.6	46.5	1.3	13.9	5.5	11.6	35.1	nSv/h	-30.715675	26.716265
0.7	52.8	1.6	11.8	2.4	5.4	29.9	nSv/h	-30.715663	26.716247
0.9	52.8	0.6	5.5	1.5	3.3	22.5	nSv/h	-30.715643	26.716217
1	59.1	0.1	5.5	3.6	7.5	27.7	nSv/h	-30.71563	26.716148
0.9	59.1	0.5	7.6	3.5	7.5	29.6	nSv/h	-30.715587	26.716088
0.7	46.5	0.3	7.6	4.6	9.5	27.7	nSv/h	-30.715507	26.715972
0.7	48.5	1.2	9.7	2.5	5.4	26.8	nSv/h	-30.715435	26.715902
0.9	63.2	1.3	11.8	3.5	7.5	34.5	nSv/h	-30.715355	26.715862
0.9	52.8	0.4	3.4	0.5	1.2	18.9	nSv/h	-30.71525	26.715785
0.8	57	2	13.9	2.4	5.4	33	nSv/h	-30.71516	26.715688
0.8	57	2	13.9	2.4	5.4	33	nSv/h	-30.715135	26.715605
0.9	63.3	1	13.9	6.5	13.7	41.5	nSv/h	-30.715077	26.715523
1.1	67.5	0.3	7.6	4.6	9.6	33.6	nSv/h	-30.714927	26.715442
0.8	57	1.1	11.8	4.5	9.6	34.5	nSv/h	-30.714865	26.7154
1	67.5	2.2	13.9	1.4	3.3	34.2	nSv/h	-30.714823	26.715385
0.8	59.1	1.7	13.9	3.4	7.5	35.3	nSv/h	-30.714805	26.71536
0.6	48.7	2	13.9	2.4	5.4	30.6	nSv/h	-30.714778	26.71529
0.7	48.7	1.4	9.7	1.5	3.3	25.1	nSv/h	-30.714712	26.715243
0.6	40.3	1.7	9.7	0.4	1.2	21.1	nSv/h	-30.714598	26.715163
0.7	52.9	1.6	11.8	2.4	5.4	29.9	nSv/h	-30.714547	26.71513

0.7	54.9	1.9	16	4.5	9.6	37.7	nSv/h	-30.714487	26.715092
0.7	63.3	2.9	22.3	5.4	11.7	47.4	nSv/h	-30.714417	26.715057
0.9	65.4	1.7	13.9	3.4	7.5	37	nSv/h	-30.714342	26.715092
1.2	77.9	2	11.8	0.4	1.2	33.6	nSv/h	-30.714278	26.715127
1.7	98.8	0.2	7.6	4.5	9.6	42.4	nSv/h	-30.714252	26.715078
1.6	103	1.1	16	7.5	15.8	56.3	nSv/h	-30.714187	26.715017
1.4	113.3	1.5	30.6	17.6	36.7	89.4	nSv/h	-30.714238	26.714917
1.4	100.8	1.1	22.2	12.6	26.3	69.8	nSv/h	-30.71394	26.715317
0.9	71.7	1.5	18.1	7.5	15.8	49.4	nSv/h	-30.713927	26.715365
1.1	69.6	0.7	9.7	4.5	9.6	36.1	nSv/h	-30.713907	26.715435
0.3	38.2	2.6	18.1	3.4	7.5	33.2	nSv/h	-30.713923	26.715563
0.5	42.4	2.2	13.9	1.4	3.3	27.2	nSv/h	-30.713987	26.715622
1.1	63.3	0	3.4	2.6	5.4	25.7	nSv/h	-30.714042	26.715693
1.6	88.3	0.1	3.4	1.5	3.3	30.6	nSv/h	-30.714118	26.715792
1.6	90.4	0	3.4	4.6	9.6	40.2	nSv/h	-30.714165	26.71593
1.4	86.3	0	7.6	7.6	15.8	47.3	nSv/h	-30.7142	26.716068
0.8	52.8	0	7.6	7.7	15.8	37.6	nSv/h	-30.714253	26.716187
1.1	65.3	0.7	7.6	2.5	5.4	29.6	nSv/h	-30.714313	26.7163
0.7	48.6	1.4	9.7	1.4	3.3	25.1	nSv/h	-30.714367	26.716435
0.8	57	1.8	11.8	1.4	3.3	29.4	nSv/h	-30.714458	26.716507
0.1	25.7	2.4	16	2.4	5.4	26.1	nSv/h	-30.714548	26.71661
0.3	29.8	1.2	9.7	2.5	5.4	21.5	nSv/h	-30.714638	26.716657
0.1	34	4	26.4	4.3	9.5	41.2	nSv/h	-30.714733	26.716752
0.5	50.7	3.6	22.2	2.3	5.4	38.7	nSv/h	-30.714838	26.716792
0.9	71.6	3.8	22.2	1.3	3.3	42.9	nSv/h	-30.71494	26.716872
1.1	71.6	1.4	9.7	1.4	3.3	31.6	nSv/h	-30.715025	26.716928
1.2	71.7	0	7.6	5.6	11.6	36.5	nSv/h	-30.715117	26.716997
0.7	59.1	2.7	20.2	4.4	9.6	42.6	nSv/h	-30.715245	26.71706
0.7	59.1	2.1	18.1	5.4	11.6	42.4	nSv/h	-30.715358	26.717125
0.8	54.9	0	7.6	8.7	17.9	41.5	nSv/h	-30.715465	26.717227
1.1	65.4	0	5.5	8.7	17.9	45.3	nSv/h	-30.715553	26.717322
0.8	61.2	0.3	13.9	9.6	20	46.1	nSv/h	-30.715657	26.71738
1.1	75.8	1.2	13.9	5.5	11.7	43.4	nSv/h	-30.71575	26.71744
0.8	65.4	2.2	20.2	6.4	13.7	47.8	nSv/h	-30.715843	26.717512
1	73.8	1.4	16	6.5	13.7	46.4	nSv/h	-30.715938	26.717592
0.8	67.5	1.4	22.3	11.6	24.2	58.8	nSv/h	-30.716025	26.717668
0.9	69.6	0	16	12.7	26.3	55.8	nSv/h	-30.716113	26.717742
1.2	84.2	0	16	15.8	32.5	70	nSv/h	-30.716195	26.717818
1.1	82	0.8	18.1	10.6	22.1	57.3	nSv/h	-30.716297	26.717873
1.6	98.7	0	11.8	10.6	22.1	59.3	nSv/h	-30.7164	26.71794

Table S: Badfontein radio-elements and their concentrations

K[ppm]	K[cpm]	U[ppm]	U[cpm]	Th[ppm]	Th[cpm]	Dose	Dose units	Latitude (°)	Longitude (°)
0.7	42.4	0	3.4	5.7	11.6	29.5	nSv/h	-30.647988	26.543533
0.9	52.8	0	3.4	4.6	9.6	29.2	nSv/h	-30.647982	26.543525
0.8	57	1.7	13.9	3.4	7.5	34.7	nSv/h	-30.647967	26.5435
0.6	54.9	1.6	18.1	7.5	15.8	44.6	nSv/h	-30.647917	26.543448
0.3	36.1	1.4	18.1	8.5	17.9	41.1	nSv/h	-30.647842	26.543437
0.5	42.4	0.4	11.8	7.6	15.8	35.4	nSv/h	-30.647758	26.543415
0.9	54.9	0.5	7.6	3.5	7.5	28.4	nSv/h	-30.64767	26.54339
0.9	61.2	0.9	9.7	3.5	7.5	32	nSv/h	-30.647577	26.543345
1	61.2	0.5	7.6	3.5	7.5	30.2	nSv/h	-30.647507	26.543282
0.7	63.3	2.7	20.2	4.4	9.6	43.8	nSv/h	-30.647422	26.543223
0.9	69.5	2.7	20.2	4.4	9.6	45.6	nSv/h	-30.647333	26.543155
0.7	59.1	2.5	18.1	3.4	7.5	39	nSv/h	-30.647245	26.543078
0.6	50.7	2.9	16	0.3	1.2	29.7	nSv/h	-30.647153	26.543
0.7	52.8	2	13.9	2.4	5.4	31.8	nSv/h	-30.647055	26.542928
0.8	61.2	1.6	16	5.5	11.6	41.1	nSv/h	-30.646958	26.54286
0.9	65.3	0.3	11.8	7.6	15.8	41.9	nSv/h	-30.646858	26.542798
0.7	54.9	0.8	13.9	7.6	15.8	40.9	nSv/h	-30.646773	26.542735
1.1	67.5	0.5	7.6	3.5	7.5	31.9	nSv/h	-30.646678	26.542657
1.2	75.7	0.9	9.7	3.5	7.5	36.1	nSv/h	-30.64657	26.542573
1.3	90.4	1.8	16	4.4	9.5	47.6	nSv/h	-30.646473	26.5425
1.4	92.6	2.3	16	2.4	5.4	44.8	nSv/h	-30.646372	26.542428
1.1	82.1	2.4	20.2	5.4	11.7	50.8	nSv/h	-30.646277	26.542357
1.2	80	2.3	16	2.4	5.4	41.3	nSv/h	-30.646175	26.542292
1.1	73.7	1.7	13.9	3.4	7.5	39.4	nSv/h	-30.64608	26.542228
1	65.4	1.3	11.8	3.5	7.5	35.1	nSv/h	-30.645975	26.542158
1	69.6	0.7	13.9	7.6	15.8	45	nSv/h	-30.645865	26.542083
0.9	71.7	1.5	20.2	9.5	20	54.7	nSv/h	-30.64576	26.542005
1.3	94.7	2.2	20.2	6.4	13.7	56	nSv/h	-30.645657	26.541928
1.1	80	2	18.1	5.4	11.7	48.3	nSv/h	-30.645557	26.541858
1.3	84.2	1.4	13.9	4.5	9.6	44	nSv/h	-30.645465	26.54179
0.9	71.7	1.7	20.2	8.5	17.9	53	nSv/h	-30.645362	26.541722
1	71.7	0.3	13.9	9.6	20	49	nSv/h	-30.645258	26.541658
0.6	61.2	1.2	22.3	12.6	26.3	58.7	nSv/h	-30.645163	26.541592
1.2	84.2	0.9	16	8.5	17.9	52.7	nSv/h	-30.645068	26.541528
1.5	90.4	0.6	9.7	4.5	9.5	41.9	nSv/h	-30.644968	26.541462
1.7	105	0.7	11.8	5.5	11.6	49.6	nSv/h	-30.644862	26.541395
1.4	92.5	0.9	13.9	6.5	13.7	49.7	nSv/h	-30.644788	26.541327
1	84.2	3.2	24.3	5.3	11.7	55.2	nSv/h	-30.644753	26.541297
0.8	71.7	3	24.3	6.4	13.7	53.4	nSv/h	-30.64643	26.542487
0.6	48.7	0	13.9	11.7	24.2	47.2	nSv/h	-30.646383	26.542552

1.2	71.7	0	5.5	11.8	24.2	57	nSv/h	-30.646327	26.542652
1.6	100.9	1.4	13.9	4.4	9.6	48.7	nSv/h	-30.64628	26.542745
1.5	105.1	2.9	20.2	3.3	7.5	53.9	nSv/h	-30.646225	26.542845
1.5	92.4	1.5	11.8	2.4	5.4	41	nSv/h	-30.646158	26.542968
1.4	82	0	5.5	4.6	9.5	37	nSv/h	-30.646107	26.543042
1.2	67.4	0	3.4	4.6	9.5	33.5	nSv/h	-30.646047	26.543135
1.1	65.4	0.7	7.6	2.5	5.4	29.6	nSv/h	-30.64599	26.543218
0.9	61.2	0.4	9.7	5.6	11.6	35.5	nSv/h	-30.645935	26.54332
0.8	61.2	1.6	16	5.5	11.6	41.1	nSv/h	-30.645887	26.54343
0.7	63.3	2.2	20.2	6.4	13.7	47.2	nSv/h	-30.645833	26.543542
0.7	50.7	0.9	11.8	5.5	11.6	34.4	nSv/h	-30.64578	26.543648
0.5	44.5	1.9	16	4.5	9.6	34.7	nSv/h	-30.645727	26.543758
0.8	61.2	2.1	16	3.4	7.5	37.7	nSv/h	-30.645668	26.543868
1.1	77.9	1.4	16	6.5	13.7	47.5	nSv/h	-30.645607	26.54397
1.2	84.2	1.8	18.1	6.5	13.7	51.2	nSv/h	-30.645552	26.544058
1	65.4	1.1	11.8	4.5	9.6	36.8	nSv/h	-30.645478	26.544142
0.6	44.5	0	7.6	7.7	15.8	35.1	nSv/h	-30.64544	26.544203
0.9	50.7	0	3.4	5.7	11.6	31.9	nSv/h	-30.645362	26.544273
0.8	57	1.5	13.9	4.5	9.6	36.4	nSv/h	-30.6453	26.544372
0.8	61.1	2.4	16	2.4	5.4	36	nSv/h	-30.645247	26.54446
0.6	44.5	1.1	11.8	4.5	9.6	31	nSv/h	-30.64521	26.544535
0.7	48.7	1.3	11.8	3.5	7.5	30.4	nSv/h	-30.645593	26.543622
0.8	50.8	0.8	7.6	2.5	5.4	25.5	nSv/h	-30.645622	26.543652
0.9	54.8	0.8	7.6	2.5	5.4	26.7	nSv/h	-30.645702	26.543737
0.8	52.8	0	5.5	6.6	13.7	35	nSv/h	-30.645785	26.543825
1.1	65.3	0	5.5	7.7	15.8	41.9	nSv/h	-30.645848	26.543907
1.1	75.8	1.2	13.9	5.5	11.7	43.4	nSv/h	-30.645922	26.544002
1.2	84.2	1.6	16	5.5	11.6	47.6	nSv/h	-30.645982	26.544092
1.1	75.8	0.8	11.8	5.5	11.6	41.4	nSv/h	-30.646052	26.544183
1.1	67.4	0	5.5	6.6	13.7	39.3	nSv/h	-30.646117	26.544267
1	61.2	0	5.5	4.6	9.6	30.9	nSv/h	-30.646175	26.544343
0.8	54.9	0.7	9.7	4.5	9.6	32	nSv/h	-30.646235	26.544432
0.9	59.1	0.5	7.6	3.5	7.5	29.6	nSv/h	-30.646298	26.544507
1.3	80	0.6	9.7	4.5	9.6	39	nSv/h	-30.646375	26.544592
1.2	75.8	0.6	9.7	4.5	9.6	37.9	nSv/h	-30.64645	26.544678
0.9	67.5	0.7	13.9	7.6	15.8	44.4	nSv/h	-30.646537	26.544763
0.6	52.8	1.4	16	6.5	13.7	40.5	nSv/h	-30.646615	26.544848
0.6	48.7	1.5	13.9	4.5	9.6	34	nSv/h	-30.646677	26.544923
0.8	52.8	0.4	9.7	5.6	11.6	33.1	nSv/h	-30.646737	26.54498
0.6	48.7	0.6	11.8	6.6	13.7	35.5	nSv/h	-30.64681	26.545063
0.6	44.4	0.4	11.8	7.6	15.8	36	nSv/h	-30.646903	26.545162
0.8	59	0.1	11.8	8.6	17.9	41.8	nSv/h	-30.646953	26.545213

APPENDIX B: List of peer reviewed papers related to this project

Uranium, thorium and potassium occurrences in the vicinity of hot springs in the northern neotectonic belt in the Eastern Cape Province, South Africa. Journal of Radioanal Nuclear Chemistry (2014) 301:351–363. Springer.

Neotectonic belts, remote sensing and groundwater potentials in the Eastern Cape Province, South Africa. International Journal of Water Resources and Environmental Engineering, Vol.5 (6), pp.332-350, June, 2013.
http://www.academicjournals.org/article/article1383046118_Madi and Zhao.pdf

Insights on Structural, Petrographical, Mineralogical and Geochemical Approach on the Grahamstown Kaolin Deposit Genesis in the Eastern Cape, South Africa. International Journal of Sciences: Basic and Applied Research (IJSBAR)(2013) Volume 10, No 1, pp 146-163

The Role of Extensional Fractures and Quartz veins in the Formation of Kaolin Deposit from the Dwyka Tillite in Grahamstown, Eastern Cape Province, South Africa. 1st International Conference on Clays and Clay Minerals in Africa and 2nd International Conference on Geophagia in southern Africa. Bloemfontein, 19-21 October 2011.